

**OZONE RETRIEVAL ERRORS ASSOCIATED WITH CLOUDS IN TOTAL  
OZONE MAPPING SPECTROMETER (TOMS) DATA**

by

**XIONG LIU**

**A DISSERTATION**

**Submitted in partial fulfillment of the requirements  
for the degree of Doctor of Philosophy in  
The Department of Atmospheric Science  
of  
The School of Graduate Studies  
of  
The University of Alabama in Huntsville**

**HUNTSVILLE, ALABAMA**

**2002**

**DISSERTATION APPROVAL FORM**

Submitted by Xiong Liu in partial fulfillment of the requirements for the degree of Doctor of Philosophy in Atmospheric Science.

Accepted on behalf of the Faculty of the School of Graduate Studies by the dissertation committee:

\_\_\_\_\_ Committee Chair  
(Date)

\_\_\_\_\_

\_\_\_\_\_

\_\_\_\_\_

\_\_\_\_\_

\_\_\_\_\_

\_\_\_\_\_ Department Chair

\_\_\_\_\_ College Dean

\_\_\_\_\_ Graduate Dean

**DISSERTATION APPROVAL FORM**

Submitted by Xiong Liu in partial fulfillment of the requirements for the degree of Doctor of Philosophy in Atmospheric Science.

Accepted on behalf of the Faculty of the School of Graduate Studies by the dissertation committee:

M. Neuchard 11/15/02 Committee Chair  
(Date)

P. K. Bhasia

Stephen A. Floyd

D. Horn

Sunder. A. C.

M. Neuchard for Kim

R. Melch Department Chair

J. J. College Dean

A. J. H. 11/15/02 Graduate Dean

## ABSTRACT

The School of Graduate Studies  
The University of Alabama in Huntsville

Degree Doctor of Philosophy College/Dept. Science/Atmospheric Science

Name of Candidate Xiong Liu

Title Ozone Retrieval Errors Associated with Clouds in Total Ozone Mapping Spectrometer (TOMS) Data.

This study characterizes TOMS Ozone Retrieval Errors (OREs) associated with incorrect Cloud-Top Pressures (CTPs) and with assuming opaque Lambertian clouds, investigates these errors' effects on tropospheric ozone derivation, and analyzes ozone anomalies over TOMS data. Large errors occurring in TOMS assumed CTPs and inaccurate CTP-caused OREs are most significantly from inappropriately added ozone below clouds. Because OREs are usually within the TOMS retrieval precision when Cloud Optical Depth (COD)  $\geq 20$ , assuming angular-independent cloud reflection is good. Because of In-Cloud Ozone Absorption Enhancement (ICOAEN), assuming opaque clouds can introduce large positive OREs even for optically thick clouds. For a 2-12 km water cloud of COD 40 with 20.8 DU ozone homogeneously distributed inside the cloud, the ORE is 17.8 DU at nadir view. The ICOAEN effect depends strongly on viewing geometry and inter-cloud ozone amount and distribution; it is typically 5-13 DU over the tropical Atlantic and Africa and 1-7 DU over the tropical Pacific for deep convective clouds. The TOMS Partial Cloud Model (PCM) is good because negative PCM effect partly cancels other positive errors. At COD  $\leq 5$ , the TOMS algorithm retrieves approximately the correct total ozone because of compensating errors. With increasing COD up to 20-40, negative PCM effect decreases more dramatically than positive effects, so overall positive ORE increases and is dominated by the ICOAEN effect. The ICOAEN effect can largely underestimate tropospheric ozone derived from cloudy/clear difference techniques. The convective cloud differential and cloud-clear pair methods use minimum ozone above clouds to cancel positive errors. A Positive or Negative Ozone Anomaly (POA/NOA) is defined to occur if the ozone/reflectivity correlation coefficient in a region is  $\geq 0.5$  or  $\leq -0.5$ . Average fractions of OA occurrence are 31.8% and 35.8% in Nimbus-7 and Earth-Probe TOMS data, respectively. Most tropical NOAs result from large



cloud-height errors; corrections lead to 50-70% POAs in the tropics because of mainly the ICOAEN effect. POAs with fractions of 30-60% occur in marine stratocumulus regions west of South Africa and South America. OREs over clear and cloudy areas cause about half the ozone/reflectivity slope; greater ozone production from frequent low-altitude clouds and rich ozone precursors may cause the remainder. The knowledge of TOMS OREs has important implications for ozone/trace gas retrieval from other satellites.

Abstract Approval:

Committee Chair

M. J. Church 11/18/02  
(Date)

Department Chair

[Signature]

Graduate Dean

[Signature] 12/15/02

## ACKNOWLEDGMENTS

First and foremost I earnestly thank my advisor, Dr. Mike Newchurch, for his exceptional guidance, constant encouragement, and constructive discussions through my graduate study. I am indebted to Dr. Jae Kim for sharing his enthusiasm in this research and his knowledge in TOMS applications. I would like to thank Dr. Pawan K. Bhartia, Dr. Sundar Christopher, and Dr. Qingyuan Han for their valuable suggestions and comments. I thank Dr. Charles Wellemeyer, Dr. John Qu, Dr. Xiaoping Bao, Dr. Richard McPeters, Dr. Robert Hudson, Dr. Jerry Ziemke, and Dr. Susil Chandra for enlightening discussions during my summer study at GSFC. My appreciation goes to Dr. Rob Loughman for providing technical assistance in setting up the Gauss-Seidel radiative transfer model.

I appreciate all the members of the ozone group for their help and support. Thanks to all my friends and colleagues in the Department of Atmospheric Science for their help and the wonderful time we enjoyed together.

Thanks to my parents for their expectation, encouragement, and support since my childhood. Special thanks to my wife, Dan Liu, for her unconditional support.

This work was supported under NASA grant NAG5-10965 and NAG5-11096.

## TABLE OF CONTENTS

|  |      |
|--|------|
| LIST OF FIGURES .....  | x    |
| LIST OF TABLES .....   | xvi  |
| LIST OF ACRONYMS AND ABBREVIATIONS .....   | xvii |
| LIST OF SYMBOLS .....  | xx   |
| CHAPTER  |      |
| 1. INTRODUCTION .....  | 1    |
| 1. Background and Motivation .....   | 1    |
| 2. Problems over Cloudy Areas in TOMS Data.....  | 3    |
| 3. Potential Sources of Ozone Retrieval Errors Associated with Clouds in TOMS Data ..... | 4    |
| 4. Objectives and Organizations .....  | 6    |
| 2. TOMS INSTRUMENTS, TOMRAD, AND TOMS V7 ALGORITHM .....                                 | 8    |
| 1. TOMS Instruments .....  | 8    |
| 2. TOMRAD .....  | 9    |
| 3. Radiance Calculation for the Look-up Table of the TOMS V7 Algorithm .....             | 10   |
| 4. The TOMS V7 Algorithm.....  | 12   |
| 1. Partial Cloud Model .....   | 13   |
| 2. Ozone Retrieval.....  | 14   |
| 3. OCCURRENCE OF OZONE ANOMALIES OVER CLOUDY AREAS IN TOMS DATA .....                    | 18   |
| 1. Methodology.....  | 18   |
| 2. Occurrence of Ozone Anomalies .....   | 23   |
| 3. Summary.....  | 29   |
| 4. CLOUD-HEIGHT-RELATED OZONE RETRIEVAL ERRORS .....                                     | 31   |
| 1. Cloud-Height Errors in TOMS Data.....   | 31   |
| 2. Ozone Retrieval Errors Induced by Incorrect Cloud Heights .....                       | 33   |

|    |   |    |
|----|---|----|
| 1. | Radiation Interpolation Error.....  | 34 |
| 2. | Ozone Retrieval Error Above Clouds.....   | 36 |
| 3. | Ozone Retrieval Error Below Clouds.....   | 39 |
| 4. | Correction of Cloud-Height-Related Ozone Retrieval Errors .....   | 41 |
| 3. | Summary.....  | 44 |
| 5. | THE ASSUMPTION OF OPAQUE LAMBERTIAN CLOUD SURFACES ON OZONE<br>RETRIEVAL .....  | 46 |
| 1. | Radiative Transfer Models and Model Setup .....   | 46 |
| 1. | Polarized Plane-Parallel Gauss-Seidel Radiative Transfer Model.....   | 47 |
| 2. | Ray Tracing Code.....   | 48 |
| 3. | Ozone Absorption Coefficients, Rayleigh Scattering Coefficients, Molecular<br>Depolarization Factors, and Polarization..... | 49 |
| 4. | Ozone Profiles and Temperature Profiles.....  | 50 |
| 5. | Radiance Look-up Table in the TOMS V7 Algorithm .....   | 50 |
| 6. | Cloudy Treatment and Cloud Optical Properties.....  | 51 |
| 7. | Radiance Comparisons .....  | 56 |
| 8. | Viewing Geometry .....  | 56 |
| 2. | Ozone Retrieval Errors Associated with Clouds.....  | 58 |
| 1. | Methodology .....   | 60 |
| 2. | Lambertian and PCM Effects .....  | 64 |
| 1. | Viewing Geometry .....  | 64 |
| 2. | Cloud Optical Properties .....  | 67 |
| 3. | Cloud Optical Depth .....   | 70 |
| 4. | Cloud Geometrical Depth.....  | 73 |
| 5. | Atmospheric Ozone Profiles .....  | 75 |
| 6. | EP vs. N7 TOMS Measurement Wavelengths .....  | 75 |
| 7. | Summary of the Lambertian and PCM Effects .....   | 75 |

|     |   |     |
|-----|---|-----|
| 3.  | Effect of Ozone Absorption Enhancement in Clouds.....                                   | 77  |
| 1.  | Viewing Geometry .....  | 81  |
| 2.  | Cloud Optical Properties .....  | 81  |
| 3.  | Cloud Optical Depth .....   | 83  |
| 4.  | Ozone Amount in the Clouds .....  | 85  |
| 5.  | Cloud Geometrical Depth.....  | 86  |
| 6.  | Ozone Distribution in the Clouds.....   | 87  |
| 7.  | Atmospheric Ozone Profiles .....  | 89  |
| 8.  | N7 vs. EP TOMS Measurement Wavelengths .....  | 90  |
| 9.  | Vertical Distribution of Ozone Absorption in the Clouds.....                            | 90  |
| 1.  | Vertical Distribution of Ozone Absorption in the Clouds<br>for the Base Condition ..... | 91  |
| 2.  | Vertical Distributions vs. Cloud Optical Depth .....                                    | 94  |
| 3.  | Vertical Distributions vs. Cloud Optical Properties.....                                | 94  |
| 4.  | Vertical Distributions vs. Cloud Locations.....   | 94  |
| 5.  | E-folding Depth .....   | 97  |
| 10. | Summary for the ICOAEN Effect.....  | 98  |
| 4.  | Effect of Below-Cloud Ozone Absorption .....  | 99  |
| 5.  | Overall Ozone Retrieval Errors Associated with Clouds .....                             | 101 |
| 3.  | Ozone Retrieval Errors Associated with Partial Clouds .....                             | 106 |
| 4.  | Possibility of Directly Correcting Ozone Retrieval Errors Associated with Clouds.....   | 107 |
| 5.  | Summary.....  | 112 |
| 6.  | EFFECTS OF OZONE RETRIEVAL ERRORS ON TROPOSPHERIC OZONE<br>DERIVATION .....             | 115 |
| 1.  | Total Ozone Difference Between Tropical Cloudy and Clear Areas.....                     | 116 |
| 2.  | Correction of Incorrect Tropospheric Climatology from Ozone-sonde Data.....             | 119 |

|    |   |     |
|----|---|-----|
| 3. | Sources of Cloudy Total Ozone Excess.....                                   | 122 |
| 1. | Dynamical Influence of Deep Convection on Total-Ozone Distribution .....    | 122 |
| 2. | Photochemical Production over Convective Clouds .....                       | 123 |
| 3. | Ozone Absorption Enhancement in the Clouds.....                             | 125 |
| 4. | Ozone Retrieval Errors in Tropospheric Ozone Derivation.....                | 127 |
| 5. | Errors in Tropospheric Ozone Derivation Using the CCP and CCD Methods ..... | 134 |
| 6. | Summary.....  | 136 |
| 7. | ANALYSIS OF ANOMALY OCCURRENCE.....   | 142 |
| 1. | Ozone Anomaly Distribution After the $\Delta P$ Correction .....            | 142 |
| 2. | Seasonal and Latitudinal Distribution of Ozone Anomalies .....              | 149 |
| 3. | Analysis of Ozone Anomaly Occurrence Over Cloudy Areas.....                 | 151 |
| 1. | Ozone Retrieval Errors Associated with Clouds .....                         | 151 |
| 2. | Planetary-Scale and Synoptic-Scale Activities.....                          | 151 |
| 3. | Marine Stratocumulus Clouds and Enhanced Tropospheric Ozone .....           | 153 |
| 4. | Solar Zenith Angle and Satellite Zenith Angle.....                          | 159 |
| 4. | Summary.....  | 159 |
| 5. | Effects of Ozone Anomalies on TOMS Applications.....                        | 161 |
| 8. | CONCLUSION.....   | 163 |
|    | APPENDIX A: NEGLECT OF POLARIZATION ON RADIANCE AND OZONE RETRIEVAL.....    | 166 |
| 1. | Clear-Sky Conditions.....   | 167 |
| 2. | Cloudy-Sky Conditions.....  | 173 |
| 3. | Summary.....  | 176 |
|    | APPENDIX B: TOMS OZONE RETRIEVAL EFFICIENCY FACTORS .....                   | 178 |
|    | REFERENCES.....   | 182 |

## LIST OF FIGURES

| Figure | Page  |
|--------|---|
| 1.1    | A schematic diagram for possible OREs associated with clouds in the TOMS V7 algorithm.....5   |
| 3.1    | Anomalous ozone distribution over cloudy areas located in South America on January 1, 1980 (left) and in the south Atlantic Ocean on July 15, 1980 (right). (a) Distribution of total ozone. (b) Distribution of reflectivity. (c) Relationship between total ozone and reflectivity.....19   |
| 3.2    | Average frequency distribution of cloud fields during the 1979-1992 N7 TOMS period (a) and the 1997-1999 EP TOMS period (b). .....20  |
| 3.3    | Frequency of correlation coefficients (in each bin of 0.1) between the TOMS TOC and the TOMS 380-nm reflectivity in 5°-longitude × 5°-latitude areas in the Northern and Southern Hemispheres during January 1-15, 1980 (a and b) and July 1-15, 1980 (c and d). Thin curves are for each day and the thick curve is the average curve over the period.....22           |
| 3.4    | OAs in 1979-1992 N7 TOMS data and 1997-1999 EP TOMS data. (a) Average spatial fraction distribution of POAs in N7 TOMS data from 1979 to 1992. (b) Same as (a) except for NOAs. (c) and (d) Same as (a) and (b) except in 1997-1999 EP TOMS data. ....24  |
| 3.5    | Same as Figure 3.4 except for the linear regression slopes between ozone and reflectivity for OAs.....25  |
| 3.6    | Variation of annual average fractions and ozone/reflectivity slopes of POAs and NOAs. ....27  |
| 3.7    | Effects of the 1982-1983 and 1997-1998 El Niño events on OA distribution. (a) Fraction distribution of NOAs in non-El Niño period from December 1981 to February 1982. (b) Same as (a) except in El Niño period from December 1982 to February 1983. (c) and (d) same as (a) and (b) except for the 1997-1998 El Niño event.....28                                      |
| 4.1    | (a) Monthly average pressure difference between THIR and ISCCP CTP as a function of THIR CTP in January and July 1980. The vertical bars are the ±1 standard errors. The x-axis values are the same for January and July but the x-axis values for July are shifted by 25 hPa to avoid overlapping. (b) Histogram distribution of cloud-top pressure difference. ....32 |
| 4.2    | Radiation interpolation error as a function of viewing geometry (a), ozone profiles (b), and cloud fraction (c). For (a) and (c), the L275 is used, the SZA and VZA are 30°, and the cloud reflectivity is 90%.. .....35  |
| 4.3    | Error in retrieved OZAC as a function of viewing geometry (a), ozone profiles (b), and cloud fraction (c). For (a) and (c), the L275 is used, the SZA and VZA are 30°, and the cloud reflectivity is 90%. .....37   |
| 4.4    | Error in added OZBC as a function of viewing geometry (a), ozone profiles (b), and cloud fraction (c). For (a) and (c), the L275 is used, the SZA and VZA are 30°, and the cloud reflectivity is 90%. .....40   |

|     |   |    |
|-----|---|----|
| 4.5 | An example of total ozone distribution over the western Pacific Ocean (160°E-170°E, 2°N-5°N) on October 4, 1980. (a) TOMS retrieved total ozone vs. TOMS-measured 380-nm reflectivity. (b) TOMS-assumed and THIR-measured CTP vs. reflectivity. (c) Total ozone after the $\Delta P$ correction vs. reflectivity.....   | 42 |
| 4.6 | Spatial distribution of TOC after the $\Delta P$ correction (a) and reflectivity (b) for the case in Figure 4.5.....  | 43 |
| 5.1 | Phase functions at N7 TOMS wavelengths (indicated by different colors) for cloud droplets: water cloud droplets with an effective radius of 10 $\mu\text{m}$ and an effective variance of 0.1 (solid), same water cloud droplet but with a Henyey-Greenstein phase function (dashed and dotted), HEX with an effective radius of 30 $\mu\text{m}$ and an effective variance of 0.1 (dotted), and POLY with an effective radius of 30 $\mu\text{m}$ and an effective variance of 0.1 (dashed)..... | 55 |
| 5.2 | (a) Differences in calculated radiances between using PPGSRAD and TOMRAD at several selected N7 TOMS wavelengths for a surface reflectivity of 8% and 80%. (b) Differences in the retrieved total ozone from corresponding calculated radiances using the TOMS V7 algorithm.....  | 57 |
| 5.3 | Calculated radiances normalized by solar flux at 380-nm (left) and retrieved cloud surface reflectivities at 380 nm (right) for a WC of COD positioned at 2-12 km as a function of viewing geometry. The four rows correspond to SZAs 0°, 30°, 60°, and 75° (indicated by a red asterisk symbol on the x-axis), respectively. The AZA ranges from 0° to 180° anti-clockwise.....  | 59 |
| 5.4 | Comparison of scenes between forward simulation and retrieval. (a) Full cloudy scene in the forward calculation. (b) Assumed scene in the TOMS retrieval.....   | 61 |
| 5.5 | ISCCP D1 CTP vs. COD for deep convective clouds in the tropics (10°S-10°N) in October 1983. The solid horizontal and vertical lines indicate the average CTP and COD, respectively. The dashed lines are the $\pm 1$ standard deviation values from the corresponding average values.....   | 63 |
| 5.6 | OREs in total ozone (left) and OREs in OZAC (right) at different SZAs (0°, 30°, 60°, and 75°) for a forward WC of COD 40 at 2-12 km. The low-latitude ozone file L275 is used except that no ozone is put below the cloud-tops.....   | 65 |
| 5.7 | Lambertian and PCM effects for a WC of COD 40 positioned at 2-12 km. (a) The sum of Lambertian and PCM effects as a function of derived ECF. (b) The Lambertian effect as a function of GPL (the ECF is 1). (c) The PCM effect as a function of ECF. The $\Delta\Omega_t$ , $\Delta\Omega_a$ , and $\Delta\Omega_b$ indicate the error in total ozone, error in OZAC, and error in OZBC, respectively.....  | 66 |
| 5.8 | Error distribution in total ozone for a cloud of COD 40 at 2-12 km for WCHG (left), HEX (middle), and POLY (right). The low-latitude ozone file L275 is used except that no ozone is put below the cloud-top.....   | 68 |
| 5.9 | Lambertian effect (left) and Lambertian-PCM effect (right) for a cloud with COD 40 at 2-12 km. (a) WCHG. (b) HEX. (c) POLY. The low-latitude ozone file L275 is used except that no ozone is put below the cloud-top. The results are shown at selected viewing geometries (SZA = 0°, 30°, 60°, and 75°; VZA = 0°, 30°, 50°, and 70°; AZA = 0°, 90°, and 180°).....   | 69 |

|      |  |    |
|------|--|----|
| 5.10 | Similar to Figure 5.9 except for WC at 2-12 km with COD 1 (a), 2 (b), 5 (c), 10 (d), 20 (e), 40 (f), and 100 (g), respectively. ....   | 72 |
| 5.11 | Similar to Figure 5.9 except for a WC of COD 40 at 2-3 km (a), 2-7 km (b), 7-12 km (c), 11-12 km (d), respectively. ....   | 74 |
| 5.12 | Similar to Figure 5.9 except using ozone profiles L225 (a), L325 (b), M325 (c), M375 (d), and M425 (e), respectively. (f) Results calculated at EP TOMS wavelengths using ozone profile L275. ....   | 76 |
| 5.13 | Comparison of EICO between direct calculation from Equation (5.11) at 317 nm and ozone retrieval for the base case. ....   | 79 |
| 5.14 | Retrieved EICO as a function of viewing geometry for a WC of COD 40 at 2-12 km. The low-latitude ozone profile L275 is used except that the 20.8 DU inter-cloud ozone is homogeneously distributed in the cloud. The red asterisk symbol on the x-axis indicates the SZA. ....   | 80 |
| 5.15 | PPLand EICO as a function SZA and VZA for a WC of COD 40 at 2-12 km. (a) PPL vs. SZA. (b) PPL vs. VZA. (c) and (d) same as (a) and (b) except for EICO. The low-latitude ozone profile L275 is used except that the 20.8 DU inter-cloud ozone is homogeneously distributed in the cloud. ....  | 82 |
| 5.16 | EICO as a function of VZA for a cloud of COD 40 at 2-12 km with different optical properties: WC (plus), WCHG (multiplier), HEX (diamond), and POLY (triangle) at SZA 0° and 75°. The low-latitude ozone profile L275 is used except that the 20.8 DU inter-cloud ozone is homogeneously distributed in the cloud. ....  | 83 |
| 5.17 | EICO as a function of COD for a WC of 2-12 km at three sets of viewing geometries. The low-latitude ozone profile L275 is used except that the 20.8 DU inter-cloud ozone is homogeneously distributed in the cloud. ....   | 84 |
| 5.18 | EICO (solid) and the ratio of EICO to the AICO (dashed) as a function of AICO for a WC of 2-12 km at three sets of viewing geometries. The low-latitude ozone profile L275 is used except that the amount of ozone in cloud is as specified in the x-axis and homogeneously distributed in clouds. ....  | 85 |
| 5.19 | The ratio of EICO to the AICO as a function of cloud thickness for a WC of COD 40 at three sets of viewing geometries. The low-latitude ozone profile L275 is used except that the amount of inter-cloud ozone is homogeneously distributed. Solid lines are for clouds with CBH fixed at 2 km and dashed lines are for clouds with CTP fixed at 12 km. ....   | 86 |
| 5.20 | (a) Ozone absorption coefficients vs. altitude for different inter-cloud ozone profiles: original L275 ozone profile (profile 1), well-mixed (profile 2), homogenous (profile 3), increasing ozone with altitude (profile 4), decreasing ozone with altitude (profile 5), homogeneous in the upper 2 km elsewhere no ozone (profile 6), and homogenous in the lower part 2 km elsewhere no ozone (profile 7). Profiles 1-4 contain 20.8 DU ozone and profiles 6-7 contain 4.2 DU ozone. (b) Retrieved inter-cloud ozone vs. VZA at SZA 30° corresponding to the seven inter-cloud ozone profiles for WC of COD 40 at 2-12 km. .... | 88 |
| 5.21 | The ratio of EICO to AICO vs. VZA for a WC of COD 40 at 2-12 km at SZA 0° and 75° using ozone profiles L225, L275, L325, M325, M375, M425, and L275 (at EP wavelengths). ....  | 90 |

|      |   |     |
|------|---|-----|
| 5.22 | Ratios of retrieved EICO to AICO in each 0.5-km cloud layer as a function of altitude for a WC of COD 40 at 2-12 km at three sets of viewing geometries. (a) Upward radiance. (b) Downward radiance. The ozone profile L275 is used except that 20.8 DU ozone is homogeneously distributed in the clouds.....   | 92  |
| 5.23 | Ratios of retrieved EICO to AICO in each 0.5-km cloud layer as a function of altitude for 2-12 km clouds with different COD and COPs at three sets of viewing geometries. The ozone profile L275 is used except that ozone is homogeneously distributed in the clouds. ....   | 95  |
| 5.24 | Same as Figure 5.23 except for WCs of COD 40 at different locations.....  | 96  |
| 5.25 | E-folding depth as a function of VZA for a 2-12 km WC with different CODs and COPs at SZA 30°. The L275 is used excepted that ozone is homogeneously distributed in the clouds.....   | 97  |
| 5.26 | Effective ozone below cloud bottoms as a function of VZA for WC with different CODs and cloud locations at SZA 30°. The low-latitude ozone profile L275 is used.....  | 100 |
| 5.27 | Comparison of retrieved total ozone between using the TOMS V7 algorithm ( $R_s = 80\%$ ) and forcing the ECF to be the same as the FCF ( $f_c = 1$ ) at SZA 30°. (a) For a WC of COD 1 at 2-12 km. (b) For a WC of COD 40 at 2-12 km. The low-latitude ozone profile L275 is used. The $\Delta\Omega_t$ , $\Delta\Omega_a$ , and $\Delta\Omega_b$ indicate the error in total ozone, error in OZAC, and error in OZBC, respectively.....  | 102 |
| 5.28 | Errors in total ozone (circle), OZAC (plus), and OZBC (multiplier) as a function of COD at SZA 30° and VZA 30° for 2-12 km water clouds. The low-latitude ozone profile L275 is used.....   | 103 |
| 5.29 | Comparison of retrieved errors in total ozone vs. VZA among assuming minimum full cloud reflectivity as 40%, 60%, 80% (i.e., the TOMS V7 algorithm), 100%, and forcing the ECF to be 1 for a WC of COD 1 with different cloud locations at SZA 30°. (a) A 2-12 km cloud. (b) A 2-3 km cloud. (c) A 11-12 km cloud. The low-latitude ozone profile L275 is used.....   | 105 |
| 5.30 | Lambertian-PCM and opaque effects as a function of FCF at three sets of viewing geometries for 2-12 km WC. (a) Lambertian-PCM effect for COD 1. (b) Lambertian-PCM effect for COD 40. (c) Opaque effect for COD 1. (d) Opaque effect for COD 40. The low-latitude ozone profile L275 is used.....   | 108 |
| 5.31 | Same as Figure 5.30 except for clouds positioned at 2-3 km.....   | 109 |
| 5.32 | Comparison of errors in total ozone at SZA 30° vs. VZA between using the TOMS V7 algorithm and forcing the ECF to be the FCF for different FCFs. (a) For WC of COD 1 at 2-12 km. (b) For WC of COD 1 at 2-3 km. The low-latitude ozone profile L275 is used.....  | 110 |
| 6.1  | Annually averaged parameters in 5°-longitude $\times$ 5°-latitude areas during 1979-1983. (a) Average THIR CTP for high-reflectivity clouds (reflectivity $\geq 80\%$ and THIR CTP $\leq 300$ hPa). (b) Cloud-height-induced errors in ozone above high-reflectivity clouds. (c) Difference in the TOC between high-reflectivity cloudy areas and nearby clear areas (reflectivity $\leq 20\%$ ) before the $\Delta P$ correction. (d) Same as (c) but after the $\Delta P$ correction..... | 117 |
| 6.2  | (a) Same as Figure 6.1 (c) except for clouds with reflectivity $\geq 80\%$ in 1997-2000 EP TOMS data. (b) Difference in the Cloudy/Clear TOC difference between N7 TOMS data (1979-1983) and EP TOMS data (1997-2000).....  | 118 |

|      |   |     |
|------|---|-----|
| 6.3  | Annually averaged parameters in $5^\circ$ -longitude $\times$ $5^\circ$ -latitude areas in 1979-1983 TOMS data. (a) Errors in the added ozone below high-reflectivity clouds caused by the incorrect tropospheric climatology used in TOMS retrieval. (b) Errors in the clear total column ozone caused by imperfect retrieval efficiency and incorrect tropospheric climatology. (c) Values in Figure 6.1 (d) minus values in (a) and plus values in (b). (d) Average upper tropospheric column ozone between CTP and tropopause derived from SHADOZ climatology during 1998-2000..... | 120 |
| 6.4  | Histograms of ozone between 100 and 200 hPa. (a) Linear regression slope between TOMS OZAC and THIR CTP for measurements with reflectivity greater than 80% and THIR CTP between 100-200 hPa in the tropics ( $10^\circ\text{S}$ - $10^\circ\text{N}$ ) in 1980. (b) SHADOZ measurements between 100 and 200 hPa at eight tropical stations in 1998-1999.....   | 124 |
| 6.5  | Derived ICOAEN effect for $5^\circ$ -longitude $\times$ $5^\circ$ -latitude areas during 1979-1983 TOMS data. (a)-(d) Seasonally averaged ICOAEN effect for the winter, spring, summer, and fall, respectively. (e) Annually averaged ICOAEN effect.....  | 126 |
| 6.6  | Same as Figure 6.5 except for errors in the derived stratospheric ozone column from high-reflectivity clouds (reflectivity $\geq 80\%$ and THIR CTP $\leq 300$ hPa).....  | 129 |
| 6.7  | Same as Figure 6.5 except for the derived SOC from high-reflectivity clouds (reflectivity $\geq 80\%$ and THIR CTP $\leq 300$ hPa) before correcting the errors shown in Figure 6.6. ....   | 130 |
| 6.8  | Same as Figure 6.7 except for after correcting the errors shown in Figure 6.6, i.e., the difference between Figure 6.7 and Figure 6.6.....  | 131 |
| 6.9  | Same as Figure 6.5 except for the derived tropospheric ozone column from high-reflectivity clouds (reflectivity $\geq 80\%$ and THIR CTP $\leq 300$ hPa) before correcting $\Delta\Omega_{strat}$ and $\Delta\Omega_{clr}$ . ....   | 132 |
| 6.10 | Same as Figure 6.9 except for after correcting $\Delta\Omega_{strat}$ and $\Delta\Omega_{clr}$ . ....   | 133 |
| 6.11 | (a) Same as Figure 6.6 (e) except using the CCP cloud points. (b) Same as Figure 6.6 (e) except using the CCD cloud points.....   | 136 |
| 6.12 | (a) Annually averaged SOC derived using CCP cloud points during the 1979-1983 N7 TOMS data before correcting $\Delta\Omega_{strat}$ . (b) Same as (a) except after correcting $\Delta\Omega_{strat}$ . (c) Same as (a) except for the derived tropospheric ozone before correcting $\Delta\Omega_{strat}$ and $\Delta\Omega_{clr}$ . (d) Same as (a) except after correcting $\Delta\Omega_{strat}$ and $\Delta\Omega_{clr}$ . ....   | 138 |
| 6.13 | Same as Figure 6.12 except using the CCD cloud points.....  | 139 |
| 7.1  | Same as Figure 3.3 except after the $\Delta P$ correction. The solid and dashed thick curves are the average distributions over the period after and before the $\Delta P$ correction, respectively.....  | 143 |
| 7.2  | OAs in 1978-1983 period after the $\Delta P$ correction. (a) Average spatial fraction distribution of POAs. (b) Same as (a) except for NOAs. (c) and (d) are the changes in fractions of POAs and NOAs because of the $\Delta P$ correction.....  | 145 |
| 7.3  | Same as Figure 7.2 except for the linear regression ozone/reflectivity slopes of OAs. ....  | 146 |

|     |   |     |
|-----|---|-----|
| 7.4 | (a) and (b) same as Figure 3.7 (a) and (b) except after the $\Delta P$ correction, (c) comparison of daily ISCCP CTPs (diamond) used in the TOMS V7 ozone retrieval and collocated THIR CTPs (plus) during 1979-1984 averaged over the eastern Pacific Ocean ( $10^{\circ}\text{S}$ - $0^{\circ}\text{S}$ , $160^{\circ}\text{W}$ - $120^{\circ}\text{W}$ ) for scenes with reflectivity greater than 40%.  | 148 |
| 7.5 | Seasonal and latitudinal variation of OAs during 1979-1983 after the $\Delta P$ correction. (a) and (b) are zonal average fractions of occurrence for POAs and NOAs, respectively, (c) and (d) are zonal average ozone/reflectivity slopes for POAs and NOAs, respectively.   | 150 |
| 7.6 | (a) Seasonal variations of fraction of POA occurrence after the $\Delta P$ correction during 1979-1983 over WCSAF ( $20^{\circ}\text{S}$ - $10^{\circ}\text{S}$ , $5^{\circ}\text{W}$ - $10^{\circ}\text{E}$ ), WCSAM ( $20^{\circ}\text{S}$ - $10^{\circ}\text{S}$ , $85^{\circ}\text{W}$ - $75^{\circ}\text{W}$ ), South America ( $20^{\circ}\text{S}$ - $10^{\circ}\text{S}$ , $60^{\circ}\text{W}$ - $40^{\circ}\text{W}$ ), and the India Ocean ( $15^{\circ}\text{S}$ - $5^{\circ}\text{S}$ , $80^{\circ}\text{E}$ - $100^{\circ}\text{E}$ ), (b) same as (a) except for ozone/reflectivity slope.                     | 154 |
| 7.7 | (a) Monthly mean tropospheric ozone profiles (thin curves) measured at Ascension (1998-2000) along with the tropospheric portion of TOMS standard ozone profile L275 (solid curve). Each thin curve is identified by a number (1-9 means January-September) or a character (O, N, and D refers to October, November, and December, respectively). (b) ISCCP D1 CTP vs. COD in October 1983 over WCSAF ( $20^{\circ}\text{S}$ - $10^{\circ}\text{S}$ , $5^{\circ}\text{W}$ - $10^{\circ}\text{E}$ ). Solid line is the average CTP and the two dashed lines are the deviations of 1 standard deviation from the average value. | 156 |
| 7.8 | (a) Monthly variation of tropospheric ozone measured at Ascension during 1998-2000 (solid), the retrieved ozone for a cloudy-sky with a WC of COD 15 at 1.5-2.5 km (dotted line), and the retrieved ozone for a clear-sky with ground reflectivity of 5%. (b) Monthly variation of the observed ozone/reflectivity slope (circle) over WCSAF ( $20^{\circ}\text{S}$ - $10^{\circ}\text{S}$ , $5^{\circ}\text{W}$ - $10^{\circ}\text{E}$ ) and simulated ozone/reflectivity slopes under various cloudy conditions.  | 157 |
| A.1 | The difference in the calculated reflected radiance at TOA (left) and transmitted radiance at ground surface (right) with and without polarization at 312 nm for four different SZAs ( $0^{\circ}$ , $30^{\circ}$ , $60^{\circ}$ , and $75^{\circ}$ ). The red asterisk symbol on the abscissa indicates the SZA.   | 168 |
| A.2 | The difference in the retrieved ozone and reflectivity from forward-calculated radiances with and without polarization. The TOMS V7 algorithm retrieves the ozone and reflectivity.   | 169 |
| A.3 | A schematic diagram that explains how the error in the calculated radiance from the neglect of polarization causes errors in the retrieved ozone and reflectivity using the TOMS V7 algorithm.  | 170 |
| A.4 | (a) Comparison of the ozone differences with and without polarization between using the TOMS V7 algorithm and directly calculating from the N-value differences. (b) Same as (a) Except for reflectivity.   | 172 |
| A.5 | (a) and (b) same as Figure A.1 (left) and (right) except for a cloudy-sky with a WC of COD 1 at 2-6 km and for SZAs $0^{\circ}$ and $30^{\circ}$ . (c) and (d) same as (a) and (b) except for COD 40.   | 174 |
| A.6 | Same as Figure A.2 except for a cloudy-sky with a WC of COD 40 at 2-6 km.   | 175 |
| B.1 | Ozone retrieval efficiency factors as function of pressure level for different viewing geometries, surface reflectivities, and surface pressures. The TOMS standard profile L275 is used.   | 180 |

## LIST OF TABLES

| Table |  | Page |
|-------|--|------|
| 2.1   | Characteristics of TOMS instruments on N7, M3, ADEOS, and EP satellites. ....  | 9    |
| 2.2   | TOMS triplets of wavelengths (when two wavelengths are listed, the wavelength in parenthesis applies to EP and ADEOS TOMS instruments only, the other applies to N7 and M3 TOMS instruments). ....   | 12   |
| 5.1   | Effective absorption and scattering coefficients, and molecular depolarization factor at N7 and EP TOMS wavelengths. ....  | 50   |
| 5.2   | Refractive indexes and optical properties for water clouds.....  | 52   |
| 5.3   | Refractive indexes and optical properties for HEX and POLY.....  | 54   |
| 5.4   | Average values and ranges of Lambertian-PCM, Lambertian, and PCM effects.....  | 71   |
| 6.1   | Comparison of average values for the derived parameters using all cloud points, CCP cloud points, and CCD cloud points, respectively during 1979-1983 N7 TOMS period over the Atlantic Ocean and Africa (15°S-15°N, 60°W-60°E) and the Pacific Ocean (15°S-15°N, 120°E-120°W)..... | 133  |

## LISTS OF ACRONYMS AND ABBREVIATIONS

|           |   |
|-----------|---|
| ADEOS     | ADvanced Earth Observing Satellite                |
| AICO      | Actual Inter-Cloud Ozone                          |
| AZA       | Relative AZimuthal Angle                          |
| BCOA      | Below-Cloud Ozone Absorption                      |
| CBH       | Cloud-Base Height                                 |
| CCD       | Convective Cloud Differential                     |
| CCP       | Cloud-Clear Pair                                  |
| CGD       | Cloud Geometrical Depth                           |
| COD       | Cloud Optical Depth                               |
| COP       | Cloud Optical Property                            |
| CTH       | Cloud-Top Height                                  |
| CTP       | Cloud-Top Pressure                                |
| DU        | Dobson Unit                                       |
| ECF       | Effective Cloud Fraction                          |
| ED        | E-folding Depth                                   |
| EICO      | Effective Inter-Cloud Ozone                       |
| EP        | Earth Probe                                       |
| FCF       | Forward Cloud Fraction                            |
| GEOS-CHEM | Global Earth Observing System CHEMistry           |
| GOME      | Global Ozone Monitoring Experiment                |
| GPL       | Geometrical Path Length                           |
| HEX       | HEXagonal Column Ice Crystals                     |
| ICOAEN    | Inter-Cloud Ozone Absorption ENhancement          |
| ISCCP     | International Satellite Cloud Climatology Project |

|           |   |
|-----------|---|
| ITCZ      | InterTropical Convergence Zone  |
| M3        | Meteor-3  |
| MFCR      | Minimum Full-Cloud Reflectivity                                       |
| MOZART    | Model for Ozone And Related Chemical Tracers                          |
| N7        | Nimbus-7  |
| NCAR      | National Center for Atmospheric Research                              |
| NCEP      | National Center for Environment Prediction                            |
| NMC       | National Meteorological Center  |
| NOA       | Negative Ozone Anomaly  |
| NOAA      | National Oceanic and Atmospheric Administration                       |
| OA        | Ozone Anomaly   |
| OMI       | Ozone Monitoring Instrument   |
| OPL       | Optical Path Length   |
| ORE       | Ozone Retrieval Error   |
| OZAC      | OZone Above Clouds  |
| OZBC      | OZone Below Clouds  |
| PCM       | Partial Cloud Model   |
| POA       | Positive Ozone Anomaly  |
| POLY      | POLYcrystals  |
| PPGSRAD   | Polarized Plane-parallel Gauss-Seidel RADiative Transfer Model        |
| PPL       | Photon Path Length  |
| SBUV      | Solar Backscatter UltraViolet   |
| SCIAMACHY | Scanning Imaging Absorption SpectroMeter for Atmospheric CHartographY |
| SHADOZ    | Southern Hemisphere ADditional OZonesonde                             |
| SOC       | Stratospheric Ozone Column  |
| SZA       | Solar Zenith Angle  |
| THIR      | Temperature Humidity Infrared Radiometer                              |

|        |  |
|--------|--|
| TOA    | Top of the Atmosphere                              |
| TOC    | Total Ozone Column                                 |
| TOMRAD | TOMS RADiative transfer code                       |
| TOMS   | Total Ozone Mapping Spectrometer                   |
| UV     | Ultra-Violet                                       |
| V7     | Version-7  |
| VZA    | View Zenith Angle                                  |
| WC     | Water Clouds                                       |
| WCHG   | Water Clouds with Henyey-Greenstein Phase Function |
| WCSAF  | West Coast of South AFrica                         |
| WCSAM  | West Coast of South AMerica                        |
| WMO    | World Meteorological Organization                  |

## LIST OF SYMBOLS

Most symbols follow Nimbus-7 TOMS data products user's guide [McPeters *et al.*, 1996] or standard references.

|   |   |
|---|---|
| $\lambda$   | wavelength [nm]   |
| $\varepsilon$   | retrieval efficiency factor   |
| $\beta_{\lambda,O_3}$   | ozone absorption coefficient at wavelength $\lambda$ [ $m^{-1}$ ]   |
| $\alpha_{\lambda,O_3}$  | ozone absorption depth per DU of ozone  |
| $\Delta\Omega_{calc}$   | calculated effective ozone in the clouds [DU]   |
| $\rho(h)$   | ozone density at height $h$ in the clouds [DU $m^{-1}$ ]  |
| $\Delta\Omega_{rad}, \Delta\Omega_a, \Delta\Omega_b$  | radiation interpolation error, error in ozone above clouds, and error in ozone below clouds [DU]  |
| $\Delta\Omega_{strat}, \Delta\Omega_{cldhgt}, \Delta\Omega_{uptrop}, \Delta\Omega_{ICOAEN}, \Delta\Omega_{nonlinear}, \Delta\Omega_{excess}, \Delta\Omega_{clr}, \Delta\Omega_{trop}$ | error in derived stratospheric ozone, cloud-height-induced error, upper tropospheric ozone between cloud-top and tropopause, error due to the ICOAEN effect, non-linearity calibration error, $\Delta\Omega_{excess} = \Delta\Omega_{ICOAEN} + \Delta\Omega_{nonlinear}$ , error in clear-sky due to imperfect retrieval efficiency, and error in derived satellite derived tropospheric ozone ( $\Delta\Omega_{trop} = \Delta\Omega_{clr} - \Delta\Omega_{strat}$ ) [DU] |
| $\Delta\Omega_t, \Delta\Omega_b, \Delta\Omega_a$  | error in total ozone column ( $\Delta\Omega_t = \Omega'_t - \Omega_t$ ), error in ozone below clouds ( $\Delta\Omega_b = \Omega'_b - \Omega_b$ ), and error in ozone above clouds ( $\Delta\Omega_a = \Omega'_a - \Omega_a$ ) [DU]  |
| $\Omega'_t, \Omega'_b, \Omega'_a$   | retrieved total ozone column, retrieved ozone below clouds, and retrieved ozone above clouds [DU]   |
| $\Omega, \Omega_0, \Omega_i$  | total ozone column amount, initial total ozone amount, and $i$ th retrieved ozone total amount [DU]   |
| $\Omega_{astrat}, \Omega_{bstrat}, \Omega_{atrop}, \Omega_{btrop}$  | stratospheric ozone after correcting $\Delta\Omega_{strat}$ , stratospheric ozone before correcting $\Delta\Omega_{strat}$ , tropospheric ozone after correcting $\Delta\Omega_{trop}$ , and tropospheric ozone before correcting $\Delta\Omega_{trop}$ [DU]  |
| $\Omega_{corrected}, \Omega_{uncorrected}$  | ozone column after and before correcting ozone retrieval errors [DU]  |
| $\Omega_{lower}, \Omega_{higher}$   | retrieved ozone using lower latitude and higher latitude ozone profiles [DU]  |
| $\Omega_t, \Omega_b, \Omega_a$  | true total ozone column, true ozone below clouds, and true ozone above clouds in the forward calculation [DU]   |

|  |  |
|--|--|
| $\tau, \tau_{O_3}, \tau_{\lambda, O_3}$          | optical depth, ozone absorption optical depth, and ozone absorption optical depth at wavelength $\lambda$  |
| $\omega_0$                                       | single scattering albedo   |
| $\theta_0, \theta, \phi$                         | solar zenith angle, view zenith angle, and relative azimuthal angle [°]  |
| $f_{\text{prof}}$                                | weight given to the higher latitude profile  |
| $\rho_{\text{std}}(P), \rho_{\text{act}}(P)$     | ozone density at pressure level $P$ in the TOM standard ozone profile, and ozone density at pressure level $P$ in the actual ozone profile [DU hPa <sup>-1</sup> ]   |
| $A_{\lambda}, \overline{A_{\lambda}}$            | radiance normalized to the solar flux $F_{\lambda}$ radiance at wavelength $\lambda$ , radiance normalized to the solar flux $F_{\lambda}$ for the entire band centered at wavelength $\lambda$ [sr <sup>-1</sup> ]      |
| $C_{\text{abs}}, C_{\text{ext}}, C_{\text{sca}}$ | absorption cross section, extinction cross section, and scattering cross section [m <sup>2</sup> ]   |
| $e$  | relative intensity error   |
| $enh(h)$   | ratio of EICO to AICO at a certain height $h$ in the clouds  |
| $F_{\lambda}$                                    | solar flux at wavelength $\lambda$ [W $\mu\text{m}^{-1} \text{cm}^{-2}$ ]  |
| $f_c$  | cloud fraction   |
| $f_i$  | fraction of radiation reflected toward satellite in the direction of $\theta$ that reaches satellite   |
| $G$  | average geometric cross-sectional area [m <sup>2</sup> ]   |
| $g$  | asymmetry factor   |
| $h_{cb}, h_{ct}$                                 | cloud-base height and cloud-top height [m]   |
| $I_{O_3}^{\downarrow}, I_{no\ O_3}^{\downarrow}$ | calculated downward radiances at ground surface with and without ozone in the clouds [W $\mu\text{m}^{-1} \text{cm}^{-2} \text{sr}^{-1}$ ]   |
| $I, I_{\text{meas}}, I_{\lambda}$                | radiance, measured radiance, and radiance at wavelength $\lambda$ [W $\mu\text{m}^{-1} \text{cm}^{-2} \text{sr}^{-1}$ ]  |
| $I_{\text{clear}}, I_{\lambda, \text{clear}}$    | clear-sky radiance for surface reflectivity 8%, $I_{\text{clear}}$ at wavelength $\lambda$ [W $\mu\text{m}^{-1} \text{cm}^{-2} \text{sr}^{-1}$ ]   |
| $I_{\text{cloudy}}, I_{\lambda, \text{cloudy}}$  | cloudy-sky radiance for cloudy surface reflectivity 80%, $I_{\text{cloudy}}$ at wavelength $\lambda$ [W $\mu\text{m}^{-1} \text{cm}^{-2} \text{sr}^{-1}$ ]   |
| $I_m, I_a, I_s$                                  | backscattered radiance, backscattered radiance contributed by purely atmospheric Rayleigh scattering, and backscattered radiance contributed by surface reflection [W $\mu\text{m}^{-1} \text{cm}^{-2} \text{sr}^{-1}$ ] |

|   |   |
|---|---|
| $I_{O_3}, I_{no\ O_3}$                        | calculated backscattered radiance at top of the atmosphere for radiances with and without ozone in the clouds [ $W\ \mu m^{-1}\ cm^{-2}\ sr^{-1}$ ] |
| $I_s, I_v$                                    | calculated radiance without polarization (scalar) and with polarization (vector) [ $W\ \mu m^{-1}\ cm^{-2}\ sr^{-1}$ ]                              |
| $lat_m, lat_{lower}, lat_{higher}$            | latitude for a measurement, lower latitude, and higher latitude [ $^\circ$ ]  |
| $l_{eff}$                                     | effective photon path length [m]  |
| $n$   | number of absorbers   |
| $N_\lambda, N_{meas,\lambda}, N_{0,\lambda}$  | N-value at wavelength $\lambda$ , measured N-value at wavelength $\lambda$ , and calculated N-value at wavelength $\lambda$ using $\Omega_0$        |
| $n(r_i)$                                      | number of particles with radius $r_i$ in a unit volume [ $m^{-3}$ ]   |
| $P_{mn}(\theta)$                              | phase matrix at scattering angle $\theta$ (m, n = 1, 2, 3, 4)   |
| $P_s, P_g, P_c$                               | pressure of reflecting surface, ground surface pressure, and cloud-top pressure (hPa)   |
| $Q$   | absorption efficiency   |
| $r_\lambda, r_{i,\lambda}$                    | residue at wavelength $\lambda$ , residue at wavelength $\lambda$ using $\Omega_i$  |
| $r_{eff}, v_{eff}$                            | effective radius [ $\mu m$ ] and effective variance   |
| $r_i$   | radius in terms of equivalent geometrical cross-sectional area [ $\mu m$ ]  |
| $R_s, R_g, \Delta R$                          | surface reflectivity, ground surface reflectivity, error in reflectivity [%]  |
| $r_{trip}, r_{trip(lower)}, r_{trip(higher)}$ | triplet residue, triplet residue using lower latitude ozone profiles, and triplet residue using higher latitude ozone profiles                      |
| $S_\lambda$                                   | triangular slit function at wavelength $\lambda$  |
| $s_\lambda$                                   | sensitivity of N-value to ozone at wavelength $\lambda$ [ $DU^{-1}$ ]   |
| $S_b$   | fraction of the reflected radiation scattered back to the surface by the atmosphere   |
| $sr_\lambda$                                  | sensitivity of N-value to reflectivity at wavelength $\lambda$ [ $\%^{-1}$ ]  |

## CHAPTER 1

### INTRODUCTION

#### 1.1 Background and Motivation

Tropospheric ozone plays a key role in the chemical processes [Logan *et al.*, 1981] and energy budget of the troposphere [Fishman *et al.*, 1979; Ramanathan and Dickinson, 1979]. It is of global interest as a greenhouse gas and the primary source of the OH radical [Jacob *et al.*, 2000], which controls the lifetimes of a large number of gases [Cunnold *et al.*, 1997]. Increasing human influences on the atmosphere in the form of biomass burning, fossil fuel combustion, and industrial and agricultural emissions have resulted in increased amounts of tropospheric ozone. This increased tropospheric ozone is of great concern because of its deleterious effects on human health and vegetation [Chameides *et al.*, 1994]. Ozone is considered to be responsible for most of the crop damage caused by air pollution in the United States [Logan *et al.*, 1999; Chameides *et al.*, 1994]. The few locations of ozonesonde observations [Logan, 1985; Logan *et al.*, 1999] along with occasional aircraft campaigns [Emmons *et al.*, 2000] provide very limited spatial coverage. Although tropospheric ozone cannot be routinely retrieved from current space-based measurements, several methods have been developed to derive tropospheric ozone from Total Ozone Mapping Spectrometer (TOMS) measurements. These methods include the tropospheric ozone residual method [Fishman and Brackett, 1997; Fishman *et al.*, 1990], the modified ozone residual method [Hudson and Thompson, 1998; Kim *et al.*, 1996], the Convective Cloud Differential (CCD) method [Ziemke *et al.*, 1998], and the Cloud-Clear Pair (CCP) method [Newchurch *et al.*, 2002]. While these techniques often compare favorably with ozonesonde measurements at a few locations, they sometimes differ significantly, by 10-20 Dobson Units (DU,  $1 \text{ DU} = 2.69 \times 10^{16} \text{ molecules/cm}^2$ ) from each other [Newchurch *et al.*, 2001],

in some critical areas and also disagree in important respects with current model calculations of tropospheric ozone (e.g., model for ozone and related chemical tracers or MOZART [Brasseur *et al.*, 1998], and Global Earth Observing System CHEMistry or GEOS-CHEM global 3-D tropospheric chemistry and transport model [Bey *et al.*, 2001]). The differences among different satellite retrievals and models indicate uncertainty in the satellite retrievals or significant gaps in our understanding of critical processes.

The CCP and CCD methods are based on the cloud/clear difference from TOMS ozone observations. Although different in detail, both methods derive stratospheric ozone from tropical high-altitude and high-reflectivity clouds close to tropopause, and the tropospheric ozone is just the difference between clear-sky total ozone and the derived stratospheric ozone. According to the principles of these techniques, Ozone Retrieval Errors (OREs) associated with clouds are critical to tropospheric ozone derivation. Because tropospheric ozone constitutes only about 10% of the Total Ozone Column (TOC), a small error in the TOC might lead to a significant error in the derived tropospheric ozone. However, in the development of these statistical techniques, various sampling methods (e.g., using monthly minimum or monthly mean ozone above high-altitude clouds as stratospheric ozone) are employed to derive the monthly mean tropospheric ozone. The sampling method that best matches with ozonesonde measurements at a few locations is applied to derive tropospheric ozone at other locations. Although adjusting the sampling methods to measurements improves comparisons at a few sites, such adjustments might also cause misunderstanding of the physics. For example, clouds with monthly minimum ozone above clouds might not be the clouds closer to tropopause. Furthermore, the accuracy of tropospheric ozone at locations where no measurements are available could be questioned. For example, in the tropics, the derived tropospheric ozone differs by 7-11 DU in September 1997 between the CCP and CCD methods, although both of them agree well with measurements at selected locations [Newchurch *et al.*, 2002; Ziemke *et al.*, 1998]. Therefore, in order to obtain reliable tropospheric ozone, it is necessary to understand OREs, especially over cloudy areas where ozone retrieval is complicated by the clouds' presence. Furthermore, knowledge of these errors could help one understand the differences in the derived tropospheric ozone among the various satellite retrievals and models.

More than half of the Earth's surface is covered with clouds [Rossow *et al.*, 1996]. Accurate retrieval of atmospheric constituents over cloudy areas from satellite, aircraft, and ground remote sensing measurements is very important in determining the overall retrieval accuracy. However, instrumental measurements in the ultraviolet, visible, and infrared range are strongly influenced by the presence of the clouds in the Earth's atmosphere. First, clouds prevent instruments from accurately measuring constituents above clouds (e.g., for ground measurements) or below clouds (e.g., for space-borne measurements). Second, microphysical (e.g., effective particle radius, shape, composition, and phase) and macrophysical (e.g., cloud-top height, cloud fractional coverage, cloud optical depth, and cloud morphology) behaviors of clouds, which are required for accurately evaluating the observed radiances from such instruments, are not easily available and are highly variable both temporally and spatially. Therefore, accurate retrieval of atmospheric components over cloudy areas is very complicated and remains a most challenging goal. Failure to account for clouds might lead to large errors in interpreting the measurements. In most of the applicational retrieval algorithms, clouds are highly idealized. For example, the TOMS Version-7 (V7) algorithm assumes optically thick clouds as opaque Lambertian surfaces [McPeters *et al.*, 1996]. However, detailed studies are required to evaluate the assumptions about clouds on ozone retrieval. Knowledge about OREs associated with clouds in the TOMS V7 algorithm not only helps one understand errors propagated in the derived tropospheric ozone from cloud/clear difference techniques and other applications using TOMS measurements, but also provides insights into errors associated with clouds in satellite remote sensing retrieval of other important atmospheric components.

## **1.2 Problems over Cloudy Areas in TOMS Data**

Thompson *et al.* [1993] and Hudson *et al.* [1995] noticed that there is an unrealistically high degree of statistical correlation between TOMS Version-6 TOC and reflectivity in regions of marine stratocumulus clouds. This correlation is due mainly to an oversimplified assumption of latitudinal dependence of the Cloud-Top Pressure (CTP) in the TOMS V6 algorithm. The monthly mean International Satellite Cloud Climatology Project (ISCCP) and a more accurate Partial Cloud Model (PCM) have been used in the current TOMS V7 algorithm [McPeters *et al.*, 1996]. Although these improvements largely reduced the overestimate of TOC in these marine stratocumulus regions [McPeters and Labow, 1996],

some discrepancies remain. One significant discrepancy involves the difference between the assumed CTP and the actual CTP. The TOMS V7 algorithm uses the monthly ISCCP climatology to determine CTPs, thereby reducing the difference between assumed and actual CTPs compared to previous versions; however, TOMS V7 algorithm still does not use the actual value for the altitude of the cloud top.

Using Nimbus-7 (N7) TOMS V7 data, we discovered a peculiar distribution of 40 DU more TOC over high cloudy regions than over neighboring clear regions in the northern central United States on June 29, 1989, where there was a well-studied strong convective thunderstorm [Poulida *et al.*, 1996]. The actual Cloud-Top Height (CTH) is ~11-14 km, much higher than the TOMS assumed CTH of ~ 6 km. Because the actual cloud is much higher, correcting the cloud height will increase the total ozone difference. Either OREs in addition to incorrect cloud heights or actual geophysical phenomena or both are responsible for the ozone excess over cloudy areas. How frequently such anomalous ozone distributions occur in the TOMS V7 level-2 data needs to be investigated, and ozone anomalies due to OREs need to be separated from those due to geophysical phenomena.

### **1.3 Potential Sources of Ozone Retrieval Errors Associated with Clouds in TOMS Data**

Under clear-sky conditions, one of the largest known error sources in ozone retrieval is the imperfect retrieval efficiency to the lower troposphere ozone because not enough photons penetrate the lower troposphere [Hudson *et al.*, 1995; Klenk *et al.*, 1982]. There are many more uncertainties in ozone retrieval under cloudy conditions. Figure 1.1 is a diagram showing possible sources of OREs associated with cloudy conditions.

The TOMS assumed CTP from monthly mean ISCCP C2 dataset could be very different from the actual CTP, leading to large OREs in the retrieval. High-reflectivity clouds (i.e., reflectivity  $\geq 80\%$ ) are treated as Lambertian surfaces in the TOMS V7 algorithm. The actual clouds are not Lambertian surfaces even for optically thick water clouds [Knibbe *et al.*, 2000; Kurosu *et al.*, 1997]. Kurosu *et al.* [1997] estimated that cloud reflection for clouds with infinite cloud optical thickness ranges from 0.95 to 1.14 at solar zenith angle  $30^\circ$ . High-altitude clouds might consist of ice crystals or mixed-phase particles whose optical properties are very different from those of water cloud droplets and highly variable spatially and temporally [Macke *et al.*, 1996]. The bidirectional reflectance is also scattering dependent for optically

thick ice clouds and significantly different from water clouds [Mishchenko *et al.*, 1996]. Because the multiple scattering cannot wash out the angular-dependent scattering in the phase function for both water and ice clouds, the assumption of angular-independent Lambertian clouds might lead to additional OREs.

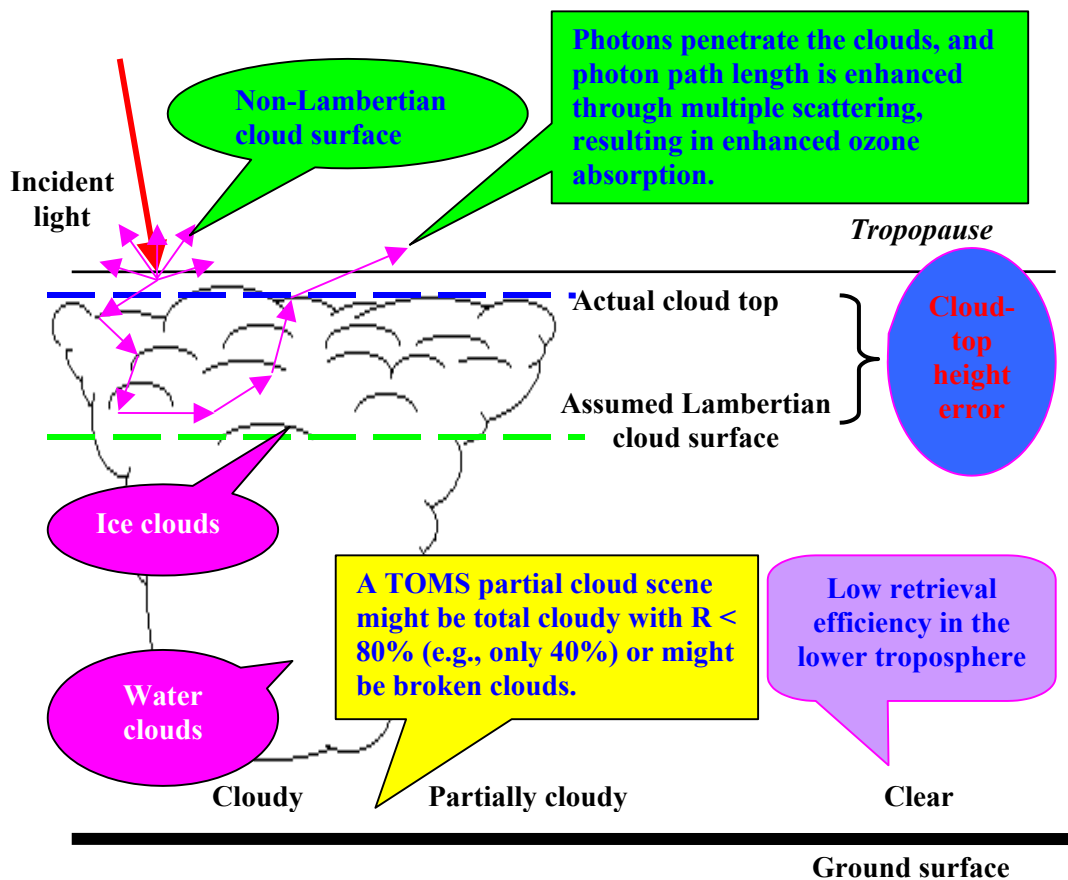


**Figure 1.1** A schematic diagram for possible OREs associated with clouds in the TOMS V7 algorithm.

Another assumption about optically thick clouds is that clouds are treated as opaque, neglecting the multiple scattering and ozone absorption inside clouds. In the ultraviolet and visible region, photons can penetrate the clouds and the coupling of multiple scattering and absorption in the clouds results in a strong absorption enhancement [Kylling *et al.*, 1997; Mayer *et al.*, 1998]. As for ground-based zenith sky

or global irradiance measurements, the absorption path length can be enhanced by a factor of up to 10 [Erle *et al.*, 1995]; Kurosu *et al.*, 1997; Mayer *et al.*, 1998]. Consistently, abnormal increases up to 200 DU in the derived ozone have been reported in many studies over heavily cloudy skies without taking in-cloud multiple scattering effects into account [Brewer and Kerr, 1973; Dobson and Normand, 1962; Fioletov *et al.*, 1997; Mayer *et al.*, 1998]. As for space-borne measured backscattered radiation, the path enhancement is relatively smaller, typically about a factor of 2 [Kurosu *et al.*, 1997]. The absorption enhancement in the clouds was recognized as a limiting factor in accurately retrieving the CTH from the backscattered radiances in and around O<sub>2</sub>-A band [Fischer and Grassl, 1991; Saiedy *et al.*, 1965; Wu, 1985]. The neglect of photon penetration inside clouds can lead to a significant error in the retrieved CTP by up to 100-200 hPa for optically thick clouds [Saiedy *et al.*, 1965; Wu, 1985]. As for ozone retrieval from backscattered radiances, significant errors can occur if the amount of ozone in the clouds is significant.

In the current operational TOMS V7 algorithm, a pixel with reflectivity ranging from 8% to 80% is treated as a linear combination of a cloudy part with Lambert-reflectivity of 80% and a clear-sky part with ground reflectivity of 8% with the Effective Cloud Fraction (ECF) as a free parameter [McPeters *et al.*, 1996]. This PCM will be applied in the future Ozone Monitoring Instrument (OMI) products for retrieving ozone and other trace gases [Bhartia, 2001; Chance, 2001]. In reality, the reflectivity of the cloud part might be much smaller than 80% but with a larger cloud fraction, or it might have a larger cloud reflectivity but with a smaller cloud fraction. The uncertainty in cloud fraction and cloud reflectivity might cause significant OREs. Therefore, the assumption of 80% as Minimum Full-Cloud Reflectivity (MFCR) needs to be evaluated in terms of ozone retrieval.

Koelemeijer and Stammes [1999] investigated the effects of clouds on ozone column retrieval from Global Ozone Monitoring Experiment (GOME) measurements. They found that the influence of clouds on the retrieved TOC depends primarily on the CTH, Cloud Optical Depth (COD), and cloud fraction. Some of the effects of clouds on GOME measurements are expected on TOMS measurements as well. But some effects of clouds might be different on TOMS measurements because the GOME instrument and ozone retrieval method are very different. The TOMS instrument measures the backscattered radiance at six ultraviolet channels and uses a triplet of wavelengths to retrieve the TOC

[McPeters *et al.*, 1996]. The GOME instrument resolves the ozone absorption structures between 325-335 nm and derives TOC using the differential optical absorption spectroscopy method. One limitation in these authors' analysis of cloud effects is that they assume the Cloud Geometrical Depth (CGD) to be 1 km. Because the amount of ozone in a 1-km cloud is small, the assumption of 1-km clouds can largely underestimate the large enhanced ozone absorption inside geometrically thick clouds.

#### **1.4 Objectives and Organizations**

This dissertation has two main objectives. The first objective is to theoretically characterize and quantify the following problems on TOMS ozone retrieval by using radiative transfer models: incorrect CTH, the assumption of opaque and Lambertian cloud surfaces, and the TOMS V7 PCM. The second objective is to analyze anomalous ozone distributions over cloudy areas in TOMS V7 level-2 data and to separate ozone anomalies due to OREs from those due to geophysical phenomena. The overall objective is to understand OREs associated with clouds in the TOMS V7 level-2 data and to analyze the effects of these errors on applications using TOMS data.

This dissertation is organized as follows. Chapter 2 describes the general characteristics of TOMS instruments, the details of the TOMS V7 algorithm, and its forward model, TOMS RADiative transfer code (TOMRAD). In Chapter 3, we analyze the total ozone distribution over cloudy areas compared with neighboring clear areas using TOMS V7 level-2 data during 1979-1992 from N7 satellite and during 1997-1999 from Earth Probe (EP) satellite. Because of the frequent occurrence of ozone anomalies found over cloudy areas, we investigate theoretically with radiative transfer codes the effects of incorrect CTHs on ozone retrieval (Chapter 4) and the assumption of opaque Lambertian cloud surfaces on ozone retrieval (Chapter 5). In Chapter 6, we indirectly estimate the effect of ozone absorption in the clouds and analyze the effects of ozone associated with clouds on the derived tropospheric ozone using the CCP and CCD methods. Chapter 7 explains the occurrence of ozone anomalies with respect to OREs and geophysical phenomena. Chapter 8 concludes this study.

## CHAPTER 2

### TOMS INSTRUMENTS, TOMRAD, AND TOMS V7 ALGORITHM

#### 2.1 TOMS Instruments

Experiments have been conducted with TOMS instruments on board satellites N7 (October 1978 – May 1993), Meteor-3 (M3) (August 1991 – December 1994), ADvanced Earth Observing Satellite (ADEOS) (August 1996 – June 1997), and EP (June 1996 – present) to provide daily high-resolution global maps of atmospheric TOC. Table 2.1 lists the characteristics of the TOMS instruments on board the satellites [*Herman et al.*, 1996; *Krueger et al.*, 1998; *McPeters et al.*, 1996; *McPeters et al.*, 1998]. Satellites N7, ADEOS, and EP were launched in sun-synchronous orbits with the equator crossing time around local noon. Satellite M3 was launched in an orbit processed relative to the Earth-Sun line within a period of 212 days. So the local equator crossing time changed with the same period. The TOMS instantaneous field of view is  $3^\circ \times 3^\circ$ . A scanning mirror scans perpendicular to the orbital plane in  $3^\circ$  steps from  $51^\circ$  ( $54^\circ$  for ADEOS TOMS) on the right side of the spacecraft nadir to  $51^\circ$  ( $54^\circ$  for ADEOS TOMS) on the left, for a total of 35 (37 for ADEOS TOMS) samples. The pixel size at nadir ranges from  $26 \times 26 \text{ km}^2$  to  $63 \times 63 \text{ km}^2$ . The TOMS instrument measures the backscattered Earth radiance at six near-ultraviolet bands, of which the slit function is triangular with a nominal 1-nm bandwidth. But the wavelengths are different on board each of these satellites. Periodically, the TOMS scanner is positioned to view a ground aluminum diffuser plate to measure the incident solar irradiance. The normalized radiance, the ratio of the backscattered radiance to the incident solar irradiance, is used to retrieve ozone [*Herman et al.*, 1996; *Krueger et al.*, 1998; *McPeters et al.*, 1996; *McPeters et al.*, 1998].

**Table 2.1** Characteristics of TOMS instruments on N7, M3, ADEOS, and EP satellites.

| Satellite                               | N7       | M3      | ADEOS    | EP                    |
|---|----------|---------|----------|-----------------------|
| Vacuum Wavelength (nm)                  | 312.34   | 312.35  | 308.68   | 308.65                |
|   | 317.35   | 317.40  | 312.59   | 312.56                |
|   | 331.36   | 331.13  | 317.61   | 317.57                |
|   | 339.66   | 339.73  | 322.40   | 322.37                |
|   | 359.88   | 360.00  | 331.31   | 331.29                |
|   | 379.95   | 380.16  | 360.11   | 360.40                |
| Orbit Period (min)                      | 104      | 109     | 101      | 95*<br>100**          |
| Orbit Inclination Angle (degree)        | 99.3     | 82.5    | 98.6     | 97.4*<br>98.4**       |
| Altitude (km)                           | 955      | 1200    | 800      | 500*<br>739**         |
| Pixel Size at Nadir (km × km)           | 50 × 50  | 64 × 64 | 42 × 42  | 25 × 25*<br>39 × 39** |
| Local Equator Crossing Time (ascending) | 11:51 AM | Varying | 10:45 AM | 11:16 AM              |

\* Characteristics before December 5, 1997.

\*\* Characteristics after December 13, 1997.

## 2.2 TOMRAD

The operational algorithm for processing real-time EP TOMS data is the TOMS V7 algorithm and TOMRAD is the forward model to calculate the radiance look-up table used in the TOMS V7 algorithm. The calculation of radiance follows the formulation of [Dave, 1964], who employs successive iterations of the auxiliary equation derived from the definition of source matrix to solve the problem of diffuse reflection and transmissions of a parallel beam of radiation by a partly absorbing, non-homogeneous, and plane-parallel atmosphere. In this model, clouds are assumed as Lambertian surfaces as well as ground surfaces. Consider an atmosphere bounded by a Lambertian surface of reflectivity  $R_s$ , the backscattered radiance  $I_m$  emerging from the Top Of the Atmosphere (TOA) is the sum of purely atmospheric backscatter  $I_a$ , and reflection of the incident radiation from the reflecting surface  $I_s$ ,

$$I_m(\lambda, \theta, \theta_0, \phi, \Omega, P_0, R_s) = I_a(\lambda, \theta, \theta_0, \phi, \Omega, P_0) + I_s(\lambda, \theta, \theta_0, \Omega, P_0, R_s), \quad (2.1)$$

where  $\lambda$  is wavelength;  $\theta$  is satellite View Zenith Angle (VZA) as seen from the ground;  $\theta_0$  is Solar Zenith Angle (SZA);  $\phi$  is relative AZimuthal Angle (AZA);  $\Omega$  is ozone column amount; and  $P_s$  is the pressure of reflecting surface. The surface reflectance term can be expressed as follows:

$$I_s(\lambda, \theta, \theta_0, \Omega, P_s, R_s) = \frac{R_s T(\lambda, \theta, \theta_0, \Omega, P_s)}{1 - R_s S_b(\lambda, \Omega, P_s)} \quad (2.2)$$

and

$$T(\lambda, \theta, \theta_0, \Omega, P_s) = I_d(\lambda, \theta, \theta_0, \Omega, P_s) f_i(\lambda, \theta, \Omega, P_s), \quad (2.3)$$

where  $f_i$  is the fraction of radiation reflected toward satellite in the direction of  $\theta$  that reaches satellite;  $I_d$  is the sum of direct and diffuse radiation reaching the surface; and  $S_b$  is the fraction of the reflected radiation scattered back to the surface by the atmosphere. The denominator in Equation (2.2) accounts for multiple reflections between the reflecting surface and the atmosphere [McPeters *et al.*, 1996].

Polarization is considered in TOMRAD. To calculate radiance as described above, the following information needs to be specified: ozone absorption coefficients, Rayleigh scattering coefficients, climatological ozone and temperature profiles, viewing geometry, surface pressure, and surface reflectivity. Temperature profiles are needed because ozone absorption cross section is weakly temperature dependent.

### 2.3 Radiance Calculation for the Look-up Table of the TOMS V7 Algorithm

In the calculation of the TOMS V7 look-up table using TOMRAD, the Rayleigh scattering coefficients are based on the *Bates* [1984] values of the refractive index of the air and the King's correction factor; the ozone absorption coefficients are taken from *Bass and Paur* [1984] and *Paur and Bass* [1984]. The TOMRAD accounts for the effect of molecular anisotropy on backscattered radiance by applying a molecular depolarization factor, which is obtained from the interpolated values of King's correction factor [Bates, 1984]. The effect of Rotational Raman scattering on backscattered radiance is not included in TOMRAD, but a correction is applied to the TOMS-measured radiance. In TOMRAD, the atmosphere is treated as pseudo-spherical where the primary beam is properly attenuated for the sphericity of the Earth.

A spherical correction to the outgoing beam is applied in the forward model calculation. The climatological ozone and temperature profiles were based on Solar Backscatter UltraViolet (SBUV) above 15 km and on balloon ozonesonde measurements for lower altitudes. Each standard profile represents a yearly average for a given total ozone and latitude. These profiles are defined at Umkehr layers. A total of 26 profiles was constructed, 6 profiles at low latitude ( $\leq 15^\circ$ ), 10 profiles each at middle ( $15^\circ$ - $75^\circ$ ) and high ( $\geq 75^\circ$ ) latitudes. The profiles cover a range of 225-475 DU at low latitudes and 125-575 DU at middle and high latitudes, in steps of 50 DU [McPeters *et al.*, 1996]. For convention, the profiles are named with a letter that stands for latitudes, “L” for low latitude, “M” for mid-latitude, and “H” for high latitude, followed by the 3-digit amount of TOC in DU. For example, “L275” means a low latitude profile with a TOC of 275 DU.

Because of the finite bandwidth, TOMS does not measure a monochromatic radiance. The ozone absorption coefficients, Rayleigh scattering coefficients, molecular depolarization factors, and solar fluxes show some variation in a single TOMS bandwidth. To simulate TOMS measurements, radiances are calculated at  $\sim 0.05$ -nm intervals across each TOMS slit, using the appropriate absorption coefficients, Rayleigh scattering coefficients, and molecular depolarization factors. The normalized radiance  $\overline{A_{\lambda_0}}$  for the entire band centered at  $\lambda_0$  is given by the following expression:

$$\overline{A_{\lambda_0}} = \frac{\int A_{\lambda} F_{\lambda} S_{\lambda} d\lambda}{\int F_{\lambda} S_{\lambda} d\lambda}, \quad (2.4)$$

where  $A_{\lambda}$  is the normalized radiance at wavelength  $\lambda$ ;  $F_{\lambda}$  is the solar flux at wavelength  $\lambda$ ; and  $S_{\lambda}$  is the triangular slit function at wavelength  $\lambda$ . The radiance passing through an absorbing and scattering region can be generally described as having a dependence  $I \sim \exp(-\tau)$ . In the case of ozone absorption only, the optical depth  $\tau$  depends on the number of absorbers  $n$  in a column and absorption efficiency  $Q$ :  $I \sim \exp(-nQ)$ . The  $n$  is proportional to  $-\log_{10} I$ . The TOMS V7 algorithm therefore uses  $A_{\lambda}$  in the form of N-value  $N_{\lambda}$ , defined as follows:

$$N_{\lambda} = -100 \log_{10}(A_{\lambda}). \quad (2.5)$$

The N-value provides a unit for backscattered radiance that has a scale comparable to the ozone column [McPeters *et al.*, 1996].

For the look-up table used in the TOMS V7 algorithm, the quantities  $I_m$ ,  $I_a$ ,  $T$ , and  $S_b$  of Equations (2.1) and (2.2) are computed at the six wavelengths for all 26 standard profiles and two reflecting surface pressure levels (1.0 atm and 0.4 atm). For each of these cases,  $I_m$ ,  $I_a$  and  $T$  are calculated for ten SZAs ( $0^\circ$ ,  $30^\circ$ ,  $45^\circ$ ,  $60^\circ$ ,  $70^\circ$ ,  $77^\circ$ ,  $81^\circ$ ,  $84^\circ$ ,  $86^\circ$ , and  $88^\circ$ ) and six VZAs ( $0^\circ$ ,  $15^\circ$ ,  $30^\circ$ ,  $45^\circ$ ,  $60^\circ$ , and  $70^\circ$ ) [McPeters *et al.*, 1996].

## 2.4 The TOMS V7 Algorithm

The TOMS V7 algorithms for different TOMS instruments are similar except that the look-up tables are calculated at their corresponding wavelengths and the triplets of wavelengths are different. Table 2.2 lists the triplets of wavelengths for different TOMS instruments.

**Table 2.2** TOMS triplets of wavelengths (when 2 wavelengths are listed, the wavelength in parenthesis applies to EP and ADEOS TOMS instruments only, the other applies to N7 and M3 TOMS instruments).

| Triplets | Optical Path Length (OPL) (atm-cm) | Ozone Sensitive Wavelength $\lambda_1$ (nm) | Ozone Insensitive Wavelength $\lambda_2$ (nm) | Reflectivity Wavelength (nm) |
|----------|------------------------------------|---|---|------------------------------|
| A        | $OPL \leq 1$                       | 312   | 331   | 380 (360)                    |
| B        | $1 < OPL \leq 3$                   | 317   | 331   | 380 (360)                    |
| C        | $OPL \geq 3$                       | 331 (322)                                   | 339 (331)                                     | 380 (360)                    |

The TOMSV7 algorithm assumes that the reflected radiation can come from two levels, ground and cloud. To derive ozone for a given measurement, surface pressure and CTP need to be known. The average ground terrain pressures were converted from the National Oceanic and Atmospheric Administration (NOAA) National Meteorological Center (NMC)  $0.5^\circ$ -latitude by  $0.5^\circ$ -longitude terrain

height data [McPeters *et al.*, 1996]. The CTPs were based on ISCCP monthly data averaged over 0.5°-latitude by 0.5°-longitude grids. There are two main steps in the TOMS V7 algorithm. The first step is to derive effective reflectivity and ECF from the measured radiance at reflectivity wavelength (380 nm for N7 and M3 TOMS, 360 nm for EP and ADEOS TOMS). Then the TOC is retrieved using a triplet of wavelengths [McPeters *et al.*, 1996].

#### 2.4.1 Partial Cloud Model

A PCM is employed to determine whether the scene is clear, fully cloudy, or partially cloudy. The calculated radiances for reflection off the ground and reflection from clouds are based on tables of calculated radiances. In the absence of snow/ice cover, the maximum reflectivity is assumed to be 8% for reflection off the ground and the MFCR is assumed to be 80% for reflection from clouds. The corresponding clear and cloud radiances ( $I_{clear}$  and  $I_{cloud}$ ) at reflectivity wavelength for the assumed ground and cloud reflectivity can be determined based on the corresponding radiances in the look-up table given the viewing geometry and surface pressures. The measured radiance  $I_{meas}$  is then compared with  $I_{clear}$  and  $I_{cloud}$ . If  $I_{clear} \leq I_{meas} \leq I_{cloud}$ , then the ECF  $f_c$  is derived as

$$f_c = \frac{I_{meas} - I_{clear}}{I_{cloud} - I_{clear}}. \quad (2.6)$$

In the above equation, the independent pixel approximation is implied, applying plane-parallel radiative transfer theory to both clear and cloudy areas and neglecting the horizontal photon transport between clear and cloudy areas. The independent pixel approximation well describes the radiative process for large-scale scheme (greater than 200-500 m) and is implied in all current cloud remote sensing applications such as inferring cloud optical depth and effective droplet radius [Marshak *et al.*, 1995] and retrieving traces gases in cloudy areas [Bhartia, 2001; Chance, 2001; Marshak *et al.*, 1995]. In the ozone retrieval, calculated radiances at other shorter wavelengths are determined applying the same assumption,

$$I_\lambda = I_{\lambda,cloud} \times f_c + I_{\lambda,clear} \times (1 - f_c). \quad (2.7)$$

Then an effective reflectivity is derived from ECF

$$R_s = 0.8 \times f_c + 0.08 \times (1 - f_c). \quad (2.8)$$

If  $I_{meas} \leq I_{clear}$  or  $I_{meas} \geq I_{cloud}$ , then the scene is considered to be clear or overcast, respectively. The actual surface reflectivity is derived by from  $I_{meas}$  by inverting Equations (2.1) and (2.2):

$$R_s = \frac{I_{meas} - I_a}{T + S_b(I_{meas} - I_a)}. \quad (2.9)$$

This reflectivity is used to determine calculated radiances at other shorter wavelengths from the look-up table for clear and overcast scenes [McPeters *et al.*, 1996].

#### 2.4.2 Ozone Retrieval

The initial ozone is estimated using the pair justification method. The B-pair (317 nm and 331 nm) is used. For a given measurement, its conditions -- geometry, latitude, CTP and terrain height pressure, and surface reflectivity (or ECF if partially cloudy), are measured or derived. Then radiances are calculated at 317 nm and 331 nm from the look-up table for each tabulated ozone value. The two tabulated ozone values whose calculated B-pair N-value differences bracket the measured N-value difference are selected. The initial ozone amount  $\Omega_0$  is estimated by linearly interpolating between the two tabulated ozone values using the measured pair N-value difference and the two calculated pair N-value differences [McPeters *et al.*, 1996].

With the initial ozone estimate, the calculated N-values at all TOMS wavelengths can be determined. In general, these calculated N-values are not equal to the measured N-values. It is assumed that the reflectivity is wavelength independent in the initial ozone estimate, but this is not true for some surface conditions such as sea glint, desert dust, or ice. In addition, residual errors in the instrument calibration can produce a wavelength-dependent artifact in the measured N-values. Due to these

wavelength-dependent effects, a triplet method is used to derive a first-order correction to the initial ozone estimate by assuming that the wavelength-dependent contribution factor other than ozone is a linear function of wavelength,  $a + b\lambda$ , then

$$N_{meas,\lambda} = N_{0,\lambda} + (\Omega - \Omega_0) \left( \frac{dN_\lambda}{d\Omega} \right)_0 + a + b\lambda, \quad (2.10)$$

where  $N_{meas,\lambda}$  is the measured N-value at wavelength  $\lambda$ ;  $N_{0,\lambda}$  is the calculated N-value at wavelength  $\lambda$  using  $\Omega_0$ ; and  $(dN_\lambda/d\Omega)_0$  is the sensitivity of N-value to ozone at wavelength  $\lambda$ . Let  $r_\lambda = N_{meas,\lambda} - N_{0,\lambda}$  be the residue at wavelength  $\lambda$  and  $s_\lambda = (dN_\lambda/d\Omega)_0$ . At the wavelength 380 (or 360) nm, where the reflectivity is derived,  $s_{380} = 0$  and  $r_{380}$  is 0 (380 nm is used for example). Therefore, we can derive from Equation (2.10) that  $a = -380 b$ . And therefore, at ozone-sensitive and ozone-insensitive wavelengths,

$$r_\lambda = s_\lambda (\Omega - \Omega_0) + b(380 - \lambda). \quad (2.11)$$

Using two measurements at two wavelengths, labeled  $\lambda_1$  and  $\lambda_2$ , we can solve for the two unknowns  $\Omega$  and  $b$ . Then the  $\Omega$  is solved as

$$\Omega = \Omega_0 + \frac{r_{\lambda_1} \Delta\lambda_2 - r_{\lambda_2} \Delta\lambda_1}{s_{\lambda_1} \Delta\lambda_2 - s_{\lambda_2} \Delta\lambda_1}. \quad (2.12)$$

The selection of wavelengths  $\lambda_1$  and  $\lambda_2$ , listed in Table 2.2, is dependent on the Optical Path Length (OPL)  $\Omega_0(\sec\theta_0 + \sec\theta)$ .

Dependent on the latitude of a given measurement  $\Omega$  is derived using Equation (2.12) based on one or two sets of profiles. For latitude  $\leq 15^\circ$ , only the low latitude profiles are used; for  $15^\circ \leq$  latitude  $\leq 45^\circ$ , two  $\Omega$  values are derived using low latitude and mid-latitude profiles, respectively; for  $45^\circ <$  latitude  $<$

75°, two  $\Omega$  values are derived using mid-latitude and high latitude profiles, respectively; for latitude  $\geq 75^\circ$ , only the high latitude profiles are used. If two sets of profiles are used, the ozone is derived as follows:

$$\Omega = (1 - f_{prof})\Omega_{lower} + f_{prof}\Omega_{higher} \quad (2.13)$$

and

$$f_{prof} = \frac{|lat_m| - |lat_{lower}|}{|lat_{higher}| - |lat_m|}, \quad (2.14)$$

where  $\Omega_{lower}$  is the retrieved ozone using lower latitude profiles;  $\Omega_{higher}$  is the retrieved ozone using higher latitude profiles;  $lat_m$  is the latitude for measurement;  $lat_{lower}$  is the lower latitude;  $lat_{higher}$  is the higher latitude; and  $f_{prof}$  is the weight given to the higher latitude profile. For  $OPL \leq 1.5$ , the derived ozone from Equation (2.12) or (2.13) is the best ozone [McPeters *et al.*, 1996].

For longer  $OPL > 1.5$ , further treatment is needed for latitude interpolation. The basic principle is to determine an  $f_{prof}$  that the derived ozone are consistent using two triplets. If  $1.5 < OPL \leq 3$ , the B triplet is used for retrieval but a consistent A triplet is required; if  $OPL > 3$ , the C triplet is used for retrieval but a consistent B triplet is required. For convenience, the two triplets are called the “retrieval triplet” and the “checking triplet”, respectively. The implementation of this approach uses residues. First the ozone value  $\Omega_I$  is calculated using Equation (2.12) or (2.13). The residues are adjusted for the change in ozone at the first two wavelengths of checking triplets

$$r_{I,\lambda} = r_{0,\lambda} - s_i(\Omega_I - \Omega_0), \quad (2.15)$$

where  $r_{i,\lambda}$  ( $i = 0, 1$ ) is the residue for  $\Omega_i$  ( $i = 0, 1$ ). For each of the two profile sets, the triplet residue  $r_{trip}$  can be defined as

$$r_{trip} = r_{\lambda} - \frac{\lambda - 380}{\lambda' - 380} r_{\lambda'}, \quad (2.16)$$

where  $\lambda'$  is the ozone insensitive wavelength of the checking triplet,  $r_{\lambda}'$  is the adjusted residue at this wavelength, and  $r_{\lambda}$  is the adjusted residue at the ozone sensitive wavelength of the checking triplet. In order to find the profile that will yield consistency, i.e., the mixed  $r_{trip}$  is zero, then  $f_{prof}$  is derived as

$$f_{prof} = \frac{r_{trip}(lower)}{r_{trip}(lower) - r_{trip}(higher)}, \quad (2.17)$$

where  $r_{trip}(lower)$  and  $r_{trip}(higher)$  are the triplet residues using lower latitude and higher latitude profiles, respectively. The ozone is re-evaluated using Equation (2.13) with the new mixing fraction to obtain a new ozone value  $\Omega_2$ . Adjusted residues are calculated using Equation (2.15) and a triplet residue is calculated using Equation (2.16). If the triplet residue is  $\leq 0.1$  N-value units, then  $\Omega_2$  is adopted as the best ozone; otherwise, the process is repeated one more time, and the second result  $\Omega_3$  is accepted as the best ozone [McPeters et al., 1996].

If  $f_{prof}$  from Equation (2.14) or (2.17) is  $< 0$  when using mid- and high- latitude profiles, the process is repeated using low- and mid-latitude profiles. If  $f_{prof} > 1$  when using low- and mid-latitude profiles, the process is repeated using mid- and high-latitude profiles. Finally, if the best ozone from Equation (2.12) or (2.13) or  $\Omega_3$  differs from the initial B-pair estimated ozone by more than 50 DU, the procedure starting with Equation (2.12) is repeated with the best ozone as the initial estimate  $\Omega_0$  until the difference is less than 50 DU or at most two more iterations [McPeters et al., 1996].

## CHAPTER 3

### OCCURRENCE OF OZONE ANOMALIES OVER CLOUDY AREAS IN TOMS DATA

Although the employed PCM and monthly mean ISCCP climatology have largely reduced the correlation coefficient between TOC and reflectivity [Hsu *et al.*, 1997; McPeters and Labow, 1996], the anomalous ozone distribution found in North Dakota on June 29, 1989 facilitates us to examine the frequency of occurrence of such Ozone Anomalies (OAs) in the high-resolution footprint TOMS V7 level-2 data. Section 3.1 defines OA and describes the methods to find OAs. Section 3.2 shows the spatial distribution of OAs in TOMS V7 level-2 data.

#### 3.1 Methodology

This study uses the TOMS V7 level-2 data from N7 TOMS during the 1979-1992 period and from EP TOMS during the 1997-1999 period. The presence of sun glint and aerosols has been recognized to introduce errors to the retrieved ozone [McPeters *et al.*, 1996; McPeters *et al.*, 1996b; Torres and Bhartia, 1999; Torres *et al.*, 1998]. To focus on the effects of clouds on ozone retrieval, we correct the OREs associated with both sun glint and aerosols using the Dave reflectivity correction code [*personal communication*, C. G. Wellemeyer, 1999]. The effects of ozone correction are apparent in regions of sun glint, dust, and biomass burning. The corrected ozone is typically 2~8 DU for sun glint, 2~10 DU for biomass burning aerosols, and 2~20 DU for desert dust, consistent with the results of McPeters *et al.* [1996] and Torres and Bhartia [1999]. To avoid problems due to snow, ice, and polar stratospheric clouds at high-latitudes [McPeters *et al.*, 1996], we studied only regions between 60°S and 60°N.

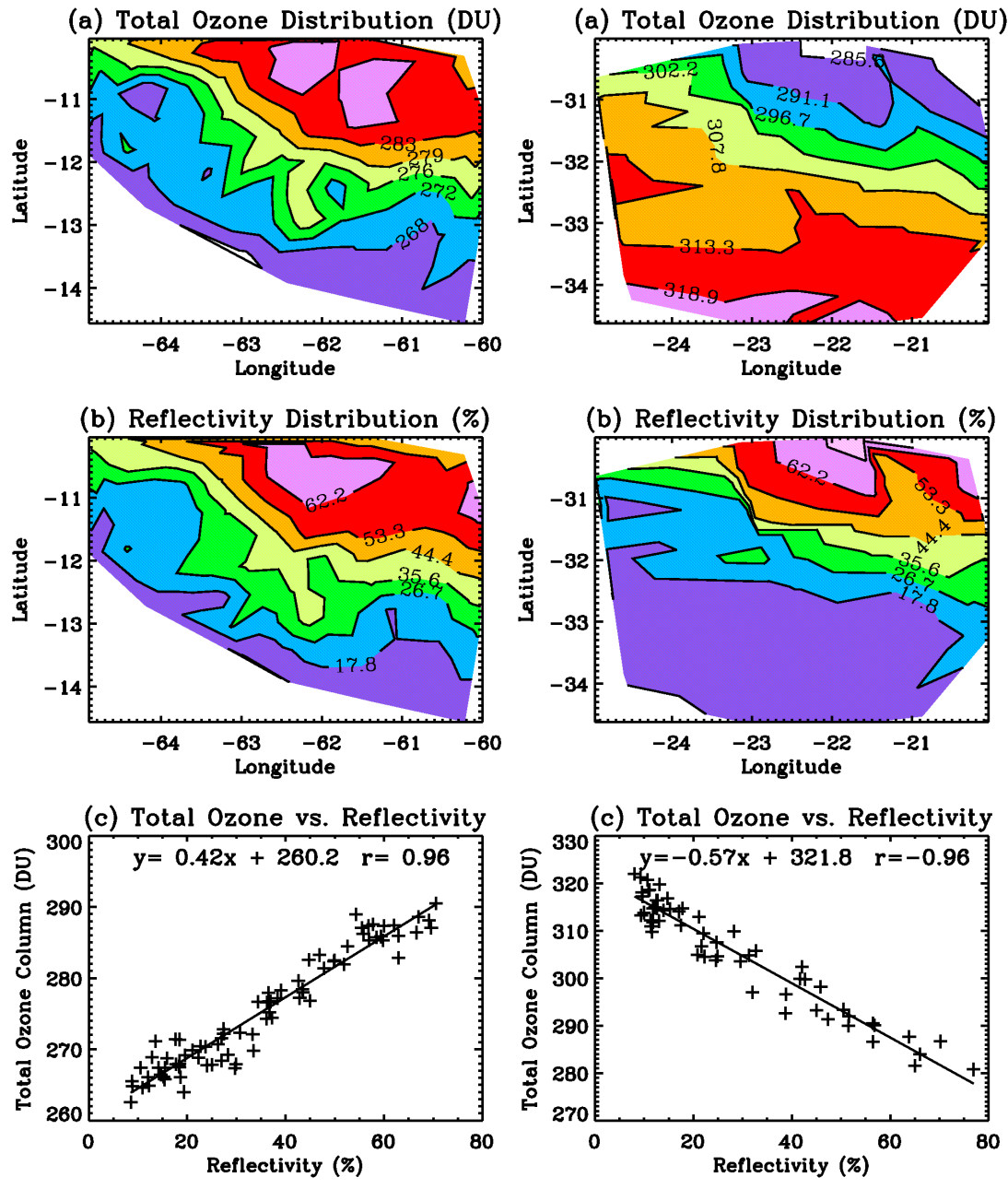


**Figure 3.1** Anomalous ozone distribution over cloudy areas located in South America on January 1, 1980 (left) and in the south Atlantic Ocean on July 15, 1980 (right). (a) Distribution of total ozone. (b) Distribution of reflectivity. (c) Relationship between total ozone and reflectivity.

Figure 3.1 shows two examples of anomalous ozone distribution over cloudy areas, one with more TOC over cloudy areas (left) and the other with less TOC over cloudy areas (right). The total ozone distribution is highly correlated positively or negatively with the TOMS-measured 380-nm reflectivity distribution. Because cloudy/clear ozone difference originates mainly from the upper troposphere and lower stratosphere, where the life-time of ozone is several months or even longer [Seinfeld and Pandis, 1997], the large change of ozone column by 30-40 DU across cloudy/clear boundary is anomalous in TOMS V7 data. Ozone retrieval errors or special geophysical phenomena must cause these OAs. We calculate the spatial correlation coefficient and linear regression slope between the daily TOC and 380-nm (in N7)/or 360-nm (in EP) reflectivity (simplified as ozone/reflectivity slope or slope) in a  $5^\circ$ -longitude by  $5^\circ$ -latitude area, which contain at least 20 measurements. The number of pixels in a  $5^\circ \times$  by  $5^\circ$  grid is about 70 on average, but is dependent on latitude and VZA, and could be up to 150. To ensure statistically significant ozone anomalies, we require that the reflectivity range in an OA be greater than

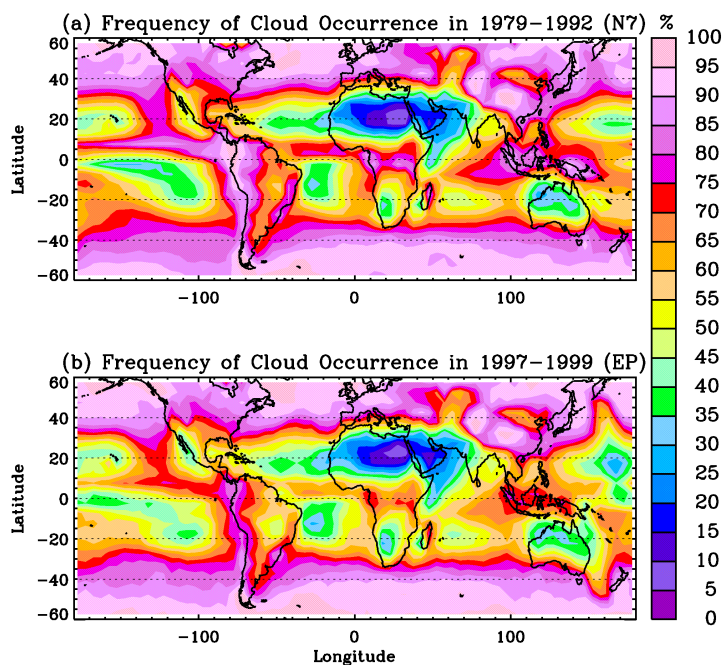


**Figure 3.2** Average frequency distribution of cloud fields during the 1979-1992 N7 TOMS period (a) and the 1997-1999 EP TOMS period (b).

30%. Therefore, such a  $5^\circ \times 5^\circ$  grid can be considered to be a cloud field that contains scenes of different cloudiness and might includes clear, partly cloudy, and overcast scenes.

Figure 3.2 shows the spatial frequency distribution of such cloud fields (i.e., reflectivity range greater than 30%) averaged over the N7 TOMS period (a) and EP TOMS period (b). The frequency is defined as the fraction of days when a cloud field occurs. During the N7 TOMS period, most of the regions contain cloud fields with a frequency greater than 60%. Especially at mid-latitude regions  $40^\circ\text{N}$  north or  $40^\circ\text{S}$  south, the frequency is typically greater than 80%. The area with the lowest frequency is North Africa, the region of Sahara desert, where the frequency is as low as  $< 5\%$ . Other areas with frequency of cloud fields less than 40% include other dessert areas such as Arabian Peninsula, northwestern of Australia, and subtropical semi-permanent high-pressure area. The frequency distribution of cloud fields during the EP TOMS period is similar except that the frequency in the tropics is smaller by  $\sim 15\%$ . This is mainly because the N7 satellite (with an altitude of 800 km) is higher than the EP satellite and therefore provides more spatial coverage in the tropics. The elevation of EP from 500 km to 740 km at the end of 1997 increases the tropical frequency by 12% but is still 10% less than the average N7 frequency. The N7/EP difference is small at mid-latitude areas because both EP and N7 TOMS provide full spatial coverage.

Figure 3.3 shows the daily frequency of correlation coefficients in the Northern Hemisphere and Southern Hemisphere in January and July 1980, respectively. Each thin curve represents the frequency distribution for one day, and the daily curves are very similar for each day. These correlation coefficients peak around zero in the hemisphere winter but shift to the right in the hemisphere summer mostly due to the summer increase in cloud occurrence [Stowe *et al.*, 1989]. There is a significant fraction of large negative or positive correlation coefficients. Because reflectivity is usually related to cloudiness, the larger correlation coefficients and slopes usually indicate larger cloudy/clear TOC differences. To characterize the frequency of occurrence of anomalous ozone distributions over cloudy areas such as the cases shown in Figure 3.1, we select the intermediate values of  $\pm 0.5$  as the criteria. If a correlation coefficient is  $\geq 0.5$  or  $\leq -0.5$ , we define it as a Positive Ozone Anomaly (POA) or a Negative Ozone Anomaly (NOA), respectively. We find all the OAs from the N7 and EP TOMS data and built yearly OA databases.

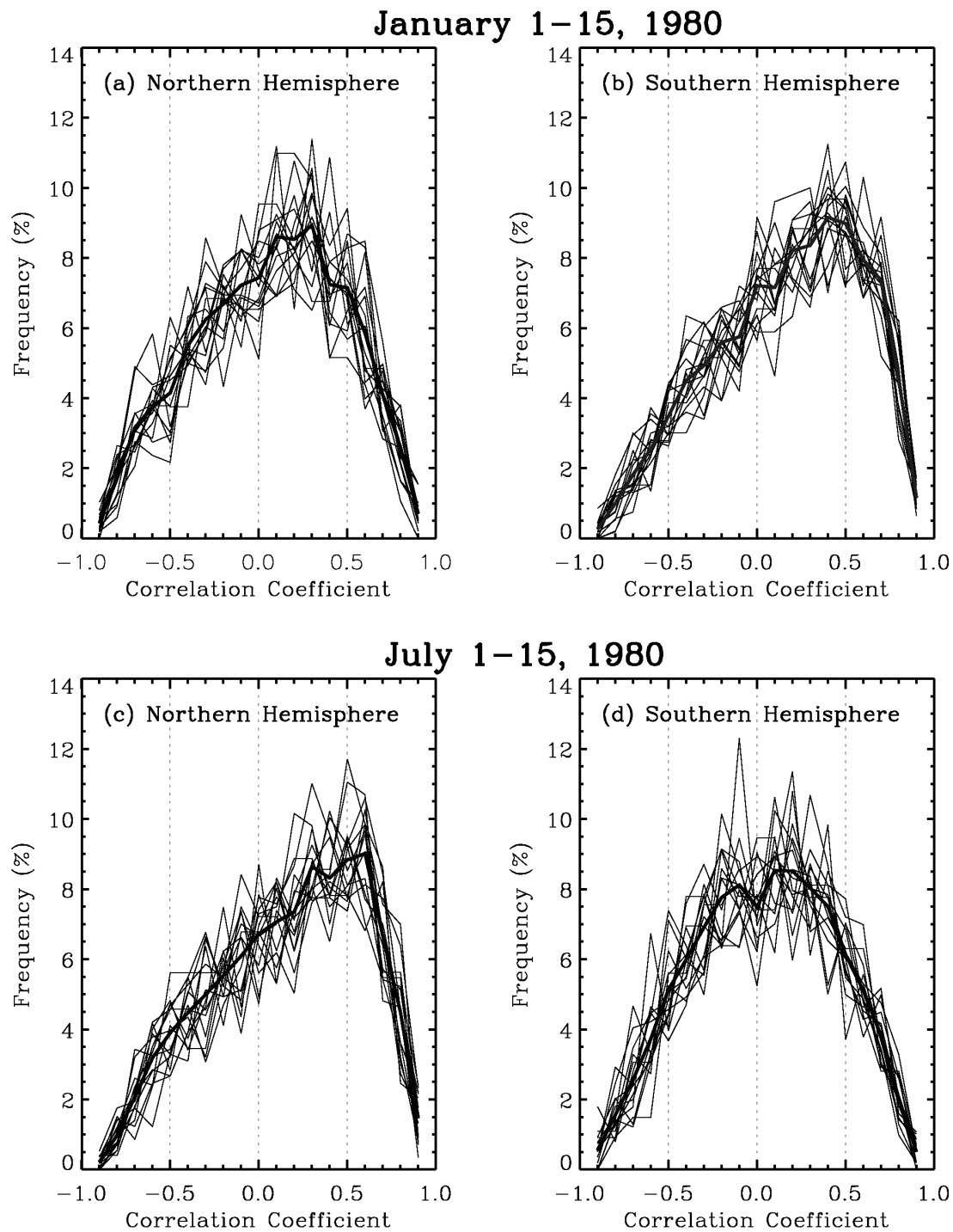


**Figure 3.3** Frequency of correlation coefficients (in each bin of 0.1) between the TOMS TOC and the TOMS 380-nm reflectivity in  $5^\circ$ -longitude  $\times$   $5^\circ$ -latitude areas in the Northern and Southern Hemispheres during January 1-15, 1980 (a and b) and July 1-15, 1980 (c and d). Thin curves are for each day and the thick curve is the average curve over the period.

### 3.2 Occurrence of Ozone Anomalies

Figures 3.4 (a) and (b) show the spatial mean fraction distribution of POAs and NOAs in the 14-year N7 TOMS period. We define fraction for a  $5^\circ \times 5^\circ$  grid as the portion of cloud fields with POAs or NOAs. The average fraction of occurrence of OAs is  $31.8 \pm 7.7\%$  (1 standard deviation). About 18% and 59% of OAs occur over both land and ocean, respectively, almost proportional to the land and ocean area coverage. The average fraction for POAs is  $21.1 \pm 10.0\%$ , almost twice that of NOAs, which is  $10.6 \pm 6.3\%$ . Ozone anomalies are not evenly distributed on the globe. Some regions are dominated with a high fraction of POAs and NOAs. Two extensive regions dominated by POAs, with fractions greater than 40%, are located in the eastern Atlantic Ocean off the West Coast of South Africa (WCSAF) and in the eastern Pacific Ocean off the West Coast of South America (WCSAM). These are regions of frequent marine stratocumulus clouds [Rossow and Schiffer, 1991; Thompson et al., 1993]. Especially over WCSAF, the average frequency of marine stratocumulus clouds is  $\sim 70\%$  from the ISCCP climatology [Thompson et al., 1993]. Other regions with POAs of fractions greater than 40% include the United States, central China, southern Australia, and tropical convective cloudy areas [Ramanathan et al., 1989; Stowe et al., 1989; Wang et al., 1996] such as central America, central Africa, and the western Pacific Ocean. Mid-latitude regions are extensively associated with high dense POAs with fraction of 15-40%. Areas of NOAs with fraction greater than 25% occur in mountainous regions in northwestern China, North Africa, the Atlantic Ocean (from southeastern United States to North Africa), and the India Ocean.

Figures 3.4 (c) and (d) show the spatial fraction distribution of POAs and NOAs in the 3-year EP TOMS period. The average fraction of occurrence of OAs is  $35.8 \pm 9.7\%$ , 4% higher than the corresponding N7 TOMS value. We can see that obvious contrasts occur between N7 and EP TOMS. There are very few POAs in tropical convective cloudy regions. However, there is a high fraction ( $\geq 40\%$ ) of NOAs distributed in the InterTropical Convergence Zone (ITCZ) oceanic regions including the tropical eastern Pacific Ocean, the tropical Atlantic Ocean, the Indian Ocean, and the Caribbean Sea. On average, there are more NOAs ( $20.5 \pm 12.7\%$ ) than POAs ( $15.3 \pm 9.1\%$ ) in EP, and the decrease in the fraction of POAs and the increase in the fraction of NOAs can be seen everywhere. But this contrast in fraction of NOAs and POAs between EP and N7 TOMS results mainly from NOA in tropical areas, and is much

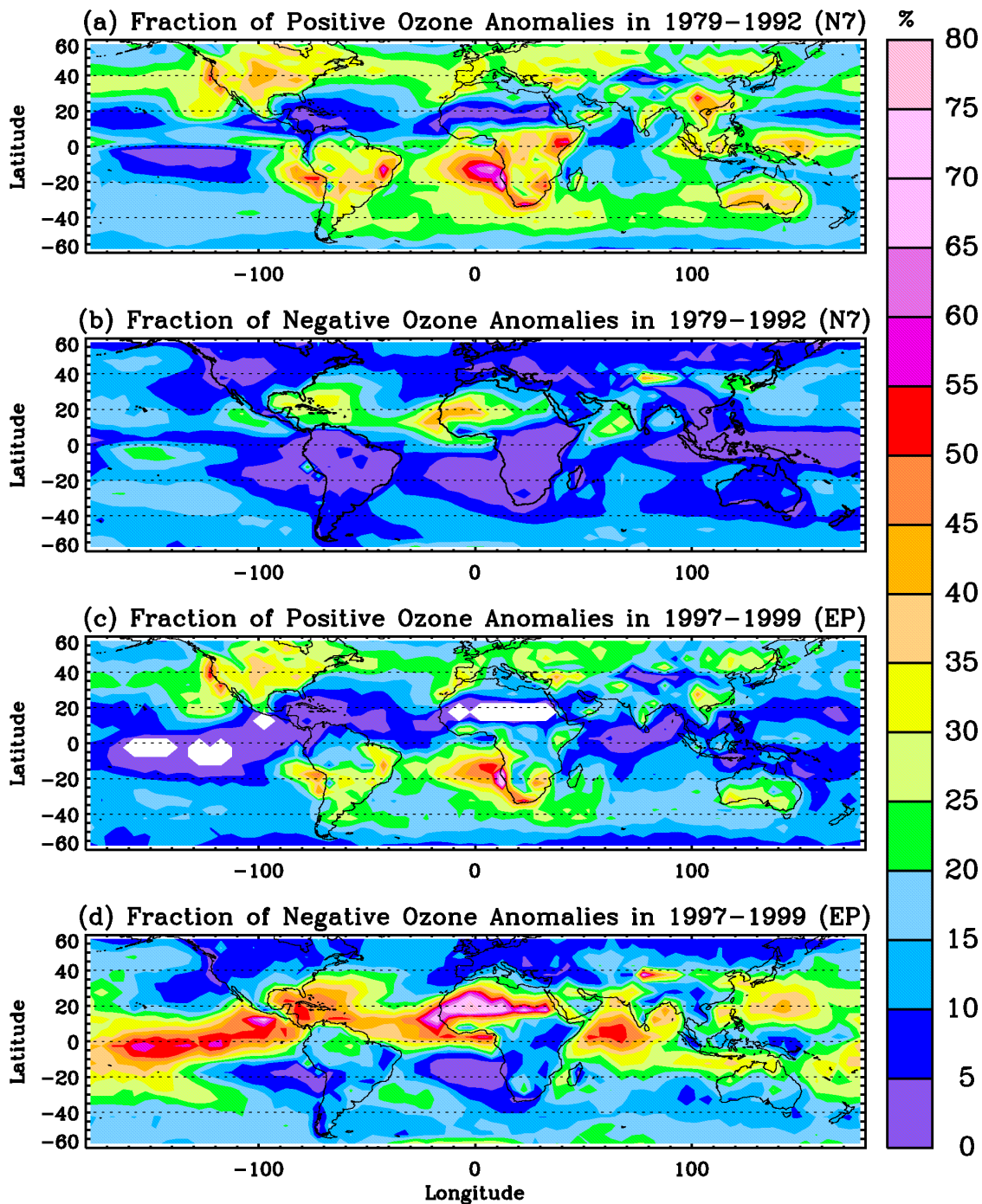


**Figure 3.4** OAs in 1979-1992 N7 TOMS data and 1997-1999 EP TOMS data. (a) Average spatial fraction distribution of POAs in N7 TOMS data from 1979 to 1992. (b) Same as (a) except for NOAs. (c) and (d) Same as (a) and (b) except in 1997-1999 EP TOMS data.

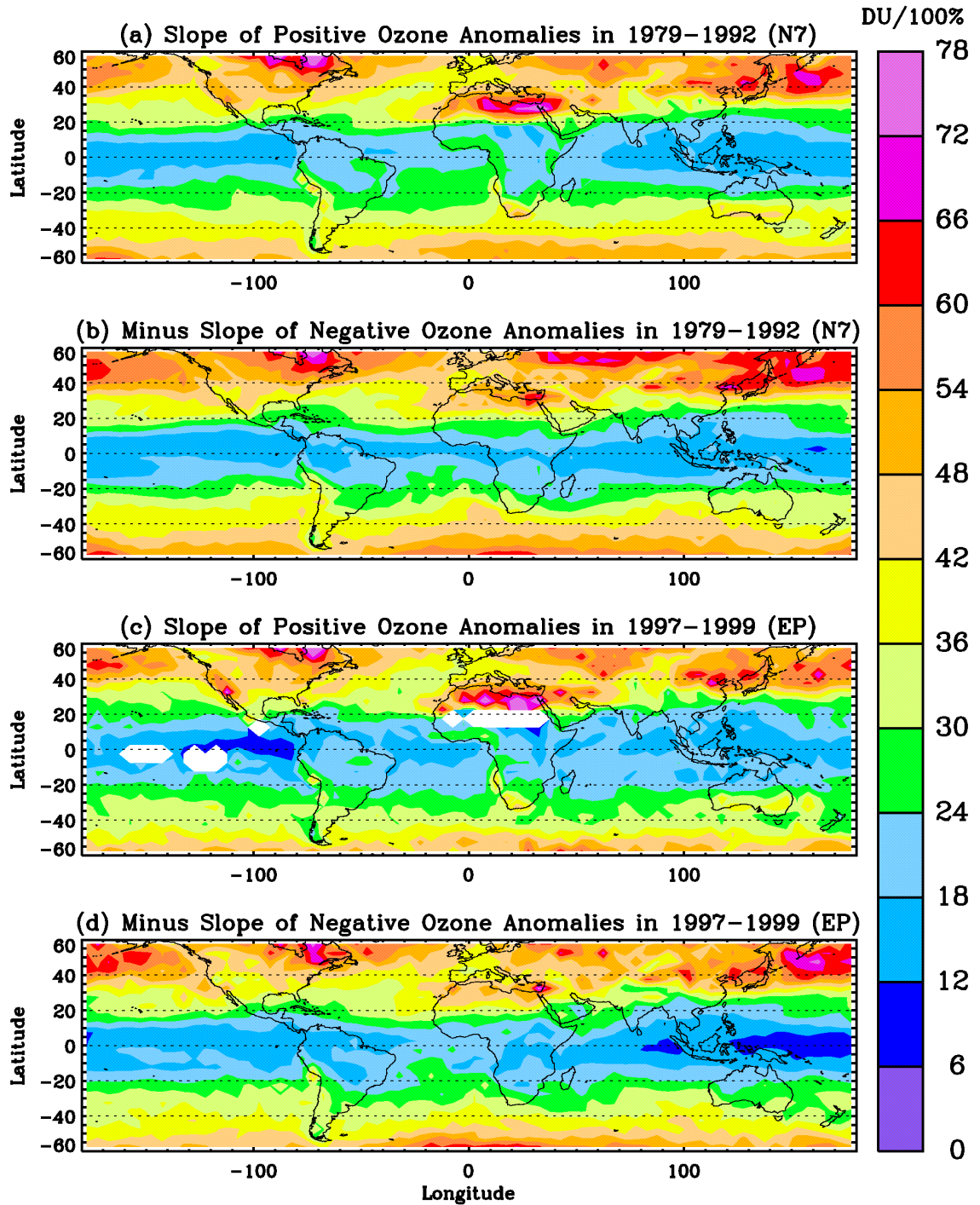


**Figure 3.5** Same as Figure 3.4 except for the linear regression slopes between ozone and reflectivity for OAs.

smaller in mid-latitudes. At mid-latitude regions ( $60^{\circ}\text{S}$ - $30^{\circ}\text{S}$ ,  $30^{\circ}\text{N}$ - $60^{\circ}\text{N}$ ), the average fractions of POAs and NOAs are 22.0% and 10.4%, respectively in N7 TOMS data and 17.5% and 14.7%, respectively in EP TOMS data. While in the tropics ( $15^{\circ}\text{S}$ - $15^{\circ}\text{N}$ ), the average fractions of POAs and NOAs are 20.2% and 9.3%, respectively in N7 TOMS data and 10.4% and 29.2%, respectively in EP TOMS data. At mid-latitudes, the total fraction of POAs and NOAs in EP TOMS is similar to that of N7 TOMS. The larger fraction of OAs by 4% in EP TOMS originates mainly from more tropical NOAs. Despite the difference in the ratio of the fraction of POAs to NOAs, the overall geographical locations of POAs and NOAs in EP TOMS data are very similar to those in N7 TOMS data.

*Ziemke et al.* [2000] have noticed the bias between EP and N7 TOMS data that the clear/cloudy TOC difference in N7 TOMS is  $\sim 5$  DU larger than that in EP. The higher ozone over cloudy areas in N7 increases the frequency of POAs and decreases the frequency of NOAs. The reason for this EP/N7 bias is not yet clear, but it is most probably due to non-linearity calibration errors in EP or N7 or both. That is to say, the actual relationship between digital counts and radiances is non-linear in either one of the TOMS or both, but is treated as linear in the TOMS calibration. This linear treatment of a non-linear calibration produces errors in high reflectivity scenes (larger digital counts) relative to low reflectivity scenes (lower digital counts). It is also not clear whether this non-linearity calibration error resides in clear or cloudy conditions. The EP instrument is the most recent, and probably best calibrated [*Stolarski et al.*, 2000; *personal communication*, S. Taylor, 1999; *personal communication*, G. Jaross, 2000], but we cannot resolve this difference currently.

Figure 3.5 shows the spatial distribution of the average ozone/reflectivity slope (magnitude) of POAs and NOAs. The magnitude of the average slope present in the anomalies is not distributed like the fraction of occurrence. The slope distribution, however, is mainly a function of latitude, increasing from about 12-30 DU/100% reflectivity (simplified as DU/100%) in tropical areas to about 40-80 DU/100% in mid-latitudes. The magnitude of the slope does not depend greatly on the sign of an anomaly, the type of surface (land/sea), or the fraction of occurrence. In spite of the contrasts in the fraction distribution of OAs between N7 TOMS and EP TOMS data, the slope distributions of OAs are very similar. Zonal asymmetry is still present in Figure 3.5. At mid-latitudes, large ozone/reflectivity slopes occur for OAs in the northern Pacific Ocean and northeastern North America as well as for POAs in North Africa and NOAs near

southern polar regions. In tropical areas, the slopes of POAs in N7 TOMS data and NOAs in EP TOMS data show a maximum in the Atlantic Ocean and minimum in the Pacific Ocean, and the slopes in the other two panels show nearly zonally invariant distributions

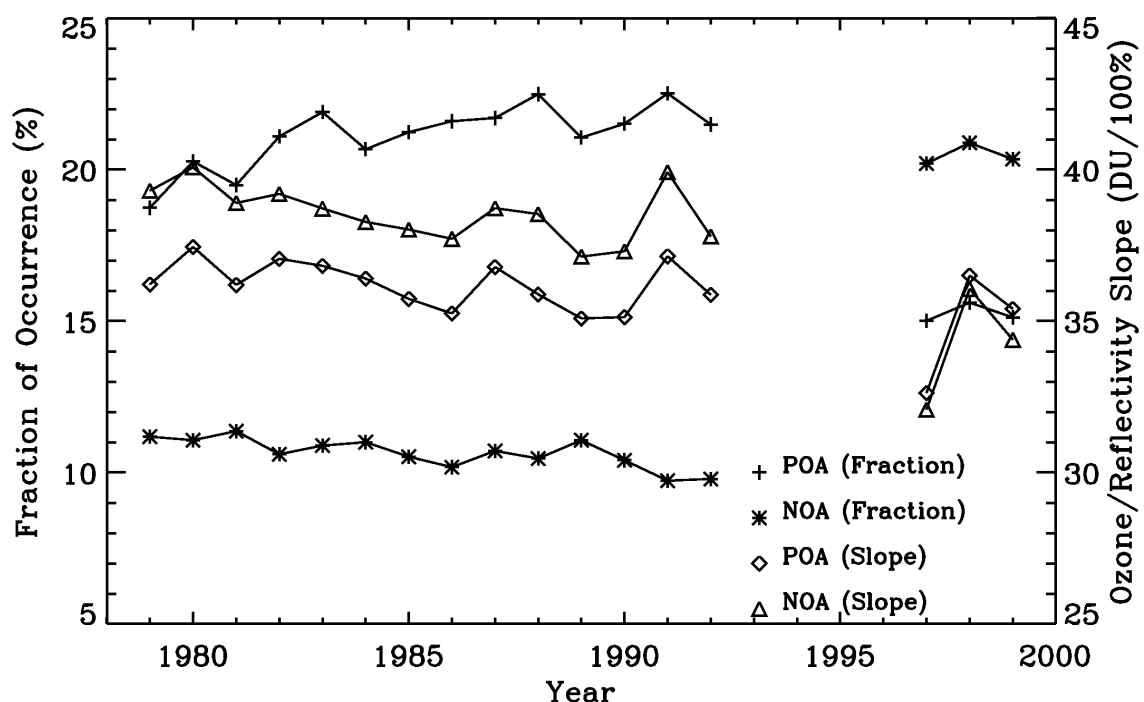


**Figure 3.6** Variation of annual average fractions and ozone/reflectivity slopes of POAs and NOAs.

The above features of fraction and slope distributions of POAs and NOAs are very consistent in every year in N7 or EP TOMS data, except in El Niño years. Figure 3.6 shows the yearly variation of the annual average fraction and ozone/reflectivity slope of OAs. In the 14-year N7 TOMS period, there is no significant annual-average variation even in El Niño years. The fraction variation is within 3%, and the slope variation is within 3 DU/100%. Because the EP period includes only 3 years, it is difficult to evaluate the annual variation of OAs. From 1997 to 1998, the average ozone/reflectivity slope increases in magnitude by  $\sim 5$  DU/100%. But there is no significant difference between 1998 (El Niño period) and 1999 (non-El Niño period). The fraction and slope of OAs in the second half-year of 1996 are comparable

to those of 1997. The increase in slope of OAs after 1997 may be related to the fact that the EP orbit was raised to 750 km [McPeters *et al.*, 1998]. The N7/EP contrast in the fraction of POAs and NOAs is obvious.

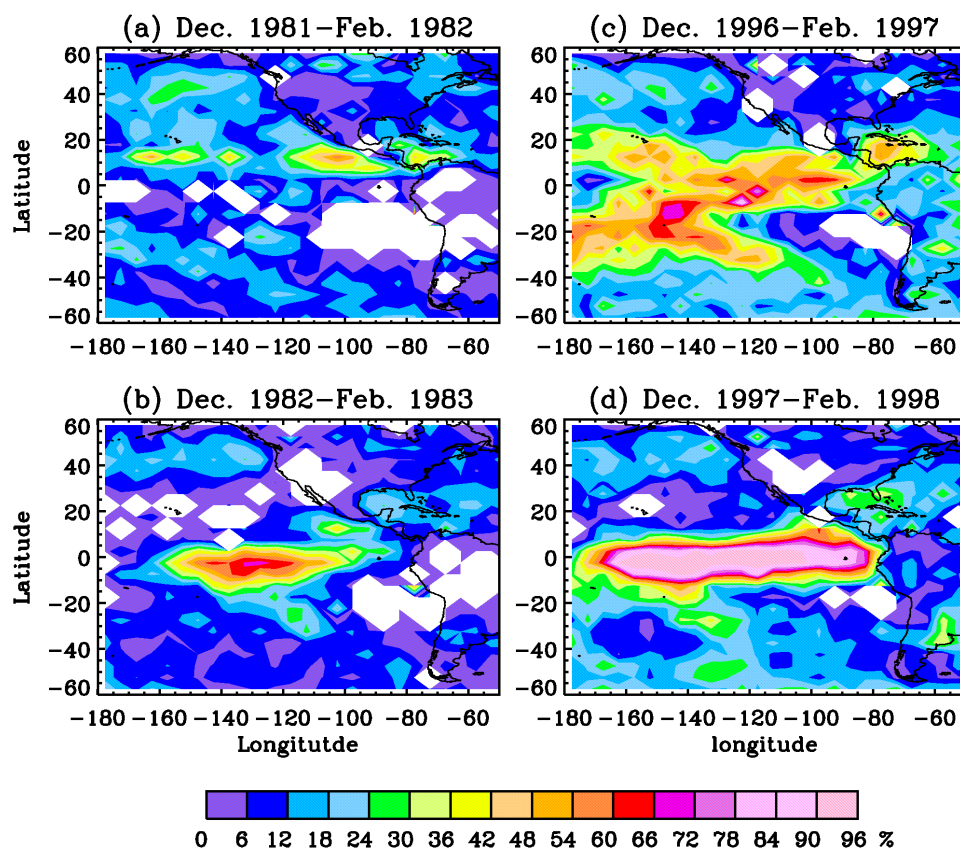


**Figure 3.7** Effects of the 1982-1983 and 1997-1998 El Niño events on OA distribution. (a) Fraction distribution of NOAs in non-El Niño period from December 1981 to February 1982. (b) Same as (a) except in El Niño period from December 1982 to February 1983. (c) and (d) same as (a) and (b) except for the 1997-1998 El Niño event.

Even though the El Niño events do not present significant changes to the annual-average fraction, they do produce significant regional effects. To show the effects of El Niño events on the OA distribution, Figure 3.7 compares the average fractions of OAs during the non-El Niño period (from December 1981 to February 1982 and from December 1996 to February 1997) and the El Niño period (from December 1982

to February 1983 and from December 1997 to February 1998). The most significant change is a ~40% increase in NOAs in the tropical eastern Pacific Ocean. This change in fraction of OAs begins significantly in November (1982-1983) or July (1997-1998), peaks from November through February, and disappears in July, time periods consistent with the duration of these two El Niño events. The effects of the 1986-1987 and 1991-1992 El Niño events on OAs are much smaller. Characterized by an anomalous increase in sea-surface temperature across the eastern and central tropical Pacific Ocean, these El Niño events shift the convection pattern from the western Pacific Ocean to the central and eastern Pacific Ocean. Correspondingly, there is a significant increase in cloud occurrence and precipitation in the eastern Pacific Ocean and a decrease in the western Pacific Ocean [Bell *et al.*, 1999; Chandra *et al.*, 1998; Wang *et al.*, 1996]. Because we are analyzing OAs over cloudy areas, the change in cloud occurrence will, of course, affect the fraction of OAs. The reasons there are more NOAs instead of POAs will be discussed in Chapter 7.

### 3.3 Summary

Among the correlation coefficients between ozone and reflectivity, we find that there is a significant portion of large negative or positive correlation coefficients. To characterize the frequency of occurrence of anomalous ozone distribution, we define that a  $5^\circ \times 5^\circ$  region contains a POA or NOA if the correlation coefficient between ozone and reflectivity is  $\geq 0.5$  or  $\leq -0.5$ , respectively. We investigate the fraction of OA occurrence and the ozone/reflectivity slope during the N7 TOMS period (1979-1992) and the EP TOMS period (1997-1999).

During the N7 TOMS period, the average fraction of OAs among all the cloud fields is  $31.8 \pm 7.7\%$ , of which 21.1% are POAs and 10.6% are NOAs. The fraction distribution of POAs shows a great spatial dependence. High fractions of POAs greater than 40% occur in WCSAF, WCSAM, tropical convective cloudy areas, central China, the United States, and southern Australia. The areas of northwestern China, the Atlantic Ocean from near southeastern United States to north Africa, and north Africa contain NOAs with fractions greater than 25%. The regions with extensive OAs are similar between N7 and EP TOMS data, but an obvious bias exists in the fraction distribution of OAs. During the EP TOMS period, the average fraction of OA occurrence is  $35.8 \pm 9.7\%$ , of which 20.5% are NOAs. This

increase in the fraction of NOAs and decrease in the fraction of POAs in EP TOMS data relative to N7 TOMS data can be seen everywhere, but more obviously in the tropical areas. The ozone/reflectivity slope distribution does not depend greatly on the sign of an anomaly, the fraction of occurrence, and the satellite (EP or N7), but it is mainly a function of latitude, increasing from about 12-30 DU/100% in the tropics to about 40-80% DU/100% in the mid-latitudes. The fraction and slope distributions of OAs do not vary much from year to year within the N7 or EP TOMS period. The annual mean fractions of POAs or NOAs in all years are within 3% and the annual mean slopes in all years are within 5 DU/100% in N7 or EP TOMS data. El Niño events do not cause much change to the annual average fraction, but they do produce significant regional effects. The 1982-1983 and 1997-1998 El Niño events increase the fraction of NOAs over the tropical eastern Pacific Ocean by ~40% during December-February.

## CHAPTER 4

### CLOUD-HEIGHT-RELATED OZONE RETRIEVAL ERRORS

This chapter investigates OREs induced by incorrect CTPs. The large cloud height error shown in Section 4.1 motivates us to study the OREs brought about by them. Section 4.2 discusses three different errors related to incorrect CTPs and describes the method to correct them.

#### 4.1 Cloud-Height Errors in TOMS Data

The assumed CTP from monthly mean ISCCP data could be very different from the actual CTP. The temporally and spatially collocated Temperature Humidity Infrared Radiometer (THIR) measurements on board N7 spacecraft are used to assess cloud-height errors in the TOMS retrieval. Because THIR pixels have higher spatial resolution than TOMS pixels, the THIR pixels (about 50 at low- and mid-latitudes) were averaged together with collocated TOMS fields of view. Cloud-top pressure is derived from the 11.5  $\mu\text{m}$  collocated THIR radiance with other auxiliary information [*Stowe et al.*, 1988; *Stowe et al.*, 1989]. Six years' (1979-1984) THIR CTP data are available in the current TOMS V7 level-2 data.

Figure 4.1 shows the monthly average CTP difference between THIR and ISCCP between 60°S and 60°N (both THIR and ISCCP cloud data are from the TOMS V7 level-2 data product) as a function of THIR CTP in January and July 1980, respectively and the histogram distribution of cloud pressure difference. Because THIR measurements with reflectivity less than 40% are less reliable, only measurements with reflectivities greater than 40% are used [*personal communication, P. K. Bhartia*, 1999]. On average, the assumed CTP is overestimated for high clouds and underestimated for low clouds. The CTP difference ranges from -300 hPa for high clouds (THIR pressure  $\leq$  200 hPa) to 150 hPa for low clouds

(THIR pressure  $\geq 750$  hPa), and is about zero for THIR CTP of  $\sim 550$  hPa. The CTP difference is smaller for low clouds compared to that for high clouds. The large CTP difference between the monthly mean ISCCP in approximately  $2.5^\circ \times 2.5^\circ$  regions and THIR data is not surprising. High, middle, and low clouds could occur in the same regions; for convective clouds, CTPs usually change during their lifetime. The monthly mean CTP, which takes the average CTP from all clouds at different altitudes, is reasonably higher than the CTPs of low clouds, and lower than the CTPs of high clouds.

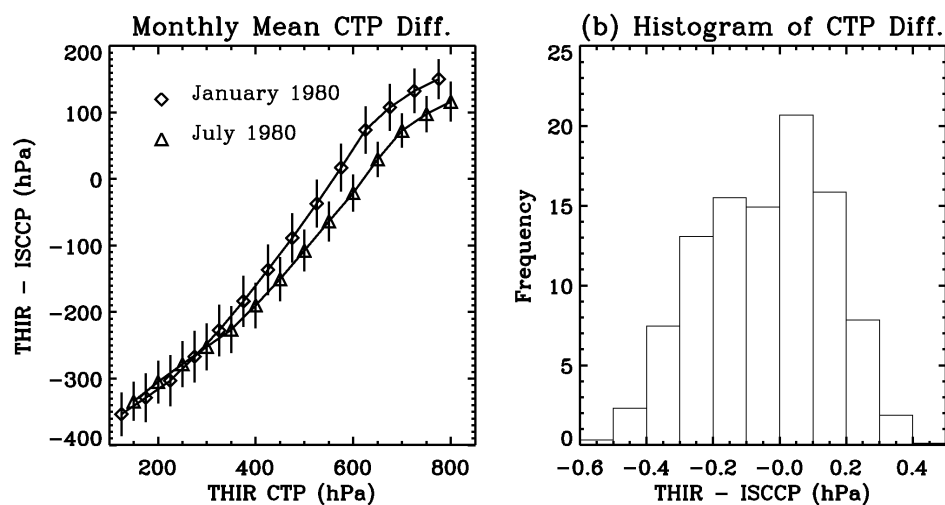


**Figure 4.1** (a) Monthly average pressure difference between THIR and ISCCP CTP as a function of THIR CTP in January and July 1980. The vertical bars are the  $\pm 1$  standard errors. The x-axis values are the same for January and July but the x-axis values for July are shifted by 25 hPa to avoid overlapping. (b) Histogram distribution of cloud-top pressure difference.

For high clouds, currently archived THIR data often report CTPs between 60 hPa and 80 hPa and sometimes lower. These pressures correspond to altitudes significantly higher than the typical tropical tropopause pressure of  $\sim 100$  hPa, indicating some errors in the derived cloud heights. The THIR data are currently being reprocessed at GSFC. In the new version THIR data, cloud-top temperatures are converted from THIR-measured radiances at  $11.5 \mu\text{m}$ , and CTPs are derived from the NCEP/NCAR  $2.5^\circ$ -longitude by  $2.5^\circ$ -latitude 6-hourly analyzed grids of temperature profiles. In this THIR cloud-height determination,

the main sources of potential error include THIR temperature measurement error and the NCEP conversion error, the combination of which yields an  $1\delta$  uncertainty in the derived CTP of about 25 hPa [Ziemke *et al.*, 2001]. In addition, the average of THIR 11.5  $\mu\text{m}$  radiances over the collocated TOMS fields of view could present a problem in cases of extremely variable cloud cover over the TOMS fields of view (e.g., broken clouds) [*personal communication, D. Larko, 2000*]. The new version THIR CTP data are seldom smaller than 100 hPa, and are about 80 hPa larger than the old version THIR data for those high clouds above 200 hPa, with smaller differences for clouds between 200-600 hPa. The new version THIR data are obviously better than the old THIR data. Unfortunately, the new THIR data are available for only a few months in 1981-1985. However, the difference between the new and old THIR data for high clouds is small compared to the large THIR-ISCCP CTP difference as shown in Figure 4.1. The THIR-ISCCP CTP difference will be still significant for both high clouds and low clouds if the difference between the two versions of THIR data has been accounted for.

#### 4.2 Ozone Retrieval Errors Induced by Incorrect Cloud Heights

In the radiance look-up table for the TOMS V7 algorithm, the radiance is computed only at 1013 hPa (1 atm) and 405 hPa (0.4 atm) pressure levels. When the assumed CTP is not at these two levels, the TOMS algorithm computes the calculated radiance by linearly interpolating/extrapolating the radiances at these levels, introducing an error in the retrieved ozone. Because it is assumed that TOMS instrument cannot detect ozone below optically thick clouds ( $R \geq 80\%$ ), the retrieval strategy is to include a climatological amount of tropospheric Ozone Below Clouds (OZBC) according to a simple monthly mean ISCCP cloud climatology [McPeters *et al.*, 1996]. On the one hand, incorrect CTPs will affect the added OZBC. On the other hand, the fact that the TOMS V7 algorithm will mistreat the ozone absorption and Rayleigh scattering between the actual and assumed cloud pressure levels affects the retrieved Ozone Above Clouds (OZAC). The above three errors associated with incorrect CTHs are called radiation interpolation error  $\Delta\Omega_{rad}$ , ORE below clouds  $\Delta\Omega_b$ , and ORE above clouds  $\Delta\Omega_a$ , respectively. The first error depends only on the assumed CTP, and the last two errors are related to both the assumed and actual CTPs.

If the actual and assumed CTPs are known, one can correct the TOMS-retrieved TOC  $\Omega_{uncorrected}$  by the following equation:

$$\Omega_{corrected} = \Omega_{uncorrected} - \Delta\Omega_{rad} - \Delta\Omega_b - \Delta\Omega_a, \quad (4.1)$$

where  $\Omega_{corrected}$  is the TOC after correcting cloud-height-induced errors. The correction terms ( $\Delta\Omega$ ) are defined in the sense that overestimates in TOC are positive. Then, we remove these errors by subtracting the overestimated ozone amount from the uncorrected column.

The TOMS V7 algorithm and TOMRAD are used to study the above three OREs induced by incorrect cloud heights. The clouds are assumed to be Lambertian cloud surface as the operational algorithm does because assuming clouds as scattered water or ice clouds does not affect the results but consumes much more computation time. Backscattered radiances are simulated using TOMRAD at certain input CTPs and then are used to inverse ozone using the TOMS V7 algorithm by assuming different CTPs. If the assumed CTP is the same as the input CTP, the difference between the input and retrieved TOC gives  $\Delta\Omega_{rad}$ . If the two sets of pressures differ, one can obtain the  $\Delta\Omega_a$  by comparing the difference between the input and retrieved OZAC after accounting for radiation interpolation errors. The ozone between the input and the assumed CTPs in the input ozone profile gives the  $\Delta\Omega_b$ . Radiances for partial clouds are simulated using the independent pixel approximation, i.e., Equation (2.7), to be consistent with those in ozone retrieval.

#### 4.2.1 Radiation Interpolation Error

Figure 4.2 (a) shows the  $\Delta\Omega_{rad}$  as a function of CTP, SZA ( $\theta_0$ ), and VZA ( $\theta$ ) for the TOMS standard low-latitude ozone profile L275 (i.e., with a TOC of 275 DU), cloud reflectivity of 90%, and latitude of  $0^\circ$ . The radiation interpolation error at 1013 hPa and 405 hPa is zero, because the look-up table used in the algorithm is computed at these two levels. Because the backscattered radiances are not linearly proportional to the CTPs, linear interpolation/extrapolation between these two levels causes some errors in the retrieved ozone. When the CTP is greater than 405 hPa,  $\Delta\Omega_{rad}$  is positive and peaks at 700 hPa with a

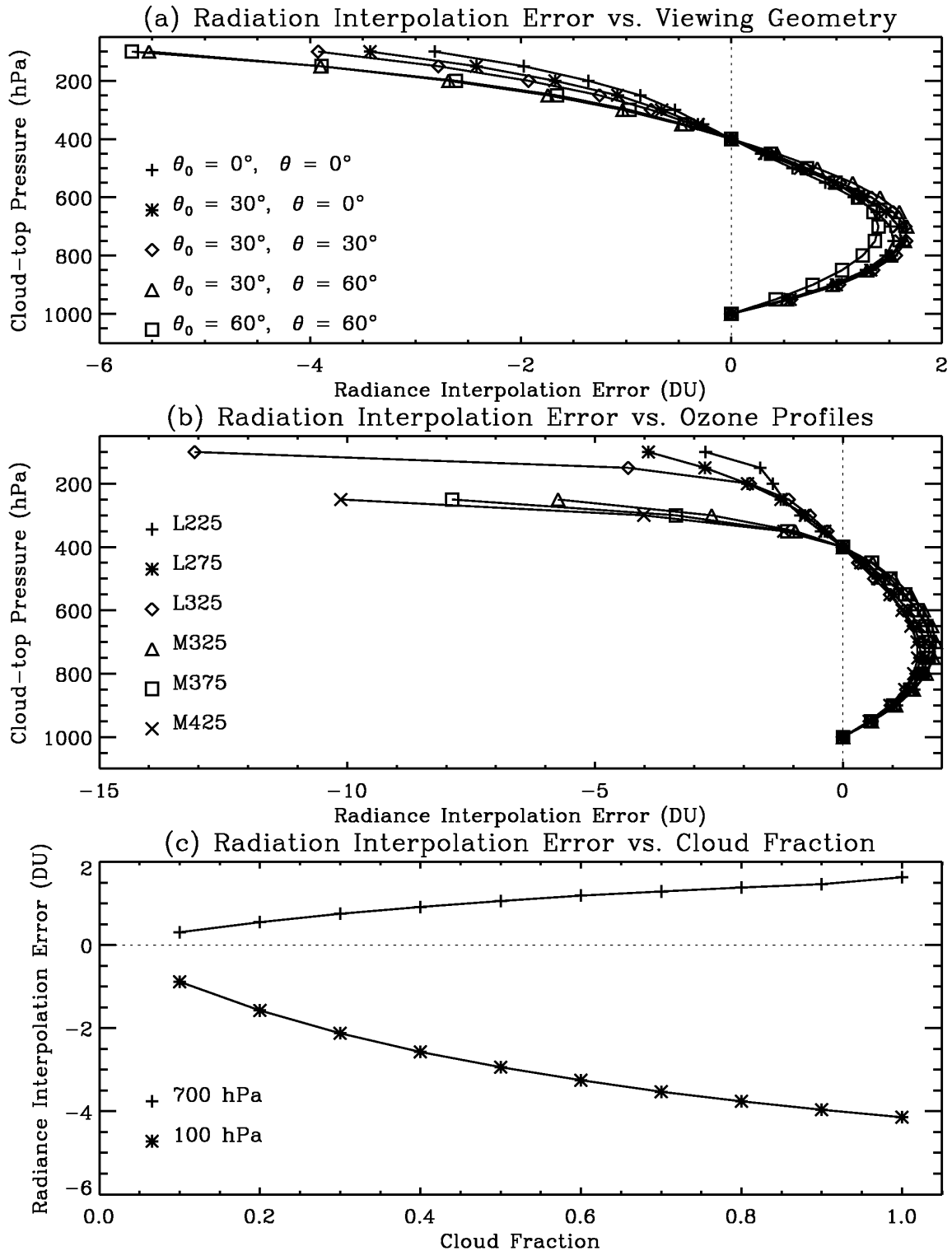


**Figure 4.2** Radiation interpolation error as a function of viewing geometry (a), ozone profiles (b), and cloud fraction (c). For (a) and (c), the L275 is used, the SZA and VZA are  $30^\circ$ , and the cloud reflectivity is 90%.

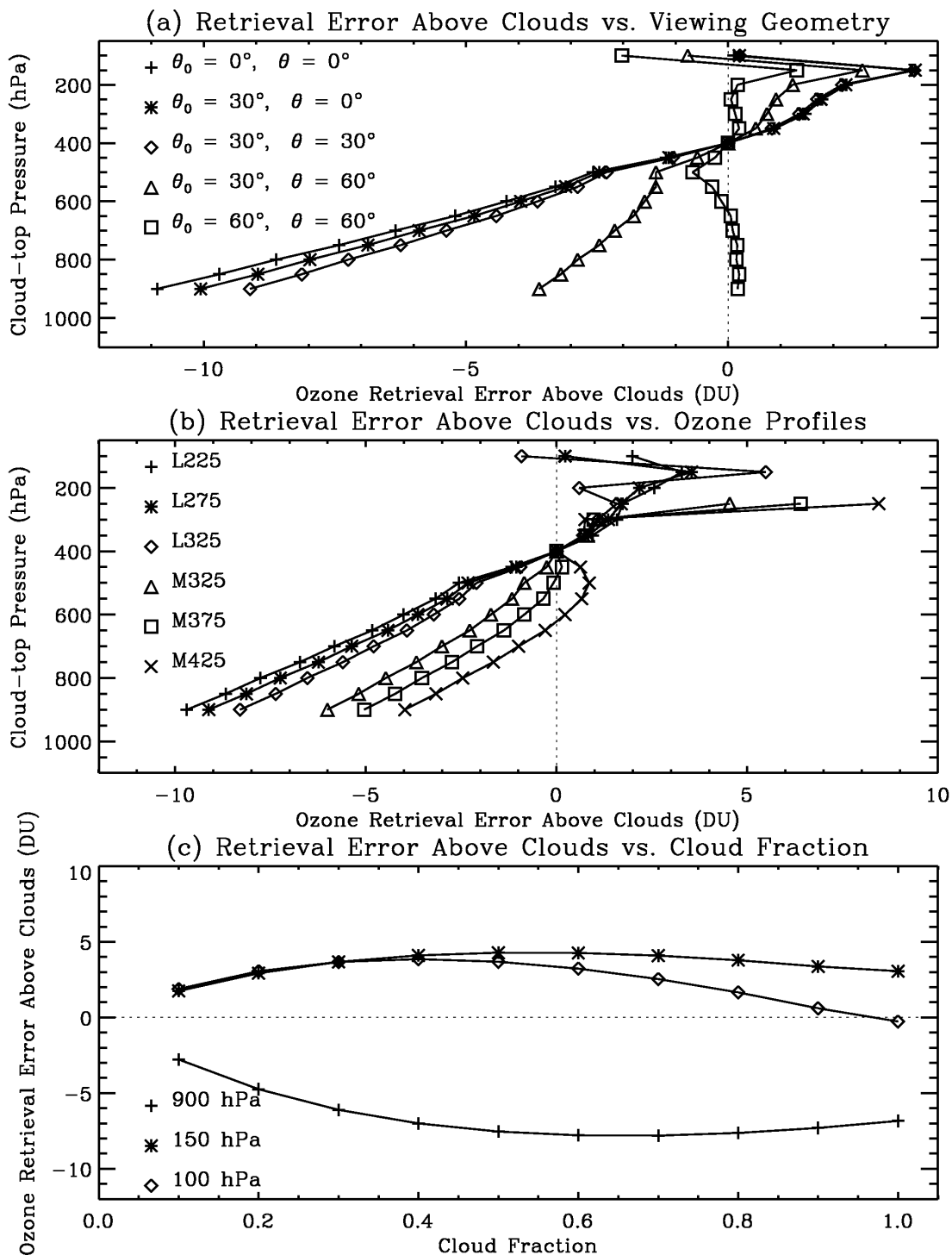
magnitude of about 1.7 DU. The viewing geometry has a small effect on  $\Delta\Omega_{rad}$  at pressures greater than 405 hPa. Because fewer photons penetrate the lower troposphere with increasing viewing geometry, the positive  $\Delta\Omega_{rad}$  at CTP less than 405 hPa decreases in magnitude. The viewing geometry has larger effects on  $\Delta\Omega_{rad}$  at altitudes above 405 hPa. For example, the  $\Delta\Omega_{rad}$  at 100 hPa is about  $-2.8$  DU at nadir and about  $-5.5$  DU at  $\theta_0 = 30^\circ$  and  $\theta = 60^\circ$ . This difference is due to the increasing interaction between Rayleigh scattering and ozone absorption with increasing viewing geometry. The  $\Delta\Omega_{rad}$  varies little with cloud reflectivity. From cloud reflectivity of 80% to 100%, positive errors decrease only 0.2 DU at 700 hPa, and negative errors decrease in magnitude by 0.8 DU at 100 hPa.

Figure 4.2 (b) shows the  $\Delta\Omega_{rad}$  at  $\theta_0 = 30^\circ$  and  $\theta = 30^\circ$  at a cloud reflectivity of 90% for different TOMS standard ozone profiles. The latitudes used in ozone retrieval are  $0^\circ$  and  $45^\circ$  for low- and mid-latitudes, respectively. Large differences in  $\Delta\Omega_{rad}$  among different ozone profiles occur at CTH above 405 hPa. The more ozone absorption immediately above clouds, the more  $\Delta\Omega_{rad}$  increases dramatically with increasing CTH. Although profiles L325 and M325 have the same TOC, the larger amount of ozone between 63-405 hPa in M325 leads to larger radiation interpolation errors. Figure 4.3 (c) shows the  $\Delta\Omega_{rad}$  at  $\theta_0 = 30^\circ$  and  $\theta = 30^\circ$  as a function of cloud fraction at pressure levels 700 hPa and 100 hPa, respectively. Other conditions are the same as in Figure 4.2 (a). The  $\Delta\Omega_{rad}$  varies monotonically with the cloud fraction although it is not linear.

Because the assumed CTP in the TOMS V7 algorithm is usually greater than 350 hPa, the  $\Delta\Omega_{rad}$  is usually within  $\pm 2$  DU in the TOMS V7 data. However, we should be careful when simulating ozone retrieval for high clouds at pressures less than 300 hPa using the TOMS V7 algorithm because of the larger  $\Delta\Omega_{rad}$  above such high-altitude clouds.

#### 4.2.2 Ozone Retrieval Error Above Clouds

Because the  $\Delta\Omega_a$  depends on both the retrieval-assumed and forward-calculated actual CTPs, we put the actual CTP at 405 hPa but assume the CTP at different pressure levels in the retrievals. Figure 4.3 (a) shows the  $\Delta\Omega_a$  as a function of assumed CTP. The  $\Delta\Omega_a$  is usually negative below 405 hPa and usually positive above 405 hPa in the upper troposphere. The  $\Delta\Omega_a$  peaks at 127 hPa (not shown), indicating that



**Figure 4.3** Error in retrieved OZAC as a function of viewing geometry (a), ozone profiles (b), and cloud fraction (c). For (a) and (c), the L275 is used, the SZA and VZA are  $30^\circ$ , and the cloud reflectivity is 90%.

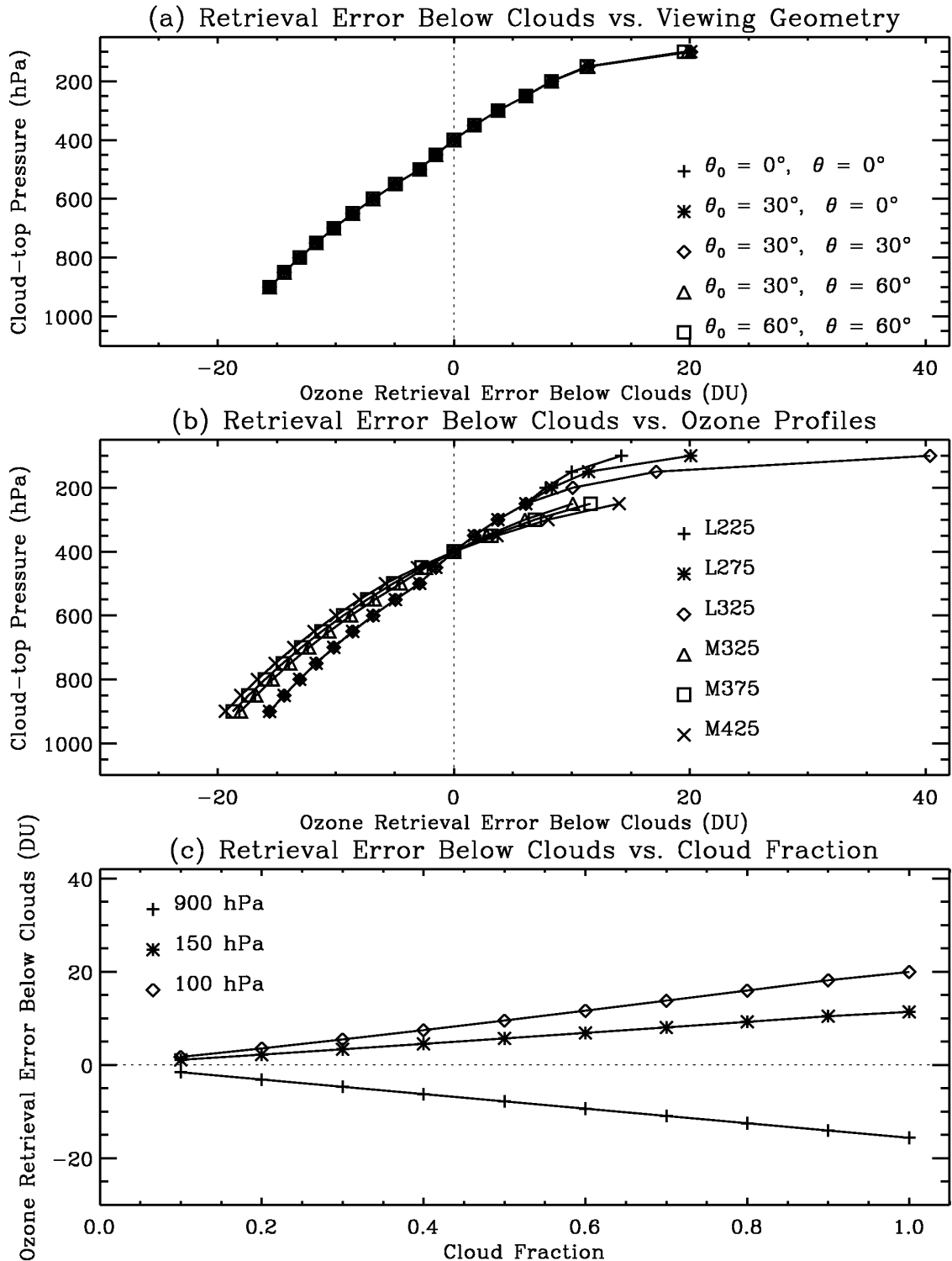
the retrieved ozone is largest at 127 hPa for this set of measured radiances. At CTP greater than 127 hPa, the  $\Delta\Omega_a$  is almost linearly proportional to the CTP for smaller viewing geometry. Atmospheric multiple scattering above the cloud increases for lower-altitude clouds, thus increasing the air mass factor [Koelemeijer and Stammes, 1999]. An underestimation of the CTH usually leads to an underestimation of  $\Delta\Omega_a$  because a larger air mass factor is implied, and vice versa. Note that transitions occur at each Umkehr levels (i.e., 500 hPa, 250 hPa, 127 hPa), suggesting the  $\Delta\Omega_a$  is also related to ozone profile shapes. A mixing of L225, L275, and L325 profiles is used in the retrieval except at 405 hPa. The transition at 127 hPa is probably related to the changes in ozone profile shapes. Because of the increasing scattering and absorbing process in the stratosphere with increasing viewing geometry, the  $\Delta\Omega_a$  diminishes with the increase of viewing geometry. The  $\Delta\Omega_a$  at  $\theta_0 = 60^\circ$  and  $\theta = 60^\circ$  does not vary much with CTP. The  $\Delta\Omega_a$  also varies with cloud reflectivity in magnitude because the multiple scattering error is largest for highest reflectivities, but it maintains a similar shape as a function of cloud heights. From cloud reflectivity of 80% to 100%, positive errors increase by  $\sim 1$  DU at 150 hPa and negative errors increase in magnitude by  $\sim 4$  DU at 900 hPa. Although the results in Figure 4.3 (a) are calculated for clouds at 405 hPa in the forward model, those results can be used to determine  $\Delta\Omega_a$  for any pair of actual and assumed CTPs to within  $\pm 0.4$  DU (within  $\pm 0.1$  DU if neither of the two levels is less than 300 hPa) by taking the difference of the abscissa value retrievals (i.e., the value at the assumed CTP minus the value at the actual CTP) between any two pressure levels.

Figure 4.3 (b) shows the  $\Delta\Omega_a$  at  $\theta_0 = 30^\circ$  and  $\theta = 30^\circ$  at a cloud reflectivity of 90% for different TOMS standard ozone profiles. The latitudes used in ozone retrieval are  $0^\circ$  and  $45^\circ$  for low- and mid-latitudes, respectively. For both low- and mid-latitude profiles, the higher the TOC is, usually the less the  $\Delta\Omega_a$  will be in the lower troposphere and the more the  $\Delta\Omega_a$  will be in the upper troposphere. Because mid-latitude ozone profiles have low-altitude ozone peaks compared to low-latitude profiles, the  $\Delta\Omega_a$  for mid-latitude profiles is less in the lower troposphere and higher in the upper troposphere. Figure 4.3 (c) shows the  $\Delta\Omega_a$  at  $\theta_0 = 30^\circ$  and  $\theta = 30^\circ$  as a function of cloud fraction at pressure levels 900 hPa, 150 hPa, and 100 hPa, respectively. Other conditions are the same as in Figure 4.3 (a). Unlike the  $\Delta\Omega_{rad}$ , the  $\Delta\Omega_a$  is not monotonic with the cloud fraction, and it peaks in magnitude at intermediate cloud fraction.

Theoretically, the  $\Delta\Omega_a$  could be as large as -11 DU (the sum of  $-9 - 2$  for  $\theta_0 = 0^\circ$  and  $\theta = 0^\circ$ ) if the actual CTP is 200 hPa but is assumed at 800 hPa. However, for tropical high-reflectivity clouds, the assumed CTP is usually  $\sim 400$  hPa, and the actual CTP is less than 400 hPa. The  $\Delta\Omega_a$  under such conditions is within 4 DU. The  $\Delta\Omega_a$  is much larger for mid-latitude high clouds.

### 4.2.3 Ozone Retrieval Error Below Clouds

Figure 4.4 shows the  $\Delta\Omega_b$  for the same conditions as Figure 4.3. The ORE below clouds is straightforward. This error is simply the amount of climatological ozone between the assumed and actual CTHs, and it does not vary with viewing geometry as shown in Figure 4.4 (a). The  $\Delta\Omega_b$  depends on the cloud-height errors, and the actual vertical ozone profile, and the ECF. When the assumed cloud height is lower than the actual height, the total ozone will be underestimated because the algorithm fails to include the tropospheric ozone between the assumed and actual cloud altitudes. Larger differences between assumed and actual CTPs result in larger errors. The  $\Delta\Omega_b$  also depends on the actual ozone profile. A larger amount of ozone between assumed and actual CTPs results in larger errors. Because TOMS observations provide no direct information about the vertical profile, the OZBC is obtained from the TOMS standard ozone profiles derived from ozonesonde climatologies. The deviation of the TOMS standard profiles from the actual profile will lead to an error in the added OZBC. This error due to inappropriate climatological ozone profiles will be discussed in Chapter 6. In this chapter, we define  $\Delta\Omega_b$  based on the TOMS standard ozone profiles. The  $\Delta\Omega_b$  is linearly proportional to the cloud fraction. Therefore, an error of 100 hPa in CTP at 40% reflectivity (ECF of 0.44) has less effect on ozone retrieval than a similar error at 80% reflectivity (ECF of 1 for reflectivities  $\geq 0.8$ ). The  $\Delta\Omega_b$  can be a significant fraction of the tropospheric column. For example, using the ozone profile L275, the ozone amount is about 8 DU between 200-400 hPa, about 16 DU between 100-400 hPa, and about 10 DU between 400-700 hPa. Comparing Figure 4.2 and Figure 4.3, one can see that the  $\Delta\Omega_b$  is much larger than the  $\Delta\Omega_a$  especially for high clouds, therefore dominating the OREs induced by incorrect cloud heights.



**Figure 4.4** Error in added OZBC as a function of viewing geometry (a), ozone profiles (b), and cloud fraction (c). For (a) and (c), the L275 is used, the SZA and VZA are  $30^\circ$ , and the cloud reflectivity is 90%.

These three errors can reinforce or cancel each other when combined. Take the L275 for example. An actual cloud height of 500 hPa, which is assumed to be at 200 hPa, results in a  $\Delta\Omega_{rad}$  of about -2 DU, a  $\Delta\Omega_a$  of about +4 DU, and a  $\Delta\Omega_b$  of about +11 DU, resulting in a corrected column +13 DU higher than the uncorrected column. An actual cloud at 200 hPa, assumed to be at 500 hPa, incurs a  $\Delta\Omega_{rad}$  of +1 DU, a  $\Delta\Omega_a$  of -4 DU, and a  $\Delta\Omega_b$  of -11 DU, resulting in a total error of -14 DU. For tropical high-reflectivity clouds, because the assumed CTP is about 400 hPa and is larger than the actual CTP, the  $\Delta\Omega_{rad}$  and  $\Delta\Omega_a$  are small and the total ozone error is dominated by the  $\Delta\Omega_b$ , resulting in an underestimation of the actual ozone columns for these scenes. For high-altitude tropical clouds the total error can be quite significant.

#### 4.2.4 Correction of Cloud-Height-Related Ozone Retrieval Errors

We designate the correction of the above three cloud-height-induced errors as the  $\Delta P$  correction. For  $\Delta\Omega_a$  and  $\Delta\Omega_{rad}$ , we use TOMRAD and TOMSV7 to build look-up tables of these errors as a function of CTP, total ozone, cloud reflectivity, SZA, and VZA. We then linearly interpolate these parameters (using the cosine of the SZA and the cosine of the VZA) to obtain these errors for all conditions. For  $\Delta\Omega_b$ , we compute the ozone amounts between any given two pressure levels using the two profiles that bracket the given total ozone, respectively, and then linearly interpolate to get the ozone amount between these levels for the given total ozone. The  $\Delta\Omega_b$  is simply this ozone amount multiplied by the ECF. The TOMS V7 algorithm interpolates/extrapolates the climatological ozone below the clouds from the first two Umkehr-layer amounts of ozone (1013-506 hPa, 506-253 hPa). Because the ISCCP CTPs are usually greater than 250 hPa, this extrapolation does not incur errors. However, when using the TOMS V7 algorithm to simulate ozone retrieval for high clouds above 250 hPa, one should take additional care to avoid this interpolation error by using the first 4 Umkehr-layer amounts of ozone. The following paragraph shows an example of applying  $\Delta P$  correction.

Figure 4.5 (a) shows a scatter-plot of the TOMS TOC vs. TOMS-measured 380-nm reflectivity in a region with a range of scenes from high convective clouds to clear areas. Ozone columns over the high clouds are about 5 DU larger than columns over the adjacent clear areas. The CTP difference between the

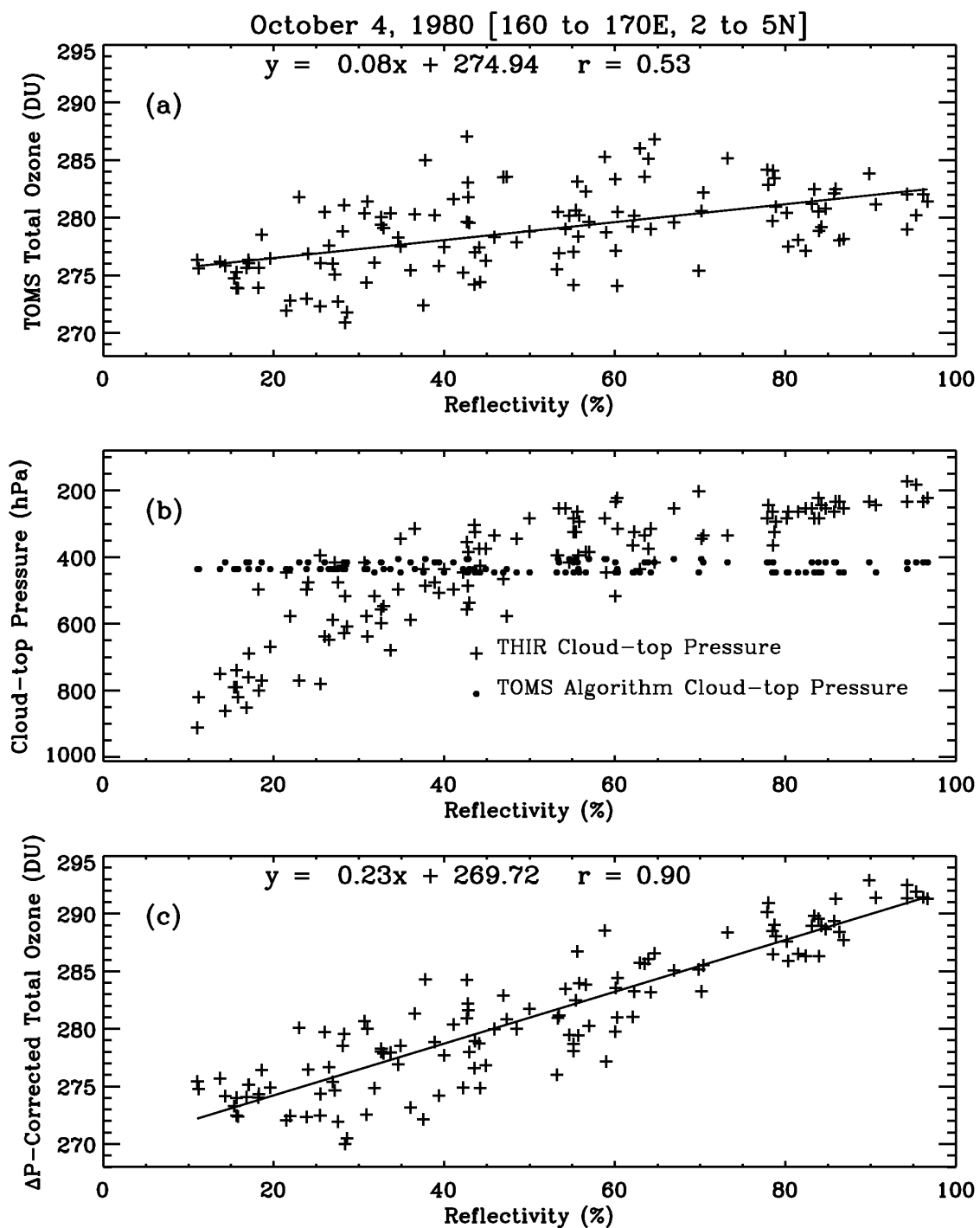


**Figure 4.5** An example of total ozone distribution over the western Pacific Ocean (160°E-170°E, 2°N-5°N) on October 4, 1980. (a) TOMS retrieved total ozone vs. TOMS-measured 380-nm reflectivity. (b) TOMS-assumed and THIR-measured CTP vs. reflectivity. (c) Total ozone after the  $\Delta P$  correction vs. reflectivity.

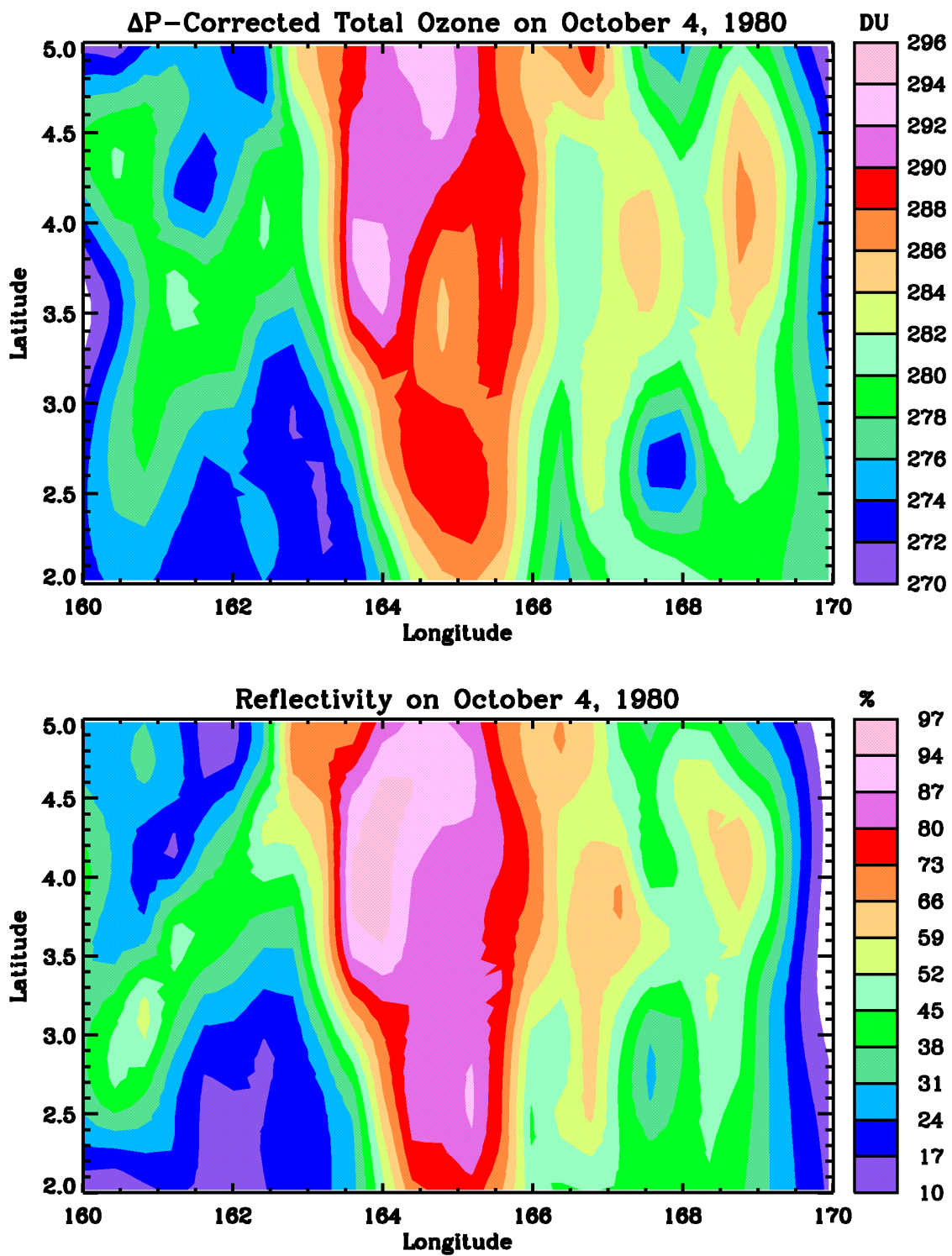


Figure 4.6 Spatial distribution of TOC after the  $\Delta P$  correction (a) and reflectivity (b) for the case in Figure 4.5.

TOMS-assumed and the THIR-measured, seen in Figure 4.5 (b), shows the TOMS assumed CTP is about 420 hPa, but the THIR pressure varies directly with the reflectivity. Compared to the THIR-measured pressure, the TOMS-assumed pressure is usually overestimated at reflectivity greater than 40% and underestimated at reflectivity less than 40%. The result of applying the  $\Delta P$  correction to this example case appears in Figure 4.5 (c). The  $\Delta P$  correction typically increases the magnitude of the slope by 15 DU/100% and results in a POA with a strong correlation. The TOC difference between the cloudy locations (reflectivity  $\geq 80\%$ ) and adjacent clear locations (reflectivity  $\leq 20\%$ ) is  $\sim 15$  DU. The spatial correlation for this case is clearly shown in the high spatial coherence between the TOC and reflectivity seen in Figure 4.6. The correction is most remarkable for high reflectivity pixels (greater than 80%), increasing the TOC by about 9 DU. Although the CTP difference between the THIR and assumed pressure is also very large for low reflectivity clouds, the correction is very small. The corrected slope drops by only 2 DU/100% when excluding the partially cloudy pixels. Due to the smaller ECF at lower reflectivity, the  $\Delta P$  correction diminishes with lower reflectivity cases. Of the 15 DU/100% slope increase, 12 DU/100% is contributed by  $\Delta\Omega_b$ . The  $\Delta\Omega_a$  and  $\Delta\Omega_{rad}$  together account for the other 3 DU/100% increase. The change in ozone due to  $\Delta P$  correction is consistent with the results shown in Section 4.2.

### 4.3 Summary

Compared with collocated THIR CTP data, the assumed ISCCP monthly mean CTPs for TOMS cloudy pixels show large errors. On average, the assumed CTH is overestimated by about 200-300 hPa for high-altitude clouds (THIR CTP  $\leq 200$  hPa) and underestimated by about 100-150 hPa for low-altitude clouds (THIR CTP  $\geq 750$  hPa). We find three OREs related to cloud height, radiation interpolation errors arising from the fact that radiances in the look-up table are computed only at 1013 hPa and 405 hPa pressure levels, errors in OZAC because of the mistreatment of ozone absorption and scattering above clouds, and errors in the added OZBC because of the inclusion of OZBC to complete the total ozone.

The radiation interpolation error  $\Delta\Omega_{rad}$  is related to the assumed CTP. It is positive above 405 hPa and peaks at 700 hPa with a value of  $\sim 1.7$  DU, and it is negative below 405 hPa and increases in magnitude with decreasing CTP. The increase of VZA or SZA increases the negative  $\Delta\Omega_{rad}$  in magnitude and slightly

decreases the positive  $\Delta\Omega_{rad}$ . The positive  $\Delta\Omega_{rad}$  does not vary much with different ozone profiles, but the negative  $\Delta\Omega_{rad}$  increases dramatically with the increase of ozone above the clouds. The  $\Delta\Omega_{rad}$  is proportional to cloud fraction but is not linear. Errors in the retrieved OZBC  $\Delta\Omega_a$  depend on the difference of the assumed and actual CTPs. For an actual cloud, the retrieved OZAC usually increases with increasing assumed CTH because of the decreasing air mass factor with increasing CTH, but it decreases below 127 hPa probably because of the change in ozone profile shapes. The  $\Delta\Omega_a$  diminishes with increasing viewing geometry. The increase amount of ozone usually decreases the  $\Delta\Omega_a$  in the lower and middle troposphere but increases the  $\Delta\Omega_a$  in the upper troposphere. The  $\Delta\Omega_a$  has a non-linear relationship with the cloud fraction. Errors in the added OZBC  $\Delta\Omega_b$  are just the climatological ozone between the assumed and actual CTPs, and depend on the assumed and actual CTPs, the actual ozone profile, and the cloud fraction. The three errors can reinforce or cancel each other when combined. But in the archived TOMS data, the  $\Delta\Omega_{rad}$  and  $\Delta\Omega_a$  are usually small, and errors in total ozone is dominated by  $\Delta\Omega_b$ . We devise a look-up table approach to correct OREs induced by incorrect CTHs.

## CHAPTER 5

### THE ASSUMPTION OF OPAQUE LAMBERTIAN CLOUD SURFACES ON OZONE RETRIEVAL

To investigate ORE due to the assumption of an opaque Lambertian cloud surface on TOMS ozone retrieval, one needs a model that treats clouds as scatters and considers in-cloud multiple scattering in simulating measured radiances, and then uses the TOMS V7 algorithm for ozone retrieval from the forward-simulated radiances. The Polarized Plane-parallel Gauss-Seidel RADiative transfer model (PPGSRAD) developed by *Herman et al.* [1995] calculates forward radiances at TOMS wavelengths. Section 5.1 below introduces PPGSRAD and describes the setup of input parameters in both PPGSRAD and TOMRAD. Section 5.2 identifies four types of OREs caused by the assumption of an opaque Lambertian cloudy surface, describes the methodology to obtain these four errors, and shows results individually of the four errors for forward full clouds, along with the overall OREs. Section 5.3 shows OREs for forward partial clouds. Section 5.4 discusses the possibility of correcting these OREs.

#### 5.1 Radiative Transfer Models and Model Setup

The method described above uses different models between simulation and retrieval. Because TOMRAD calculates look-up table radiance for the TOMS V7 algorithm, it is necessary to reduce the model bias between PPGSRAD and TOMRAD by forcing all the input parameters to these models except for clouds to be as much the same as possible. These input parameters include ozone absorption coefficients, Rayleigh scattering coefficients, molecular depolarization factors, ozone profiles, and temperature profiles. To simulate clouds in PPGSRAD, one needs to specify optical properties for clouds

including single scattering albedo, asymmetry factor, and phase matrix. Clouds are treated as either water clouds or ice clouds. The Bohren-Huffman Mie code embedded in PPGSRAD calculates optical properties for water clouds. Ray Tracing code developed by *Macke et al.* [1996a] calculates optical properties for ice clouds.

Chapter 2 describes in detail the TOMRAD and the TOMS V7 algorithm. This section first introduces the PPGSRAD and Ray Tracing Code and specifies how to set up input parameters consistently in both TOMRAD and PPGSRAD; then describes cloud treatment and calculated cloud optical properties for use in PPGSRAD; and finally compares the radiances calculated by TOMRAD and PPGSRAD under clear-sky conditions, when they are comparable.

### **5.1.1 Polarized Plane-Parallel Gauss-Seidel Radiative Transfer Model**

*Herman and Browning* [1965] originally published the PPGSRAD. Since then, *Herman and Browning* [1975], *Herman et al.* [1980], and *Herman et al.* [1994] have incorporated many modifications into the original model. The PPGSRAD employs the Gauss-Seidel iterative technique over optical depth of the radiative transfer equation's formally integrated form to calculate the steady-state vector intensity including all significant orders of scattering [*Herman and Browning*, 1965]. In this Gauss-Seidel scheme, the iterative procedure begins with the assumption that the intensity distribution is zero. The incident intensity field's zero and single order of scattering gives the first guess to the intensity distribution at the bottom of the first layer (starting from the TOA). This intensity distribution is then used to approximate the intensity integration over the optical thickness of the first layer to obtain the emergent intensities from the second layer. This process is continued through the entire atmosphere, layer by layer, thus giving initial guesses to the entire intensity field. The above process is repeated through the entire atmosphere, each time using the most recently calculated intensities in the numerical evaluation. The process continues until successive values of the same variable agree to within some predetermined tolerance. The method's major drawback has been the time required to solve for the emergent intensities for optically thick atmospheres, time increasing directly with optical depth [*Herman et al.*, 1980; *Herman and Browning*, 1965]. *Herman et al.* [1980] developed a semi-analytic method of fitting polynomials to the intensity field as a function of optical depth and incorporated it into the Gauss-Seidel iterative technique. This semi-analytic technique

enables the integration over optical depth to be performed analytically, thus permitting accurate and rapid solutions for optically thick atmospheres; to a larger extent, this technique reduces the time restriction in the Gauss-Seidel method.

When ground surface reflection is considered, the solution of the radiative transfer is as follows. First the solution is calculated for incident sunlight and zero surface reflectivity; then another solution is found for an isotropic intensity at the surface. The two solutions can be combined for any value of surface reflectivity according to the following equation:

$$I_m(\lambda, \theta, \theta_0, \phi, \tau, R_g) = I_\alpha(\lambda, \theta, \theta_0, \phi, \tau) + \frac{R_g T(\lambda, \theta, \theta_0, \tau, P_g)}{(1 - R_g S_b(\lambda, \tau, P_g))}, \quad (5.1)$$

where the  $I_\alpha$  is the radiance for zero ground surface albedo;  $I_m$  is the total radiance;  $R_g$  is the ground surface reflectivity; and  $P_g$  is the ground surface pressure. The formulation for the contribution of surface in PPGSRAD is essentially the same as that in TOMRAD as shown in Equations (2.1) and (2.2).

Both PPGSRAD and TOMRAD consider polarization and employ iterative techniques to solve the radiative transfer equation. But PPGSRAD uses a Gauss-Seidel iterative technique of the formally integrated radiative transfer equation, and TOMRAD employs a successive iteration of the auxiliary equation derived from the source matrix's definition. Although the formulation for surface contribution is similar in PPGSRAD and TOMRAD, the PPGSRAD applies it only to the ground surface, and TOMRAD treats clouds and aerosols as Lambertian surfaces and neglects the internal reflection and absorption in clouds or layers of aerosols. Because the multiple scattering due to clouds and aerosols is not explicitly considered in a cloudy atmosphere, TOMRAD computes radiances much more quickly than PPGSRAD does. In addition, TOMRAD can compute radiances at several SZAs simultaneously, and PPGSRAD calculates radiances at a SZA at a time; therefore, computing radiances is faster in TOMRAD than in PPGSRAD even for a clear atmosphere.

### 5.1.2 Ray Tracing Code

The Ray Tracing Code developed by *Macke et al.* [1996a] is used to calculate optical properties for ice crystals. This model describes the scattering and polarization properties of randomly oriented,

nonspherical ice crystals based on geometric optics approximation, because particle sizes of most atmospheric ice crystals are much larger than the wavelengths of solar radiation [Heymsfield and Platt, 1984]. The multiple reflection-refraction processes of incoming rays are repeated until the remaining energy of the internal Stokes vectors is below  $10^{-6}$  times the incident energy. This ray tracing is repeated for a large number of particle orientations and incoming light rays. Diffraction of the light incident on the particles' geometrical cross section is treated by explicitly solving the diffraction integral in the far-field approximation. The ray-tracing and diffraction results are added by weighting their corresponding cross sections. The extinction coefficient is assumed as two, according to the geometric optics approximation [Bohren and Huffman, 1998]. The ray tracing code can be applied to solve for optical properties of particle shapes ranging from various hexagonal symmetric particles to highly complex-shaped deterministic and random fractals.

### 5.1.3 Ozone Absorption Coefficients, Rayleigh Scattering Coefficients, Molecular Depolarization Factors, and Polarization

The ozone absorption coefficients [Bass and Paur, 1984; Paur and Bass, 1984], Rayleigh scattering coefficients [Bates, 1984], and molecular depolarization factors [Bates, 1984] used in the TOMS V7 algorithm are used in PPGSRAD. Look-up table radiances in the TOMS V7 algorithm are the sum of radiances at 45 0.05-nm intervals across each of the 1.1 nm TOMS bandwidths weighted by solar flux and a triangular slit function. However, it is impractical to do such calculation in PPGSRAD because of the computation burden. Instead, effective ozone absorption coefficients, Rayleigh scattering coefficients, and molecular depolarization are derived by weighting the corresponding spectral coefficients across each 1.1 nm bandwidth of EP and N7 TOMS by the product of solar flux and a triangular slit function (similar to Equation (2.4) by replacing  $A_\lambda$  with corresponding coefficients). Table 5.1 shows the derived effective ozone absorption coefficients, Rayleigh scattering coefficients, and molecular depolarization factors. Note that these calculated coefficients are not exactly identical to the effective coefficients given in the TOMS V7 user guides [McPeters *et al.*, 1996], but they are used consistently in both TOMRAD and PPGSRAD for this study. Although the neglect of polarization speeds up the radiance calculation by about nine times, we usually do not neglect polarization unless specified because the neglect of polarization can cause errors

in the calculated reflected radiance by up to 4% even for a cloud of COD 40. See Appendix A for the discussion of the effects of neglecting polarization on calculated radiances, retrieved ozone columns, and retrieved reflectivities for both clear and cloudy conditions.

**Table 5.1** Effective absorption and scattering coefficients, and molecular depolarization factor at N7 and EP TOMS wavelengths.

| Wavelength<br>(nm) | Effective<br>Absorption<br>Coefficient<br>( $\text{atm}\cdot\text{cm}^{-1}$ ) at<br>$0^\circ\text{C}$ $C_\theta$ | Temperature-<br>Dependent<br>Coefficients* |                      | Rayleigh<br>Scattering<br>Coefficient<br>( $\text{atm}^{-1}$ ) | Molecular<br>Depolarization<br>Factor |
|--------------------|--|--|----------------------|--|---------------------------------------|
|                    |  | $C_1 \times 10^{-3}$                       | $C_2 \times 10^{-5}$ |  |                                       |
| 308.65             | 3.2458   | 7.6171                                     | 3.6686               | 1.0772   | 0.0317                                |
| 312.34             | 1.9031   | 5.4964                                     | 2.9201               | 1.0231   | 0.0316                                |
| 317.35             | 0.9958   | 3.1354                                     | 1.7046               | 0.9556   | 0.0313                                |
| 322.37             | 0.5392   | 1.7557                                     | 1.0391               | 0.8938   | 0.0311                                |
| 331.06             | 0.1703   | 0.7102                                     | 0.4227               | 0.7978   | 0.0306                                |
| 339.66             | 0.0346   | 0.3876                                     | 0.2758               | 0.7153   | 0.0306                                |
| 359.88             | 0.0000   | 0.0000                                     | 0.0000               | 0.5604   | 0.0301                                |
| 379.55             | 0.0000   | 0.0000                                     | 0.0000               | 0.4462   | 0.0295                                |

\* Ozone absorption coefficient =  $C_\theta + C_1 T + C_2 T^2$  (where T is in degree  $^\circ\text{C}$ ).

#### 5.1.4 Ozone Profiles and Temperature Profiles

The TOMS standard climatological ozone and temperature profiles [McPeters *et al.*, 1996] are used in PPGSRAD. These profiles, specified at 11-Umkehr layers, are interpolated to generate much higher-resolution profiles for radiance calculation in TOMRAD. The generated 82-layer (1 km/layer) profiles from TOMRAD serve as input into PPGSRAD.

#### 5.1.5 Radiance Look-up Table in the TOMS V7 Algorithm

To be consistent with the setups in PPGSRAD, a new look-up table for the TOMS V7 algorithm is calculated with TOMRAD using the derived effective ozone absorption coefficients, Rayleigh scattering coefficients, and molecular depolarization factors for a plane-parallel atmosphere. The original look-up table contains radiances calculated only at 1.0 atm and 0.4 atm. Radiances at other levels are linearly interpolated in the pressure coordinate, leading to radiance interpolation errors as shown in Chapter 4 of

this dissertation. To avoid the radiation interpolation error, the look-up table radiance is calculated at ten pressure levels from 1 atm to 0.1 atm at 10 0.1-atm intervals. With the use of these ten pressure levels, radiance interpolation errors are within 0.1 DU under most conditions.

### 5.1.6 Cloudy Treatment and Cloud Optical Properties

Clouds are treated as homogeneous and plane-parallel layers. Dependent on cloud type, temperature, and cloud age, the phase of the cloud may be liquid, ice, or mixed phase. The cloud type of most concern in this study is the optically thick tropical convective cloud. For this type of cloud with large geometrical thickness, the upper part of the cloud might consist of ice crystals, and the lower part may consist of liquid water droplets. The ISCCP cloud retrieval algorithm considers clouds with CTP below 440 hPa as ice clouds [Rossow *et al.*, 1996]. For simplicity, clouds are treated as either spherical Water Clouds (WC) or nonspherical ice clouds.

The classic Mie theory well characterizes the optical properties of WC. However, the optical properties of ice clouds are largely dependent on their particle shapes and sizes. Many experimental studies indicate the shapes of atmospheric ice crystals range from relatively regular hexagonal cylinders to aggregates of those to highly complex polycrystals [Macke *et al.*, 1996b]. The most common shape of ice crystal used in theoretical analysis is the regular hexagonal crystal [Fu and Liou, 1993; Kinne *et al.*, 1989; Sun and Shine, 1995; Takano and Liou, 1989]. Regular hexagonal crystals, either single or aggregated, produce strong halo features in the phase function [Macke, 1993; Macke *et al.*, 1996a; Takano and Liou, 1989]. Ground-based, in-situ nephelometer and aircraft radiance measurements of cirrus clouds show that ice clouds' scattering phase functions are rather featureless, with no obvious halos [Foot, 1988; Francis, 1995; Posse and Hoyningen-Huene, 1995], indicating that real atmospheric ice crystals are typically composed of particles with very complicated and highly irregular shapes [Arnott *et al.*, 1994; Francis, 1995; Sassen *et al.*, 1994]. Macke *et al.* [1996b] modeled ice particles by considering both random fractals and hexagonal column/plates with imposed random facet tilts and found that the irregularity, and more important, the randomness of the ice particle shape are important to suppress the halo features of regular hexagonal crystals. To model scattering properties of irregular ice crystals, Macke *et al.* [1996b] proposed a randomized version of the second-generation triadic Koch fractal. This type of ice crystal, called a

polycrystal, was also adopted by *Mishchenko et al.* [1996] and *Mishchenko et al.* [1999]. The phase function of polycrystals is relatively featureless, showing no deep or wide side-scattering minimum, no strong rainbow typical of water droplets, and no pronounced halo features characteristics of regular hexagonal crystals [*Mishchenko et al.*, 1996]. This relatively smooth function is in qualitative agreement with laboratory and in situ measurements of real ice crystals [*Foot*, 1988; *Francis*, 1995; *Posse and Hoyningen-Huene*, 1995]. This phase function of polycrystals (second generation) essentially coincides with the phase function of a stochastically rough, nonspherical ice particle with a large standard deviation of surface radius and slope. The excellent agreement suggests that these two types indeed capture the scattering character of highly variable and irregular natural ice crystals [*Mishchenko et al.*, 1996]. In this study, we model ice crystals as regular HEXagonal column ice crystals (HEX) or POLYcrystals (POLY) that represent either idealized or more realistic types of ice crystals.

The refractive indexes are obtained from *Hale and Querry* [1973] for WC. *Han et al.* [1994] made a global survey of WC and found the average effective radius is  $\sim 10 \mu\text{m}$ . Water clouds are modeled with a gamma distribution with an effective radius of  $10 \mu\text{m}$  and an effective variance of 0.10, which has been used in ISCCP cloud retrieval [*Mishchenko et al.*, 1999; *Mishchenko et al.*, 1996; *Rossow and Schiffer*, 1991; *Rossow et al.*, 1996]. The optical properties are calculated using the Bohren-Huffman Mie Code. Table 5.2 shows the refractive indexes, asymmetry factor, and single scattering albedo at TOMS wavelengths.

**Table 5.2** Refractive indexes and optical properties for water clouds.

| Wavelength ( $\mu\text{m}$ ) | Refractive Index |           | Asymmetry Factor (g) | Single Scattering Albedo ( $\omega_0$ ) |
|------------------------------|------------------|-----------|----------------------|---|
|                              | Real             | Imaginary |                      |   |
| 0.3086                       | 1.3479           | 1.405E-8  | 0.8674               | 0.9999947                               |
| 0.3123                       | 1.3474           | 1.327E-8  | 0.8675               | 0.9999950                               |
| 0.3174                       | 1.3469           | 1.227E-8  | 0.8674               | 0.9999955                               |
| 0.3224                       | 1.3463           | 1.130E-8  | 0.8673               | 0.9999959                               |
| 0.3311                       | 1.3453           | 9.678E-9  | 0.8674               | 0.9999965                               |
| 0.3397                       | 1.3442           | 8.158E-9  | 0.8674               | 0.9999971                               |
| 0.3599                       | 1.3421           | 5.148E-9  | 0.8675               | 0.9999983                               |
| 0.3800                       | 1.3406           | 3.072E-9  | 0.8672               | 0.9999988                               |

The refractive indexes for clear ice are obtained from *Warren* [1984]. For both HEX and POLY, a  $-2$  power law size distribution is assumed with an effective radius of  $30 \mu\text{m}$  and effective variance of  $0.1 \mu\text{m}$  [*Doutriaux-Boucher et al.*, 2000; *Mishchenko et al.*, 1996; *Rossow et al.*, 1996]. Unlike spherical liquid WC, there are discrepancies in the definitions of effective radius for ice clouds due to the nonsphericity of ice crystals [*McFarquhar and Heymsfield*, 1997]. The following definitions of effective radius  $r_{eff}$  and effective variance  $v_{eff}$  [*Hansen and Travis*, 1974; *Mishchenko et al.*, 1996] are adopted:

$$r_{eff} = \frac{1}{G} \sum_{i=1}^k r_i \pi r_i^2 n(r_i) \quad (5.2)$$

and

$$v_{eff} = \frac{1}{G r_{eff}^2} \sum_{i=1}^k (r_i - r_{eff})^2 \pi r_i^2 n(r_i), \quad (5.3)$$

where  $r_i$  is the radius in terms of equivalent geometrical cross-sectional area;  $n(r_i)$  is the number of particles with  $r_i$  according to a  $-2$  power law size distribution in a unit volume; and  $G$  is the average geometric cross-sectional area,

$$G = \sum_{i=1}^k \pi r_i^2 n(r_i). \quad (5.4)$$

The optical properties are calculated at six discrete sizes (i.e.,  $k = 6$ ): 10, 18, 26, 34, 42, and  $50 \mu\text{m}$ , respectively, giving an effective radius of  $30 \mu\text{m}$  and effective variance of 0.1. For hexagon column crystals, the aspect ratio (length to diameter ratio) is assumed as 2, as used in *Mishchenko et al.* [1999] and *Mishchenko et al.* [1996]. In the Ray Tracing Code, the number of random particle orientation is 30,000 and the number of incoming rays for each orientation is 300, as recommended in *Macke et al.* [1996b]. The distortion parameter for POLY is 0.18, and the phase function of POLY will be insensitive to the further increase of distortion parameter [*personal communication*, *A. Macke*, 2001]. The average single scattering albedo  $\omega_0$ , the asymmetry factor  $g$ , and the phase matrix  $P_{mn}(\theta)$  ( $m, n = 1, 2, 3, 4$ ) over the size distribution are defined,

$$\langle x \rangle = \frac{\sum_{i=1}^k x(r_i) n(r_i) C_{sca}(r_i)}{\sum_{i=1}^k n(r_i) C_{sca}(r_i)}, \quad x = P_{mn}(\theta), g, \text{ or } \omega_0, \quad (5.5)$$

where  $C_{sca}(r_i)$  is the scattering cross section for a particular  $r_i$ . The average cross section is defined as

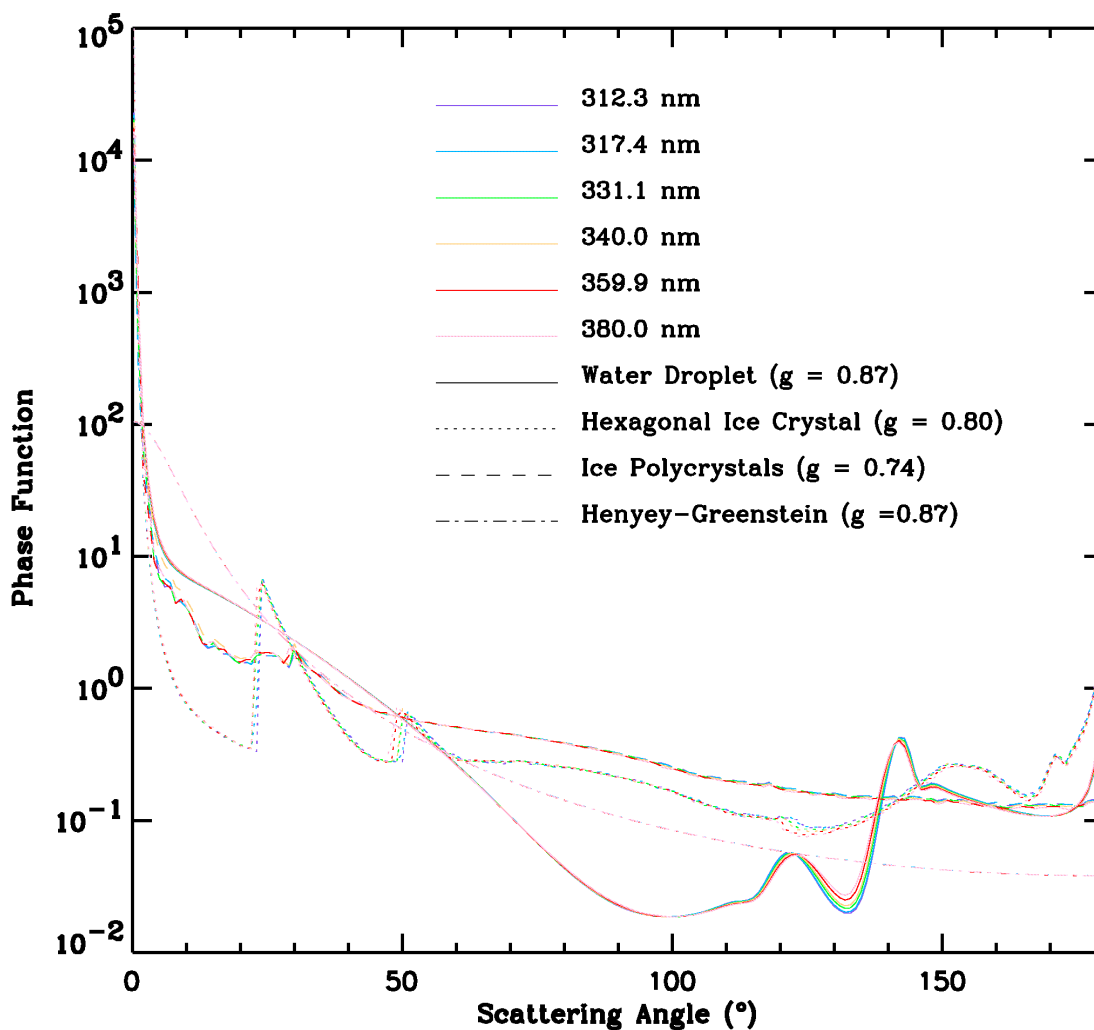
$$\langle x \rangle = \frac{\sum_{i=1}^k x(r_i) n(r_i)}{\sum_{i=1}^k n(r_i)}, \quad x = C_{sca}(r_i), C_{abs}(r_i), \text{ or } C_{ext}(r_i). \quad (5.6)$$

Table 5.3 shows the refractive indexes, single scattering albedos, and asymmetry factors for HEX and POLY at N7 TOMS wavelengths. The calculated asymmetry factors are comparable within 0.01 to those calculated by *Macke et al.* [1996b], *Mishchenko et al.* [1996], and *Doutriaux-Boucher et al.* [2000] at visible wavelengths 0.55  $\mu\text{m}$  or 0.63  $\mu\text{m}$ .

**Table 5.3** Refractive indexes and optical properties for HEX and POLY.

| Wavelength<br>( $\mu\text{m}$ ) | Refractive Index |           | Hexagonal Column Ice<br>Crystals (HEX) |        | Polycrystals (POLY) |        |
|---------------------------------|------------------|-----------|--|--------|---------------------|--------|
|                                 | Real             | Imaginary | $\omega_0$                             | $g$    | $\omega_0$          | $g$    |
| 0.3123                          | 1.3314           | 5.012E-9  | 0.9999927                              | 0.7972 | 0.9999962           | 0.7320 |
| 0.3174                          | 1.3304           | 4.825E-9  | 0.9999930                              | 0.7985 | 0.9999964           | 0.7305 |
| 0.3311                          | 1.3279           | 4.345E-9  | 0.9999940                              | 0.7995 | 0.9999969           | 0.7341 |
| 0.3397                          | 1.3265           | 4.069E-9  | 0.9999946                              | 0.8005 | 0.9999972           | 0.7383 |
| 0.3599                          | 1.3235           | 3.503E-9  | 0.9999955                              | 0.8021 | 0.9999978           | 0.7372 |
| 0.3800                          | 1.3212           | 3.053E-9  | 0.9999964                              | 0.8042 | 0.9999982           | 0.7360 |

The phase functions of WC, HEX, and POLY, calculated at N7 TOMS wavelengths are shown in Figure 5.1. The phase functions for WC show a primary strong rainbow at  $\sim 140^\circ$  and a secondary rainbow at  $\sim 120^\circ$ . The phase functions for HEX show pronounced halos at  $\sim 23.5^\circ$  and  $\sim 50^\circ$ . Note that the halo angles slightly decrease with increasing wavelength, and these decreases explain why halo angles at TOMS wavelengths are larger than those at visible wavelengths,  $22^\circ$  and  $46^\circ$ . The phase functions for POLY are



**Figure 5.1** Phase functions at N7 TOMS wavelengths (indicated by different colors) for cloud droplets: water cloud droplets with an effective radius of  $10 \mu\text{m}$  and an effective variance of 0.1 (solid), same water cloud droplet but with a Henyey-Greenstein phase function (dashed and dotted), HEX with an effective radius of  $30 \mu\text{m}$  and an effective variance of 0.1 (dotted), and POLY with an effective radius of  $30 \mu\text{m}$  and an effective variance of 0.1 (dashed).

rather smooth and featureless compared to those of WC and HEX. The three phase functions shown in Figure 5.1 exhibit large differences, exceeding an order of magnitude at some scattering angles. That is why the corresponding asymmetry factors are significantly different among them. The phase functions are only slightly wavelength dependent.

### 5.1.7 Radiance Comparisons

Although the input parameters are consistent in both TOMRAD and PPGSRAD as much as possible, there is bias between these two models. To quantify the bias between these two models, the calculated radiances are compared for using these two models for the following conditions: surface reflectivity  $R_s = 8\%$ ,  $80\%$ , L275, SZA  $\theta_0 = 0^\circ, 15^\circ, 30^\circ, 45^\circ, 60^\circ, 70^\circ$ , and  $75^\circ$ , VZA  $\theta = 0^\circ, 15^\circ, 30^\circ, 45^\circ, 60^\circ$ , and  $70^\circ$ , AZA  $\Phi = 0^\circ, 30^\circ, 60^\circ, 90^\circ, 120^\circ, 150^\circ$ , and  $180^\circ$ . Figure 5.2 (a) shows the relative difference between models in the calculated radiances as a function of SZA at  $\theta = 30^\circ$  and  $\Phi = 90^\circ$ . On average, the calculated radiance using PPGSRAD is smaller by  $0.21 \pm 0.06\%$  at  $312.3$  nm and larger by  $0.04 \pm 0.03\%$  at  $380.0$  nm for  $R_s = 8\%$ , and is smaller by  $0.16 \pm 0.08\%$  at  $312.3$  nm and larger by  $0.11 \pm 0.04\%$  at  $380.0$  nm for  $R_s = 80\%$ . Figure 5.2 (b) shows the retrieved ozone difference by inverting the two sets of radiances into the TOMS V7 algorithm at  $\theta = 30^\circ$  and  $\Phi = 90^\circ$ . On average, the retrieved ozone from PPGSRAD is larger by  $0.65 \pm 0.20$  DU for  $R_s = 8\%$  and  $0.35 \pm 0.20$  DU for  $R_s = 80\%$ , corresponding to the smaller radiance value at  $312.3$  nm. These differences in both radiances and retrieved ozone are relatively small and are one method of establishing the accuracy of calculating forward radiance using PPGSRAD. The calculated radiance using PPGARAD is accurate within  $\sim 0.21\%$  relative to the radiances calculated using TOMRAD, and the retrieved ozone from PPGSRAD-calculated radiances is accurate within  $\sim 0.65$  DU. Errors in both radiance and retrieved ozone are expected to be smaller for cloudy conditions as we can see that those errors decrease from  $R_s = 8\%$  to  $R_s = 80\%$ .

### 5.1.8 Viewing Geometry

For the following sections, radiances are calculated at SZA  $\theta_0 = 0^\circ, 15^\circ, 30^\circ, 45^\circ, 60^\circ, 70^\circ$ , and  $75^\circ$ ; VZA  $\theta$  from  $0^\circ$  to  $70^\circ$  every  $5^\circ$ ; and AZA  $\Phi = 0^\circ, 30^\circ, 60^\circ, 90^\circ, 120^\circ, 150^\circ$ , and  $180^\circ$ . The average

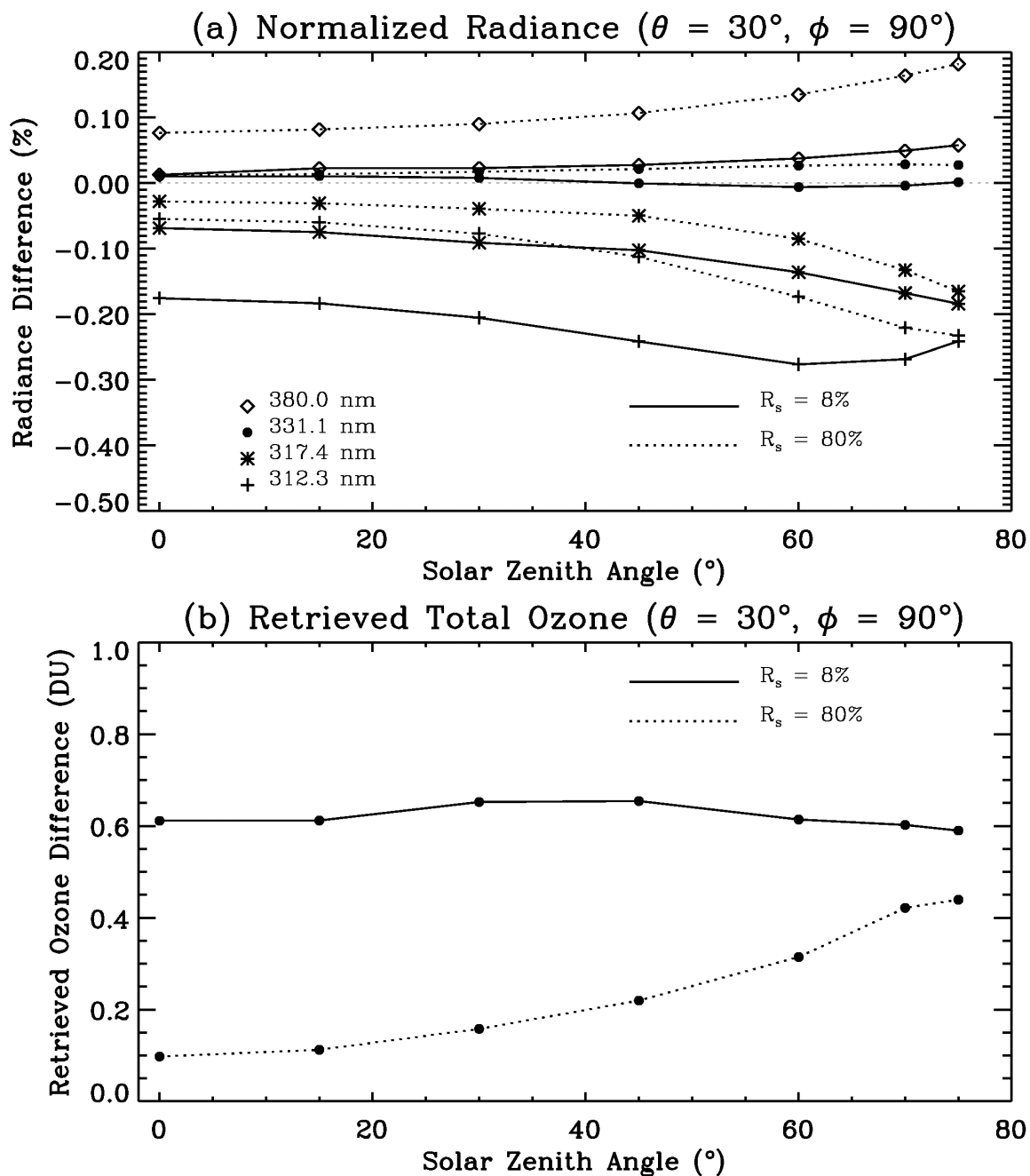


**Figure 5.2** (a) Differences in calculated radiances between using PPGSRAD and TOMRAD at several selected N7 TOMS wavelengths for a surface reflectivity of 8% and 80%. (b) Differences in the retrieved total ozone from corresponding calculated radiances using the TOMS V7 algorithm.

values and standard values seen in the following context are the statistics from all the above viewing geometry unless specified. However, results are shown in figures only at selected angles.

## 5.2 Ozone Retrieval Errors Associated with Clouds

In the TOMS V7 algorithm, optically thick clouds are treated as Lambertian cloudy surfaces. However, the cloud reflection is not Lambertian [Knibbe *et al.*, 2000; Kurosu *et al.*, 1997]. Figure 5.3 (left) shows the distribution of calculated 380-nm normalized backscattered radiances at TOA for  $\theta_0 = 0^\circ$ ,  $30^\circ$ ,  $60^\circ$ , and  $75^\circ$ , respectively. The SZA is identified by a red asterisk symbol on the abscissa. A WC of COD 40 is placed at 2-12 km. The radiance shows large dependence on viewing geometry due to the variation of optical path length with viewing geometry and the phase function of Mie scattering clouds. Figure 5.3 (right) shows the corresponding retrieved Lambert-equivalent cloud surface reflectivity at 380 nm. Corresponding to the radiance, the retrieved reflectivity varies significantly with viewing geometry, ranging from 57% to 231%. The larger the SZA is, the larger the variance. At  $\theta_0 = 0^\circ$ , reflectivity ranges from 60% to 90%. The largest variance in reflectivity occurs at  $\theta_0 = 75^\circ$  with reflectivity ranging from 57% to 231%. The large angular distribution in the retrieved reflectivity indicates that cloud reflection is not Lambertian. A further increase in COD does not make a cloud much more Lambertian. For example, the retrieved reflectivity for a cloud of COD 100 at 2-12 km ranges from 69% to 236%. Although ozone retrieval is less sensitive to the viewing geometry than the retrieved reflectivity is, the assumption of cloud reflection to be angular-independent could still be a matter for accurate ozone retrieval. The effect of assuming cloud reflection to be Lambertian on ozone retrieval is called the “Lambertian effect.”

It is also noted that a significant number of the scene reflectivities in Figure 5.3 (right) are less than 80%. According to the TOMS V7 PCM, these scenes are treated as partially cloudy even if the corresponding scenes in the forward calculation are overcast. Even for a cloud of COD 100, this misinterpretation of overcast as partially cloudy still exists. The scene misinterpretation due to using the PCM, called the “PCM effect,” might introduce errors in the ozone retrieval. The sum of Lambertian and PCM effects is called the “Lambertian-PCM effect.”

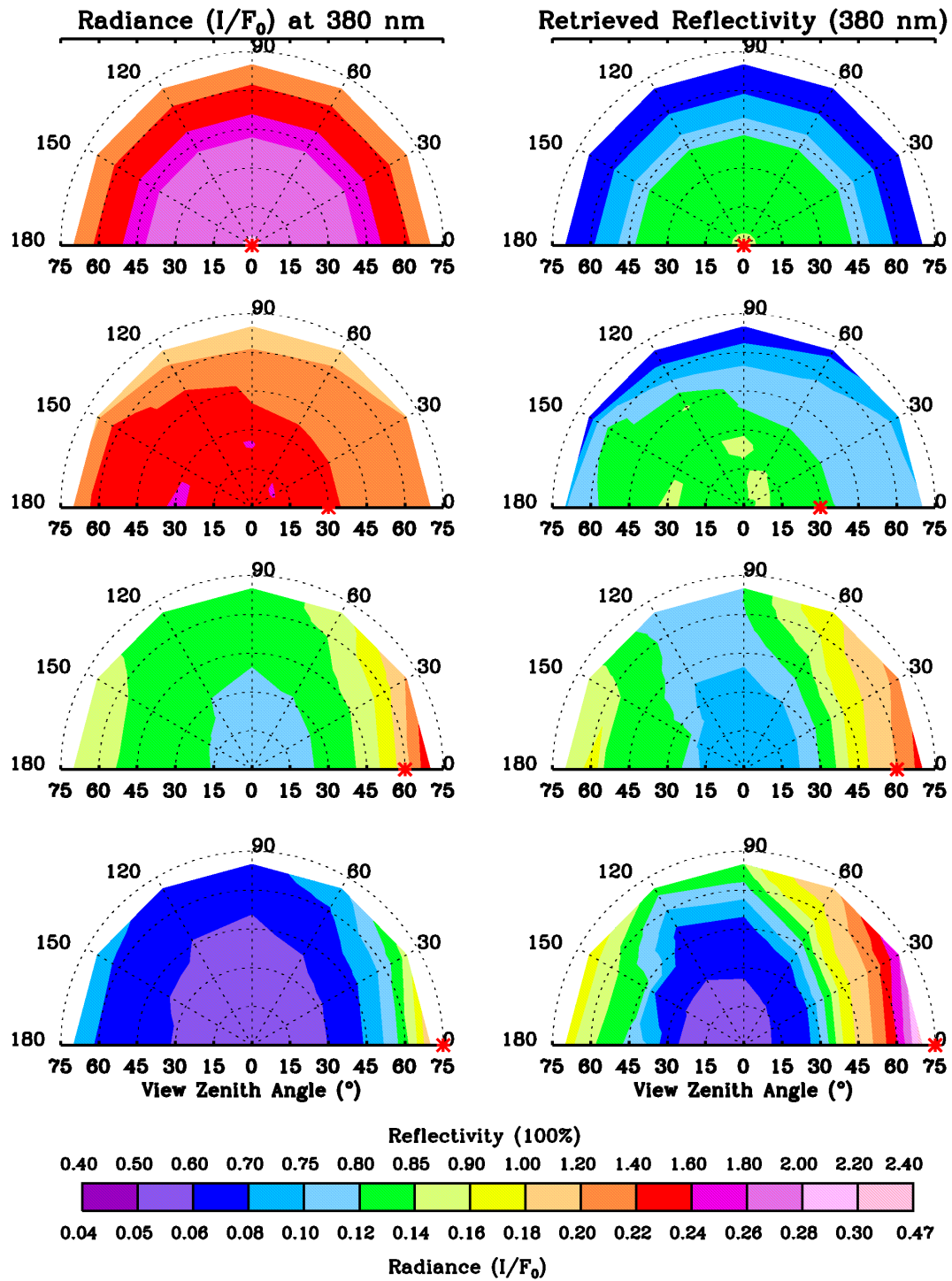


**Figure 5.3** Calculated radiances normalized by solar flux at 380-nm (left) and retrieved cloud surface reflectivities at 380 nm (right) for a WC of COD positioned at 2-12 km as a function of viewing geometry. The four rows correspond to SZAs  $0^{\circ}$ ,  $30^{\circ}$ ,  $60^{\circ}$ , and  $75^{\circ}$  (indicated by a red asterisk symbol on the x-axis), respectively. The AZA ranges from  $0^{\circ}$  to  $180^{\circ}$  anti-clockwise.

The TOMS V7 algorithm treats clouds with scene reflectivities greater than 80% as opaque surfaces; i.e., the clouds screen the tropospheric ozone column below them. The cloud part of those partially cloudy scenes is also treated as being opaque. However, backscattered photons penetrate the clouds, and the in-cloud multiple scattering enhances ozone absorption in the clouds [Erle *et al.*, 1995; Kurosu *et al.*, 1997; Mayer *et al.*, 1998]. This ozone absorption enhancement in clouds, which is not taken into account in the TOMS V7 algorithm, will affect ozone retrieval. The effect due to ozone absorption enhancement in clouds on ozone retrieval is called the “Inter-Cloud Ozone Absorption ENhancement (ICOAEN) effect.”

Backscattered photons can also penetrate below the cloud layer; therefore, a part of the ozone below the cloud layer (from the cloud bottom down to the ground) might be measured especially for optically thin clouds, introducing additional errors to the retrieved ozone. The effect due to ozone absorption below cloud bottoms on ozone retrieval is called the “Below-Cloud Ozone Absorption (BCOA) effect.” The sum of ICOAEN and BCOA effects is called the “Opaque effect.”

The above four effects usually coexist in the presence of clouds. However, to aid in clearer understanding of OREs associated with clouds in the TOMS V7 algorithm, the Lambertian, PCM, ICOAEN, and BCOA effects are investigated separately in this study. The combination of these effects gives the overall OREs associated with clouds. To simplify discussion, the Forward Cloud Fraction (FCF) is set as 1. Ozone retrieval errors associated with forward partial clouds are investigated in Section 5.3.

### 5.2.1 Methodology

Figure 5.4 shows the actual scene setup in the forward simulation and the corresponding scene assumed in the TOMS V7 algorithm. In the forward calculation, the cloud fraction is set as 1 with CTP  $P_c$ . However, in the TOMS V7 retrieval, the scene is assumed to be a cloudy sky of reflectivity  $\geq 80\%$  at  $P_c$  with a cloud fraction  $f_c$  ( $0 \leq f_c \leq 1$ ) and a clear sky of reflectivity  $\leq 8\%$  at 1 atm with a fraction  $1 - f_c$ . If  $0 < f_c < 1$ , the cloud reflectivity is 80% and the ground reflectivity is 8%.

In Figure 5.4 (a),  $\Omega_t$ ,  $\Omega_a$ , and  $\Omega_b$  are the TOC, OZAC, and OZBC, respectively, from the given ozone profile. In the retrieval, the retrieved TOC  $\Omega'_t$  still consists of two parts: the added OZBC ( $\Omega'_b$ ) and

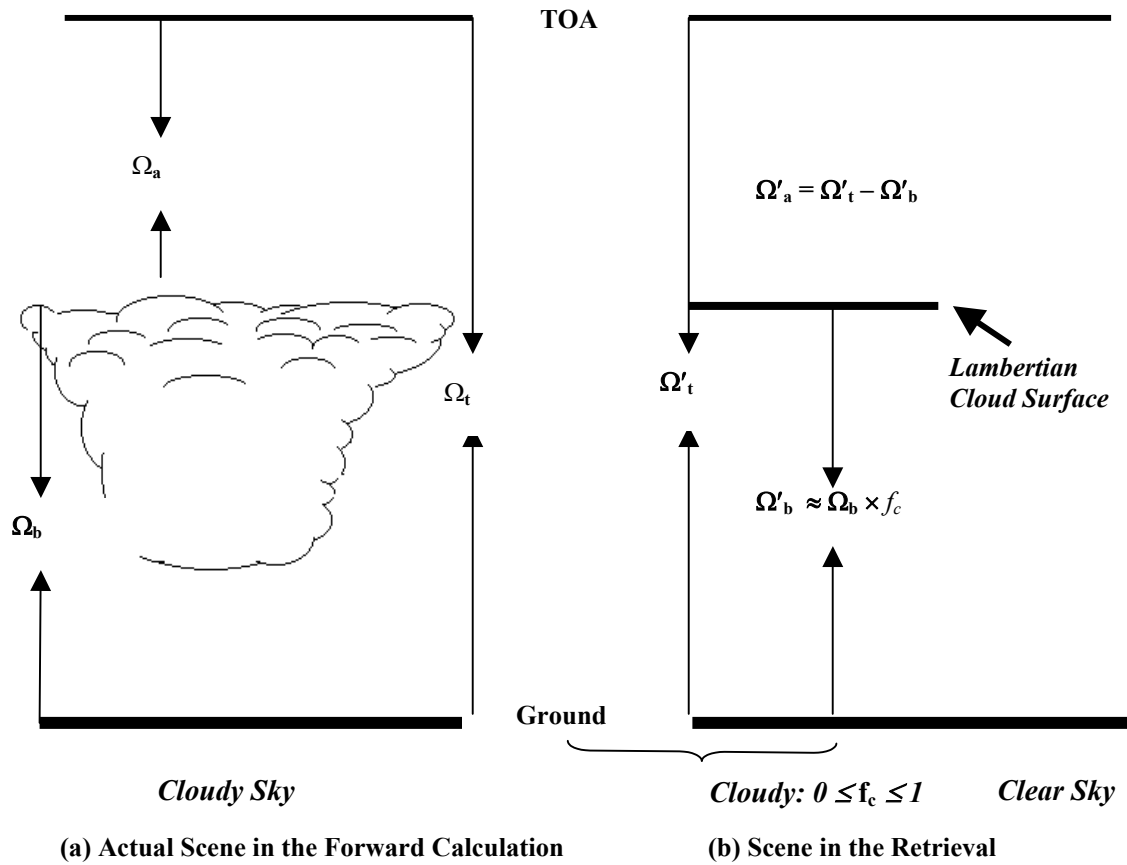


**Figure 5.4** Comparison of scenes between forward simulation and retrieval. (a) Full cloudy scene in the forward calculation. (b) Assumed scene in the TOMS retrieval.

the directly retrieved ozone ( $\Omega'_a$ ). The  $\Omega'_b$ , which is reported in the TOMS V7 level-2 data, is approximately the product of  $\Omega_b$  and  $f_c$  as long as the ozone profiles for ozone retrieval are not very different from the ozone profile used in forward simulation. If the actual cloud is opaque and the ozone retrieval is perfect,  $\Omega'_a$  should be equal to  $\Omega_a$  with  $\Omega'_b$  equal to  $\Omega_b$ . Corresponding to the fact that the retrieved ozone consists of two parts, the error in TOC ( $\Delta\Omega_t$ ) is decomposed into the error in OZAC ( $\Delta\Omega_a$ ) and the error in OZBC ( $\Delta\Omega_b$ ). These errors  $\Delta\Omega_t$ ,  $\Delta\Omega_a$ , and  $\Delta\Omega_b$  are defined as the difference between the retrieved quantities and the forward-calculation quantities as follows:

$$\Delta\Omega_t = \Omega'_t - \Omega_t, \quad (5.7)$$

$$\Delta\Omega_a = \Omega'_a - \Omega_a, \quad (5.8)$$

and

$$\Delta\Omega_b = \Omega'_b - \Omega_b. \quad (5.9)$$

If no ozone is placed below the clouds, the ICOAEN and BCOA effects are zero. This configuration simulates an opaque cloud in terms of ozone absorption although photons still penetrate the cloud. Therefore, we can study the effect due to Lambertian and PCM effects. The forward radiance calculated using PPGSRAD with no ozone below the clouds is inverted to retrieve the TOC. The difference between the TOC and the input TOC in the forward calculation gives the Lambertian-PCM effect on ozone retrieval. The ozone below the clouds is included in the TOC but is treated as nonexistent in the forward calculation to simulate opaque clouds. If the cloud fraction is set as 1 in the retrieval by modification of the TOMS V7 algorithm, the PCM effect diminishes to zero and only the Lambertian effect is present. Assuming the PCM effect and the Lambertian effect are independent, we can obtain the PCM effect by subtracting the Lambertian effect from the Lambertian-PCM effect. To investigate the ICOAEN effect only, two sets of backscattered radiances are calculated using PPGSRAD, one without ozone in the clouds and the other with ozone in the clouds. The difference between the retrieved TOC with and without ozone gives the ICOAEN effect. This method assumes that the Lambertian and PCM effects are the same for both cases with and without ozone in the cloud, so the difference in the retrieved ozone is due to ozone absorption inside the clouds. The method of comparing the cases with and without absorbers (or absorption) in the cloud has been applied to study absorption and effective path length enhancements in clouds [Feigelson, 1984; Kurosu *et al.*, 1997; Mayer *et al.*, 1998; Saiedy *et al.*, 1965; Twomey *et al.*, 1967]. Similarly, the BCOA effect can be obtained by comparing the difference in the retrieved ozone between areas with and without ozone below tcloud bases in the forward ozone profile.

The focus of this study is to investigate OREs associated with tropical high-reflectivity convective clouds. Figure 5.5 shows a scattered plot of ISCCP D1 CTP vs. COD for deep convective clouds in the tropics (10°S-10°N) in October 1983. Each point represents an average value of all the deep convective

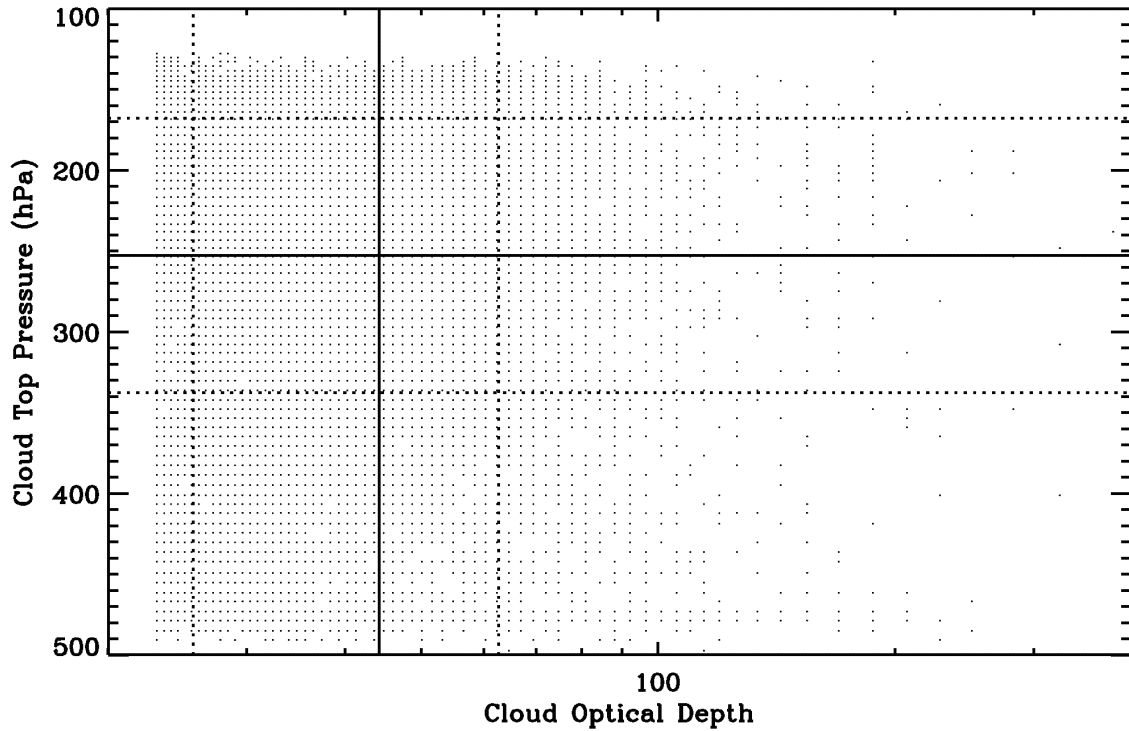


**Figure 5.5** ISCCP D1 CTP vs. COD for deep convective clouds in the tropics (10°S-10°N) in October 1983. The solid horizontal and vertical lines indicate the average CTP and COD, respectively. The dashed lines are the  $\pm 1$  standard deviation values from the corresponding average values.

cloudy pixels in a  $2.5^\circ$ -latitude  $\times$   $\sim 2.5^\circ$ -longitude area. The COD ranges from 23 to 379 with a mean value of  $44.2 \pm 18.4$ . The CTP ranges from 127 hPa to 503 hPa with a mean value of  $252.8 \pm 84.9$  hPa. The average cloud-top albedos (the ratio of upward flux to downward flux) for the calculation in Figure 5.3 are 77%, 77%, 79%, 81%, 85%, 87%, and 88% at each specified SZA, respectively. The average albedos are close to 80%, indicating the selection of COD 40 is a good representative for optically thick clouds (TOMS V7 algorithm treats such a scene as nearly overcast). Based on ISCCP observations and the TOMS PCM, we choose a WC with a COD of 40 positioned at 2-12 km to represent a typical cloud for this study. The TOMS standard low-latitude ozone and temperature profiles L275 are used as representative profiles. Terrain is not considered, and ground surface pressure is 1.0 atm. Typically, radiance calculation is done at N7 TOMS wavelengths. Although the ISCCP cloud retrieval algorithm considers deep convective clouds to be ice clouds, we typically treat them as water clouds because there is a large uncertainty in the optical

properties of ice clouds and water clouds are most commonly used in applications. Instead, we will perform sensitivity studies to study how OREs differ between water clouds and ice clouds. Other sensitivity studies will be performed on the effects of COD, the amount and distribution of ozone in the cloud, CGD, atmospheric profiles, and measurement wavelengths (e.g., N7 vs. EP TOMS) on ozone retrieval.

## 5.2.2 Lambertian and PCM Effects

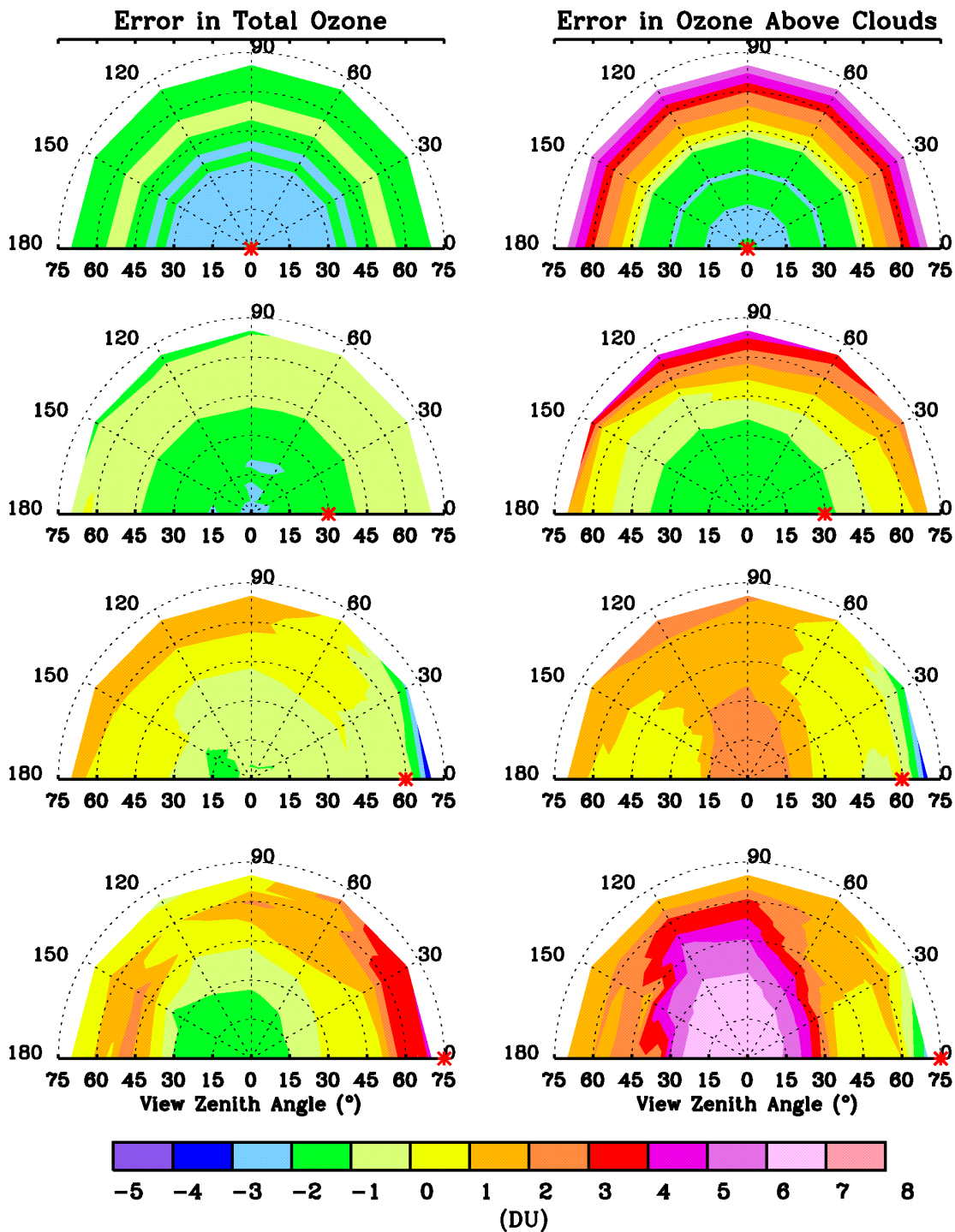
When there is no ozone below clouds in the forward simulation, the Lambertian and PCM effects coexist. This section describes how the Lambertian and PCM effects vary with viewing geometry, Cloud Optical Property (COP), COD, CGD, atmospheric profiles, and measurement wavelengths. A summary of the Lambertian and PCM effects is presented at the end of this section.

### 5.2.2.1 Viewing Geometry

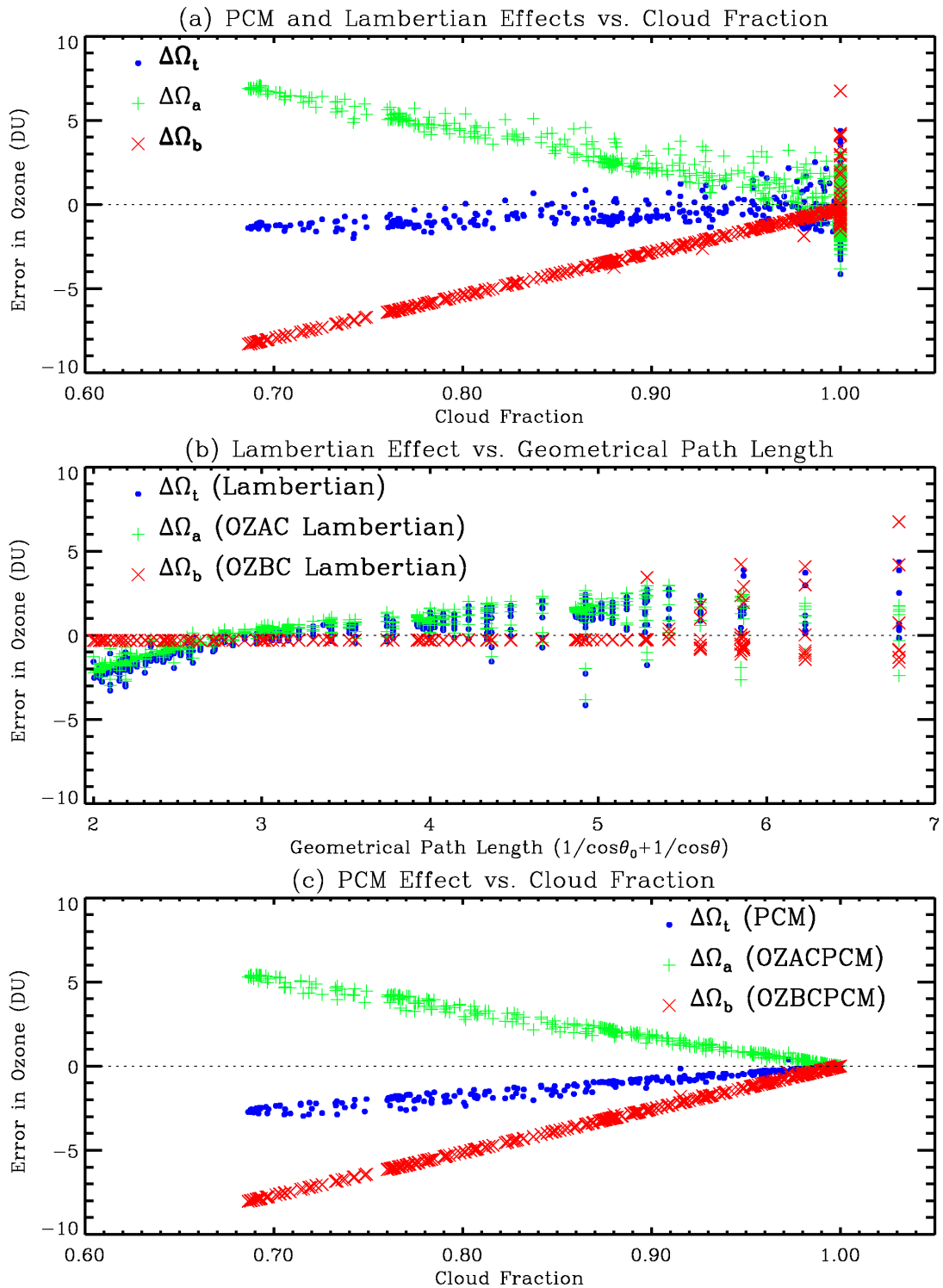
Figure 5.6 shows the distribution of  $\Delta\Omega_t$  (left) and  $\Delta\Omega_a$  (right) for a WC of COD 40 at 2-12 km. The TOMS standard ozone profile L275 is used except that OZBC is forced to be zero to exclude ozone absorption below clouds. The error distributions represent the sum of Lambertian and PCM effects on TOC (left) and OZAC (right), respectively. The error patterns are dependent on SZA, VZA, and AZA. Larger variance occurs at larger SZA. The  $\Delta\Omega_t$  ranges from  $-4.1$  DU to  $4.4$  DU with an average error  $-0.7 \pm 1.1$  DU; the  $\Delta\Omega_a$  ranges from  $-3.8$  DU to  $7.1$  DU, with an average error of  $-1.2 \pm 2.5$  DU. Large positive errors ( $> 4$  DU) in  $\Delta\Omega_a$  correspond to scenes with retrieved reflectivity less than 80% in Figure 5.3, indicating the  $\Delta\Omega_a$  is related to the retrieved ECF.

Figure 5.7 (a) shows the  $\Delta\Omega_t$ ,  $\Delta\Omega_a$ , and  $\Delta\Omega_b$  due to Lambertian-PCM effect as a function of ECF. We can see that  $\Delta\Omega_a$  is mainly positive and  $\Delta\Omega_b$  is mainly negative except at the ECF of 1. These two errors usually cancel each other and lead to small errors in the TOC. With decreasing ECF, both  $\Delta\Omega_a$  and  $\Delta\Omega_b$  increase in their magnitudes. At the EFC of 1, the  $\Delta\Omega_b$  varies from  $-2$  DU to  $7$  DU mainly because of profile difference between retrieval and forward calculation. When the OPL is  $\geq 1.5$ , higher-latitude profiles may be used in the retrieval, and the retrieved  $\Omega'_b$  can be larger than  $\Omega_b$  by up to  $\sim 7$  DU.

Water Clouds (OD = 40, 2–12 km), L275, No O<sub>3</sub> Below Clouds



**Figure 5.6** OREs in total ozone (left) and OREs in OZAC (right) at different SZAs (0°, 30°, 60°, and 75°) for a forward WC of COD 40 at 2–12 km. The low-latitude ozone file L275 is used except that no ozone is put below the cloud-tops.



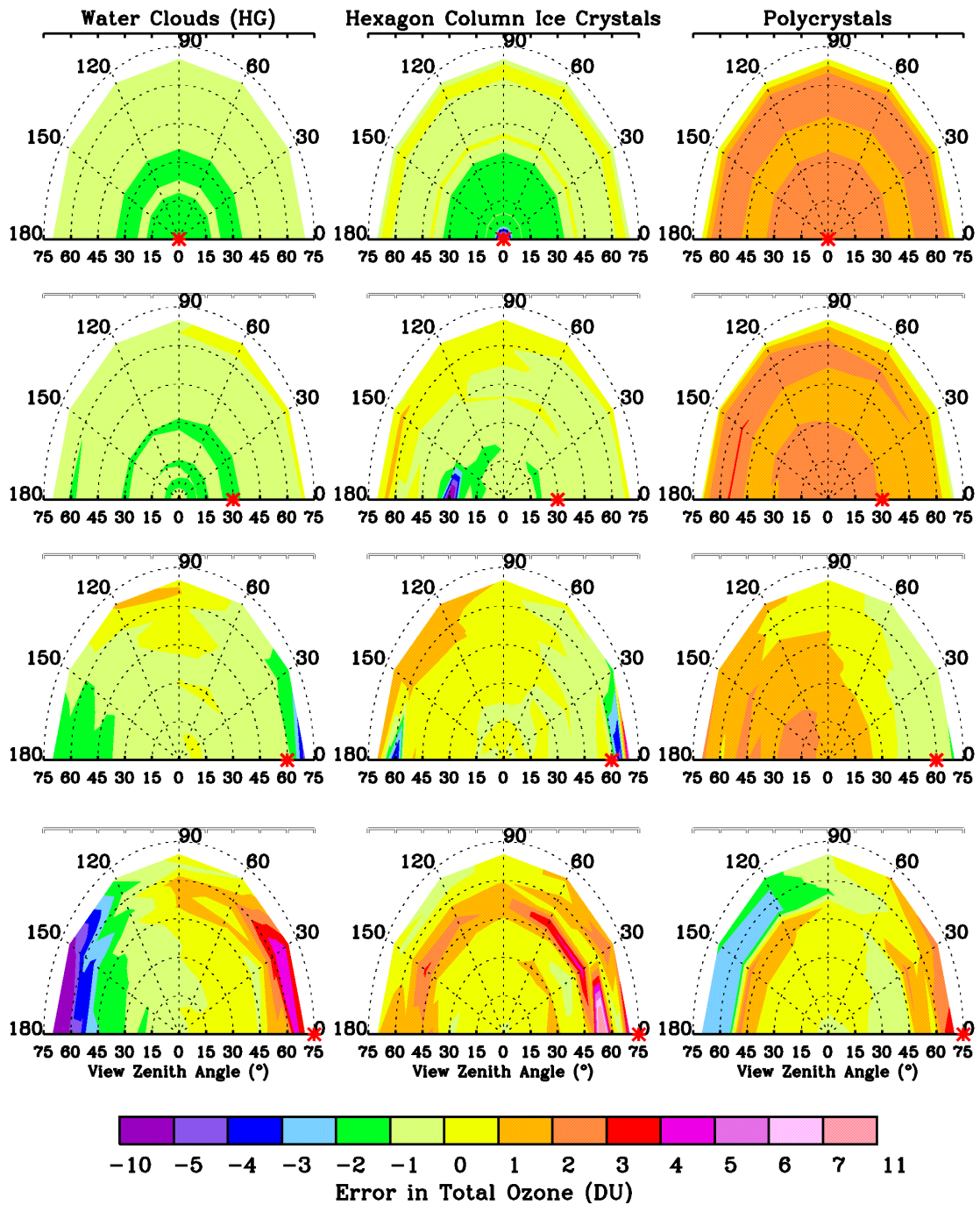
**Figure 5.7** Lambertian and PCM effects for a WC of COD 40 positioned at 2-12 km. (a) The sum of Lambertian and PCM effects as a function of derived ECF. (b) The Lambertian effect as a function of GPL (the ECF is 1). (c) The PCM effect as a function of ECF. The  $\Delta\Omega_t$ ,  $\Delta\Omega_a$ , and  $\Delta\Omega_b$  indicate the error in total ozone, error in OZAC, and error in OZBC, respectively.

Figure 5.7 (b) shows the  $\Delta\Omega_t$ ,  $\Delta\Omega_a$ , and  $\Delta\Omega_b$  due to the Lambertian effect as a function of Geometrical Path Length (GPL), which is defined as  $1/\cos\theta_0 + 1/\cos\theta$ . The ECF is fixed as 1 in the retrieval to avoid the PCM effect. In this case,  $\Delta\Omega_t$ ,  $\Delta\Omega_a$ , and  $\Delta\Omega_b$  correspond to the Lambertian effect, the Lambertian effect for OZAC (OZAC Lambertian effect), and the Lambertian effect for OZBC (OZBC Lambertian effect), respectively. Because  $\Delta\Omega_b$  is close to zero except at larger GPL because of profile difference between retrieval and forward calculation,  $\Delta\Omega_t$  is very close to  $\Delta\Omega_a$  except at larger GPL. The Lambertian effect ranges from  $-4.1$  to  $4.4$  DU with an average error of  $0.2 \pm 1.3$  DU. It is negative for  $\text{GPL} < \sim 2.8$  and positive for  $\text{GPL} > \sim 3$ . Ozone retrieval errors due to the Lambertian effect are within the TOMS retrieval precision of 1.5% [McPeters *et al.*, 1996], indicating that the assumption of cloud reflection as Lambertian for a WC of COD of 40 is fairly good for ozone retrieval when averaged over all viewing geometries.

The difference between Figures 5.7 (a) and (b) indicates the PCM effect, shown in Figure 5.7 (c). In this case,  $\Delta\Omega_t$ ,  $\Delta\Omega_a$ , and  $\Delta\Omega_b$  correspond to the PCM effect, the PCM effect for OZAC (OZACPCM), and the PCM effect for OZBC (OZBCPCM), respectively. Errors are zero at the ECF of 1 just because of the definition of the PCM effect. The positive OZACPCM and negative OZBCPCM effects almost cancel, leading to a much smaller PCM effect. Because the OZBC Lambertian effect is mostly zero, the negative OZBCPCM dominates  $\Delta\Omega_b$  in Figure 5.7 (a). It is straightforward that  $\Delta\Omega_b$  increases in magnitude with decreasing ECF according to its definition. When the ECF is close to 1, the PCM effect is almost zero and the Lambertian effect dominates the Lambertian-PCM effect; when the ECF becomes smaller, the PCM effect increasingly dominates the Lambertian-PCM effect.

### 5.2.2.2 Cloud Optical Properties

To show how the Lambertian and PCM effects vary with COPs, we compare the error pattern due to Lambertian-PCM effects for four different COPs: WC, Water Clouds with Henyey-Greenstein phase function (WCHG), HEX, and POLY. The WC and WCHG have the same single scattering albedo and asymmetry factor. Figure 5.6 (left) shows the error distribution in TOC for WC and Figure 5.8 shows similar results for WCHG (left panel), HEX (middle panel), and POLY (right panel). It can be seen that the



**Figure 5.8** Error distribution in total ozone for a cloud of COD 40 at 2-12 km for WCHG (left), HEX (middle), and POLY (right). The low-latitude ozone file L275 is used except that no ozone is put below the cloud-top.

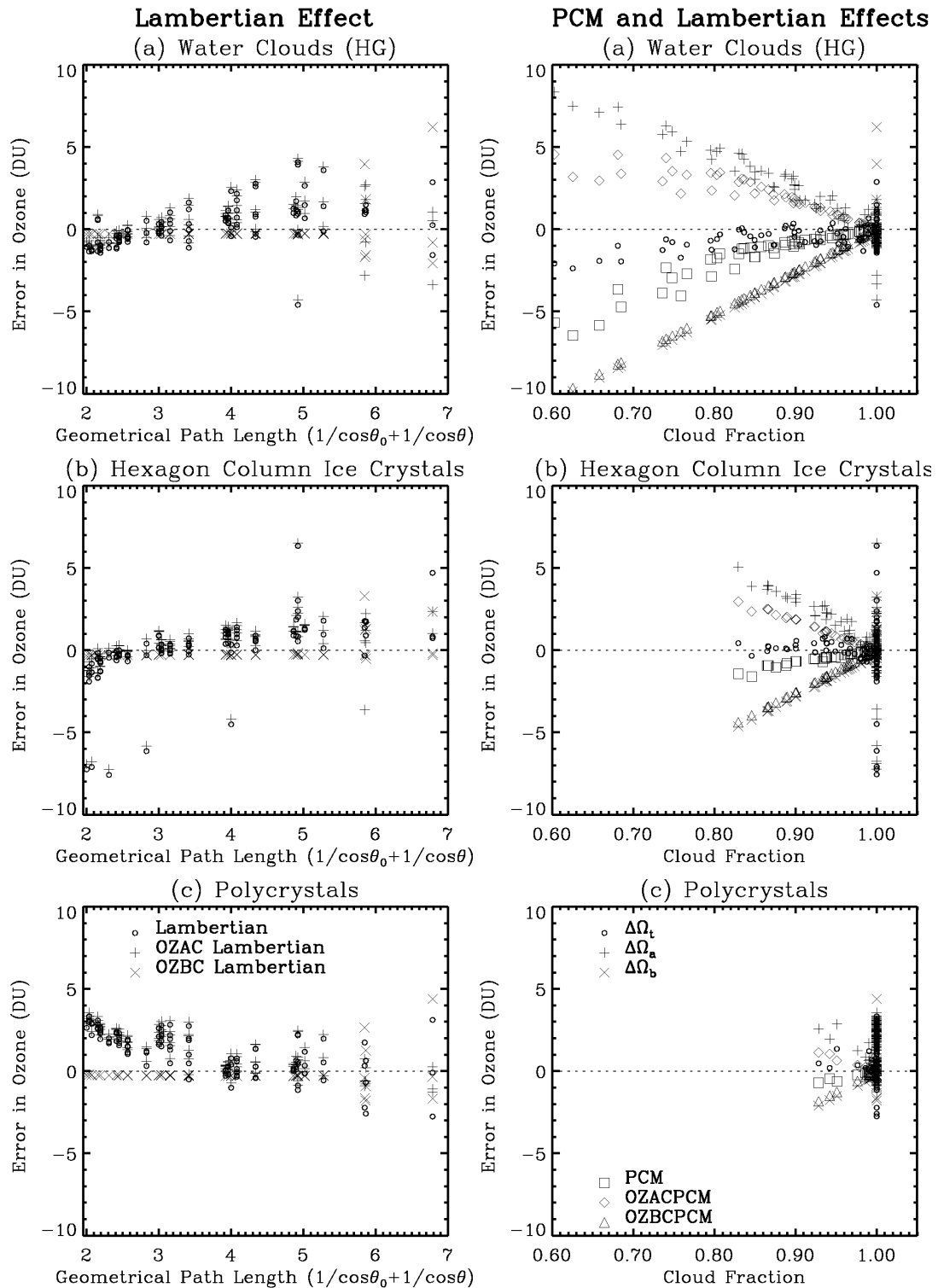


**Figure 5.9** Lambertian effect (left) and Lambertian-PCM effect (right) for a cloud with COD 40 at 2-12 km. (a) WCHG. (b) HEX. (c) POLY. The low-latitude ozone file L275 is used except that no ozone is put below the cloud-top. The results are shown at selected viewing geometries (SZA = 0°, 30°, 60°, and 75°; VZA = 0°, 30°, 50°, and 70°; AZA = 0°, 90°, and 180°).

Lambertian-PCM effect varies with different COPs. For WCHG, there are large negative errors at  $\theta_0 = 75^\circ$ ,  $\theta = 60\sim 70^\circ$ , and  $\phi = 150\sim 180^\circ$ . Because the simulated radiances at those angles are very close to the corresponding simulated clear-sky radiance with a ground Lambertian surface, the derived ECF at those angles is very small, leading to large negative errors caused by underestimating the cloud fraction. For HEX, there are several spots with large negative or positive errors probably due to some spikes in the calculated phase function. However, the average errors for different COPs are within  $\pm 2$  DU:  $-0.8 \pm 1.1$  DU,  $-0.6 \pm 1.0$ ,  $-0.1 \pm 1.3$ , and  $1.4 \pm 1.2$  DU for WC, WCHG, HEX, and POLY, respectively.

Figure 5.9 (left) shows the Lambertian effect as a function of GPL for WCHG (a), HEX (b), and POLY (c), respectively. The Lambertian effect is different for different COPs. Especially, the error distribution for POLY is very different from that for the other three COPs. The errors in TOC and OZAC are positive at smaller viewing geometry for POLY and negative for other COPs. Figure 5.9 (right) shows the Lambertian-PCM and PCM effects as a function of ECF for WCHG (a), HEX (b), and POLY (c), respectively. The obvious difference lies in the range of ECF. The derived ECF for POLY is always greater than 0.9, indicating that POLY is most Lambertian. The derived ECF ranges from zero to one, indicating that WCHG is least Lambertian. The difference in the range of cloud fraction leads to the difference in error distribution. However, the essential feature is similar so that the near cancellation of negative errors in OZBC and positive errors in OZAC leads to smaller errors in the TOC. Table 5.4 shows the error ranges and average errors due to the Lambertian and PCM effects for different COPs.

### 5.2.2.3 Cloud Optical Depth

Figure 5.10 shows the Lambertian and PCM effects for different CODs (1, 2, 5, 10, 20, 40, and 100). A WC is positioned at 2-12 km in the forward calculation. Table 5.4 shows the error ranges and average errors due to Lambertian and PCM effects. Figure 5.10 (left) shows the Lambertian effect as a function of GPL for different CODs. The OZBC Lambertian effect is almost the same for different CODs, about zero except at larger GPL. At smaller CODs, the Lambertian effect is mainly positive except for

**Table 5.4** Average values and ranges of Lambertian-PCM, Lambertian, and PCM effects.

|                           | Cloud Type | Profile | Cloud COD | Location (km) | Lambertian-PCM Effect |                              | Lambertian Effect |                             | PCM effect       |                              |
|---------------------------|------------|---------|-----------|---------------|-----------------------|------------------------------|-------------------|-----------------------------|------------------|------------------------------|
|                           |            |         |           |               | Error Range (DU)      | Avg. Error $\pm$ 1 s.d. (DU) | Error Range (DU)  | Avg. Error $\pm$ 1s.d. (DU) | Error Range (DU) | Avg. Error $\pm$ 1 s.d. (DU) |
| <b>Base case</b>          | WC         | L275    | 40        | 2-12          | -4.1 – 4.4            | -0.8 $\pm$ 1.1               | -4.1 – 4.4        | -0.2 $\pm$ 1.3              | -3.0 – 0.4       | -0.5 $\pm$ 0.8               |
| <b>Optical properties</b> | WCHG       | L275    | 40        | 2-12          | -9.8 – 4.8            | -0.6 $\pm$ 1.0               | -4.6 – 4.8        | 0.1 $\pm$ 1.2               | -8.2 – 0.0       | -0.7 $\pm$ 1.2               |
|                           | HEX        | L275    | 40        | 2-12          | -7.6 – 10.9           | -0.1 $\pm$ 1.3               | -7.6 – 10.9       | 0.0 $\pm$ 1.4               | -1.6 – 0.3       | -0.2 $\pm$ 0.3               |
|                           | POLY       | L275    | 40        | 2-12          | -2.8 – 3.3            | 1.4 $\pm$ 1.2                | -2.8 – 3.3        | 1.4 $\pm$ 1.2               | -0.8 – 0.4       | 0.0 $\pm$ 0.1                |
| <b>COD</b>                | WC         | L275    | 1         | 2-12          | -18.3 – 4.0           | -12.4 $\pm$ 3.6              | -3.4 – 10.0       | 6.0 $\pm$ 2.5               | -22.3 – 0.0      | -18.4 $\pm$ 4.1              |
|                           | WC         | L275    | 2         | 2-12          | -16.8 – 2.7           | -11.0 $\pm$ 3.3              | -4.3 – 8.5        | 4.2 $\pm$ 2.4               | -18.9 – 0.0      | -15.2 $\pm$ 3.9              |
|                           | WC         | L275    | 5         | 2-12          | -12.5 – 4.9           | -8.1 $\pm$ 2.7               | -3.9 – 6.1        | 1.3 $\pm$ 2.0               | -13.9 – 0.3      | -9.4 $\pm$ 2.8               |
|                           | WC         | L275    | 10        | 2-12          | -8.0 – 4.9            | -5.2 $\pm$ 2.1               | -4.1 – 4.8        | 0.0 $\pm$ 1.8               | -9.5 – 0.0       | -5.2 $\pm$ 2.0               |
|                           | WC         | L275    | 20        | 2-12          | -4.6 – 4.7            | -2.4 $\pm$ 1.5               | -4.4 – 4.7        | -0.3 $\pm$ 1.5              | -5.6 – 0.0       | -2.2 $\pm$ 1.3               |
|                           | WC         | L275    | 100       | 2-12          | -4.0 – 4.0            | -0.3 $\pm$ 1.2               | -4.0 – 4.0        | -0.2 $\pm$ 1.2              | -1.2 – 0.0       | -0.1 $\pm$ 0.3               |
| <b>Cloud Location</b>     | WC         | L275    | 40        | 2-3           | -12.2 – 4.2           | 1.1 $\pm$ 2.0                | -12.2 – 4.5       | 1.3 $\pm$ 2.1               | -0.8 – 0.0       | -0.2 $\pm$ 0.2               |
|                           | WC         | L275    | 40        | 2-7           | -7.2 – 3.9            | 0.4 $\pm$ 1.3                | -7.2 – 4.2        | 0.7 $\pm$ 1.6               | -1.3 – 0.0       | -0.3 $\pm$ 0.4               |
|                           | WC         | L275    | 40        | 11-12         | -4.1 – 3.9            | -0.8 $\pm$ 1.2               | -4.1 – 3.9        | -0.2 $\pm$ 1.4              | -3.0 – 0.3       | -0.6 $\pm$ 0.8               |
|                           | WC         | L275    | 40        | 7-12          | -4.1 – 3.9            | -0.8 $\pm$ 1.2               | -4.2 – 4.4        | -0.2 $\pm$ 1.4              | -3.0 – 0.4       | -0.6 $\pm$ 0.8               |
| <b>Profile</b>            | WC         | L225    | 40        | 2-12          | -3.0 – 2.4            | -0.9 $\pm$ 0.9               | -3.1 – 2.5        | -0.4 $\pm$ 1.1              | -2.6 – 0.0       | -0.5 $\pm$ 0.7               |
|                           | WC         | L325    | 40        | 2-12          | -5.7 – 6.7            | -0.7 $\pm$ 1.4               | -5.7 – 6.7        | -0.2 $\pm$ 1.6              | -2.9 – 0.0       | -0.5 $\pm$ 0.7               |
|                           | WC         | M325    | 40        | 2-12          | -10.1 – 4.4           | -1.7 $\pm$ 2.8               | -10.4 – 4.2       | -1.8 $\pm$ 2.7              | -10.6 – 3.0      | 0.10 $\pm$ 3.6               |
|                           | WC         | M375    | 40        | 2-12          | -11.2 – 4.8           | -1.8 $\pm$ 3.3               | -11.5 – 7.1       | -2.0 $\pm$ 3.2              | -11.4 – 4.4      | 0.2 $\pm$ 4.5                |
|                           | WC         | M425    | 40        | 2-12          | -11.7 – 8.0           | -3.7 $\pm$ 3.4               | -11.7 – 11.0      | -2.3 $\pm$ 4.2              | -8.2 – 1.8       | -1.4 $\pm$ 2.0               |
| <b>EP</b>                 | WC         | L275    | 40        | 2-12          | -10.5 – 3.0           | -0.5 $\pm$ 1.1               | -4.9 – 3.0        | -0.0 $\pm$ 1.3              | -10.8 – 0.0      | -0.5 $\pm$ 0.8               |

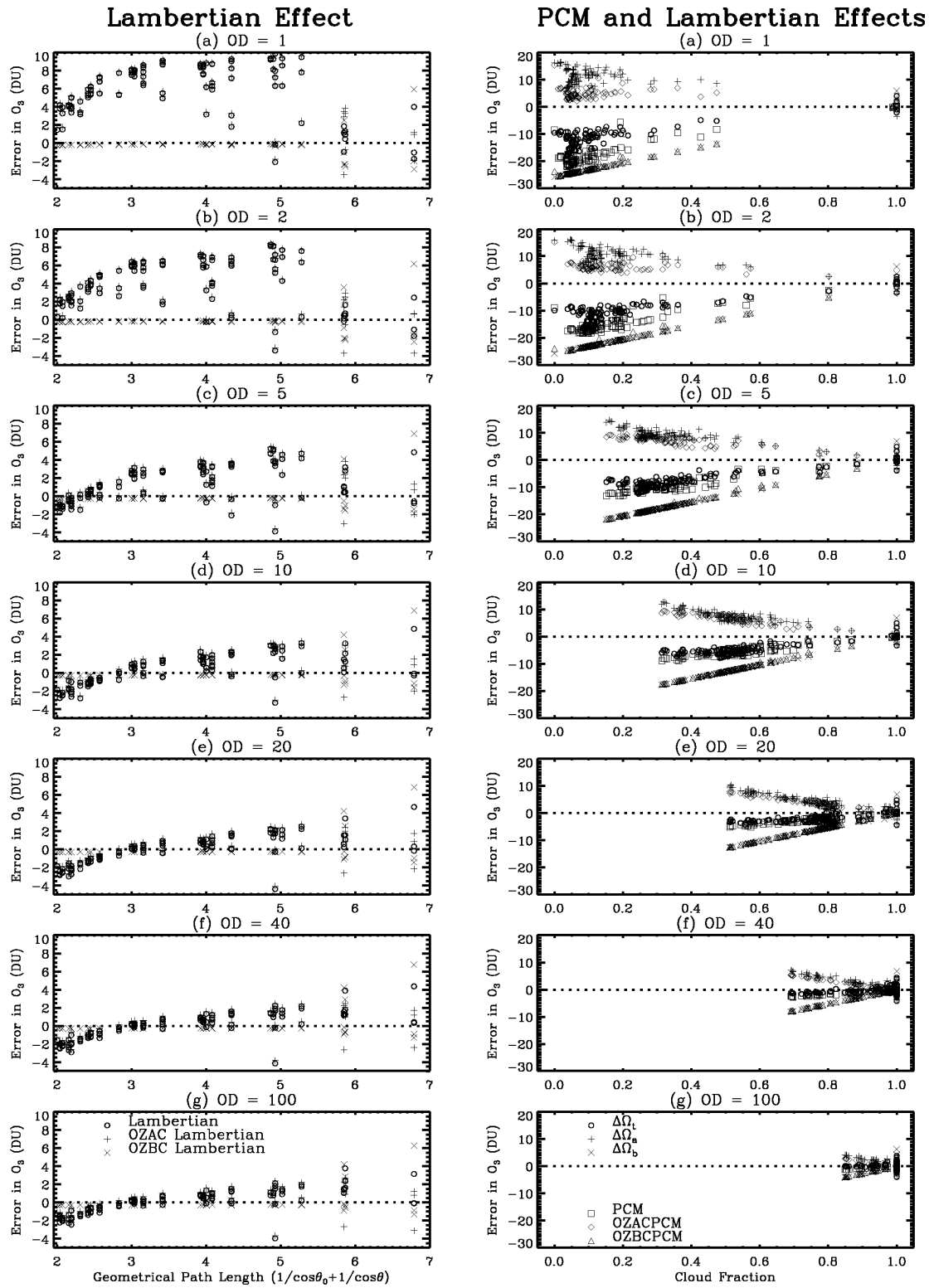


**Figure 5.10** Similar to Figure 5.9 except for WC at 2-12 km with COD 1 (a), 2 (b), 5 (c), 10 (d), 20 (e), 40 (f), and 100 (g), respectively.

centered around zero. Figure 5.10 (right) shows the Lambertian-PCM and PCM effects for different CODs. The derived ECF increases with increasing COD as expected because the increase in COD leads to higher cloud reflectivity. With decreasing COD, the six types of errors increase in their magnitudes. The negative errors in OZBC still tend to cancel the positive errors in OZAC. However, the overall errors in the TOC become significant at  $COD \leq 10$ . For example, at a COD of 10, the average error is  $-5.2 \pm 2.1$  DU due to Lambertian-PCM effects and  $-5.2 \pm 2.0$  due to the PCM effect only. At a COD of 1, the average error is about  $-12.4 \pm 3.6$  DU due to Lambertian-PCM effects and  $-18.4 \pm 4.1$  due to the PCM effect only. The large negative error at smaller CODs comes primarily from the fact that the cloud fraction is largely underestimated and less ozone is added below the clouds.

#### 5.2.2.4 Cloud Geometrical Depth

Figure 5.11 shows the Lambertian and PCM effects for different CGDs (2-3 km, 2-7 km, 11-12 km, and 7-12 km). A WC of COD 40 is placed at different locations. Table 5.4 shows the error ranges and average errors due to the Lambertian and PCM effects. Figure 5.11 (left) shows the Lambertian effect as a function of GPL. The Lambertian effect varies with CTH. For clouds with the same CTH at 12 km, there is almost no difference in the Lambertian effect. For low-altitude clouds (e.g., 2-3 km, and 2-7 km), the OZBC Lambertian effect is close to zero even with larger viewing geometry because there is not much difference in the lower troposphere among the low-, mid-, and high-latitude profiles with a TOC of 275 DU. With decreasing CTH, the Lambertian effect is more scattered, more positive at most angles, but with some large negative errors at large SZAs and VZAs on the solar side. The average error increases with decreasing CTH and the error range becomes wider.

Figure 5.11 (right) shows the Lambertian-PCM and the PCM effects for different CGDs. The Lambertian-PCM and PCM effects do not change if CTH is fixed. Due to more Rayleigh scattering at low-altitudes, low-altitude clouds are more Lambertian and the derived ECF is closer to 1. With decreasing CTH, the negative OZBCPCM and positive OZACPCM decrease in their magnitude. Similar to the situation with the Lambertian effect, errors in TOC due to the Lambertian-PCM effect are more positive at most angles except with some large negative values at some angles. The error range decreases with increasing CTH, from  $-12.2$  to  $4.2$  DU, from  $-7.2$  to  $3.9$  DU, and from  $-4.1$  to  $3.9$  DU for cloud locations at

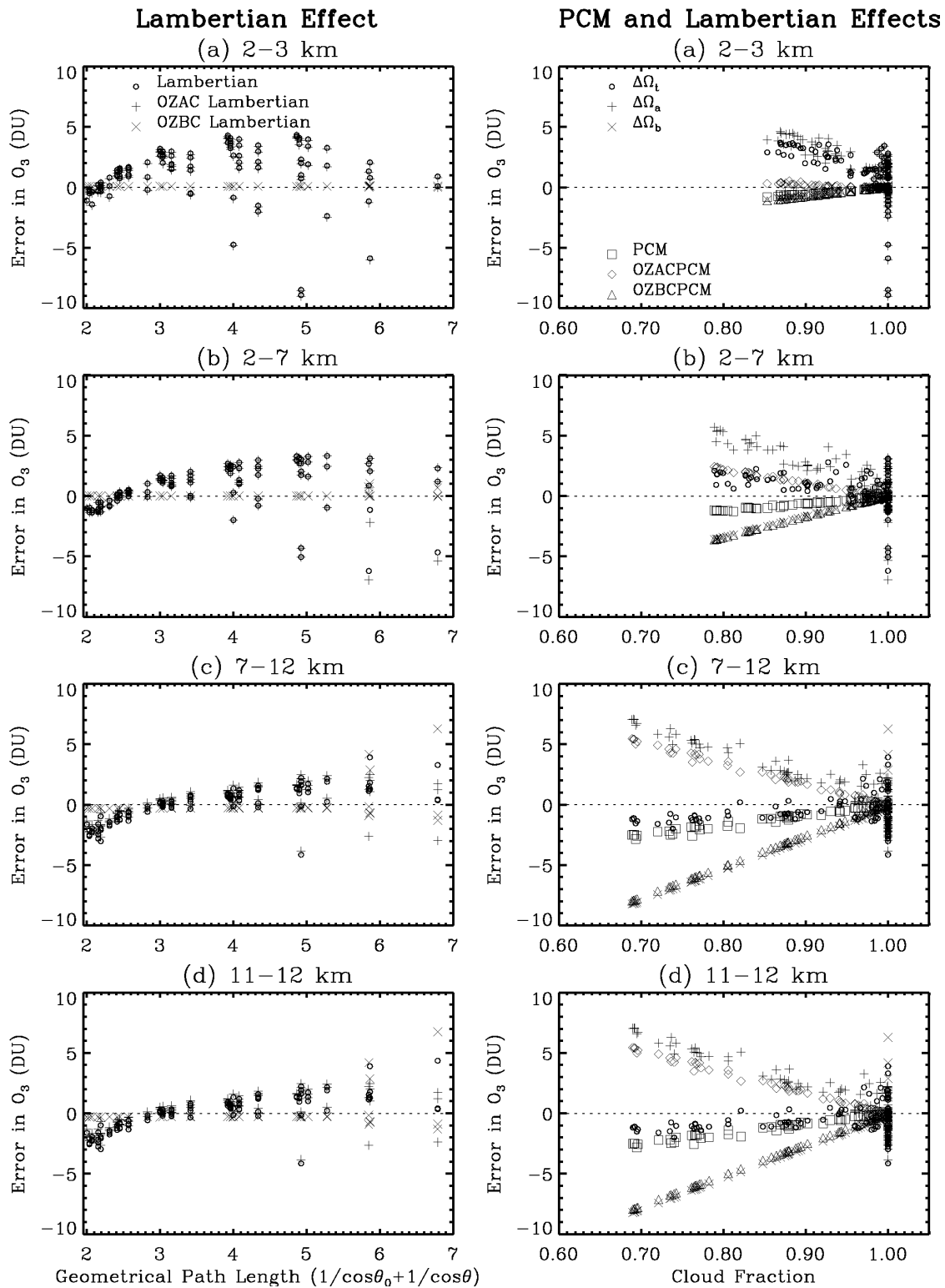


**Figure 5.11** Similar to Figure 5.9 except for a WC of COD 40 at 2-3 km (a), 2-7 km (b), 7-12 km (c), 11-12 km (d), respectively.

2-3 km, 2-7 km, 7-12 km, respectively. The average errors due to the Lambertian-PCM effects are rather small:  $1.3 \pm 2.1$  DU,  $0.7 \pm 1.6$  DU,  $-0.2 \pm 1.4$  DU, and  $-0.2 \pm 1.4$  DU for cloud locations at 2-3 km, 2-7 km, 7-12 km, and 11-12 km, respectively.

### 5.2.2.5 Atmospheric Ozone Profiles

Figure 5.12 shows the Lambertian and PCM effects for different TOMS standard ozone profiles (L225, L325, M325, M375, and M425). For using mid-latitude profiles, the latitude assumed in the ozone retrieval is assumed at  $45^\circ$ . Table 5.4 shows the error ranges and average errors due to the Lambertian and PCM effects. With increasing TOC in the forward ozone profiles, both the Lambertian and PCM effects are slightly more scattered. Especially, errors using mid-latitude ozone profiles are much more scattered and less orderly compared to errors using low-latitude ozone profiles. The average error due to the Lambertian-PCM effect is almost the same for the three low-latitude profiles:  $-0.9 \pm 0.9$  DU,  $-0.8 \pm 1.1$  DU, and  $-0.7 \pm 1.4$  DU for L225, L275, and L325, respectively. For the three mid-latitude ozone profiles, the average error increases in magnitude with increasing TOC:  $-1.7 \pm 2.8$  DU,  $-1.8 \pm 3.3$  DU, and  $-3.7 \pm 3.4$  DU for M325, M375, and M425, respectively. However, the average error is within 1.5% of the TOC for different ozone profiles.

### 5.2.2.6 EP vs. N7 TOMS Measurement Wavelengths

The Lambertian and PCM effects are also investigated at EP TOMS wavelengths. Figure 5.12 (f) shows the Lambertian effect (left), and Lambertian-PCM and PCM effects (right) for a WC of COD 40 at 2-12 km. The Lambertian and PCM effects for EP TOMS are similar to these effects for N7 TOMS. The average errors due to the Lambertian-PCM, Lambertian, and PCM effects, are  $-0.5 \pm 1.1$  DU,  $-0.0 \pm 1.3$  DU,  $-0.5 \pm 0.8$  DU, respectively.

### 5.2.2.7 Summary of the Lambertian and PCM Effects

According to the above results, the Lambertian effect varies with COP, COD, CTH, and ozone profile. Table 5.4 summarizes the average errors and error ranges for the base condition and sensitivity

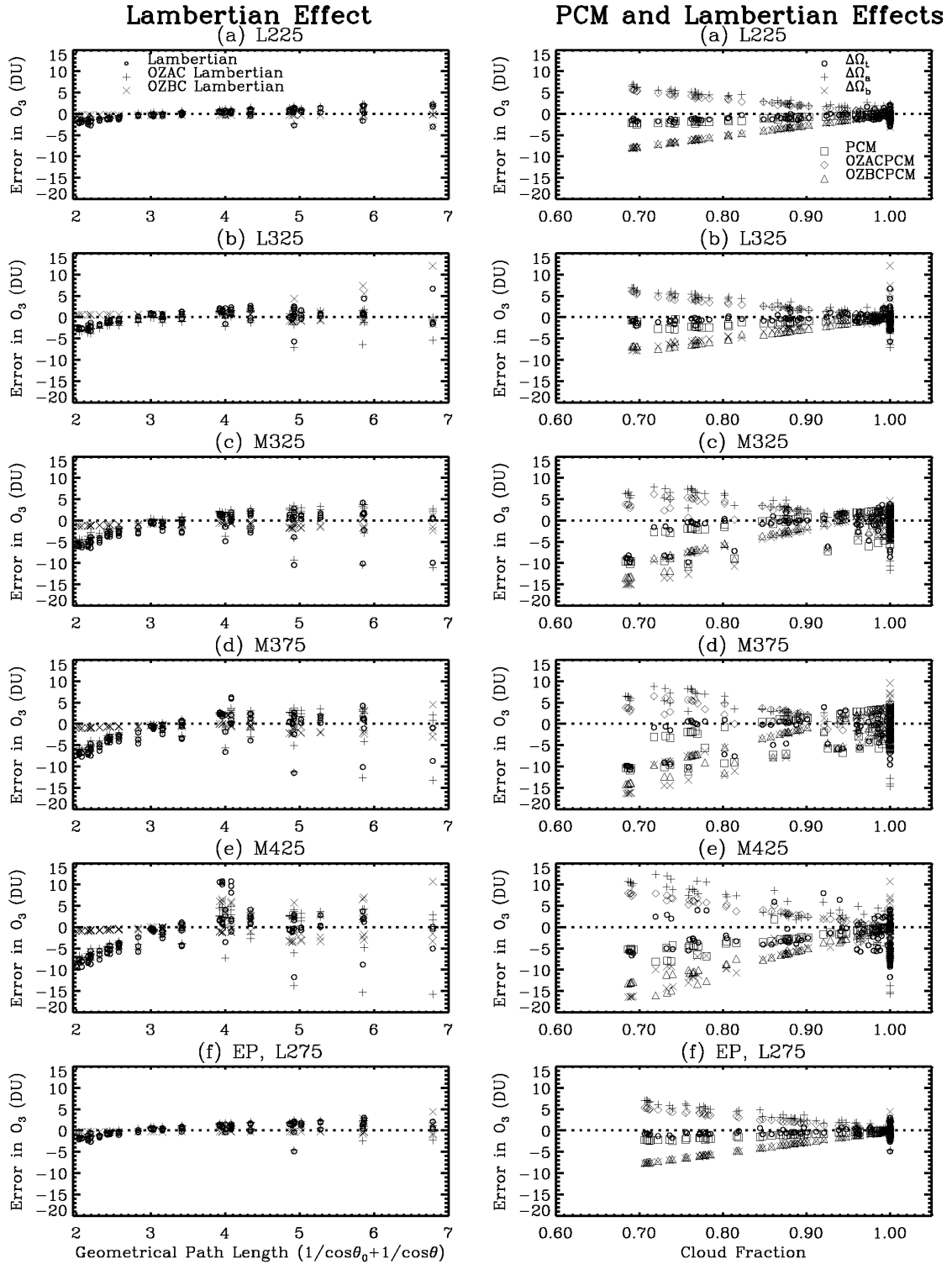


**Figure 5.12** Similar to Figure 5.9 except using ozone profiles L225 (a), L325 (b), M325 (c), M375 (d), and M425 (e), respectively. (f) Results calculated at EP TOMS wavelengths using ozone profile L275.

cases. The OZAC Lambertian effect results from several factors, including the air mass factor difference above clouds due to Rayleigh scattering and multiple cloud reflections between the simulated scattering clouds and the Lambertian clouds, profile difference between retrieval and forward-calculation, and some slightly nonlinear wavelength-dependence in the cloud reflection. The OZBC Lambertian effect arises from the profile difference between retrieval and forward calculations so that the added OZBC from the retrieval is not the same as the original one. However, the OREs due to the Lambertian effect is usually within 1.5% of the TOC except when the COD is  $< 20$ .

As seen from Table 5.4, the PCM effect also varies with COP, COD, CTH, and zone profiles. The negative OZBCPCM effect is due primarily to the cloud fraction's being underestimated, with less ozone added below clouds. The positive OZACPCM effect is due to the air mass factor difference between forward full-cloud conditions and partial clouds in the retrieval. The negative OZACPCM effect is always larger than the positive OZACPCM effect, so the overall PCM effect is negative. The larger the cloud fraction being underestimated, the larger the OZACPCM and OZBCPCM effects, the larger the PCM effect will be. The underestimation in the cloud fraction is a direct result of the used PCM in the TOMS V7 algorithm, and is largely determined by COD. When COD is  $\geq 20$ , the overall PCM effect is less than 2.5 DU on average, i.e., within 1% of the TOC. The average PCM effect decreases to  $-18.4 \pm 4.1$  DU when COD decreases to 1.

Like the Lambertian and PCM effects, their sum (i.e., the Lambertian-PCM effect) is mainly dependent on the COD. At COD  $\geq 20$ , the average OREs is usually within 1.5% of the TOC and within the retrieval precision of TOMS ozone products. The small error due to the Lambertian and PCM effects indicates that the assumption of angular-independent cloud reflection is fairly good for ozone retrieval when the COD greater than 20.

### **5.2.3 Effect of Ozone Absorption Enhancement in Clouds**

This section discusses the effect of ozone absorption enhancement in clouds on ozone retrieval, i.e., the ICOAEN effect. In the forward calculation, two sets of backscattered radiances are computed using PPGSRAD, one with ozone in the cloud and the other without ozone in the cloud. In the retrieval, these two sets of radiances are inverted to retrieve the TOCs. The difference in the retrieved TOC between

radiances with and without ozone in the cloud represents the ICOAEN effect. In other words, the ICOAEN effect is the Effective Inter-Cloud Ozone (EICO) as seen by the sensor or the ORE in the TOC and OZAC due to ozone absorption in the cloud. As a base condition, a homogeneous WC of COD 40 is positioned at 2-12 km, and the L275 profile is used except the same amount of ozone (20.8 DU) is homogeneously distributed in the cloud for the case with ozone in the cloud. We will first show the ICOAEN effect as a function of viewing geometry for the base case, then perform sensitivities of the ICOAEN effect to COP, COD, CGD, ozone amount in clouds, ozone distribution in clouds, atmospheric profiles, and measurement wavelengths (i.e., N7 vs. EP TOMS).

From the two sets of calculated radiances, the effective Photon Path Length (PPL) can be derived according to the following equation [Feigelson, 1984; Kurosu *et al.*, 1997; Mayer *et al.*, 1998]:

$$\frac{I_{O_3}}{I_{no\ O_3}} \approx \exp(-\tau_{O_3}) = \exp(-\beta_{O_3} l_{eff}), \quad (5.10)$$

where  $I_{O_3}$  and  $I_{no\ O_3}$  are the calculated backscattered radiance at TOA for radiances with and without ozone in clouds, respectively;  $\tau_{O_3}$  is the ozone absorption optical depth;  $\beta_{O_3}$  is the ozone absorption coefficient in the cloud; and  $l_{eff}$  is the effective PPL in the cloud for backscattered photons emerging at TOA. The above equation assumes that the ozone absorption coefficient is uniformly distributed throughout the cloud layer, and the absorption is sufficiently smaller so that scattering and absorption can be considered as independent processes [Kurosu *et al.*, 1997]. Because the ozone absorption coefficient is slightly temperature dependent,  $\beta_{O_3}$  decreases with increasing altitude for homogeneous ozone distribution in the cloud. The average ozone absorption coefficient at 317 nm is  $9.87 \times 10^{-4} \text{ km}^{-1}$ ,  $8.89 \times 10^{-4} \text{ km}^{-1}$ , and  $9.46 \times 10^{-5} \text{ km}^{-1}$  for 1 DU distributed at 2-3 km, 11-12 km, and 2-12 km, respectively. However, assuming a constant  $\beta_{\lambda}$  as the average ozone absorption coefficient throughout the cloud has a small effect on the derived PPL. In addition, the average ozone absorption coefficient at 317 nm is fairly small,  $1.89 \times 10^{-3} \text{ km}^{-1}$  for 20 DU distributed in a 2-12 km cloud. Therefore, we can apply Equation (5.10) to derive the PPL.

The product of  $\beta_{O_3}$  and  $l_{eff}$  is the ozone absorption optical depth in the cloud  $\tau_{\lambda, O_3}$ , which is also equal to the product of ozone absorption optical depth per DU of ozone  $\alpha_{\lambda, O_3}$ , the EICO as seen by the

sensor  $\Delta\Omega_{calc}$ , and the GPL that is implicitly taken into account in the TOMS V7 algorithm. Then we can obtain the following:

$$\frac{I_{O_3}}{I_{no\ O_3}} \approx \exp(-\tau_{O_3}) = \exp\{-\alpha_{\lambda,O_3} \Delta\Omega_{calc} (\frac{1}{\cos\theta_0} + \frac{1}{\cos\theta})\}. \quad (5.11)$$

Therefore, we can directly calculate the EICO from the ratio of radiance with ozone to that without ozone at one ozone-absorbing wavelength without using the TOMS V7 algorithm. Equation (5.11) even applies for inhomogeneous ozone distribution as long as the  $\alpha_{\lambda,O_3}$  is approximately constant. The  $\alpha_{\lambda,O_3}$  is constant if ozone absorption coefficient is not temperature dependent.

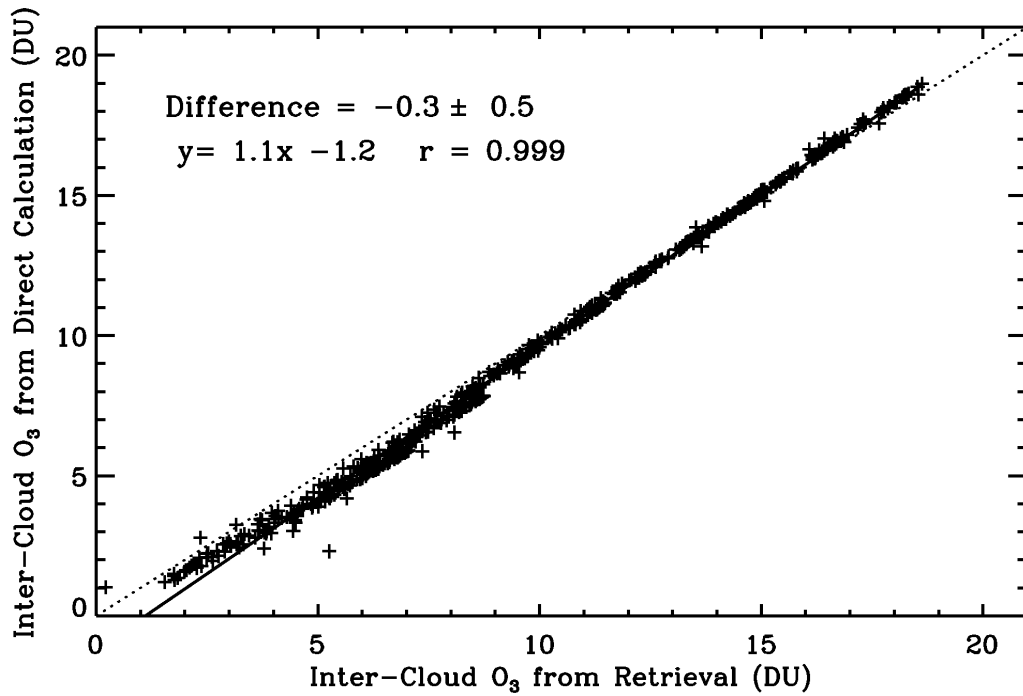


**Figure 5.13** Comparison of EICO between direct calculation from Equation (5.11) at 317 nm and ozone retrieval for the base case.

Figure 5.13 shows a comparison of EICO for the base case between direct calculation at 317 nm and from TOMS V7 retrieval at all the viewing geometries (7 SZAs, 15 VZAs, and 7 AZAs). There is an excellent relationship between these two sets of EICO with a correlation of 0.999. On average, the EICO from direct calculation is smaller by  $0.3 \pm 0.5$  DU than that from retrieval. Comparisons at other ozone absorbing wavelengths show similar correlations as well, but the slopes and offsets are slightly different. The excellent comparison indicates that using the triplet method in the retrieval cannot remove the error induced by ozone absorption in clouds because the PPL in clouds does not vary much with TOMS wavelengths. Also, the good comparison suggests it is much faster to compute the ICOAEN effect from direct calculation because the radiances need to be calculated at only one ozone-absorbing wavelength.

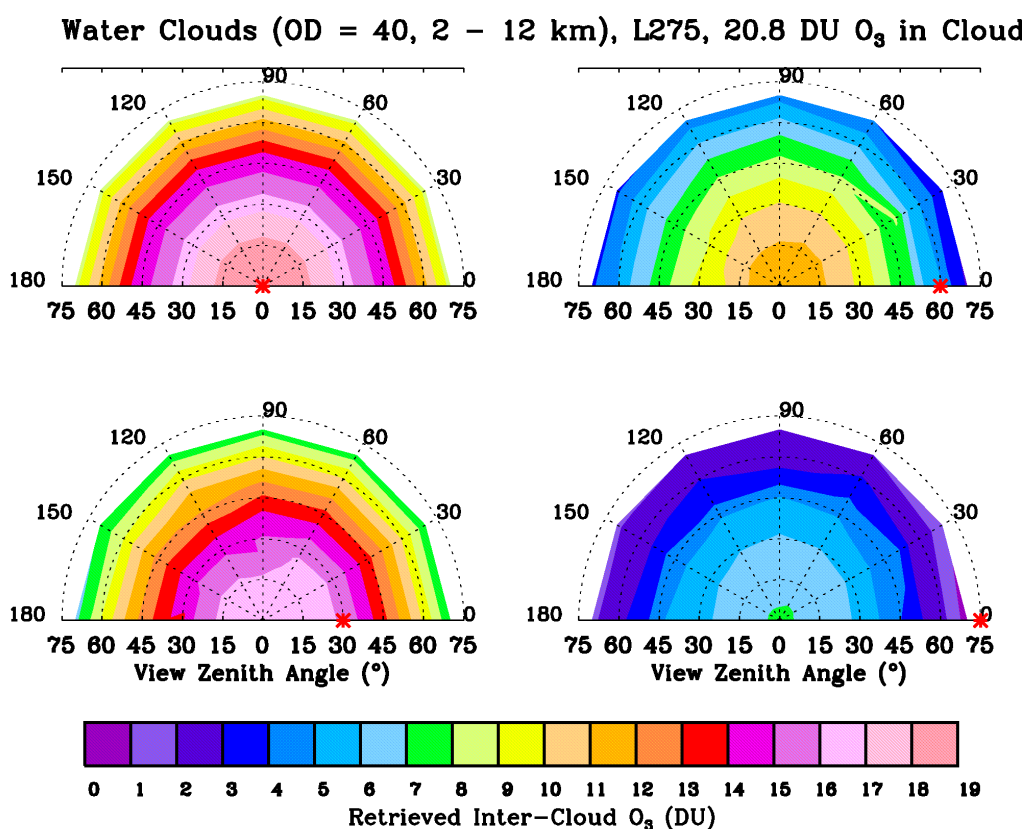


**Figure 5.14** Retrieved EICO as a function of viewing geometry for a WC of COD 40 at 2-12 km. The low-latitude ozone profile L275 is used except that the 20.8 DU inter-cloud ozone is homogeneously distributed in the cloud. The red asterisk symbol on the x-axis indicates the SZA.

### 5.2.3.1 Viewing Geometry

Figure 5.14 shows the EICO as a function of viewing geometry from retrieval for the base condition. The a priori amount of ozone in the cloud is 20.8 DU. The EICO ranges from 0 to 18.6 DU. The EICO is essentially azimuthally independent, but strongly dependent on the SZA and VZA, consistent with *Saiedy et al.* [1965]. The larger the SZA and VZA, usually the larger the EICO will be. For example, the EICO is 17.7 DU at  $\theta_0 = 0^\circ$  and  $\theta = 0^\circ$  and is  $\sim 2.6$  DU at  $\theta_0 = 75^\circ$  and  $\theta = 60^\circ$ . The largest EICO of 18.6 DU occurs not exactly at nadir but at  $\theta_0 = 0^\circ$  and  $\theta = 5^\circ$ . Because of the backscattering peak at the scattering angle of  $180^\circ$  in the phase function, photons penetrate less at nadir and the EICO is smaller at nadir than at  $\theta_0 = 0^\circ$  and  $\theta = 5^\circ$ . Note that the highest EICO of 18.6 DU is close to the a priori ozone in the cloud, indicating that the sensor can see almost all the ozone in the cloud under these conditions.

Figure 5.15 shows the azimuthally averaged PPL and EICO as a function of SZA and VZA. The highest PPL is about 19 km, almost twice that of the CGD. This finding is consistent with the results by *Kurosui et al.* [1997]. At a specific VZA or SZA, the PPL and EICO decrease with increasing SZA or VZA. The PPL and EICO almost do not change by exchanging SZA and VZA because of the principle of reciprocity [*Saiedy et al.*, 1965]. The difference in the behavior with viewing geometry between PPL and EICO is because the EICO is proportional to the ratio of PPL to GPL.

### 5.2.3.2 Cloud Optical Properties

Figure 5.16 shows the ICOAEN effect as a function of VZA for WC, WCHG, HEX, and POLY, respectively, at  $\theta_0 = 0^\circ$  and  $\theta_0 = 75^\circ$ . The clouds and ozone profile are the same as in the base case except for different cloud phase functions. The ICOAEN effect does not vary much with different COPs and is within 3 DU except at nadir. The difference in the ICOAEN effect among different COPs decreases with increasing VZA and SZA. Generally, the EICO for WCHG is greater than that for WC, and the EICO for WC is greater than that for HEX, and the EICO for HEX is greater than that for POLY. For example, the EICO at  $\theta_0 = 0^\circ$  and  $\theta = 15^\circ$  is 18.2 DU, 19.4 DU, 17.9 DU, and 16.9 DU for WC, WCHG, HEX, and POLY, respectively. The difference in the EICO among WC, HEX, and POLY can be explained by their difference in phase function, as shown in Figure 5.1. The larger the asymmetry factor (i.e., the first-order

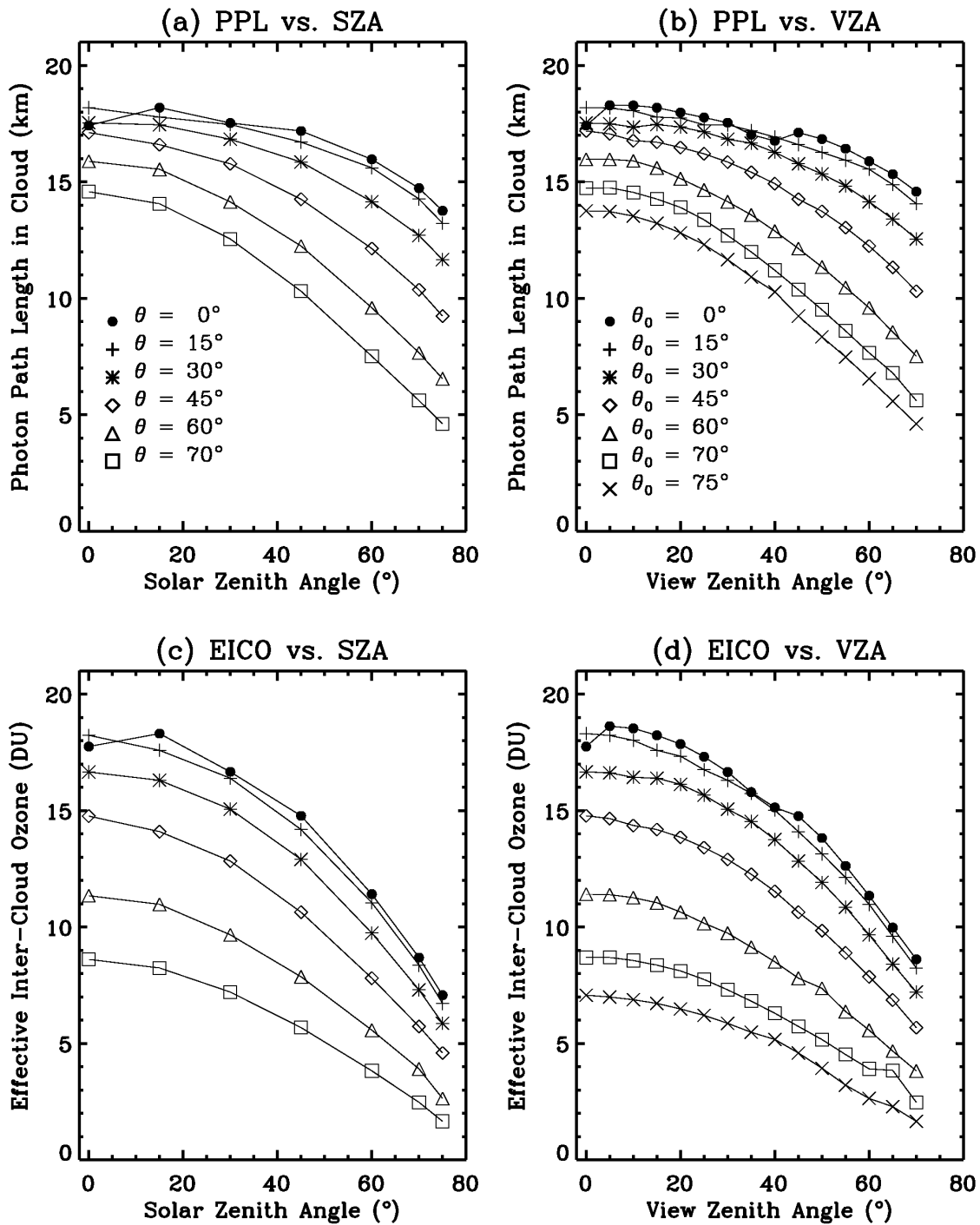
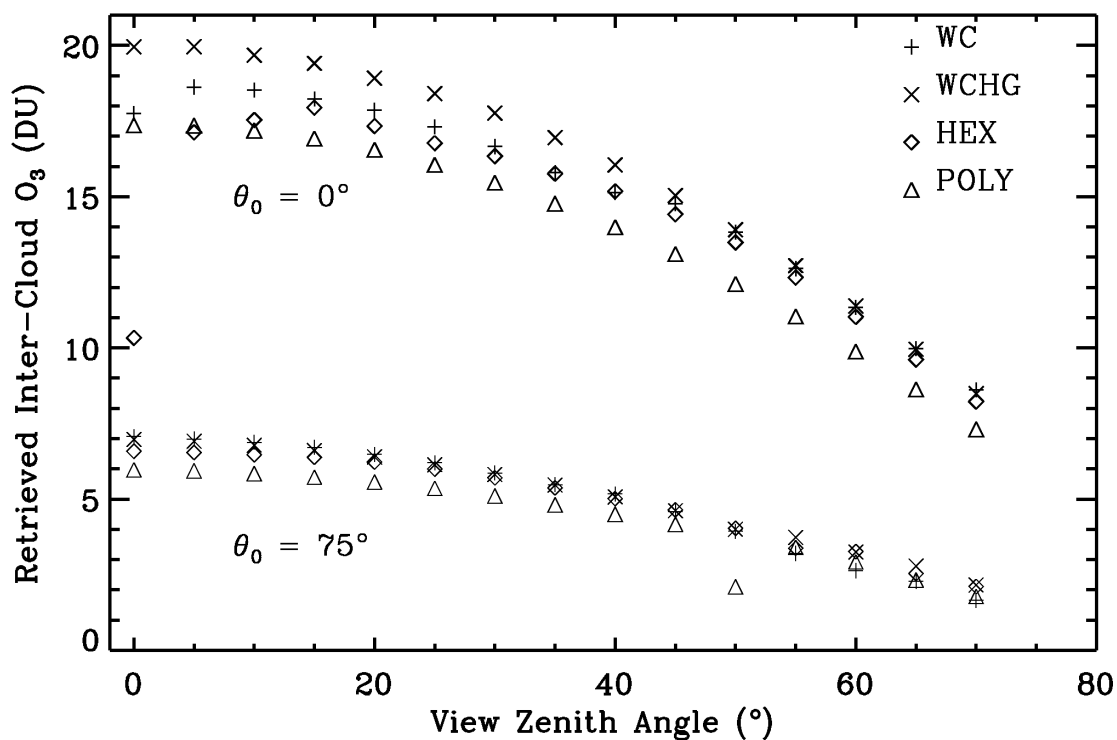


Figure 5.15 PPL and EICO as a function of SZA and VZA for a WC of COD 40 at 2–12 km. (a) PPL vs. SZA. (b) PPL vs. VZA. (c) and (d) same as (a) and (b) except for EICO. The low-latitude ozone profile L275 is used except that the 20.8 DU inter-cloud ozone is homogeneously distributed in the cloud.



**Figure 5.16** EICO as a function of VZA for a cloud of COD 40 at 2-12 km with different optical properties: WC (plus), WCHG (multiplier), HEX (diamond), and POLY (triangle) at SZA  $0^\circ$  and  $75^\circ$ . The low-latitude ozone profile L275 is used except that the 20.8 DU inter-cloud ozone is homogeneously distributed in the cloud.

phase function), the deeper the photons penetrate the cloud and therefore the larger the EICO will be. Although the same asymmetry factor is used for WC and WCHG, their difference in the ICOAEN effect arises primarily from the fact that the phase function for WCHG is smaller by a factor of five at scattering angle  $140^\circ$ – $180^\circ$ . Except for POLY, the highest EICO does not occur at nadir because of backscattering peaks in the corresponding phase functions. Especially for HEX, the EICO at nadir is only 10.3 DU because of the large backscattering peak in its phase function.

### 5.2.3.3 Cloud Optical Depth

Figure 5.17 shows the ICOAEN effect as a function of COD for a WC at 2-12 km at three sets of viewing geometries. The ozone profile is the same as in the base case except for different CODs (0.1, 0.5, 1, 2, 5, 8, 10, 20, 30, 40, 60, 80, 100, 150, 200, 300, 400, and 500). The EICO usually decreases with

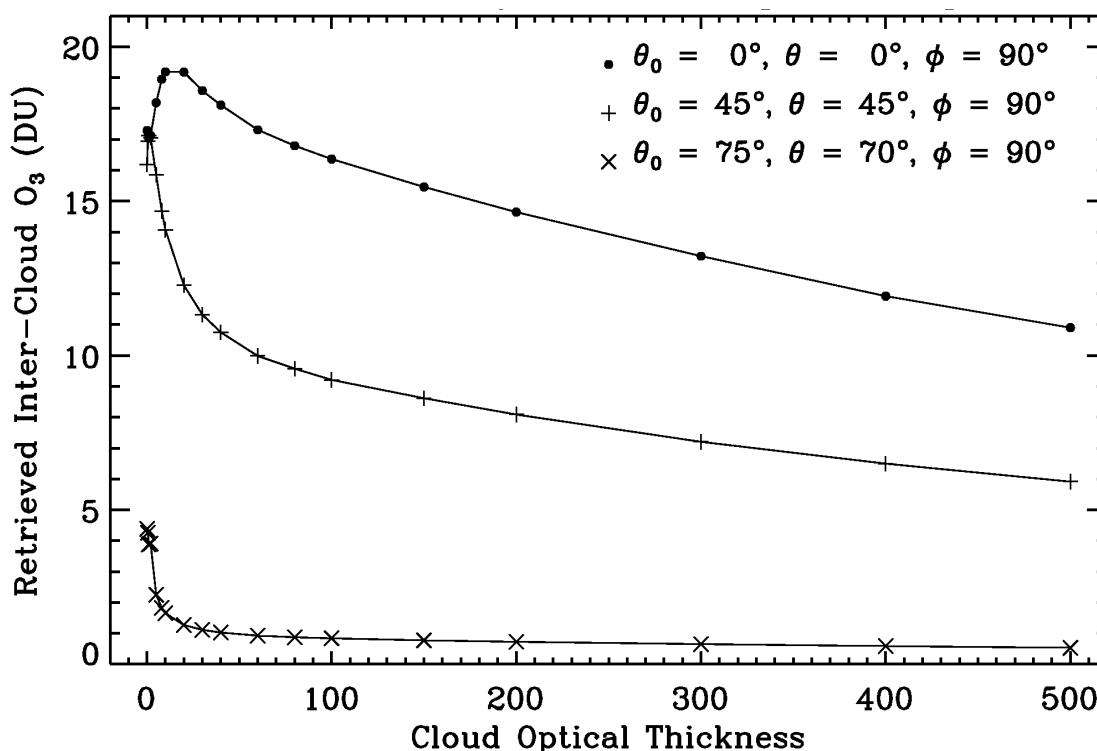


**Figure 5.17** EICO as a function of COD for a WC of 2-12 km at three sets of viewing geometries. The low-latitude ozone profile L275 is used except that the 20.8 DU inter-cloud ozone is homogeneously distributed in the cloud.

increasing COD except at small CODs. Those 2-12 km clouds with small CODs are not physical, but used for illustrating how the ICOAEN effect varies with COD. The neglect of polarization has very little effect on the ICOAEN effect. To reduce computation time, the polarization is not considered for COD greater than 100. At nadir, the EICO is about 11 DU at a COD of 500, which is  $\sim 60\%$  of the EICO with a COD of 40 but is still significant. With increasing viewing geometries, the EICO decreases more dramatically at smaller CODs and decreases less at larger CODs. At nadir, the largest EICO occurs at a COD of 10. Between zero and ten, the EICO increases with an increasing COD. Similarly, the PPL in the cloud first increases with an increasing COD, peaks at a COD of 10, and then decreases with an increasing COD. The EICO peak shifts to a smaller COD with increasing viewing geometry. The largest EICO occurs at a COD of 1 for  $\theta_0 = 45^\circ$  and  $\theta = 45^\circ$  and at a COD of 0.1 for  $\theta_0 = 75^\circ$  and  $\theta = 70^\circ$ . The EICO peak at some intermediate CODs is related to the imperfect ozone retrieval efficiency in the lower troposphere at near-ultraviolet wavelengths when the reflectivity is small [Hudson *et al.*, 1995; Klenk *et al.*, 1982]. When the

COD is very small, the cloudy atmosphere approaches a clear-sky atmosphere. The retrieved ozone for the case without ozone in the cloud is overestimated because the tropospheric part of the profile for simulation has less ozone than the TOMS standard ozone profile. The difference in the retrieved ozone between situations with and without ozone in the cloud is therefore reduced.

#### 5.2.3.4 Ozone Amount in the Clouds

Figure 5.18 (solid line) shows the ICOAEN effect as a function of Actual Inter-Cloud Ozone (AICO) for a WC at 2-12 km at three sets of viewing geometries. The ozone profile is the same as in the base condition except for different AICOs (5.2, 10.4, 15.6, 20.8, 26.0, 31.2, 36.4, and 41.6 DU). The ICOAEN effect is strongly dependent on the AICO, and the EICO is nearly linearly proportional to the AICO at the three viewing geometries. Figure 5.18 (dashed line) shows that the ratio of EICO to AICO

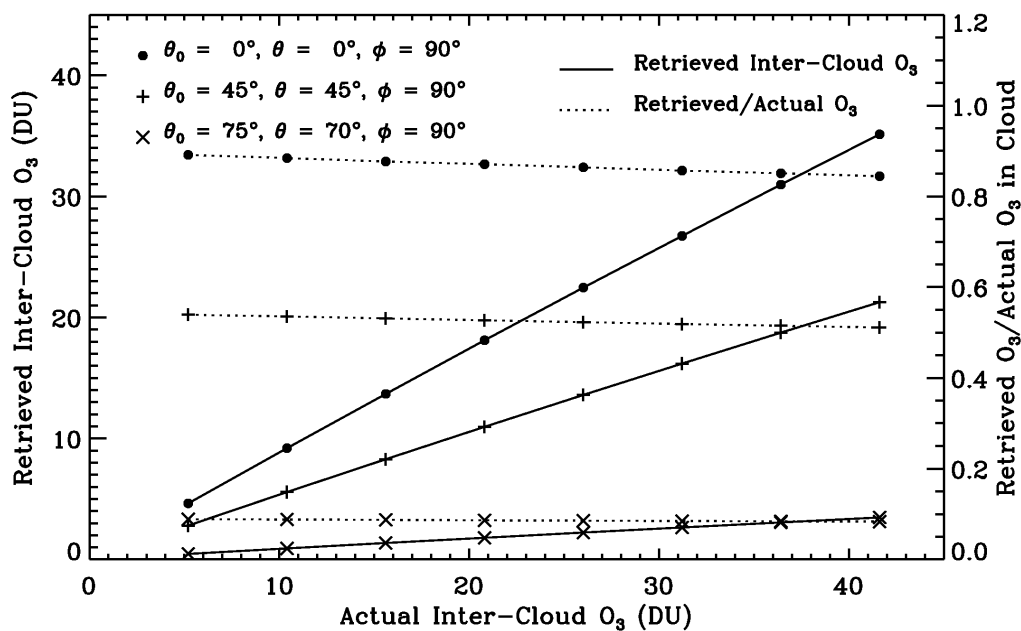


**Figure 5.18** EICO (solid) and the ratio of EICO to the AICO (dashed) as a function of AICO for a WC of 2-12 km at three sets of viewing geometries. The low-latitude ozone profile L275 is used except that the amount of ozone in cloud is as specified in the x-axis and homogeneously distributed in clouds.

slightly decreases with increasing AICO. For example, the ratio at nadir is 0.89 and 0.84 for a priori ozone of 5.2 DU and 41.6 DU, respectively. This variation with AICO is expected because the smaller the AICO, the deeper photons penetrate the cloud and the greater the ratio of EICO to AICO is.

### 5.2.3.5 Cloud Geometrical Depth

If the ozone profile does not change for different CGDs, the AICO increases with increasing CGD, so does the EICO according to Figure 5.18. Therefore, the ICOAEN effect is also greatly dependent on CGD. The larger the CGD, the larger the AICO and therefore the larger the EICO is.

Figure 5.19 shows the ratio of EICO to AICO as a function of CGD for a WC of COD 40 at three sets of viewing geometries. The ozone profiles are the same for different CGDs except that ozone is homogeneously distributed in the cloud. The ratio varies with GCD within 15%, largest for a cloud at 11-12 km (e.g., 0.95 at nadir view) and smallest for a cloud at 2-3 km (e.g., 0.81 at nadir view).

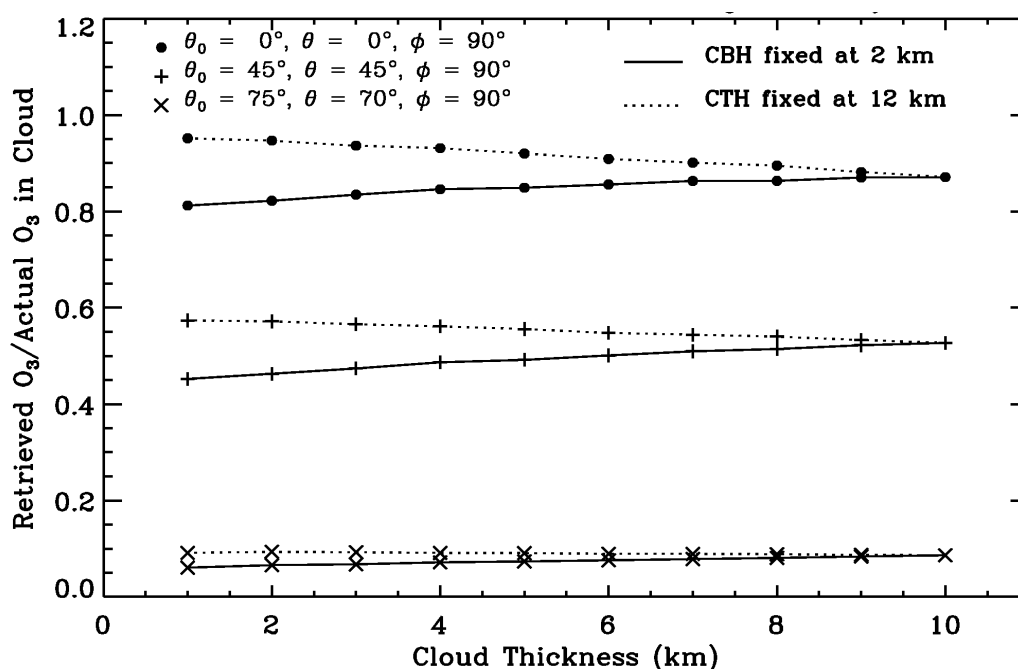


**Figure 5.19** The ratio of EICO to the AICO as a function of cloud thickness for a WC of COD 40 at three sets of viewing geometries. The low-latitude ozone profile L275 is used except that the amount of inter-cloud ozone is homogeneously distributed. Solid lines are for clouds with CBH fixed at 2 km and dashed lines are for clouds with CTP fixed at 12 km.

The solid lines in Figure 5.19 are for clouds with CBH fixed at 2 km. The larger the CGD, the higher the CTH, the smaller the cloud scattering coefficient, and the larger the AICO is. Figure 5.18 shows that the increasing ozone tends to slightly decrease the ratio of EICO to AICO. *Wu* [1985] found that oxygen absorption in the cloud at 0.7609  $\mu\text{m}$  and 0.7634  $\mu\text{m}$  (i.e., oxygen-A band) increases with increasing cloud scattering coefficient for the same COD. However, the ratio increases with increasing CTH even though the AICO and cloud scattering coefficient increases with increasing CTH. The increase of the ratio with increasing CTH is primarily a result of interaction between cloud reflection and Rayleigh scattering above the cloud. When the CTH is lower, there is more path length enhancement above the cloud because of the stronger Rayleigh scattering. For the case without ozone in the cloud, the radiance gain from lacking ozone in the cloud produces more absorption above the cloud for lower-altitude clouds. The difference in the retrieved ozone between situations with and without ozone relative to AICO increases with increasing CTH. The dashed lines in Figure 5.19 are for clouds with CTH fixed at 12 km. The larger the CGD, the lower the CBH, the smaller the cloud scattering coefficient, and the larger the AICO is. The ratio of EICO to AICO decreases with increasing CGD mainly because of the increasing AICO and decreasing cloud scattering coefficient.

#### 5.2.3.6 Ozone Distribution in the Clouds

Because photons emerging at the cloud-top can be backscattered from arbitrary regions in the cloud, the ICOAEN effect should be dependent on the ozone distribution in the cloud. We compare the ICOAEN effect for different ozone profiles in the clouds, and Figure 5.20 (a) shows seven ozone profiles in a 2-12 km cloud in terms of ozone absorption coefficient at 317 nm. These ozone profiles differ from each other only in the cloud and are the same as L275 outside the cloud. These profiles are as follows: (1) original L275, (2) constant ozone mixing ratio in the cloud, (3) ozone homogeneously distributed in the cloud, (4) linearly increasing ozone with altitude in the cloud, (5) linearly decreasing ozone with altitude in the cloud, (6) ozone homogeneously distributed in the upper 2 km of the cloud and elsewhere no ozone in the cloud, and (7) ozone homogeneously distributed in the lower 2 km of the cloud and elsewhere no ozone in the cloud. The AICO is 20.8 DU for the first 5 profiles, but only 4.2 DU for the last 2 profiles.

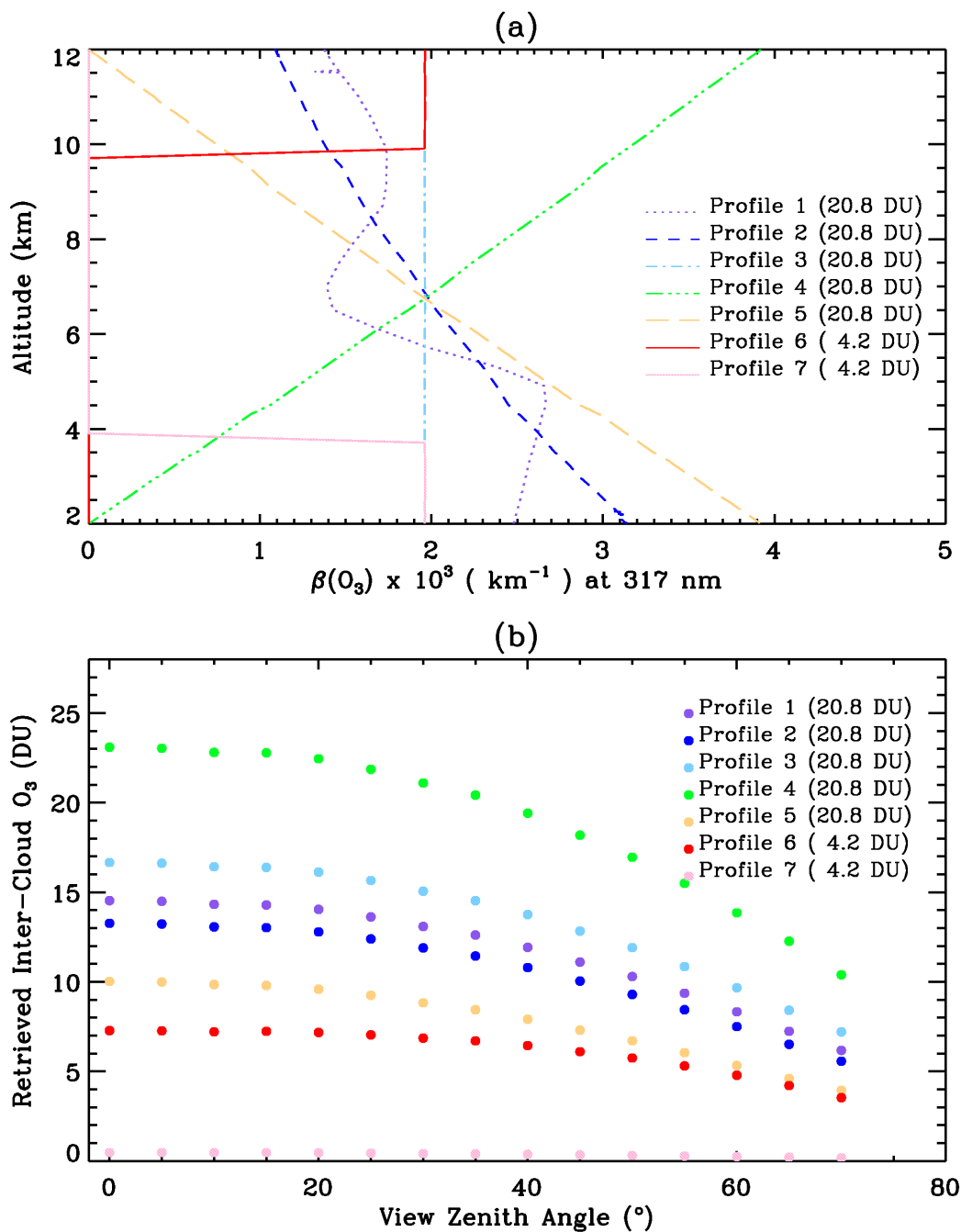


**Figure 5.20** (a) Ozone absorption coefficients vs. altitude for different inter-cloud ozone profiles: original L275 ozone profile (profile 1), well-mixed (profile 2), homogenous (profile 3), increasing ozone with altitude (profile 4), decreasing ozone with altitude (profile 5), homogeneous in the upper 2 km elsewhere no ozone (profile 6), and homogeneous in the lower part 2 km elsewhere no ozone (profile 7). Profiles 1-4 contain 20.8 DU ozone and profiles 6-7 contain 4.2 DU ozone. (b) Retrieved inter-cloud ozone vs. VZA at SZA 30° corresponding to the seven inter-cloud ozone profiles for WC of COD 40 at 2-12 km.

Figure 5.20 (b) shows the ICOAEN effect as a function of VZA for different ozone profiles at  $\theta_0 = 30^\circ$ . Exchanging VZA and SZA obtains the same EICO. A WC with a COD of 40 is positioned at 2-12 km. Among the first five profiles with 20.8 DU ozone in the cloud, the ICOAEN effect is highest for the linearly increasing ozone profile and smallest for the linearly decreasing ozone profile. At  $\theta = 0^\circ$ , the EICO is 14.5, 13.3, 16.7, 23.1, and 10.0 DU for profiles 1 to 5, respectively. The EICO for the original TOMS standard profile (profile 1) is smaller than for the homogeneous profile (profile 3) by 2 DU because less ozone is distributed in the upper part of the cloud in profile 1. The EICO for the well-mixed profile (profile 2) is smaller than those for profiles 1 and 3 for similar reasons. For the last 2 profiles, with 4.2 DU ozone in the clouds, the EICO at nadir is only 0.6 DU for profile 7 but is 8 DU for profile 6. Therefore, the ICOAEN effect is greatly dependent on ozone distribution in the clouds, and ozone distribution in the upper part of the clouds contributes more to the EICO. The vertical distribution of ozone absorption in the clouds will be investigated in detail in Section 5.2.3.9.

### 5.2.3.7 Atmospheric Ozone Profiles

Six profiles are selected to test the sensitivity of the ICOAEN effect to atmospheric ozone profiles: L225, L275, L325, M325, M375, and M425. The conditions are the same as those in the base case except for different ozone profiles. Latitudes used in ozone retrieval are  $0^\circ$  and  $45^\circ$  for low-latitude and mid-latitude ozone profiles, respectively. The ozone amounts in the cloud from these ozone profiles are 20.5, 20.8, 20.9, 31.8, 36.6, and 42.0 DU, respectively. Because the AICO is different for different ozone profiles, Figure 5.21 shows the ratio of EICO to AICO as a function of VZA for these ozone profiles at  $\theta_0 = 30^\circ$ . We can see that there is not much variation among these ozone profiles. The ratios are almost the same for the three low-latitude ozone profiles. The ratios of EICO to AICO for mid-latitude ozone profiles are slightly smaller than the corresponding ratios for low-latitude ozone profiles because there is more AICO in mid-latitude ozone profiles. Therefore, the ICOAEN effect varies with different ozone profiles mainly because of different AICOs. However, the ratio of EICO to AICO does not vary much for different ozone profiles.

### 5.2.3.8 N7 vs. EP TOMS Measurement Wavelengths

Figure 5.21 also shows the ratio of EICO to AICO as a function of VZA for EP TOMS measurement wavelengths. The model setups are the same as those in the base condition except that the radiances are calculated at EP TOMS channels. We can see that the ratio for EP TOMS is almost the same as that for N7 TOMS if other conditions are the same for both. Therefore, there is not much difference in the ICOAEN effect between N7 and EP TOMS data.

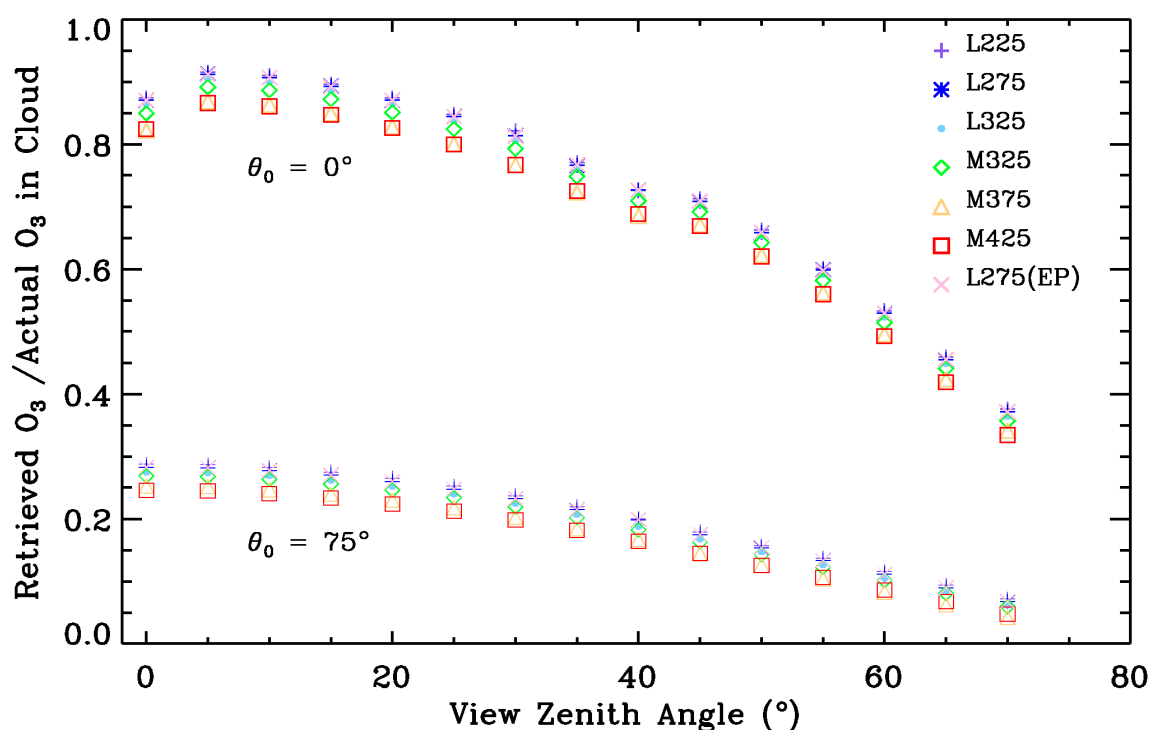


**Figure 5.21** The ratio of EICO to AICO vs. VZA for a WC of COD 40 at 2-12 km at SZA 0° and 75° using ozone profiles L225, L275, L325, M325, M375, M425, and L275 (at EP wavelengths).

### 5.2.3.9 Vertical Distribution of Ozone Absorption in the Clouds

As shown in Figure 5.20, the ICOAEN effect is significantly dependent on vertical distribution of ozone in the cloud. The method to obtain EICO also derives the vertical distribution of ozone absorption in the clouds. The cloud is divided into 20 layers and ozone is homogeneously distributed in the cloud. For

each cloud layer, two sets of radiances at 317 nm are calculated using PPGSRAD, one with ozone in the cloud except for that particular layer and the other with ozone in all layers. Using Equation (5.11), we obtain the effective ozone from all the other cloud layers (EICO'). The difference between EICO for the whole cloud and EICO' is the EICO contributed from that particular layer. The EICO of each cloud layer obtained in this way is underestimated compared to the actual contribution of that layer to the EICO because forcing ozone in one layer to be zero slightly increases ozone absorption in other layers. However, this underestimation is very small. For example, let us consider the base case (a WC of COD 40 at 2-12 km, L275). The sum of EICO for 20 cloud layers is only 3.1% smaller than the EICO for the whole cloud averaged over all the viewing geometry.

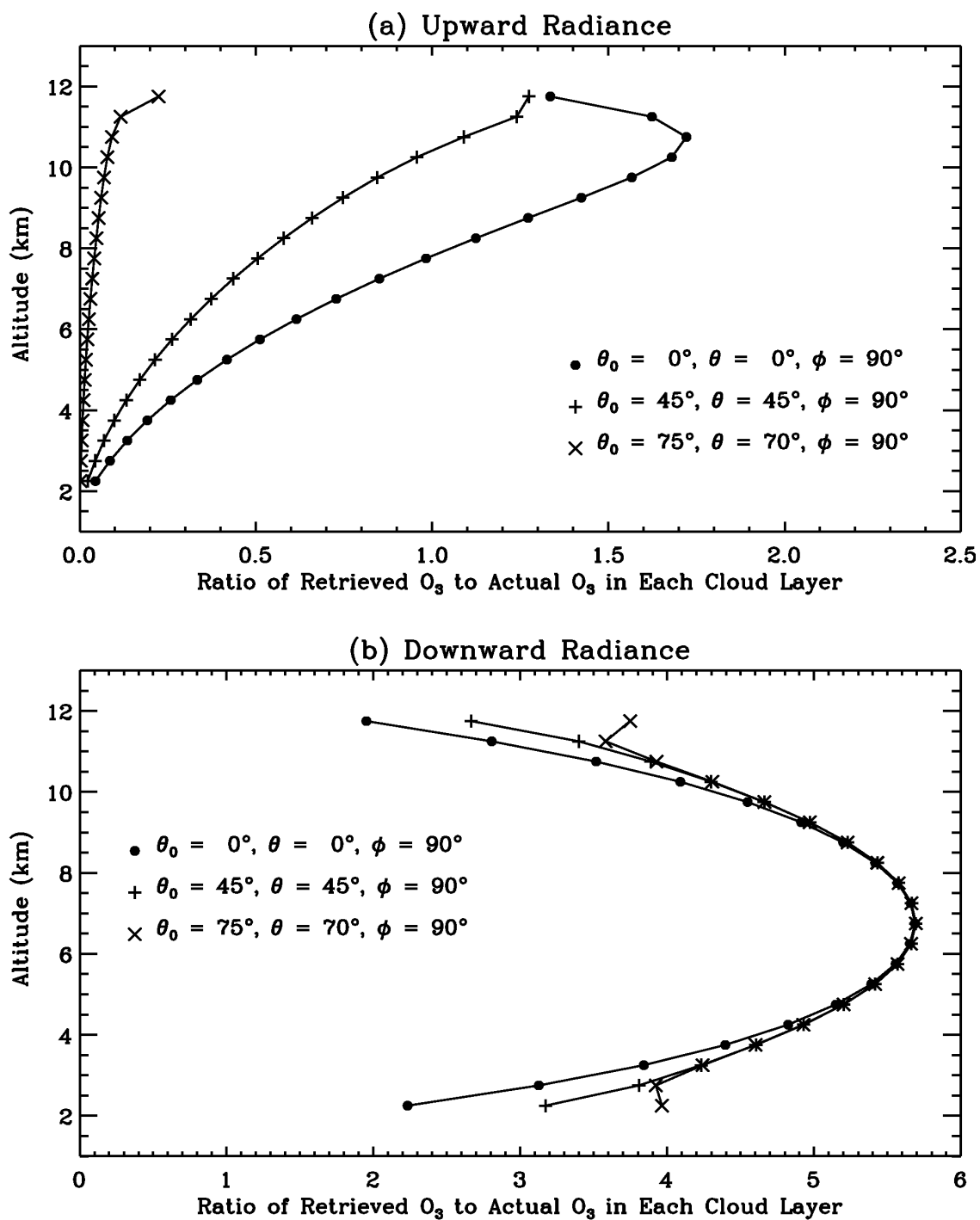
#### 5.2.3.9.1 Vertical Distribution of Ozone Absorption in the Cloud for the Base Condition

Figure 5.22 (a) shows vertical distributions of ratios of EICO to AICO in individual cloud layers for backscattered radiance at the base condition. The ratio peaks in the upper part of the cloud and the height of the peak increases with increasing viewing geometries. At larger viewing geometries, the ratio peaks in the top cloud layer, indicating that the resolution of 0.5-km cloud layer is not enough to resolve the exact peak altitude. Below the peak, the ratio decreases dramatically with decreasing altitude. At smaller viewing geometries, the ratio in the upper part of the cloud can be greater than 1 because of the enhanced ozone absorption. The ratio in the lower part of the cloud is much smaller than 1 because very few backscattered photons penetrate into the lower part of the cloud.

Figure 5.22 (b) shows similar vertical distributions of EICO ratios to AICO in individual cloud layers except for downward radiance. The EICO for downward radiance is similarly calculated based on the following equation instead of Equation (5.11):

$$\frac{I_{O_3}^\downarrow}{I_{no\ O_3}^\downarrow} = \exp(-\alpha_{\lambda, O_3} \Delta\Omega_{calc}), \quad (5.12)$$

where  $I_{O_3}^\downarrow$  and  $I_{no\ O_3}^\downarrow$  are the calculated downward radiances at ground surface with and without ozone in the clouds, respectively.  $\Delta\Omega_{calc}$  is the EICO as seen by ground sensors that measure downward radiances if



**Figure 5.22** Ratios of retrieved EICO to AICO in each 0.5-km cloud layer as a function of altitude for a WC of COD 40 at 2-12 km at three sets of viewing geometries. (a) Upward radiance. (b) Downward radiance. The ozone profile L275 is used except that 20.8 DU ozone is homogeneously distributed in the clouds.

the in-cloud multiple scattering in the retrieval is not taken into account. Equation (5.12) does not account for viewing geometry as Equation (5.11) does because the transmitted photons are illuminated at the cloud top and the PPL is almost independent of viewing geometry, especially for optically thick clouds [Kurosui *et al.*, 1997]. From Figure 5.22 (b), one can see that the ratio peaks in the middle part of the cloud. The altitude of the peak does not change with viewing geometry. The shapes of the vertical distributions are almost symmetrical around the peak and vary much less with viewing geometry. The ratios at all the layers are greater than 1, indicating that the enhancement for downward radiance is much larger than for upward radiance. The average ratio for the whole cloud at nadir is 4.5; i.e., the EICO is 4.5 times of the AICO. The main difference in the vertical distributions between upward and downward radiance arises primarily from the fact that photons transmitted to the ground have to penetrate through the cloud but photons backscattered to TOA penetrate different depths in the clouds.

Even if the ozone is not homogeneously distributed in the cloud, the vertical distributions of ratios shown in Figure 5.22 still hold as long as the absorber in the cloud is small. The EICO (both upward and downward) can be obtained based on the following equation for any arbitrary ozone distribution in the cloud:

$$EICO \approx \int_{h_{cb}}^{h_{ct}} enh(h)\rho(h)dh, \quad (5.13)$$

where  $enh(h)$  is the ratio of EICO to AICO at a certain height;  $\rho(h)$  is the ozone density at a certain height in the cloud ( $\text{DU m}^{-1}$ ); and  $h_{cb}$  and  $h_{ct}$  are the CBH and CTH, respectively. Because of homogeneous ozone distribution in the cloud, the vertical distributions of ratios are directly proportional to the vertical distributions of EICO. In addition, the EICO is proportional to the average PPL. And the average PPL equals to the product of the mean number of scattering events and mean photon free path length (the reciprocal of cloud scattering coefficient) in the cloud [Mayer *et al.*, 1998]. Therefore, the derived vertical distributions shown in Figure 5.22 also approximate the weightings for the mean number of scattering events for backscattered photons.

### **5.2.3.9.2 Vertical Distributions vs. Cloud optical Depth**

Figure 5.23 shows the vertical distributions of the retrieved ozone ratio to AICO for different CODs for backscattered radiance. A WC is positioned at 2-12 km and the same ozone profile L275 is used for different CODs. At small viewing geometry (Figure 5.23 (a)), the height and magnitude of the peak increases with increasing COD because of increasing in-cloud multiple scattering. Below the peak, the ratio decreases more dramatically with increasing COD because fewer backscattered photons penetrate the middle and lower parts of the cloud. At larger viewing geometry (Figures 5.23 (b) and (c)), we cannot see the variation of peak height and magnitude with COD because most of the peaks fall in the top 0.5-km cloud layer and are not distinguishable. However, we can clearly see that the ratio decreases with increasing COD in most of the cloud. The vertical distributions of ratios for different CODs explain why the EICO for the whole cloud usually decreases with increasing COD, as shown in Figure 5.17.

### **5.2.3.9.3 Vertical Distributions vs. Cloud Optical Properties**

Figure 5.23 also shows the vertical distributions of ozone absorption in the cloud for different COPs. A cloud of COD 40 is positioned at 2-12 km and the same ozone profile L275 is used for different COPs. The difference in the vertical distributions among different COPs is more easily seen at smaller viewing geometry (Figure 5.23 (a)). The distributions for WC and HEX are almost the same except that the ratio for HEX is slightly larger above the peak and slightly smaller below the peak than that for WC. The ratio for WCHG is greater than that for WC at each individual layer, especially in the upper part of the cloud. The peak for POLY is higher than that for the others. The ratio at each individual layer for POLY is larger in the upper part of the cloud but smaller in the middle and lower part of the cloud than that of the others. The comparison of the vertical distributions among different COPs supports their difference in the ICOAEN effect, as shown in Figure 5.16.

### **5.2.3.9.4 Vertical Distributions vs. Cloud Locations**

Figure 5.24 shows similar comparisons of vertical distributions of ozone absorption in the clouds for different cloud locations. A WC of COD 40 is positioned at different altitudes. Because the clouds are

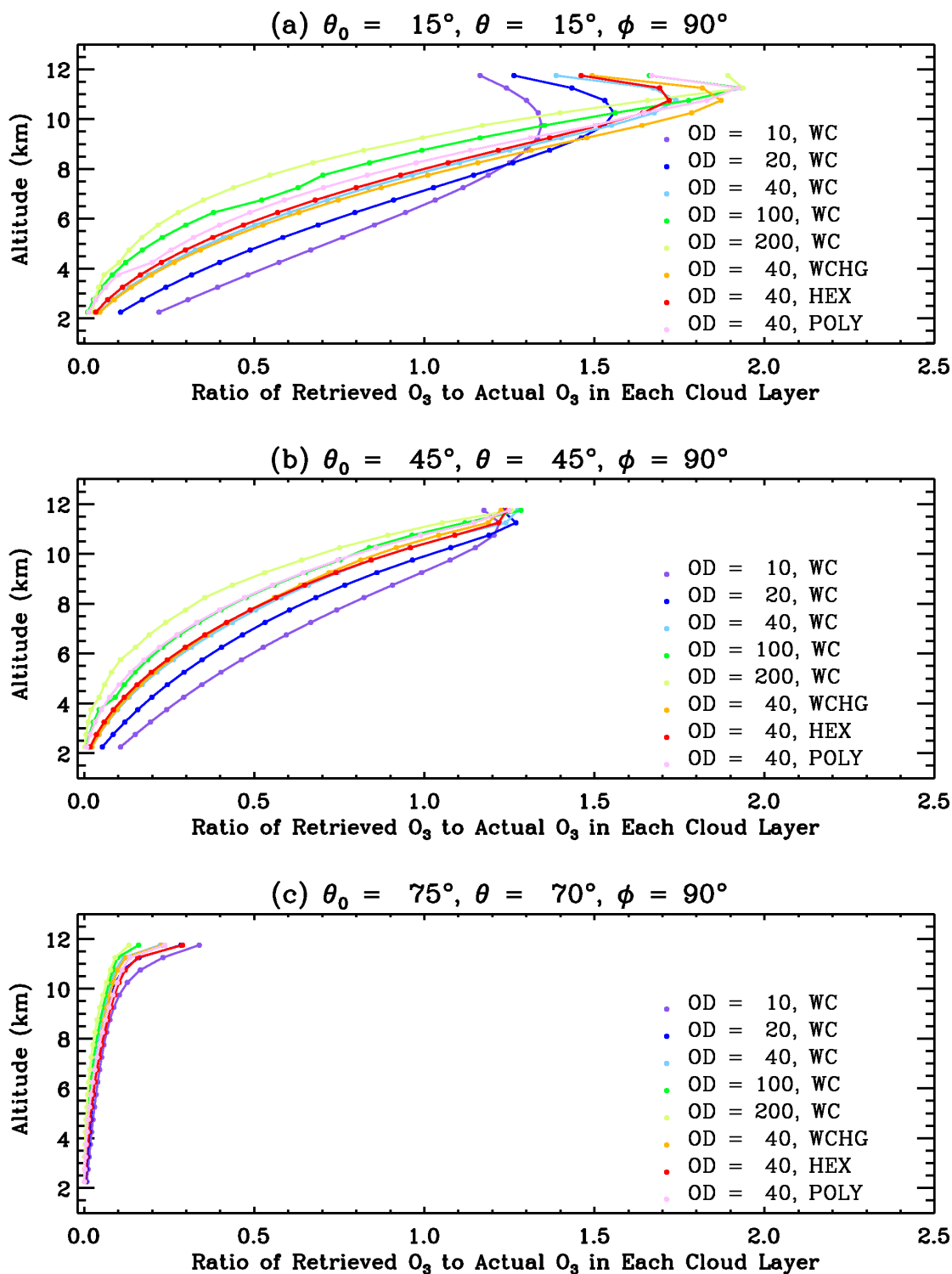


**Figure 5.23** Ratios of retrieved EICO to AICO in each 0.5-km cloud layer as a function of altitude for 2-12 km clouds with different COD and COPs at three sets of viewing geometries. The ozone profile L275 is used except that ozone is homogeneously distributed in the clouds.

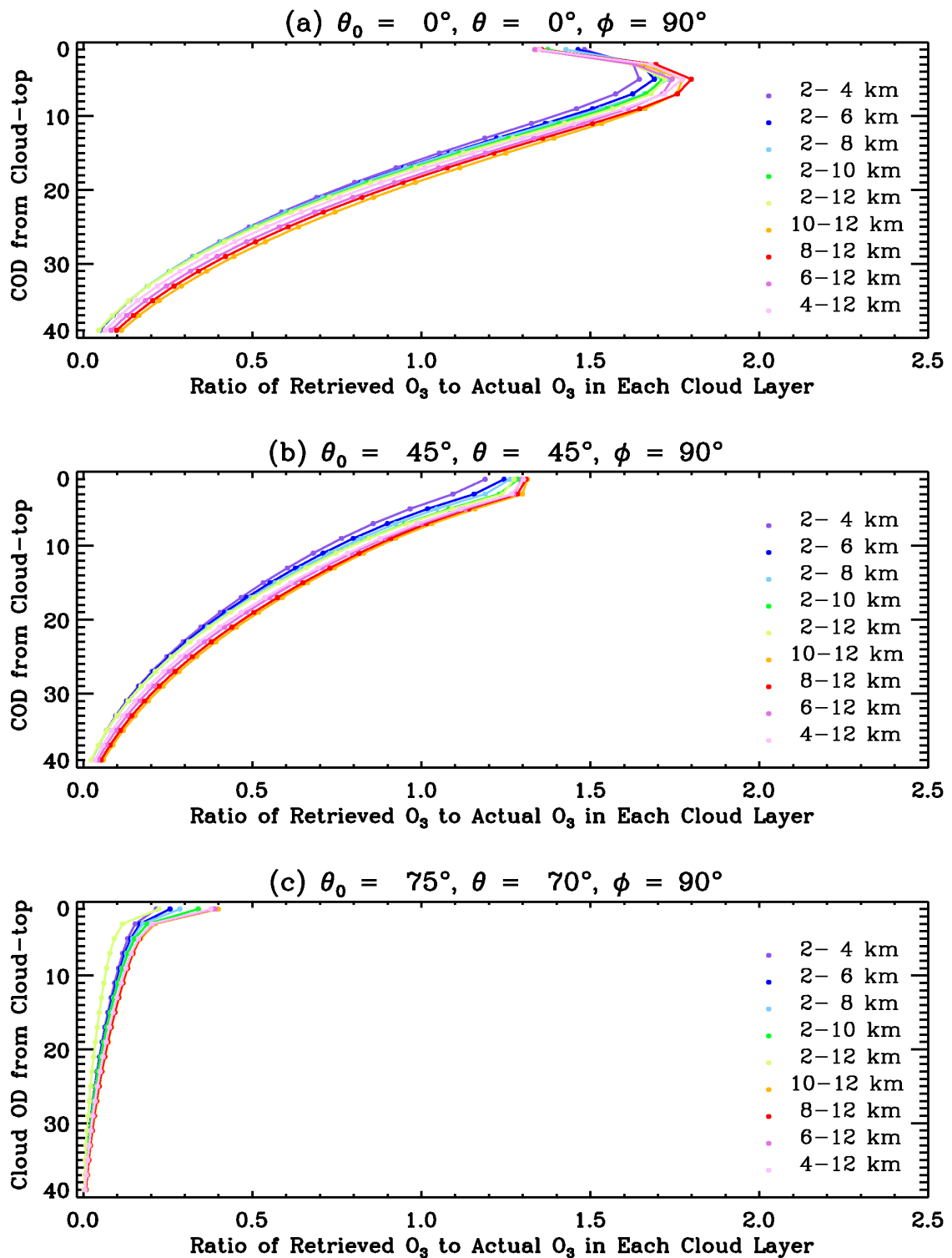
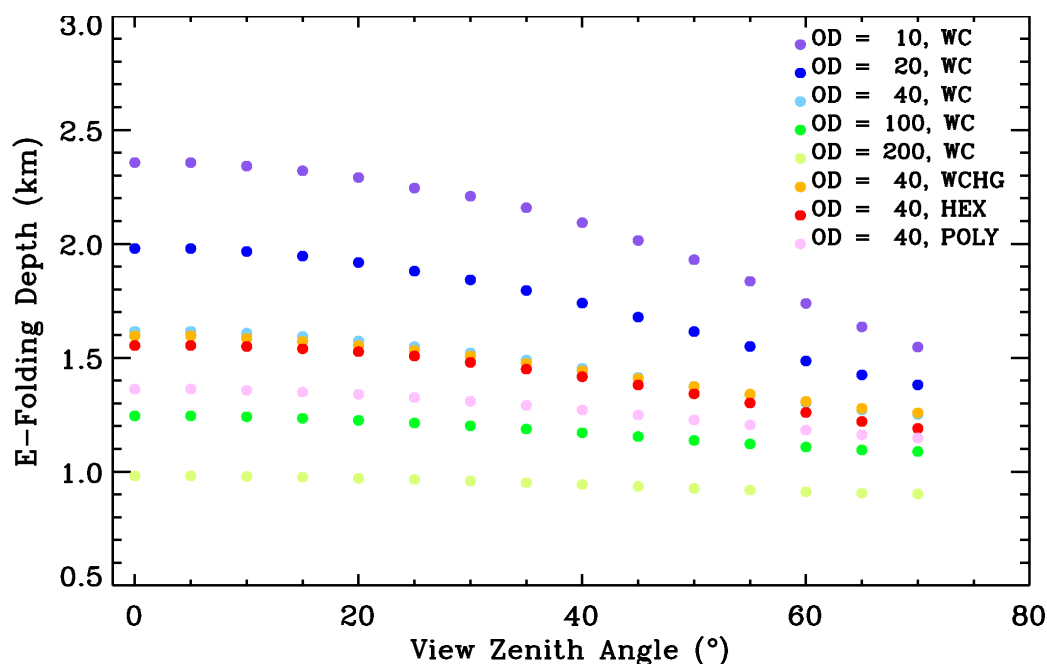


Figure 5.24 Same as Figure 5.23 except for WCs of COD 40 at different locations.

at different altitudes, the results are shown as a function of COD from cloud top instead of altitude. The ozone profile L275 is used except for homogeneous ozone distribution in the cloud. For those clouds with CBH fixed at 2 km, the ratio usually slightly increases with increasing CTH, especially in the upper part of the cloud. For those clouds with CTH fixed at 12 km, the ratio usually slightly increases with increasing CBH, especially in the lower part of the cloud. The difference in the vertical distributions among various cloud locations is consistent with the variation in the ICOAEN effect with cloud locations, as shown in Figure 5.19.

### 5.2.3.9.5 E-folding Depth

An “E-folding Depth” (ED) is defined as the depth from cloud top above which ozone absorption occupies  $1/e \approx 36.8\%$  of the total ozone absorption in the cloud. This ED approximately represents how



**Figure 5.25** E-folding depth as a function of VZA for a 2-12 km WC with different CODs and COPs at SZA 30°. The L275 is used excepted that ozone is homogeneously distributed in the clouds.

deeply backscattered photons can penetrate the cloud, and it can be used to compare the average penetration depth of backscattered photons for different conditions. One way to get the average photon penetration depth is to trace each photon using a Monte Carlo radiative transfer code.

Figure 5.25 shows the ED as a function of VZA for different CODs and COPs at  $\theta_0 = 30^\circ$ . The ED decreases with increasing VZA. The smaller the ED, the less the ED varies with VZA. The larger the COD is, the smaller the ED, and the shallower photons penetrate in the cloud. For example, the ED at  $\theta = 0^\circ$  is 2.36 km for a WC of COD 10, but it is only about 0.98 km for a WC of COD 200. The ED increases with increasing asymmetry factor. At  $\theta = 0^\circ$ , the ED for WC, WCHG, HEX, and POLY of COD 40 is 1.61, 1.59, 1.56, and 1.38 km, respectively. Note that the ED is not proportional to the EICO for a fixed AICO. At  $\theta = 0^\circ$ , the ED for a WC of COD 200 is 2.5 times that for a WC of COD 10, but the EICO for a WC of COD 200 is only 1.26 times that for a WC of COD 10. This relationship occurs because ozone enhancement in the upper part of the cloud is larger for a larger COD.

#### 5.2.3.10 Summary for the ICOAEN Effect

Because backscattered photons penetrate the cloud, ozone absorption occurs in the cloud. The sensor can see the actual ozone absorption in the cloud, causing an error in the retrieved TOC because of the assumption of opaque clouds and the added OZBC to complete the TOC. The triplet method used in the TOMS V7 algorithm cannot reduce this error. The ICOAEN effect depends significantly on viewing geometry, ozone amount in the clouds, ozone distribution in the clouds, and CGD, and it depends slightly on COD, cloud location, and COP.

The EICO decreases with increasing VZA or SZA and is azimuthally independent. The EICO near nadir is almost equal to the AICO so that the sensor effectively can see almost all the ozone in the cloud. At larger viewing geometry (e.g.,  $\theta_0 = 75^\circ$ ,  $\theta = 65^\circ$ ), the EICO is close to 0. The EICO is almost directly proportional to the AICO. The more ozone there is in the cloud, the larger the EICO. However, the ratio of EICO to AICO decreases slightly with increasing AICO. The EICO usually increases with increasing CGD because the AICO usually increases with GCD. The ICOAEN effect varies with different atmospheric ozone profiles due primarily to the fact that the amount of ozone in the cloud varies. Ozone distribution in the cloud plays a significant role in determining the EICO. Assuming a fixed amount of

ozone in the cloud, the EICO is much larger for distributions with more ozone in the upper part of the cloud than for distributions with more ozone in the lower part of the cloud. The ratio of EICO to AICO in a cloud layer peaks in the upper part of the cloud and then dramatically decreases with decreasing altitude below the peak. At smaller viewing geometry, the ratio of EICO to AICO in the upper the cloud can be greater than 1 because of enhanced ozone absorption by in-cloud multiple scattering. Because much fewer backscattered photons penetrate deep into the cloud, the ratio in the lower and middle part of the cloud is much less than 1.

The EICO varies slightly with different COPs. The smaller the asymmetry factor is for cloud particles, the smaller the EICO. Assuming high-altitude clouds as ice clouds only slightly decreases the ICOAEN effect. The ICOAEN effect usually decreases with increasing COD. For COD increases from 10 to 500 for a WC at 2-12 km with 20.8 DU homogeneously distributed in the cloud, the EICO at nadir decreases from about 18 DU to about 11 DU. Assuming the same AICO in the cloud, the ICOAEN effect slightly increases with increasing CTH for fixed CBH because of the interaction between Rayleigh scattering and ozone absorption above clouds, and slightly increases with decreasing CBH for fixed CTH because of the decreasing cloud scattering coefficient. The ICOAEN effect is expected to be the same in both EP and N7 TOMS data.

#### **5.2.4 Effect of Below-Cloud Ozone Absorption**

The method used to obtain the BCOA effect is similar to the method to obtain the ICOAEN effect except that we calculate two sets of radiances, with and without ozone below the cloud-bottom using PPGSRAD. Figure 5.26 shows the BCOA effect as a function of VZA for several cloudy conditions at  $\theta_0 = 30^\circ$ . Similar to the ICOAEN effect, the SZA and VZA are exchangeable for the BCOA effect. The TOMS standard profile L275 is used, and WC of different CODs and CGDs are positioned at different altitudes. When the BCOA effect is significant, it greatly depends on the viewing geometry and decreases with increasing viewing geometry, as the ICOAEN effect. Among these different cloudy conditions, the BCOA effect is largest for a WC of COD 1 at 11-12 km, in which 17.1 DU out of 24.1 DU AICO can be seen at the nadir view. The BCOA effect is smallest for a WC of COD 40 at 2-3 km, in which almost no ozone can be seen at the nadir view. The BCOA effect largely decreases with increasing COD. The measured OZBC

is only about 1.3 DU for a WC of COD 40 at 11-12 km. For clouds with the same COD, the BCOA effect increases with increasing CBH, because the amount of ozone below the cloud-bottoms increases. The ratio of measured ozone to actual ozone below the cloud-bottoms decreases with decreasing CBH. For example, the ratio is about 0.71 at the nadir view (e.g., 17.1 DU out of 24.1 DU) for a WC of COD 1 at 11-12 km but about 0.26 at the nadir view (e.g., 1.3 DU out of 5.0 DU) for a WC of COD 1 at 2-3 km. Because of more interaction among Rayleigh scattering, cloud reflection, and surface reflection below the cloud-bottom with lower CBH, photons that penetrate through the cloud have a smaller possibility of being backscattered to TOA.

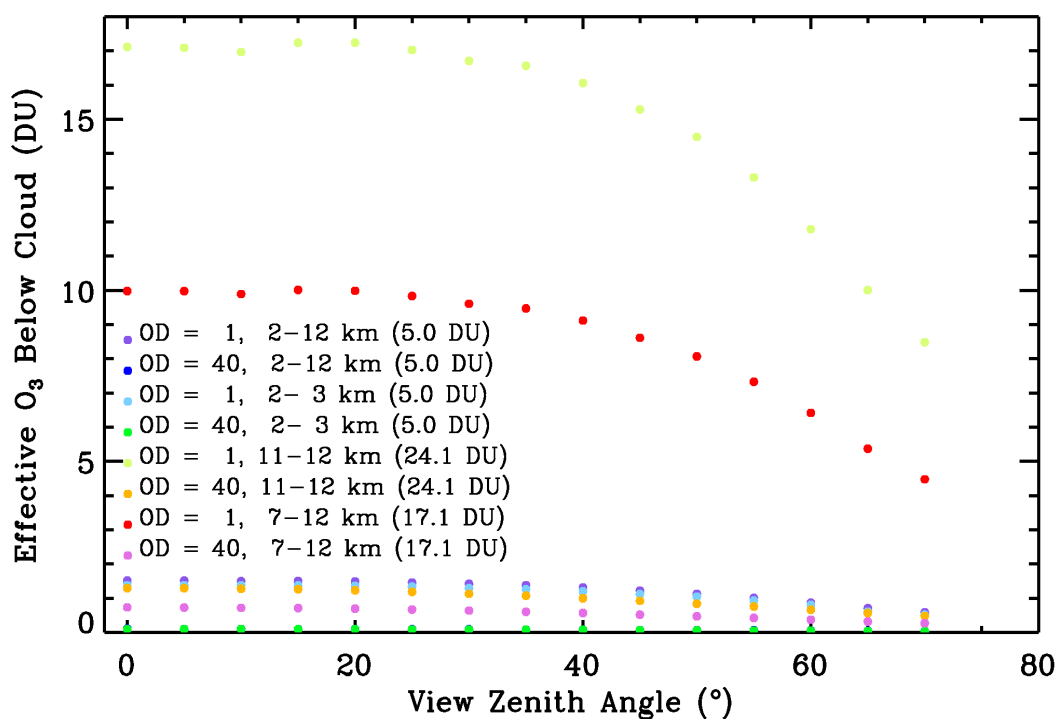


**Figure 5.26** Effective ozone below cloud bottoms as a function of VZA for WC with different CODs and cloud locations at SZA 30°. The low-latitude ozone profile L275 is used.

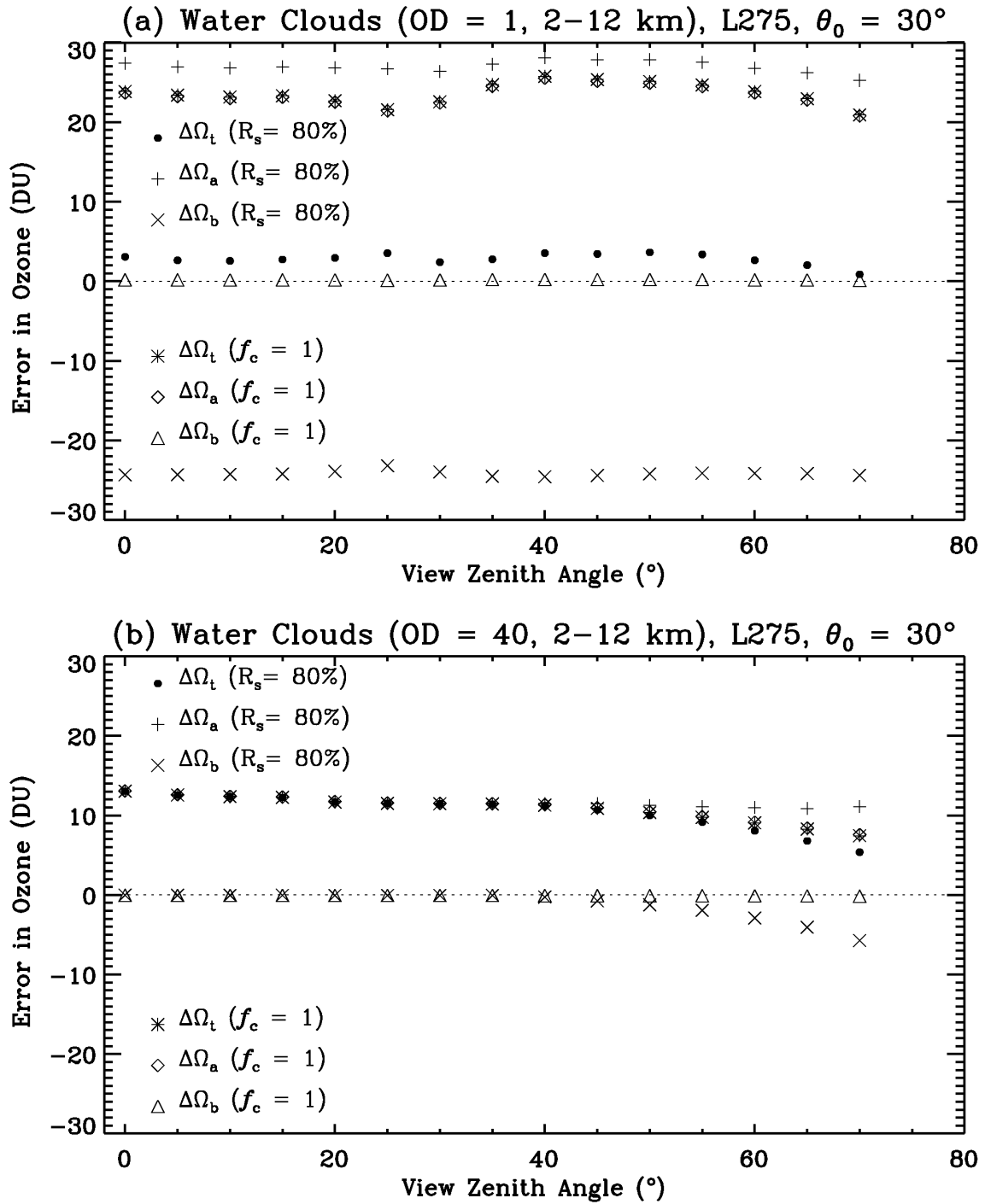
The BCOA effect is mainly dependent on the amount of ozone below the cloud-bottom and COD as well because the COD determines the number of backscattered photons that penetrate through the cloud.

For optically thick clouds, very few photons penetrate through the cloud and the BCOA effect is small. The BCOA effect becomes significant only when the cloud is optically thin and the amount of ozone below cloud-bottoms is large.

### 5.2.5 Overall Ozone Retrieval Errors Associated with Clouds

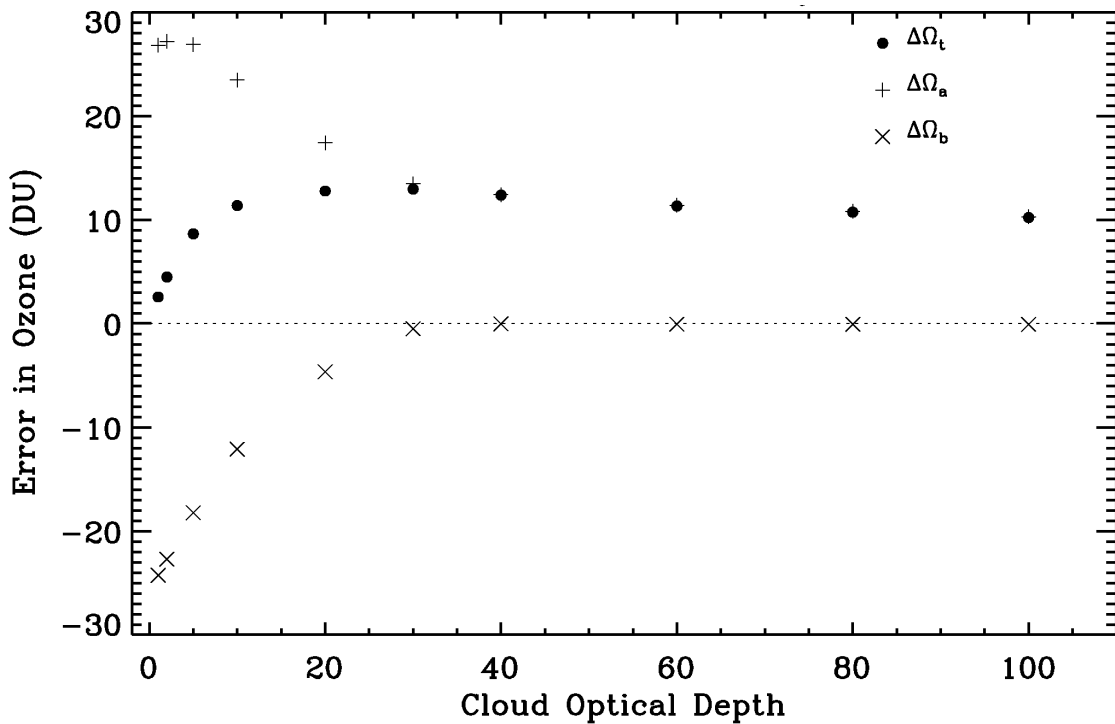
Ozone retrieval errors due to the Lambertian, PCM, ICOAEN, and BCOA effects are studied in detail in Sections 5.2.2 through 5.2.4. This section investigates the overall OREs associated with clouds (i.e., the sum of the four effects). We focus on the essential effects associated with clouds, the effects that are primarily responsible for OREs. We also investigate whether the assumption of MFCR as 80% used in the TOMSV7 PCM is good or not. To illustrate the answers to the above questions, errors in the ozone are compared between two retrievals, one using the TOMS V7 algorithm and the other using the modified TOMS V7 algorithm. The first retrieval uses the TOMS V7 PCM to derive the ECF, and the second retrieval forces the ECF to be the a priori cloud fraction (i.e., use the correct cloud fraction). The first retrieval includes all the four effects on ozone retrieval. The second retrieval includes the Lambertian, ICOAEN, and BCOA effects on ozone retrieval, and the PCM effect is zero. Because very little knowledge is available about the ozone amount and distribution in the clouds, the TOMS standard ozone profile L275 is used.

Figure 5.27 (a) shows OREs from the two retrievals as a function of VZA at  $\theta_0 = 30^\circ$  for a WC of COD 1 positioned at 2-12 km. Although it is unreasonable to have such a cloud with COD 1 spanning over 10 km, the selection of this cloud is to compare with the base case -- a WC of COD 40 at 2-12 km. It will be shown later that the conclusions drawn from this cloud apply to other reasonable clouds as well. Errors in the TOC are very small using the TOMS V7 algorithm (circle) but are largely positive using the correct cloud fraction (asterisk). Using the TOMS V7 algorithm, errors in OZAC (plus) are about 20-30 DU, primarily because of the ICOAEN, Lambertian, and PCM effects, and errors in OZBC (multiplier) are about -25 DU due primarily to the PCM effect. Largely positive errors in OZAC and largely negative errors in OZBC tend to cancel each other, leading to the approximately correct TOC. Using the correct cloud fraction, errors in OZAC (diamond) are similar to those using the TOMS V7 algorithm, and the



**Figure 5.27** Comparison of retrieved total ozone between using the TOMS V7 algorithm ( $R_s = 80\%$ ) and forcing the ECF to be the same as the FCF ( $f_c = 1$ ) at SZA  $30^\circ$ . (a) For a WC of COD 1 at 2–12 km. (b) For a WC of COD 40 at 2–12 km. The low-latitude ozone profile L275 is used. The  $\Delta\Omega_t$ ,  $\Delta\Omega_a$ , and  $\Delta\Omega_b$  indicate the error in total ozone, error in OZAC, and error in OZBC, respectively.

errors in OZBC (triangle) are almost zero. The overall errors in TOC are therefore largely positive. Figure 5.27 (b) shows results similar to Figure 5.27 (a) but for COD 40. At COD 40, the derived ECF is mostly one or very close to one. Therefore, errors in ozone using these two retrievals converge. Errors in OZBC are almost zero for both retrievals except that when the derived ECF is significantly less than 1 using the TOMS V7 algorithm, errors in OZBC are negative. Errors in OZAC are about 10-13 DU due primarily to the ICOAEN effect. The overall errors in TOC are, therefore, largely positive due primarily to the ICOAEN effect. Note that the ICOAEN effect decreases dramatically, increasing with viewing geometry, and the overall OREs in TOC decrease with increasing SZA and VZA for optically thick clouds. For example, the ORE is about 16 DU at  $\theta_0 = 0^\circ$  and  $\theta = 0^\circ$  and about 3 DU DU at  $\theta_0 = 75^\circ$  and  $\theta = 70^\circ$ .



**Figure 5.28** Errors in total ozone (circle), OZAC (plus), and OZBC (multiplier) as a function of COD at SZA  $30^\circ$  and VZA  $30^\circ$  for 2-12 km water clouds. The low-latitude ozone profile L275 is used.

Figure 5.28 shows errors in TOC using the TOMS V7 algorithm for clouds at 2-12 km with different CODs at  $\theta_0 = 30^\circ$  and  $\theta = 30^\circ$ . With increasing COD, negative errors in OZBC decrease dramatically in magnitude because of the increasing ECF in the retrieval; positive errors in OZAC decrease relatively less in magnitude because the ICOAEN effect varies slowly with COD. Errors in TOC first increase with increasing COD until the COD reaches 20-40 when the PCM effect is close to zero, and then slightly decrease with increasing COD because the ICOAEN effect slightly decreases with increasing COD. Figure 5.29 shows errors in TOC for COD 1 but for clouds at 2-3 km, 2-12 km, and 11-12 km, respectively. In addition to the two retrievals, Figure 5.29 also shows errors for retrievals by assuming MFCR as 40% and 100%, respectively. We can see that errors for more reasonable clouds at 2-3 km and 11-12 km are similar to those for the cloud at 2-12 km: errors in TOC are largely positive using the correct cloud fraction and relatively small using the TOMS V7 algorithm. But the positive errors in TOC are due primarily to the Lambertian effect for the 2-3 km cloud and due primarily to the BCOA effect for the 11-12 km cloud. Assuming MFCR as 100% does not improve the ozone retrieval much compared to using the TOMS V7 PCM. The errors assuming MFCR as 40% lie between those using the TOMS V7 PCM and the correct cloud fraction because the derived ECFs lie between those from the two retrievals.

According to the above results, the assumption of MFCR to be 80% in the TOMS V7 algorithm (i.e., the TOMS V7 PCM) is very good because the negative PCM effect offsets other positive errors to reduce the overall error. Especially for clouds with smaller CODs, the assumption of MFCR to be 80% leads to the approximately correct results. The combination of ICOAEN, BCOA, and Lambertian effects causes largely positive errors in the TOC. However, assuming MFCR as 80% significantly underestimates the cloud fraction in the retrieval and leads to largely negative errors (i.e., significant PCM effect). It is because of the compensating errors among ICOAEN, BCOA, Lambertian, and PCM effects that the TOMS V7 algorithm retrieves the approximately correct TOC. The neglect of photon penetration in the clouds in the assumption of opaque cloud surface is partly compensated for by partial clear-sky conditions. If the a priori cloud fraction is used in the retrieval, the directly retrieved OZAC effectively includes most of the ozone below the cloud because of the opaque and Lambertian effects, and the OZBC is also added to complete the TOC because of the assumption of opaque clouds. Therefore, a significant portion of the ozone below the clouds is included twice in the TOC, leading to largely positive errors. With increasing

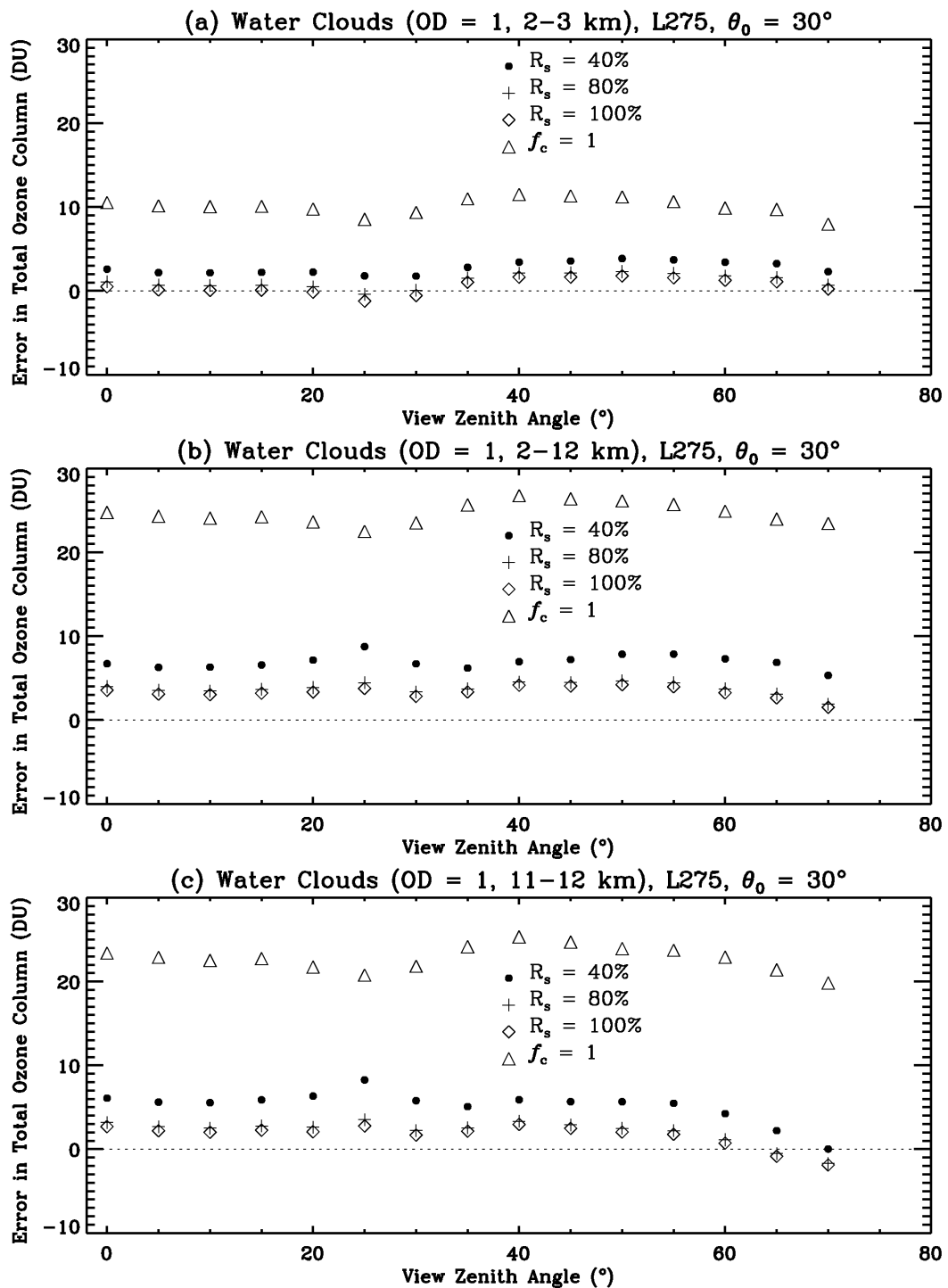


**Figure 5.29** Comparison of retrieved errors in total ozone vs. VZA among assuming minimum full cloud reflectivity as 40%, 60%, 80% (i.e., the TOMS V7 algorithm), 100%, and forcing the ECF to be 1 for a WC of COD 1 with different cloud locations at SZA  $30^\circ$ . (a) A 2-12 km cloud. (b) A 2-3 km cloud. (c) A 11-12 km cloud. The low-latitude ozone profile L275 is used.

COD, the negative PCM effect and the positive Lambertian effect decrease dramatically, but the positive opaque effect varies relatively slowly.

Therefore, positive errors in TOC increase with increasing COD until the PCM and Lambertian effects do not change much at COD 20-40; then the positive errors decrease slowly because the ICOAEN effect slowly decreases with increasing COD. However, even at COD 100, significant errors in TOC as large as 12 DU occur at nadir because a portion of the ozone in the cloud is included twice in the TOC. Note the above results subject to change if the actual inter-cloud ozone amount and distribution are very different from the assumed ones (i.e., using the TOMS standard ozone profiles).

### 5.3 Ozone Retrieval Errors Associated with Partial Clouds

For all the results in Section 5.2, the forward cloud is assumed to be fully cloudy. This section briefly discusses OREs associated with forward partial clouds. To simulate radiances for forward partial clouds, we employ the independent pixel approximation consistent with the TOMS V7 algorithm. The radiance for a partial cloud of cloud fraction  $f_c$  is the fraction-weighted sum of the radiances for a clear sky of ground reflectivity 8% and a cloudy sky of COD  $\tau$ ,

$$I(f_c, \tau, P_c) = I(\tau, P_c) \times f_c + I(R_g = 8\%, P_g) \times (1 - f_c). \quad (5.14)$$

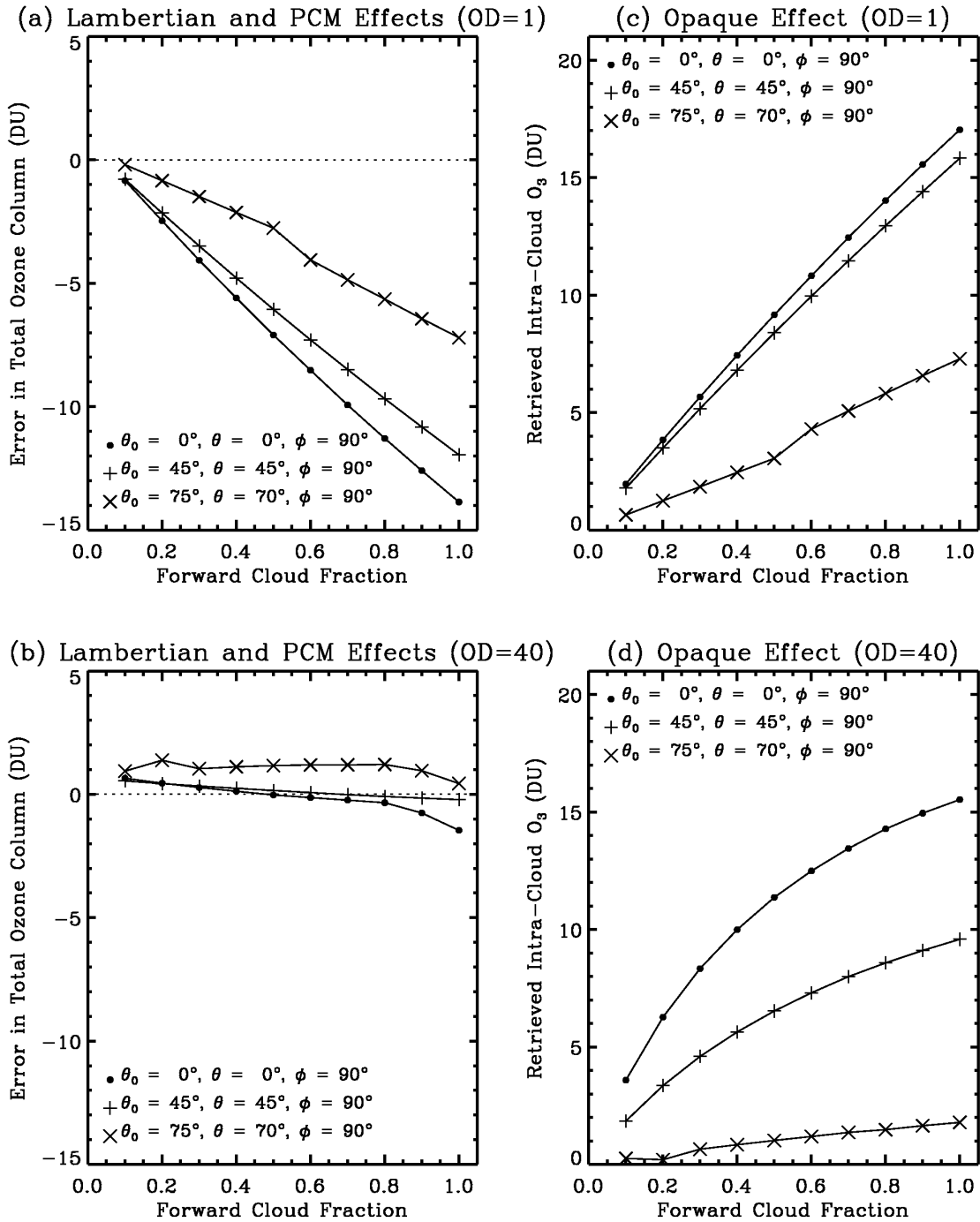
The methods to obtain the Lambertian, PCM, ICOAEN, and BCOA effects for such forward partial clouds are similar to those for forward full clouds. If we simulate the radiances for partial clouds according to Equation (5.14) without ozone in the cloud, the difference between the retrieved ozone using the TOMS V7 algorithm and the forward input ozone indicates the sum of Lambertian and PCM effects. The Lambertian effect can be obtained similarly, except forcing the ECF to be consistent with the FCF in the ozone retrieval. The sum of Lambertian and PCM effects minus the Lambertian effects gives the PCM effects. The difference in the retrieved ozone from the simulated radiances for partial clouds with and without inter-cloud ozone indicates the ICOAEN effect, and the difference in the retrieved ozone with and without ozone below cloud bottoms indicates the BCOA effect.

Figure 5.30 shows the Lambertian-PCM effect (left) and the opaque effect (right) for a 2-12 km cloud of COD 1 and 40, respectively. We can see that errors in TOC due to these different effects are proportional to FCF when errors for forward full clouds are significant. The nonlinear relationship between EICO and FCF for COD 40 is due to the large difference in the radiance between clear and cloudy conditions. Figure 5.31 shows the same results as Figure 5.30 but for a 2-3 km cloud. Similarly, there is a well-defined behavior between different effects and the FCF. Because all these effects are approximately proportional to the FCF, it is expected that the overall OREs are approximately the corresponding values for full clouds weighted by the FCF. Figure 5.32 illustrates this relationship between OREs and viewing geometry for a range of FCF. This figure compares errors associated with clouds in TOC between using the TOMS V7 algorithm and the modified algorithm (i.e., forcing the ECF to be FCF) for partial water clouds of COD 1 at (a) 2-12 km and (b) 2-3 km, respectively. The results are shown for five FCFs: 0.2, 0.4, 0.6, 0.8, and 1.0. Similar to the results for forward full clouds, errors for forward partial clouds are significantly positive using the correct cloud fraction, and are almost correct using the TOMS V7 algorithm. Errors in TOC increase in magnitude with increasing FCF.

It holds true that the assumption of MFCR as 80% in the ozone retrieval (i.e., the TOMS V7 PCM) is very good for partial clouds. The good results occur at small CODs because of the compensating positive Opaque and Lambertian effects and negative PCM effect. At CODs larger than 20-40, the Lambertian and PCM effects are negligible and the positive ICOAEN effect dominates, especially at small viewing geometry. The overall OREs at larger CODs are positive but decrease with decreasing FCF.

#### **5.4 Possibility of Directly Correcting Ozone Retrieval Errors Associated with Clouds**

When the COD is small, the negative PCM effect can offset other positive errors, leading to overall small OREs in the ozone retrieval. At larger COD when the PCM effect becomes small, the ICOAEN effect dominates the ozone retrieval errors associated with clouds. The Lambertian effect at those CODs depends on cloud properties (e.g., COD, CTH, COP) in addition to viewing geometry. To correct the Lambertian effect for accurate ozone retrieval, one needs to know CODs and COPs that are not usually available in TOMS data. Fortunately, the Lambertian effect is usually within the TOMS retrieval precision of total ozone. Then the OREs may largely result from the ICOAEN effect. At a certain viewing



**Figure 5.30** Lambertian-PCM and opaque effects as a function of FCF at three sets of viewing geometries for 2-12 km WC. (a) Lambertian-PCM effect for COD 1. (b) Lambertian-PCM effect for COD 40. (c) Opaque effect for COD 1. (d) Opaque effect for COD 40. The low-latitude ozone profile L275 is used.

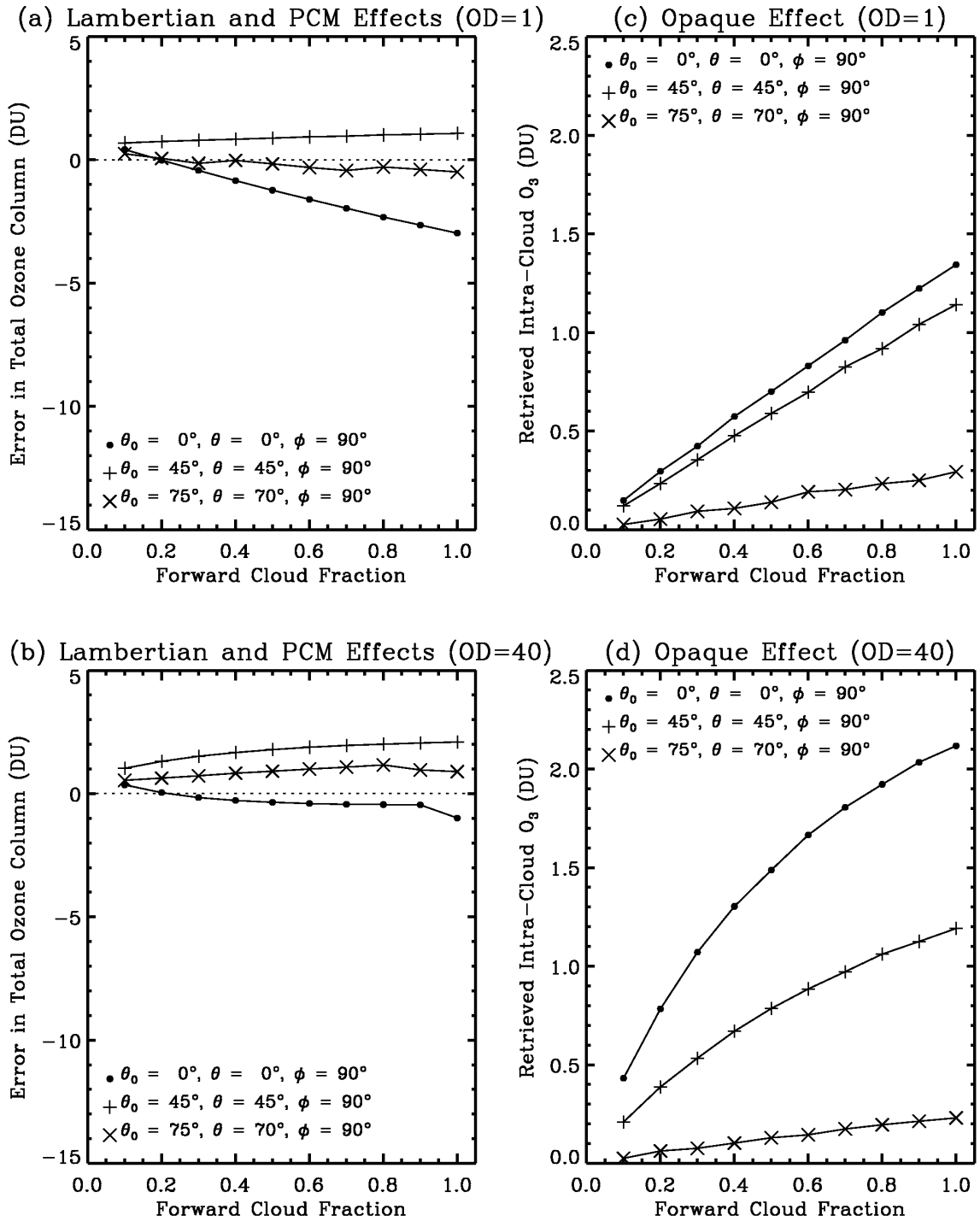
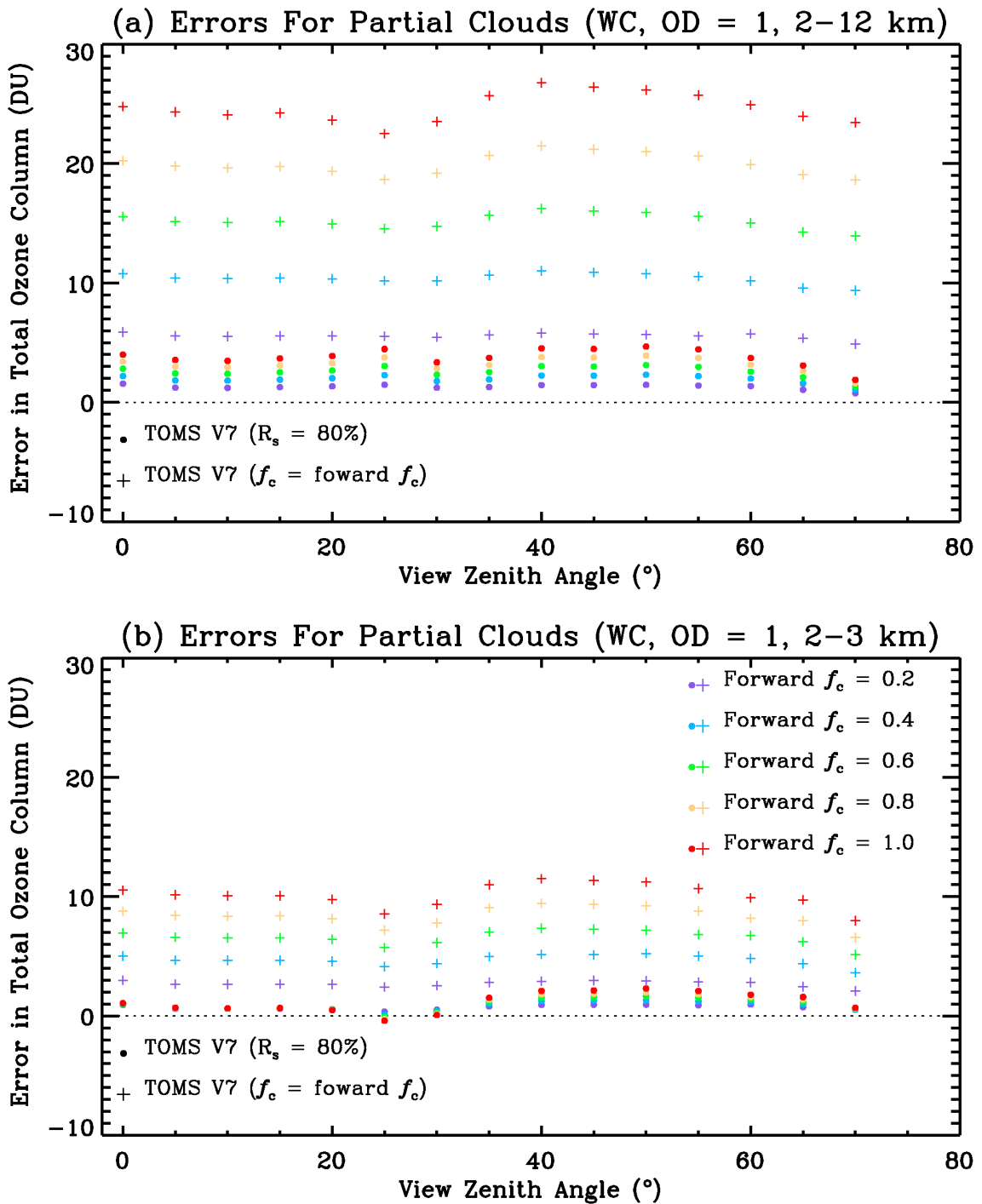


Figure 5.31 Same as Figure 5.30 except for clouds positioned at 2-3 km.



**Figure 5.32** Comparison of errors in total ozone at SZA  $30^\circ$  vs. VZA between using the TOMS V7 algorithm and forcing the ECF to be the FCF for different FCFs. (a) For WC of COD 1 at 2–12 km. (b) For WC of COD 1 at 2–3 km. The low-latitude ozone profile L275 is used.

geometry, the ICOAEN effect slightly depends on COP, COD, and CTH, but significantly varies with ozone amount and distribution in the clouds and cloud geometrical depth. With the knowledge of CTH and cloud reflectivity (or COD), it is possible to derive the cloud location by assuming certain types of clouds. The key to correcting the ICOAEN effect is then the a priori knowledge of ozone amount and distribution in the clouds.

Ozone profile measurements in cloudy conditions are very limited. The examination of ~2500 ozonesonde-measured ozone profiles at about ~20 tropical and mid-latitude ozonesonde stations finds that only 59 profiles have relative humidity greater than 80% over at least 4-km in altitude, not to say measurements under cloudy conditions. Studies using mesoscale chemical transport models indicate deep convection can redistribute surface trace gases in the clouds [Dickerson *et al.*, 1987; Pickering *et al.*, 1990; Pickering *et al.*, 1991; Pickering *et al.*, 1993]. Kley *et al.* [1996] observed near-zero ozone concentration in the both the marine boundary layer and the upper troposphere over the convective Pacific, indicating the convective lifting of the ozone-poor surface air to the upper troposphere. The measurements by Strom *et al.* [1999] of the trace gases (i.e., ozone) in two cumulonimbus anvils over western Europe indicated that much of the anvil air is rapidly transported from the surface with limited dilution. Because of the large temporal and spatial variability of surface ozone, the ozone inside the convective clouds may represent larger temporal and spatial variability as well, and its concentration might be larger or smaller than that in the corresponding clear air. Furthermore, the inter-cloud distribution of ozone does not simply follow a redistribution of surface ozone. Photolysis and heterogeneous processes in the clouds [Lelieveld and Crutzen, 1990], chemical reactions specific to thunderstorms [Ridley *et al.*, 1994], and stratospheric intrusion [Crutzen and Lawrence, 1997; Dickerson *et al.*, 1987; Poulida *et al.*, 1996; Suhre *et al.*, 1997; Winterrath *et al.*, 1999] may lead to production or loss inside the clouds. Dickerson *et al.* [1987], Poulida *et al.* [1996], and Winterrath *et al.* [1999] found enhanced ozone mixing ratios in the mid-latitude convective clouds and ascribed the enhancement to the intrusion of stratospheric air. Winterrath *et al.* [1999] also suggested that the enhanced ozone may be produced by non-lightning discharge mechanisms. Suhre *et al.* [1997] found high concentrations of ozone (100-500 ppbv) in the upper equatorial Atlantic troposphere near strong convective activities contrasting to the near-zero observation in the upper Pacific troposphere by Kley *et al.* [1996]. These very high ozone values were attributed to the downward

movement of stratospheric air due to convection or quasi-isentropic transport from the extratropical stratosphere [Crutzen and Lawrence, 1997; Suhre et al., 1997]. Overall, the limited measurements from case studies and model studies indicate that inter-cloud ozone presents large variability. Without knowledge of ozone amount and distribution in the clouds and their temporal and spatial variability, it is impossible to directly estimate the ICOAEN effect by simulating inter-cloud ozone absorption using radiative transfer models.

## 5.5 Summary

The assumption of an opaque Lambertian cloudy surface and the employed PCM can cause errors in retrieved ozone. We use PPGSRAD, which treats clouds as scattering media, to calculate the forward backscattered radiances, and then retrieve the TOC using the TOMS V7 algorithm. The input parameters to PPGSRAD and TOMRAD are as much the same as possible except for clouds to reduce the model bias. Clouds are treated as WC, WCHG, HEX, or POLY with different CODs and CGDs. We study OREs with different COPs, CODs, CGDs, ozone profiles, ozone amounts in the clouds, ozone distributions in the clouds, and TOMS measurement wavelengths (EP TOMS vs. N7 TOMS).

There are four categories of effects for an opaque Lambertian cloudy surface on ozone retrieval: Lambertian (i.e., assumption of angular-independent Lambertian surface); PCM (i.e., the used partial cloud model); ICOAEN (i.e., in-cloud ozone absorption enhancement); and BCOA (below-cloud ozone absorption) effects. For simplification, these effects are first investigated for forward full clouds. The Lambertian effect results from the air mass factor difference between simulated scattering clouds and assumed Lambertian clouds, profile difference between retrieval and forward-calculation, and some slightly nonlinear wavelength-dependence in the cloud reflection. The Lambertian effect varies with COP, COD, CTH, and ozone profile. But the OREs due to the Lambertian effect are usually within 1.5% of the TOC at  $COD \geq 20$ , indicating the assumption of angular-independent cloud reflection is fairly good. The PCM effect originates primarily from two factors: the air mass factor difference between forward full clouds and assumed partial clouds, which affects the directly retrieved ozone above clouds, and the change in the added OZBC because the ECF is different from the actual cloud fraction. The negative PCM effect also varies with COP, COD, CTH, and ozone profile, but it varies greatly with the retrieved cloud fraction,

which in turn is determined by COD. The smaller the retrieved cloud fraction, the larger the PCM effect is in magnitude. At  $COD \geq 20$ , the average PCM effect is within 2.5 DU. The ICOAEN effect occurs because backscattered photons penetrate the clouds, and the in-cloud multiple-scattering enhances ozone absorption. The ICOAEN effect depends significantly on observation viewing geometry, ozone amounts in the clouds, ozone distribution in the clouds, and CGD. The EICO decreases with increasing VZA and SZA. For homogeneous ozone distribution, the EICO is almost equal to the AICO at near nadir view but is close to 0 at larger viewing geometries (e.g.,  $\theta_0 = 75^\circ$ ,  $\theta = 65^\circ$ ). The EICO is almost directly proportional to the AICO. However, the ratio of EICO to AICO decreases slightly with increasing AICO. The increase of CGD usually increases the amount of AICO, therefore increasing the EICO. In the clouds, the sensitivity of the ICOAEN effect to ozone peaks in the upper part of the clouds and decreases dramatically with decreasing altitude below the peak. The ICOAEN effect varies slightly with different COPs; the smaller the asymmetry factor, the smaller the EICO is. Assuming clouds to be ice clouds only slightly decreases the ICOAEN effect. The ICOAEN effect usually decreases with increasing COD, decreasing by 40% when COD increases from 10 to 500. The BCOA effect occurs because backscattered photons penetrate below the cloud bottom and are partly absorbed by ozone. For optically thick clouds, very few photons penetrate through the clouds, and the BCOA effect is small. The BCOA effect is significant only when the cloud is optically thin and the amount of ozone below cloud-bottom is large. For forward partial clouds, the OREs due to various effects usually increases in magnitude with increasing FCF.

We analyze the essential effects on ozone retrieval by combining the above four effects. At smaller CODs ( $COD \leq 5$ ), OREs associated with clouds are small. The combination of ICOAEN, BCOA, and Lambertian effects leads to largely positive errors. However, the assumption of MFCR to be 80% significantly underestimates the cloud fraction compared to the FCF, leading to largely negative errors (i.e., the PCM effect). It is in the compensation errors among ICOAEN, BCOA, Lambertian, and PCM effects that the TOMS V7 algorithm retrieves the approximately correct TOC. With increasing CODs, the negative PCM effect decreases in magnitude, and the positive error from the combination of ICOAEN, BCOA, and Lambertian effects decreases as well and is dominated by the ICOAEN effect when  $COD \geq 5$ . However, the negative PCM effect decreases more dramatically than the positive error from other effects. Therefore, the overall ORE increases with increasing COD until COD reaches about 20-40 when the PCM

effect is very small. The further increase in COD slightly decreases the ORE because the ICOAEN effect slightly decreases with increasing COD. Employing PCM in the TOMS V7 algorithm is very good because the negative PCM effect due to the used PCM partly cancels the positive error due to other effects. However, because of the insufficient knowledge of ozone distribution inside the clouds, it is impossible to directly estimate the ICOAEN effect using radiative transfer models.

## CHAPTER 6

### EFFECTS OF OZONE RETRIEVAL ERRORS ON TROPOSPHERIC OZONE

#### DERIVATION

The CCP and CCD methods derive tropical tropospheric ozone from the difference between TOC over clear areas and OZAC over nearby high-altitude cloudy areas. Basically, ozone above high reflectivity clouds is derived as Stratospheric Ozone Column (SOC). One important assumption is that OZAC is the same as the corresponding ozone above the same cloud-top level under clear-sky conditions, i.e., the SOCs for clear and sky conditions are the same. Based on this assumption, errors in the retrieved OZAC will propagate into the derived tropospheric ozone. Previous chapters have demonstrated several OREs in OZAC. Incorrect CTHs in the TOMS V7 algorithm cause errors in retrieved OZAC. Chapter 5 shows that sensors can see most of the ozone in the clouds at near nadir or small SZAs even for optically thick clouds because of the ICOAEN effect. The assumption of angular-independent cloud surface reflectivity in the TOMS V7 algorithm can also introduce errors in OZAC within  $\pm 3$  DU for high reflectivity clouds. In addition, it has been shown that tropical convection seldom reaches the tropopause (e.g.,  $\sim 100$  hPa) [Folkins *et al.*, 1999; Gettelman *et al.*, 2002; Dessler, 2002] because there is a barrier in vertical mixing at 14 km ( $\sim 150$  hPa) [Folkins *et al.*, 1999]. The use of OZAC with such clouds overestimates the SOC. These errors need to be accounted for to derive accurate stratospheric ozone.

With THIR data, we can correct errors in OZAC caused by incorrect CTHs. The ozone from cloud-top to tropopause can be taken from Southern Hemisphere Additional OZonesonde (SHADOZ) climatologies. However, direct estimation of errors in OZAC caused by enhanced ozone absorption in the cloud, which may significantly overestimate OZAC dependent on ozone amount and distribution in the

clouds, is impossible because of the poor knowledge of ozone distributions in the clouds. This chapter provides an indirect way of estimating the ICOAEN effect over tropical high-altitude cloudy areas. Section 6.1 illustrates the TOMS TOC difference between cloudy and clear areas during 1979-1983 with cloud-height-induced errors corrected. In Section 6.2, the errors due to incorrect tropospheric climatology for both clear TOC and cloudy OZAC are corrected in the cloudy/clear TOC difference. In Section 6.3, we investigate the dynamic and chemical effects as well as OREs that cause cloudy/clear TOC difference and estimate the ICOAEN effect. In Section 6.4, with the knowledge of the ICOAEN effect and other errors in OZAC, we evaluate the effect of OREs on the tropospheric ozone derivation using all the high-reflectivity cloud points. Section 6.5 particularly addresses OREs in the CCP and CCD methods.

### **6.1 Total Ozone Difference Between Tropical Cloudy and Clear Areas**

We compute the daily TOC differences between cloudy areas (reflectivity  $\geq 80\%$ , THIR CTP  $\leq 300$  hPa) and neighboring clear areas (reflectivity  $\leq 20\%$ ) in a  $5^\circ$ -longitude  $\times$   $5^\circ$ -latitude grid box in tropical areas ( $15^\circ\text{S}$ - $15^\circ\text{N}$ ). With collocated THIR CTH during 1979-1983, we correct cloudy TOC and OZAC for cloud-height-induced errors using the  $\Delta P$  correction described in Chapter 4. From all the available daily cloud/clear TOC difference values, we derive a monthly mean climatology of TOC difference in each  $5^\circ \times 5^\circ$  grid along with monthly mean THIR CTH, cloud reflectivity, clear TOC, and OZAC. Figure 6.1 shows the annual average THIR CTP, the error in OZAC, and the cloudy/clear TOC difference before and after the  $\Delta P$  correction (averaged from the 12 monthly mean values). The annual average CTH ranges from 177.8 hPa to 248.8 hPa, with a mean value of  $201.7 \pm 12.4$  hPa (with 1 standard deviation that mostly reflects the spatial variation). The CTPs are usually smaller by up to 30 hPa (i.e.,  $\sim 1$  km higher) over the Pacific Ocean than over other regions. The annual average error in OZAC due to incorrect CTP ranges from  $-6.4$  DU to  $-1.6$  DU, with a mean value of  $-3.4 \pm 1.0$  DU. This error depends on the difference between assumed CTP and THIR CTP. Before the  $\Delta P$  correction, the cloudy/clear TOC difference ranges from  $-9.1$  to  $8.6$  DU, with a mean value of  $-1.0 \pm 3.3$  DU. However, the TOC difference after the  $\Delta P$  correction shows consistent positive values, ranging from  $7.5$  DU to  $21.6$  DU with a mean of  $13.3 \pm 2.0$  DU. The TOC difference is about 13-17 DU over the Pacific Ocean and about 9-13 DU over

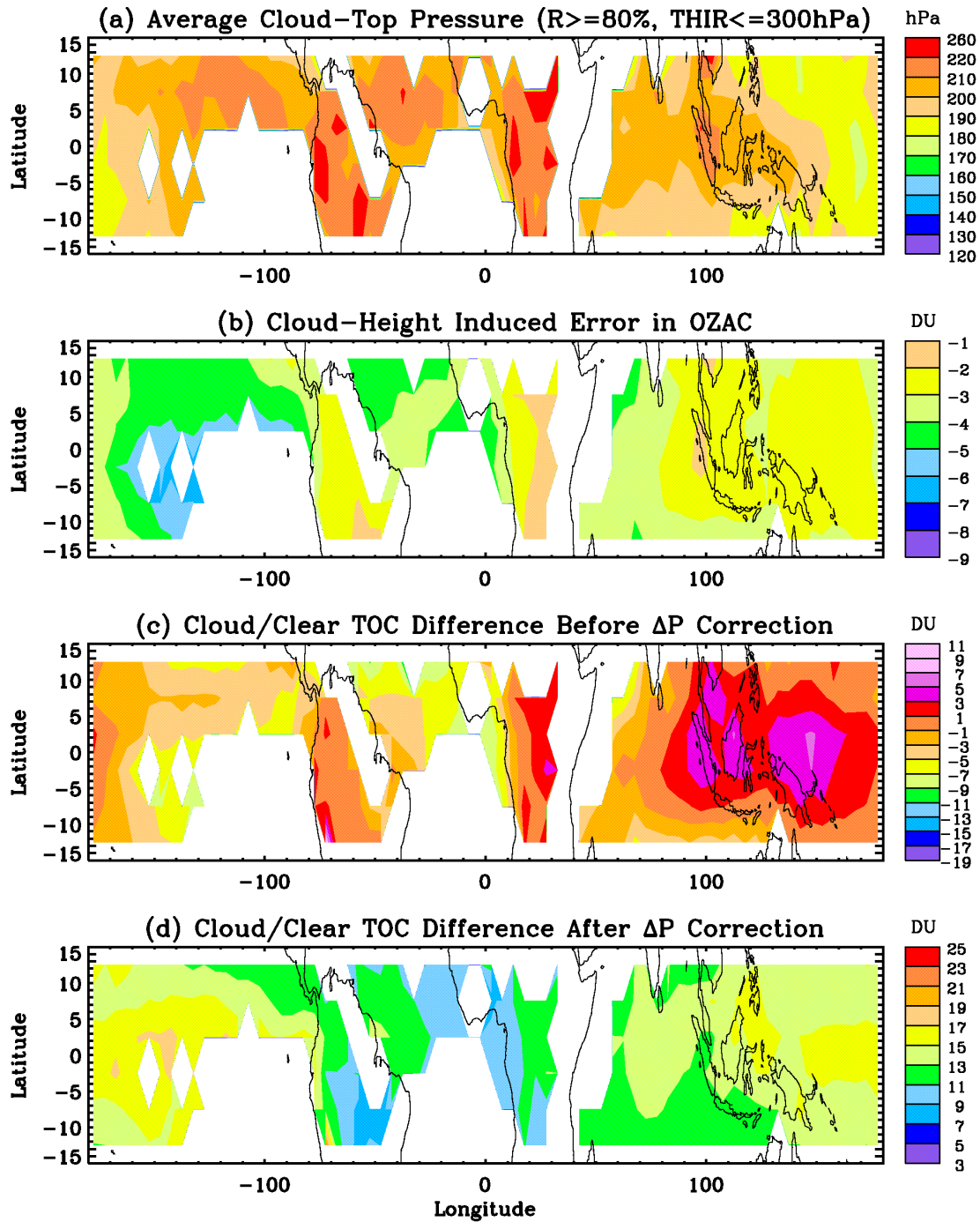


**Figure 6.1** Annually averaged parameters in  $5^\circ$ -longitude  $\times$   $5^\circ$ -latitude areas during 1979-1983. (a) Average THIR CTP for high-reflectivity clouds (reflectivity  $\geq 80\%$  and THIR CTP  $\leq 300$  hPa). (b) Cloud-height-induced errors in ozone above high-reflectivity clouds. (c) Difference in the TOC between high-reflectivity cloudy areas and nearby clear areas (reflectivity  $\leq 20\%$ ) before the  $\Delta P$  correction. (d) Same as (c) but after the  $\Delta P$  correction.

Africa and the Atlantic Ocean. The correction of incorrect cloud-height errors leads to larger TOC cloudy/clear bias and the current TOMS TOC contains much smaller cloudy/clear bias because of compensating errors.

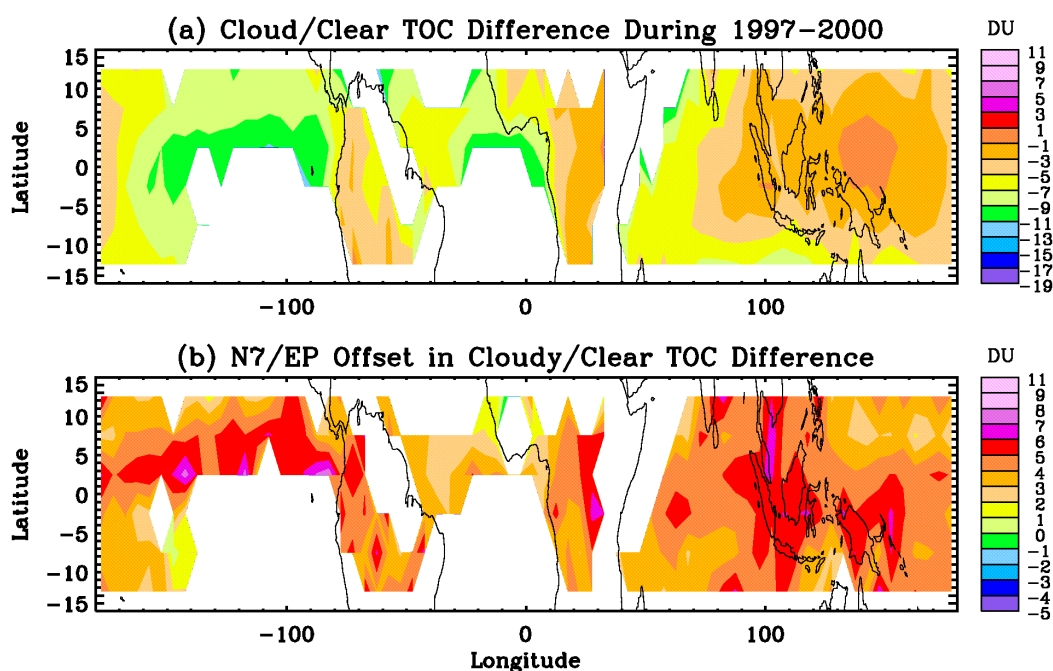


**Figure 6.2** (a) Same as Figure 6.1 (c) except for clouds with reflectivity  $\geq 80\%$  in 1997-2000 EP TOMS data. (b) Difference in the Cloudy/Clear TOC difference between N7 TOMS data (1979-1983) and EP TOMS data (1997-2000).

Figure 6.2 (a) shows the cloudy/clear TOC difference during 1997-1999 without the  $\Delta P$  correction. We can see that the annual average TOC difference is consistently smaller than during 1979-1983, ranging from -11.3 DU to 0.4 DU with a mean value of  $-5.1 \text{ DU} \pm 2.7 \text{ DU}$ . This annual average EP/N7 TOMS offset, shown in Figure 6.2 (b), ranges from 1.2 DU to 7.7 DU with a mean of  $4.4 \pm 1.1 \text{ DU}$ . This N7/EP offset also shown in OA distribution is probably related to the non-linearity calibration error in either N7 TOMS, or EP TOMS, or both as we have discussed in Section 3.2. Although no  $\Delta P$  correction is performed because of lacking actual CTPs, we expect that the TOC difference during the EP period will be

persistently positive because the magnitude of the  $\Delta P$  correction should be similar between N7 TOMS and EP TOMS data, but  $\sim 4.4$  DU smaller than the corresponding N7 TOMS values on average. Therefore, we expect that the TOC difference after the  $\Delta P$  correction during the EP TOMS period is about 9-13 DU over the Pacific Ocean and about 5-9 DU over the Atlantic Ocean and Africa.

## 6.2 Correction of Incorrect Tropospheric Climatology from Ozonesonde Data

If the added OZBC is equal to the average tropospheric ozone below the same level under clear-sky conditions, then the cloudy/clear TOC difference should be approximately the difference in ozone above cloud-top level between cloudy and clear conditions. However, this condition is not true. Because of the incorrect climatological tropospheric ozone used in the TOMS algorithm and the  $\Delta P$  correction, the added OZBC has an error of the difference between the actual and climatological ozone below cloud-top, and the clear-sky TOC suffers from the lower retrieval efficiency to lower tropospheric ozone. Both errors under clear and cloudy conditions affect the computed TOC difference. These errors needed to be corrected before we investigate errors in the derived OZAC due to other factors.

The SHADOZ ozonesonde data provide a good reference to evaluate the TOMS standard climatological tropospheric ozone. We used the SHADOZ data at Samoa (14.2°S, 170.6°W), Tahiti (18.0°S, 149.0°W), Cristobal (0.9°S, 89.6°W), Natal (5.4°S, 35.4°W), Ascension (8.0°S, 14.4°W), Nairobi (1.3°S, 36.8°E), Malindi (3°S, 40.2°E), Java (7.6°S, 112.7°E), and Fiji (18°S, 178.4°E) during 1998-2000 [Thompson *et al.*, 2002; Thompson and Witte, 1999]. Monthly mean tropospheric ozone profiles are derived at each station at a resolution of 50 hPa (up to 100 hPa). The monthly mean tropospheric ozone profiles are independent of latitude and interpolated across the longitude to get the synthetic actual data for any tropical region. Because no long-term observations are available in the Northern Hemisphere, we approximate the actual data in the Northern Hemisphere as being a six-month shift of the Southern Hemisphere observations. Large errors could occur in the approximate data especially over the Northern Atlantic Ocean and North Africa during February-May. Because the approximate values ( $\sim 36$ -48 DU) are actually taken from the Natal and Ascension measurements during August-November, they are higher than the derived tropospheric ozone by Fishman *et al.* [1990], Fishman and Brackett [1997], Hudson and Thompson [1998], and Ziemke *et al.* [1998].

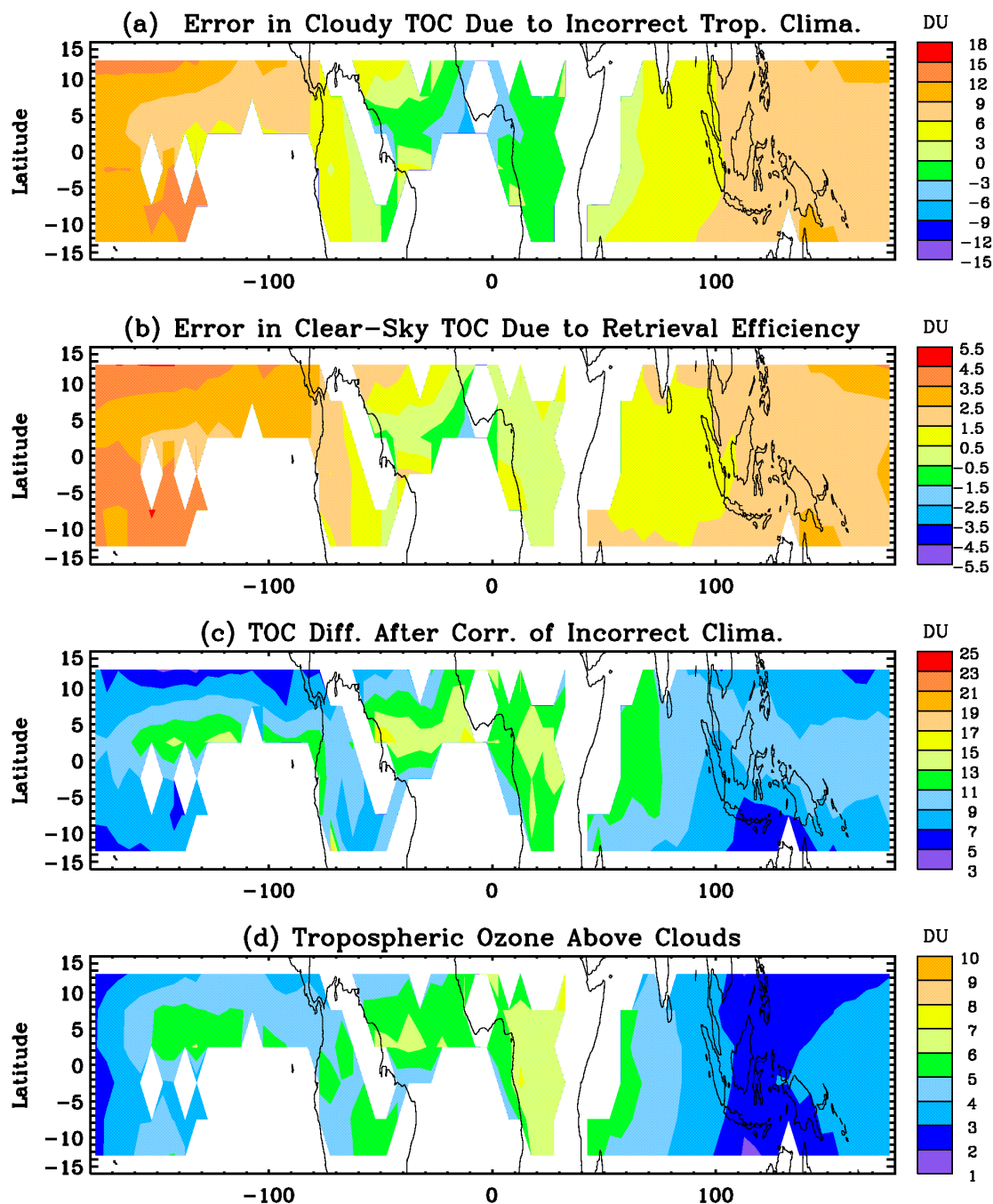


**Figure 6.3** Annually averaged parameters in  $5^\circ$ -longitude  $\times$   $5^\circ$ -latitude areas in 1979-1983 TOMS data. (a) Errors in the added ozone below high-reflectivity clouds caused by the incorrect tropospheric climatology used in TOMS retrieval. (b) Errors in the clear total column ozone caused by imperfect retrieval efficiency and incorrect tropospheric climatology. (c) Values in Figure 6.1 (d) minus values in (a) and plus values in (b). (d) Average upper tropospheric column ozone between CTP and tropopause derived from SHADOZ climatology during 1998-2000.

The error in the added OZBC is just the difference between the added OZBC and the assumed actual tropospheric ozone integrated from the terrain pressure to the average CTP. There are large negative errors up to  $-15.0$  DU over the Pacific Ocean throughout the year, and large positive errors up to  $15$  DU over the Atlantic Ocean and Africa during the biomass-burning season. Figure 6.3 (a) shows the annual mean error in added OZBC. On average, OZBC is overestimated by  $6-12$  DU over the Pacific Ocean and underestimated by  $-6-0$  DU over the Atlantic Ocean and Africa.

The deviation of the actual tropospheric ozone profile from TOMS standard tropospheric ozone profiles causes error in the derived clear TOC. To correct for the error  $\Delta\Omega$  in the clear-sky TOC due to incorrect tropospheric ozone climatology and imperfect retrieval efficiency in the lower troposphere, we use the height-resolved retrieval efficiency factors  $\varepsilon(P)$  (see Appendix B for the calculated retrieval efficiency factors) according to the following equation [Martin *et al.*, 2002]:

$$\Delta\Omega = \int_{P_s}^{P_t} ((1 - \varepsilon(P))(\rho_{std}(P) - \rho_{act}(P)))dP, \quad (6.1)$$

where  $\rho_{std}(P)$  and  $\rho_{act}(P)$  are the ozone density in terms of DU per hPa at pressure level  $P$  in the TOMS standard climatological profile and actual tropospheric ozone profile, respectively. In this study, the retrieval efficiency factors are calculated at each 50-hPa layer from 1000 hPa to 100 hPa for L275 and average viewing geometry for tropical areas ( $SZA = 20^\circ$ ,  $VZA = 20^\circ$ ,  $AZA = 90^\circ$ ), and surface reflectivity of 8%. The error in the clear-sky TOC ranges from  $-5.5$  DU to  $5.5$  DU and usually has the same sign as the error in the added OZBC. Figure 6.3 (b) shows the annual average  $\Delta\Omega$  at clear-sky regions that coexists with high-reflectivity clouds. The error is about  $1.5-4.5$  DU over the Pacific Ocean and  $-1.5-0.5$  DU over Africa. The effective retrieval efficiency factor, which is defined as the integration of high-resolved retrieval efficiency factors weighted by the profile difference at each layer, usually ranges from 0.4 to 0.9 with an average value of 0.66. This average efficiency factor of 0.66 explains that the error in clear-sky TOC is about 1/3 the error in the added OZBC.

Figure 6.3 (c) shows the annual average cloud/clear TOC difference after errors in the added OZBC and the clear-sky TOC have been corrected. We can see that there is a cloudy ozone excess over all

the regions and the TOC difference presents a wave-one pattern. The trough over the Pacific Ocean is about 7-11 DU, and the ridge over Africa and the Atlantic Ocean is about 11-15 DU. Because the approximate data are interpolated from the limited ozonesonde observations, the corrected TOC differences may contain significant errors that are about 2/3 the difference in tropospheric ozone between the actual and the approximated tropospheric ozone values. Because of the smaller TOC difference in the EP TOMS data, the corresponding cloudy/clear TOC difference after correction is expected to be ~4.4 DU smaller, i.e., 3-7 DU over the Pacific Ocean and 7-11 DU over Africa and the Atlantic Ocean. The cloudy/clear TOC difference after correction are closer to zero in the EP TOMS data, indicating that the assumption of the same stratospheric ozone between clear and cloudy areas is more valid in the EP TOMS data.

From the ozonesonde measurements, we can also obtain the approximate overestimation in the derived SOC because of the inclusion of upper tropospheric ozone. Figure 6.3 (d) shows the annual average upper troposphere ozone from CTP up to 100 mb from monthly mean ozonesonde measurements. The upper tropospheric ozone ranges from 1.8 DU to 7.8 DU depending on CTP, month, and longitude, with an average of  $4.2 \pm 1.2$  DU. The positive error in the SOC due to inclusion of upper tropospheric ozone partly cancel the negative error in the SOC due to incorrect cloud heights.

### **6.3 Sources of Cloudy Total Ozone Excess**

The remaining cloud/clear TOC difference, which results from the ozone difference above levels of high-altitude clouds, must be due to either geophysical errors or OREs or both. This section investigates the effects of dynamics, chemical production, and OREs on the observed total ozone excess relative to clear-sky conditions.

#### **6.3.1 Dynamical Influence of Deep Convection on Total-Ozone Distribution**

Deep convection that penetrates the mid-latitude tropopause will have two potential effects on the column ozone. First, the top of the convective complex will push the lower stratosphere up, resulting in a reduced SOC [Mattingly, 1977; Poulida *et al.*, 1996; WMO, 1985]. However, the work of Folkins *et al.* [1999], Gettelman *et al.* [2002], Dessler [2002], and Kley *et al.* [1996] shows that tropical convection rarely reaches the tropopause. Second, boundary layer and free tropospheric air raised in the convective columns

will be deposited into the upper troposphere [Poulida *et al.*, 1996]. Over relatively clean marine areas, this convection effect will distribute low-ozone air throughout the troposphere. There is a seasonal cycle in the tropopause height at tropical locations [Randel *et al.*, 2000], and there is a seasonal cycle in the SOC in the tropics, with lowest values in January-April [Logan, 1999], which could be due to convection, the Brewer Dobson circulation being strongest in the northern winter etc.; however, this seasonal cycle cancels out in the cloudy-clear pair used here.

Seeking evidence for these effects, we inspect the tropical (10°S-10°N) TOMS data in 1980 for reflectivities greater than 80% and THIR CTP between 100-200 hPa based on the linear regression slopes between TOMS-measured OZAC and THIR. The slopes are calculated from accumulating individual daily data in 10°-longitude  $\times$  5°-latitude areas where there are more than 10 such individual measurements. The histogram of these slopes is shown in Figure 6.4 (a), in which we have omitted slopes not significant at the 2-sigma level. The mean slope is  $4.0 \pm 3.5$  DU/100 hPa. The method used here to estimate the 100-200 hPa TOMS tropospheric ozone is similar to the cloud-slicing method used by Ziemke *et al.* [2001] to derive upper tropospheric ozone. By comparison, the tropospheric ozone between 100-200 hPa for all meteorological conditions from eight tropical 1998-2000 SHADOZ measurements is  $4.4 \pm 1.9$  DU as shown in Figure 6.4 (b), consistent with the mean TOMS slope. Fujita [1992] shows that updrafts and penetrating towers of convective clouds are typically at 1-10 km in diameter and the timescale of connective penetration events may be as short as 10 min. The small difference between TOMS observation and ozonesonde measurements indicates that either the TOMS field of view is too large to see these localized effects, or the effects actually do not occur at the time of TOMS observation.

### 6.3.2 Photochemical Production over Convective Clouds

In polluted regions, deep convection can transport boundary layer ozone precursors such as NO<sub>x</sub> and volatile organic compounds into the upper troposphere and lower stratosphere. Lightning associated with deep convective clouds would also produce a large amount of NO<sub>x</sub> to participate in ozone generation. Photolysis frequencies are strongly coupled with the cloud field; high-reflectivity clouds largely increase the actinic flux and thus increase the *j*-values to produce ozone [Madronich, 1987]. Therefore, one might expect some ozone production from these factors. However, using a photochemical model,

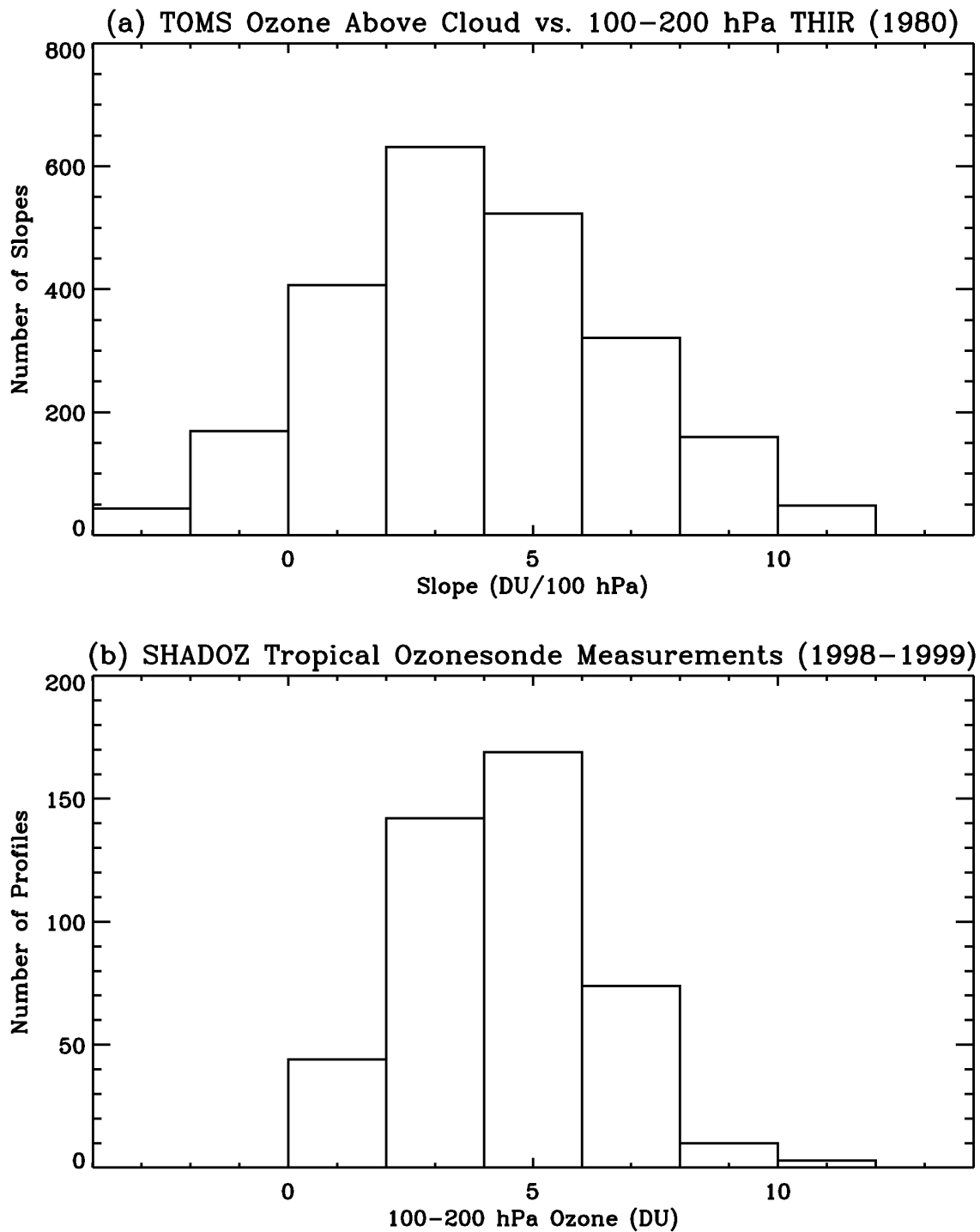


**Figure 6.4** Histograms of ozone between 100 and 200 hPa. (a) Linear regression slope between TOMS OZAC and THIR CTP for measurements with reflectivity greater than 80% and THIR CTP between 100–200 hPa in the tropics (10°S–10°N) in 1980. (b) SHADOZ measurements between 100 and 200 hPa at eight tropical stations in 1998–1999.

*Pickering et al.* [1990] estimated that the diurnally averaged net ozone production rate is only  $16 \text{ ppb day}^{-1}$  at 7 km for convective cloudy conditions. The time periods associated with the formation and dissipation of these clouds, usually on the order of a few hours, are too short for chemical ozone production to explain the observed ozone excess over cloudy areas.

### 6.3.3 Ozone Absorption Enhancement in the Clouds

Because the chemical and dynamic effects on cloudy/clear TOC difference are estimated to be small, the remaining cloudy/clear TOC differences are caused primarily by OREs. In previous sections, we have taken into account the known error from retrieval efficiency under clear-sky conditions and the error induced by incorrect CTPs under cloudy conditions. We then ascribe the remaining cloud/clear TOC differences to the assumption of Lambertian cloudy surfaces, ozone absorption enhancement in the cloud, and the non-linearity calibration error. As shown in Chapter 5, the Lambertian effect for a cloud of COD 40 at 2-12 km is about  $-1.5 \pm 0.7 \text{ DU}$ ,  $-0.9 \pm 0.3 \text{ DU}$ ,  $-0.83 \pm 1.3 \text{ DU}$ ,  $2.4 \pm 0.5 \text{ DU}$ , for WC, WCHG, HEX, and POLY, respectively under TOMS tropically averaged observation viewing geometry ( $0^\circ \leq \text{SZA} \leq 30^\circ$ ,  $0^\circ \leq \text{VZA} \leq 63^\circ$ ). Because of the unknown optical properties for those high-reflectivity convective clouds and the small magnitude of errors for different types of clouds, we assume the Lambertian effect is negligible. Because the assumption of the same SOC between cloudy and clear areas is more nearly found in EP TOMS data than in N7 TOMS data, and because the EP is most probably better calibrated [*Stolarski et al.*, 2000], we assume the non-linearity calibration error as shown in the NP/EP bias occurs in the N7 TOMS data. Then the cloudy/clear TOC difference shown in Figure 6.3 (c) subtracting the N7/EP bias results primarily from ozone absorption enhancement in the clouds. Note that the actual ozone absorption enhancement in the cloud is subject to change if the assumptions of the Lambertian effect or the non-linearity calibration error are not correct or if the approximate actual tropical tropospheric ozone from SHADOZ data is not accurate.

Figure 6.5 shows the seasonally and annually averaged OREs caused by the ICOAEN effect for high-altitude convective clouds. There is a wave-1 pattern in the ICOAEN effect, usually maximizing over the Atlantic Ocean and Africa and minimizing over the Pacific Ocean. Typically, the ICOAEN effect ranges from 5 DU to 13 DU over the Atlantic Ocean and Africa, and ranges from 1 DU to 7 DU over the

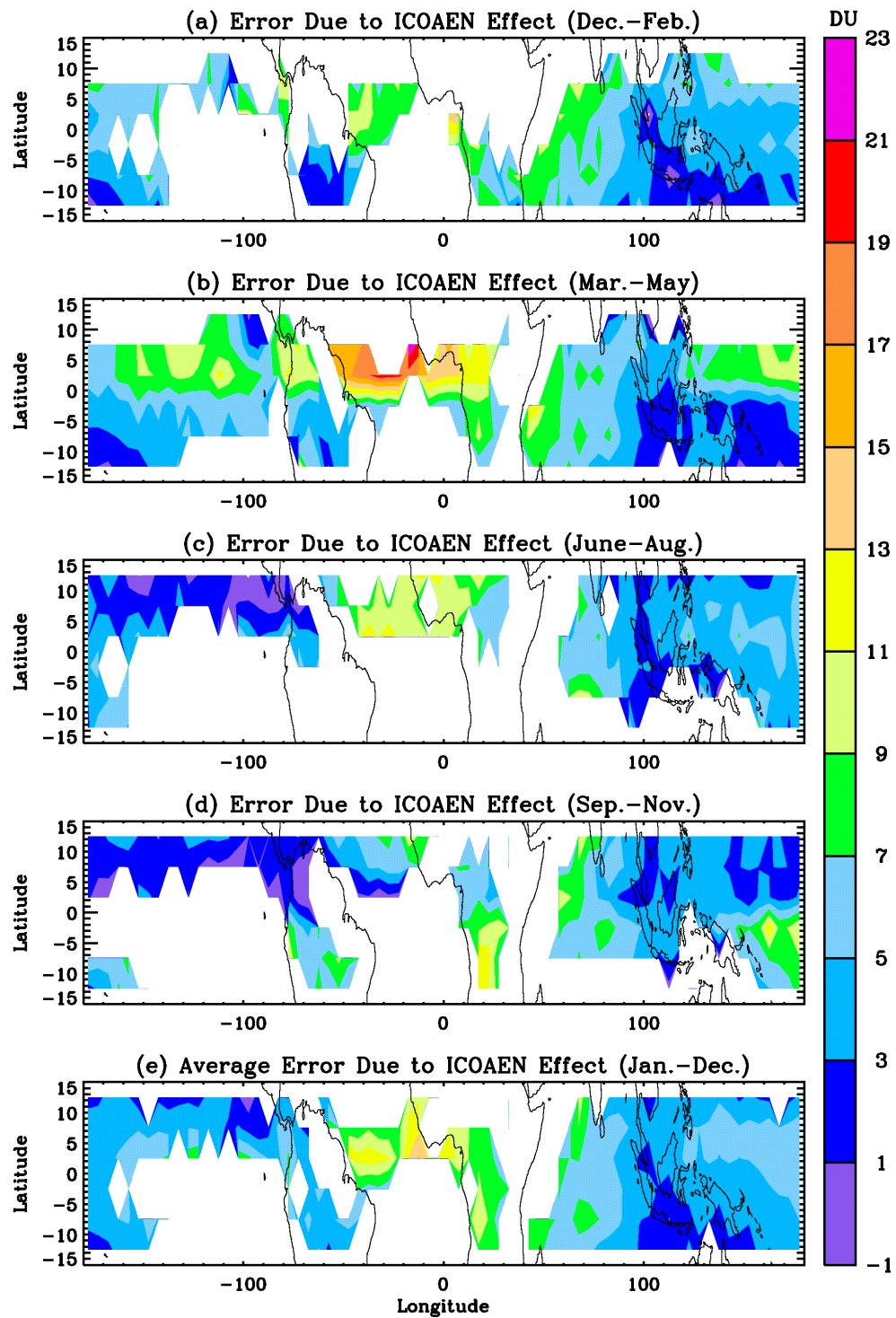


**Figure 6.5** Derived ICOAEN effect for  $5^\circ$ -longitude  $\times$   $5^\circ$ -latitude areas during 1979-1983 TOMS data. (a)-(d) Seasonally averaged ICOAEN effect for the winter, spring, summer, and fall, respectively. (e) Annually averaged ICOAEN effect.

Pacific Ocean. The wave-1 ICOAEN effect is caused by the convective redistribution of surface air. Because of the higher H<sub>2</sub>O and lower NO<sub>x</sub> marine environment over the Pacific Ocean compared to that over the Atlantic Ocean and Africa, the concentration of surface ozone is lower; therefore, the ICOAEN effect is smaller than that over the Atlantic Ocean and Africa. The negative ICOAEN effect results from the neglect of the Lambertian effect, attribution of non-linearity calibration errors to N7 TOMS data only, or error in the approximate actual tropospheric ozone. The large values of the ICOAEN effect over the north Atlantic Ocean during March-May, with a magnitude of 15-21 DU, might contain significant errors because the approximate actual tropospheric ozone from SHADOZ measurements is shifted by six months in the Northern Hemisphere. The measured monthly mean tropospheric ozone at Paramaribo (5.8°N, 55.2°W) [Thompson *et al.*, 2002] during 1999-2001 is about 28.6 DU during March-May, smaller by 14.8 DU than the approximated value over the north Atlantic Ocean. If we use ozone measurements at Paramaribo as the approximate tropospheric ozone for the north Atlantic Ocean, the ICOAEN effect will be reduced by ~10 DU to 5-11 DU.

#### 6.4 Ozone Retrieval Errors in Tropospheric Ozone Derivation

To derive SOC from ozone above high-reflectivity clouds (reflectivity  $\geq 80\%$ ), we need to correct OREs mostly associated with clouds in OZAC that affect the assumption of the same SOC between cloudy and clear areas. The error in the derived SOC  $\Delta\Omega_{strat}$  is the sum of errors resulting from incorrect CTPs  $\Delta\Omega_{cldhgt}$ , the ICOAEN effect  $\Delta\Omega_{ICOAEN}$ , the non-linearity calibration error  $\Delta\Omega_{nonlinear}$ , and the inclusion of upper tropospheric ozone  $\Delta\Omega_{uptrop}$ ,

$$\Delta\Omega_{strat} = \Delta\Omega_{cldhgt} + \Delta\Omega_{uptrop} + \Delta\Omega_{ICOAEN} + \Delta\Omega_{nonlinear}. \quad (6.2)$$

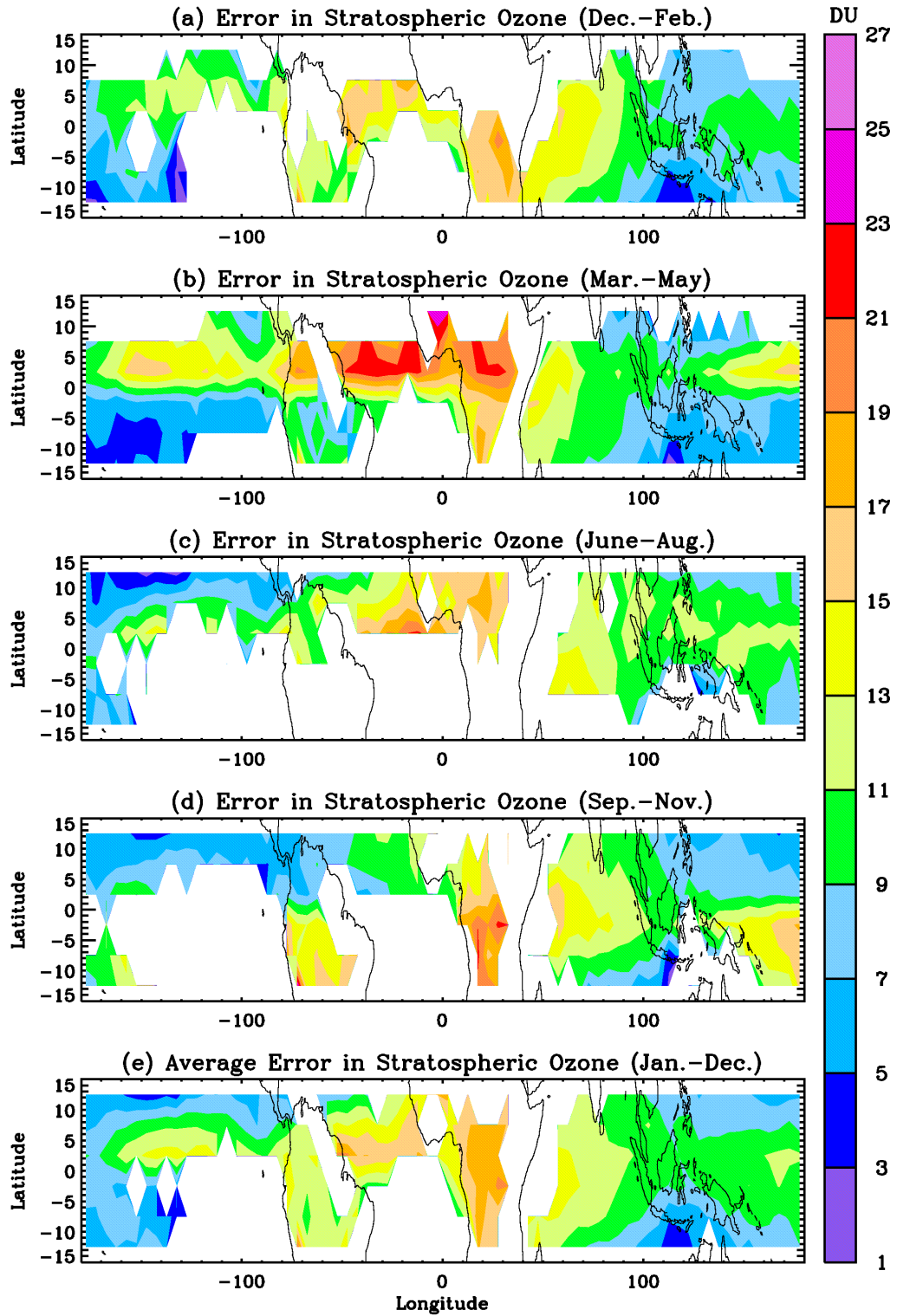
The sum of  $\Delta\Omega_{ICOAEN}$  and  $\Delta\Omega_{nonlinear}$  is the cloudy TOC excess  $\Delta\Omega_{excess}$  after correction for incorrect tropospheric climatology. Of the above four errors, only  $\Delta\Omega_{cldhgt}$  is negative, and it almost cancels  $\Delta\Omega_{uptrop}$ . Correcting these errors actually works toward making the assumption of the same cloudy and

clear SOC valid. The error in derived tropospheric ozone  $\Delta\Omega_{trop}$  is just the sum of minus  $\Delta\Omega_{strat}$  and the error in clear TOC due to imperfect retrieval efficiency and incorrect tropospheric climatology  $\Delta\Omega_{clr}$ ,

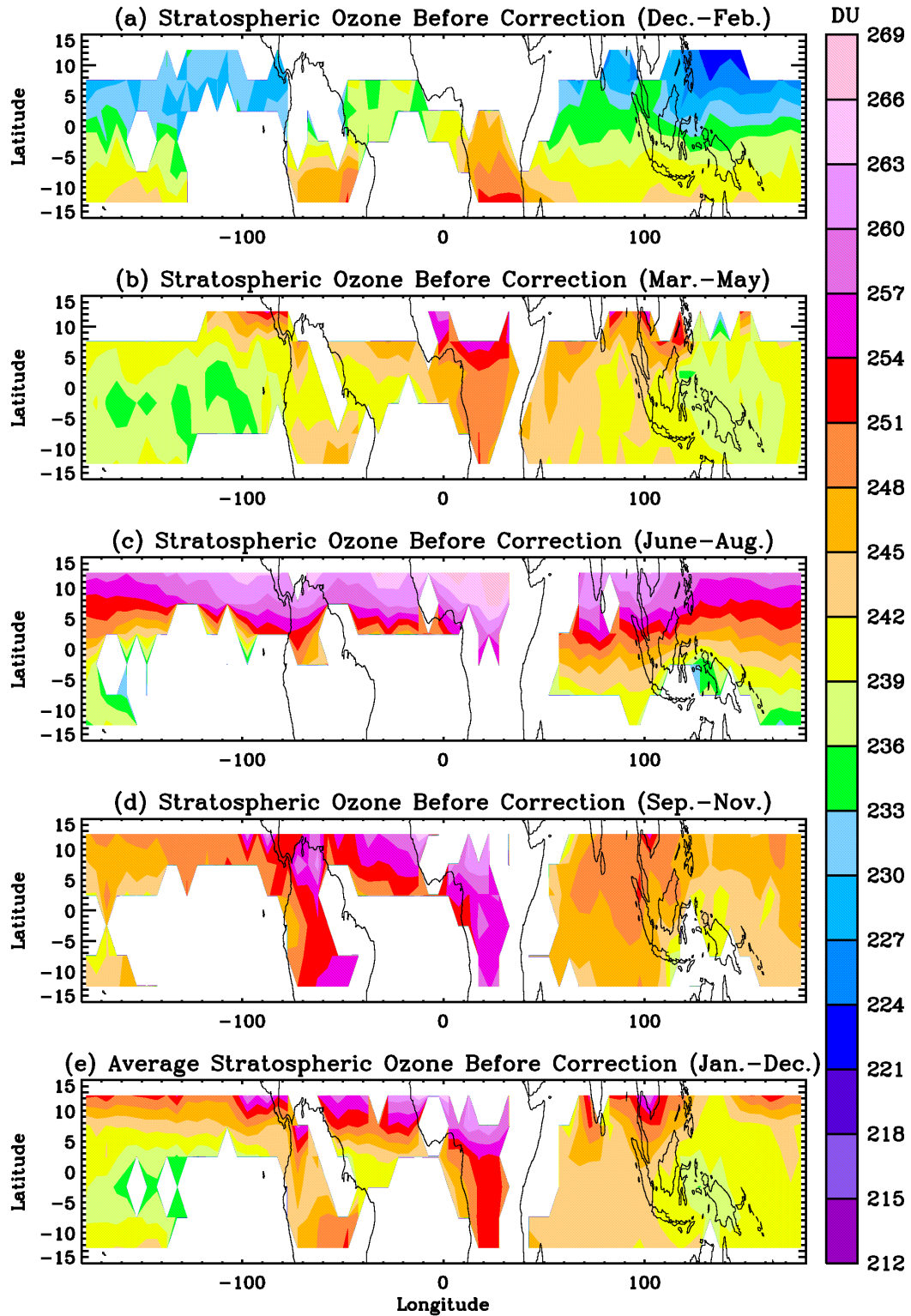
$$\Delta\Omega = \Delta\Omega_{clr} - \Delta\Omega_{strat}. \quad (6.3)$$

Figure 6.6 shows the seasonally and annually averaged error in derived stratospheric ozone  $\Delta\Omega_{strat}$ . Similar to the ICOAEN effect, the  $\Delta\Omega_{strat}$  shows a typical wave-1 pattern, with a maximum over the Atlantic Ocean and Africa and a minimum over the Pacific Ocean. The error varies with season and location, usually ranging from 3 DU to 23 DU with a mean value of  $10.8 \pm 4.4$  DU. The variation in errors results mainly from the variation of the ICOAEN effect. The  $\Delta\Omega_{strat}$  typically ranges from 11 DU to 21 DU over the Atlantic Ocean and Africa and from 5 DU to 15 DU over the Pacific Ocean. The large  $\Delta\Omega_{strat}$  over the north Atlantic Ocean and north Africa during March-May may be caused by large errors arising from approximating the actual tropospheric ozone from SHADOZ measurements.

Figures 6.7 and 6.8 show the seasonally and annually averaged SOC derived from high-reflectivity clouds during 1979-1983 before and after correcting the  $\Delta\Omega_{strat}$ , respectively. We can see that the SOC typically shows a large seasonal and latitudinal dependence directly related to the amount of UV radiation received at each latitude and season. Higher ozone occurs at latitudes and seasons with more solar insolation. Although the derived ozone is available only at regions with high-reflectivity clouds, we can still see that the SOC before correction shows a typical wave-1 pattern, peaking over the Atlantic Ocean and Africa, similar to the results by *Newchurch et al.* [2001c]. The SOC after correction is usually higher than the corresponding value before correction by  $\sim 10$  DU because of the correction. Furthermore, the SOC after the correction shows a relatively flat variation across longitudes especially in the winter and summer seasons, and the longitudinal maxima are not fixed over the Atlantic Ocean and Africa. Therefore, the persistent wave-1 pattern of SOC before the correction or seen in *Newchurch et al.* [2001c], which peaks over the Atlantic Ocean and Africa and has an amplitude of 4 DU, may result primarily from OREs associated with clouds. The actual stratospheric ozone is relatively zonally invariant. The longitudinal structure seen in Figure 6.8 may be caused by different frequencies of high clouds at different locations and the approximation of tropospheric ozone from SHADOZ data in the correction.



**Figure 6.6** Same as Figure 6.5 except for errors in the derived stratospheric ozone column from high-reflectivity clouds (reflectivity  $\geq 80\%$  and THIR CTP  $\leq 300$  hPa).



**Figure 6.7** Same as Figure 6.5 except for the derived SOC from high-reflectivity clouds (reflectivity  $\geq 80\%$  and THIR CTP  $\leq 300$  hPa) before correcting the errors shown in Figure 6.6.

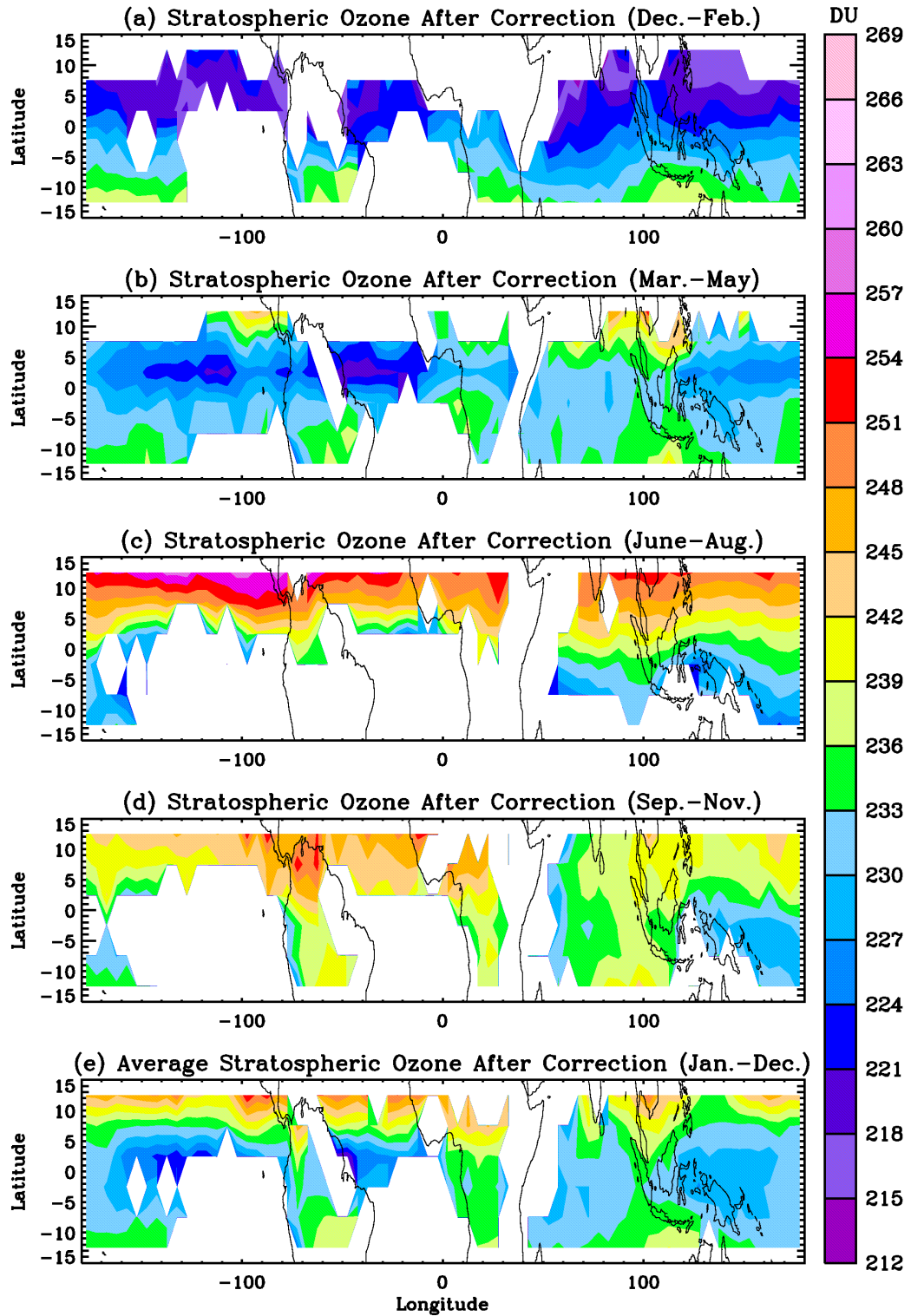
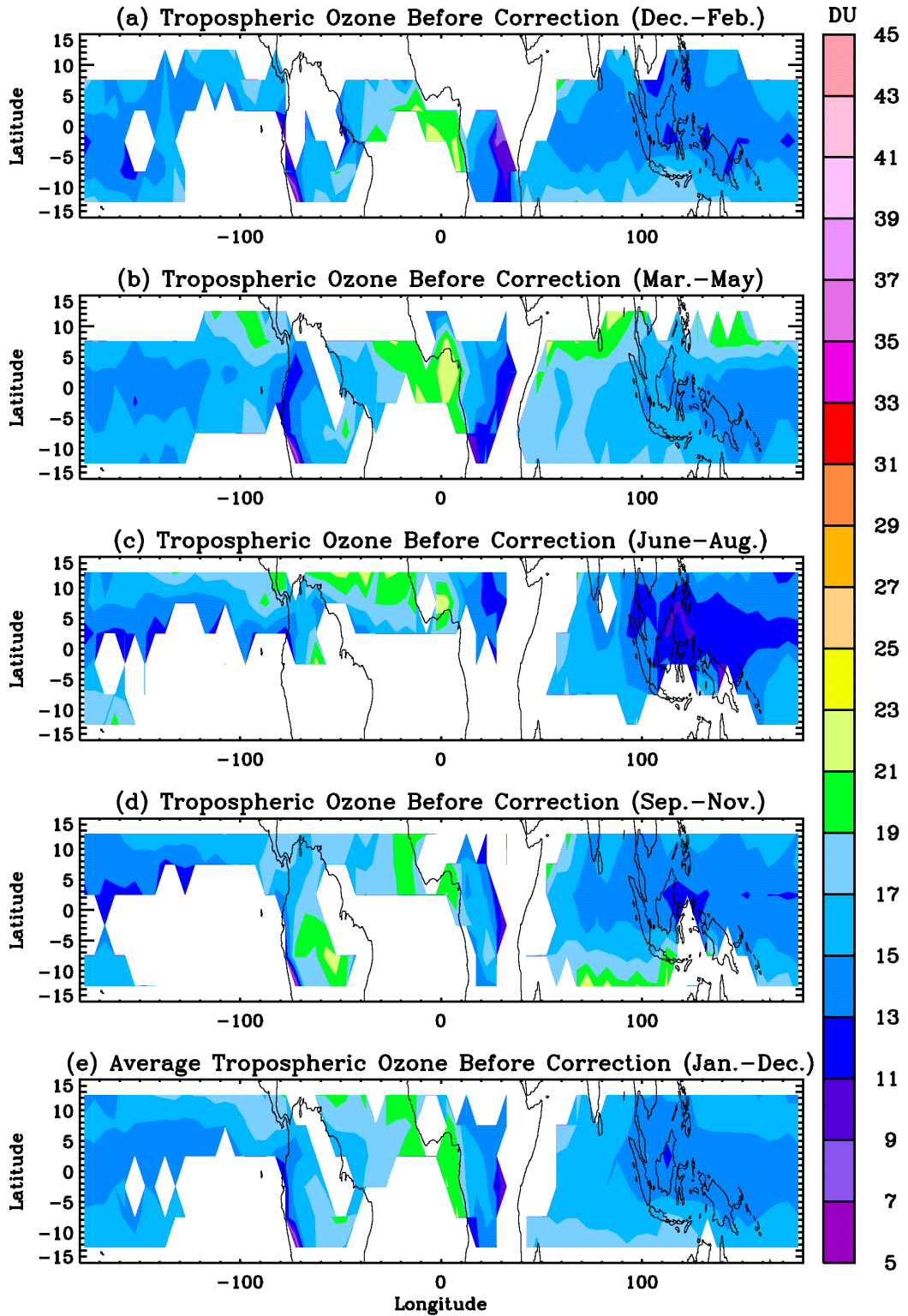


Figure 6.8 Same as Figure 6.7 except for after correcting the errors shown in Figure 6.6, i.e., the difference between Figure 6.7 and Figure 6.6.



**Figure 6.9** Same as Figure 6.5 except for the derived tropospheric ozone column from high-reflectivity clouds (reflectivity  $\geq 80\%$  and THIR CTP  $\leq 300$  hPa) before correcting  $\Delta\Omega_{strat}$  and  $\Delta\Omega_{clr}$ .

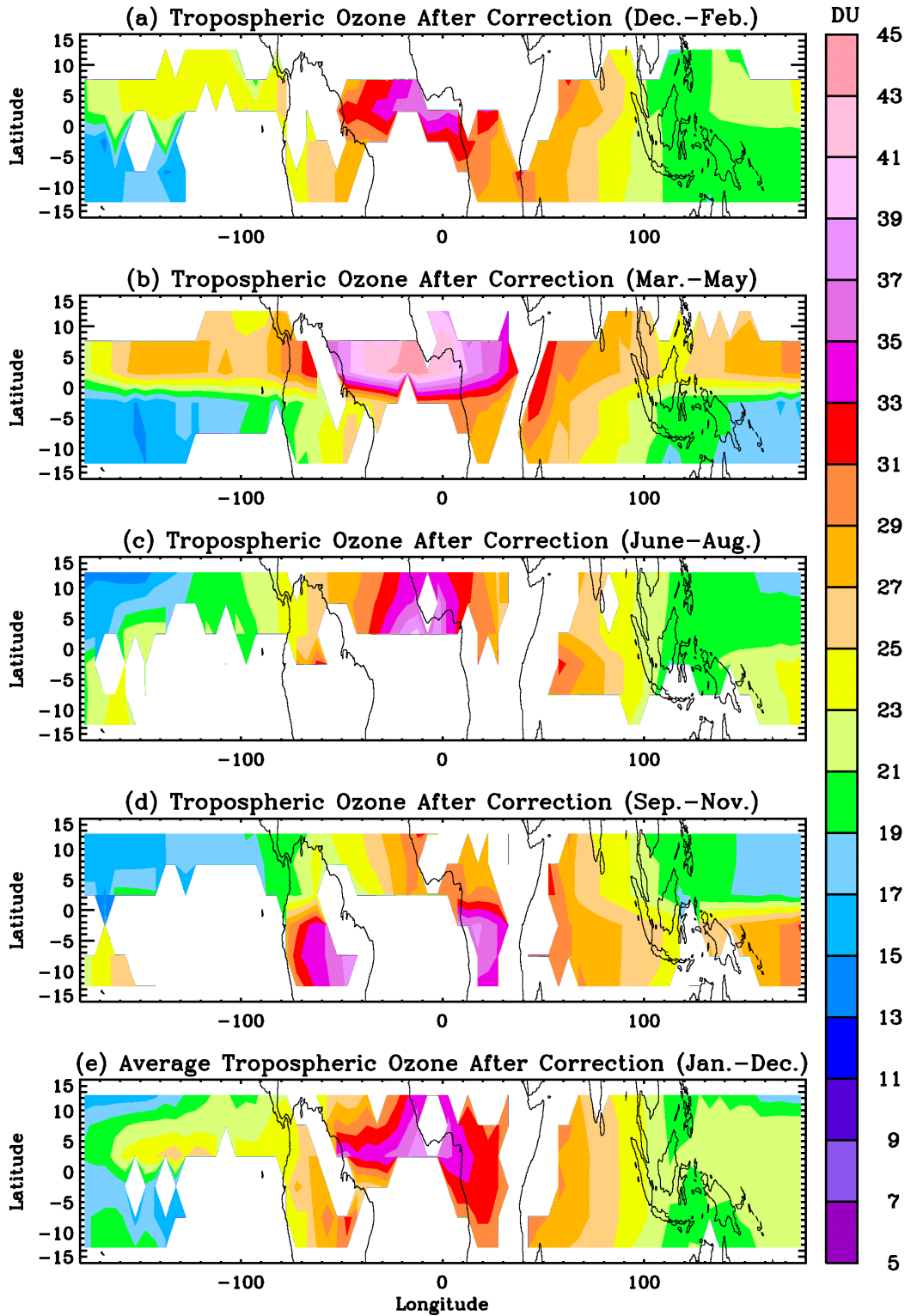


Figure 6.10 Same as Figure 6.9 except for after correcting  $\Delta\Omega_{strat}$  and  $\Delta\Omega_{clr}$ .

Figures 6.9 and 6.10 show the seasonally and annually averaged tropospheric ozone derived from the difference between clear total ozone and ozone above high reflectivity clouds during 1979-1983 before and after correcting  $\Delta\Omega_{trop}$ , respectively. Only clear-sky measurements that coexist with high-reflectivity clouds in the same grid box are used. The tropospheric ozone values before the correction are always less than 25 DU, demonstrating that they are underestimated. However, the corrected tropospheric ozone typically exhibits more realistic values and shows a wave-1 pattern that is highest over the Atlantic Ocean and Africa and lowest over the western Pacific Ocean. The much more realistic tropospheric ozone values support our analysis about OREs associated with clouds. Similar to the ICOAEN effect and  $\Delta\Omega_{trop}$ , the large tropospheric ozone value (39-45 DU) shown in March-May in the North Atlantic Ocean and north Africa are probably artifacts caused by the correction.

## 6.5 Errors in Tropospheric Ozone Derivation Using the CCP and CCD Methods

The error analysis discussed above shows that large errors occur in the derived tropospheric ozone with the use of the cloudy/clear difference method. In the above discussion, clouds with reflectivity  $\geq 80\%$  and THIR CTP  $\leq 300$  hPa are used. However, to reduce errors, the operational CCD [Ziemke *et al.*, 1998] and CCP [Newchurch *et al.*, 2002] methods use different cloud points that are closer to the tropopause. For example, to derive the SOC in a  $5^\circ \times 5^\circ$  grid in a month, the CCD method uses only those cloud points with monthly minimum ozone above the clouds, and the CCP method uses only the six cloud points with minimum ozone above the clouds within each 5 days. To see how and why the errors are reduced in the CCP and CCD methods, we repeat the same processes discussed in Section 6.1 through Section 6.4 but with the corresponding cloud points as used in the CCP and CCD methods, respectively. Table 6.1 compares the derived parameters using the CCP and CCD cloud points with those using all cloud points (reflectivity  $\geq 80\%$  and THIR CTP  $\leq 300$  hPa) for two broad regions, the Atlantic Ocean and Africa ( $15^\circ\text{S}$ - $15^\circ\text{N}$ ,  $60^\circ\text{W}$ - $60^\circ\text{E}$ ) and the Pacific Ocean ( $15^\circ\text{S}$ - $15^\circ\text{N}$ ,  $120^\circ\text{E}$ - $120^\circ\text{W}$ ). Although the CCD method does not use cloud points over the Atlantic Ocean and Africa to derive SOC, we still apply the CCD method to cloud points in these regions to evaluate how good it is to use them in deriving tropospheric ozone. The parameters include the CTP, the overestimated upper tropospheric ozone  $\Delta\Omega_{uptrop}$ , the cloud-height-induced error in OZAC  $\Delta\Omega_{clhgt}$ , the ICOAEN effect, the cloudy TOC excess  $\Delta\Omega_{excess}$  after correcting cloud-height-

induced errors and incorrect tropospheric climatology, the error in the derived stratospheric ozone  $\Delta\Omega_{strat}$ , the derived stratospheric ozone before corrections  $\Omega_{bstrat}$ , the derived stratospheric after corrections  $\Omega_{astrat}$ , the derived tropospheric ozone before corrections  $\Omega_{btrop}$ , and the derived tropospheric ozone after corrections  $\Omega_{atrop}$ . The values in Table 6.1 are averaged from all the monthly mean values in those regions.

**Table 6.1** Comparison of average values for the derived parameters using all cloud points, CCP cloud points, and CCD cloud points, respectively during 1979-1983 N7 TOMS period over the Atlantic Ocean and Africa (15°S-15°N, 60°W-60°E) and the Pacific Ocean (15°S-15°N, 120°E-120°W).

| Parameters                   | All Cloud Points          |               | CCP Cloud Points          |               | CCD Cloud Points           |               |
|------------------------------|---------------------------|---------------|---------------------------|---------------|----------------------------|---------------|
|                              | Atlantic Ocean and Africa | Pacific Ocean | Atlantic Ocean and Africa | Pacific Ocean | Atlantic Ocean and Africa* | Pacific Ocean |
| CTP (hPa)                    | 211.6 ± 16.3              | 193.0 ± 13.8  | 165.7 ± 10.8              | 163.2 ± 9.1   | 169.8 ± 16.9               | 161.9 ± 17.4  |
| $\Delta\Omega_{uptrop}$ (DU) | 5.8 ± 1.2                 | 3.4 ± 1.2     | 3.7 ± 0.8                 | 2.7 ± 1.0     | 3.9 ± 1.0                  | 2.6 ± 1.1     |
| $\Delta\Omega_{cldhgt}$ (DU) | -3.3 ± 1.1                | -3.4 ± 1.1    | -3.8 ± 1.3                | -4.0 ± 1.6    | -4.5 ± 1.6                 | -4.6 ± 1.6    |
| ICOAEN (DU)                  | 8.4 ± 4.4                 | 4.4 ± 2.8     | 3.3 ± 4.7                 | -0.1 ± 3.3    | 0.8 ± 5.2                  | -2.7 ± 3.8    |
| $\Delta\Omega_{excess}$ (DU) | 12.1 ± 3.5                | 8.6 ± 2.6     | 7.0 ± 3.8                 | 4.1 ± 3.1     | 4.5 ± 4.2                  | 1.4 ± 3.5     |
| $\Delta\Omega_{strat}$ (DU)  | 14.6 ± 4.2                | 8.6 ± 3.3     | 6.8 ± 4.0                 | 2.7 ± 3.6     | 3.9 ± 4.3                  | -0.6 ± 4.1    |
| $\Omega_{bstrat}$ (DU)       | 250.0 ± 9.1               | 241.2 ± 8.5   | 242.2 ± 8.7               | 235.9 ± 9.7   | 240.4 ± 8.9                | 233.0 ± 8.8   |
| $\Omega_{astrat}$ (DU)       | 235.4 ± 9.9               | 232.6 ± 9.4   | 235.4 ± 9.7               | 233.2 ± 9.2   | 236.5 ± 9.8                | 233.6 ± 9.2   |
| $\Omega_{btrop}$ (DU)        | 17.2 ± 3.0                | 15.0 ± 2.1    | 24.8 ± 3.2                | 20.7 ± 2.6    | 27.8 ± 3.8                 | 23.9 ± 3.3    |
| $\Omega_{atrop}$ (DU)        | 31.3 ± 5.3                | 20.8 ± 4.4    | 31.1 ± 5.3                | 20.7 ± 4.4    | 31.3 ± 5.3                 | 20.5 ± 4.4    |

\* The CCD method actually does not use the cloud points over the Atlantic Ocean and Africa.

Figures 6.11 (a) and (b) shows the annually averaged  $\Delta\Omega_{strat}$  using the CCP and CCD cloud points, respectively. Compared to Figure 6.6 (e), we can see that the  $\Delta\Omega_{strat}$  is much smaller using the CCP and CCD cloud points. With the use of the CCP cloud points, the  $\Delta\Omega_{strat}$  is smaller by 7.8 DU over the Atlantic Ocean and Africa and by 5.9 DU over the Pacific Ocean according to Table 6.1. The  $\Delta\Omega_{strat}$  is smaller by an additional ~3 DU when the CCD cloud points are used than when the CCP cloud points are used. We can see from Table 6.1 that the average CTP for CCP cloud points or CCD cloud points is smaller by 30-50 hPa than that of all cloud points, in turn decreasing the  $\Delta\Omega_{uptrop}$  by only 1-2 DU and increasing the negative  $\Delta\Omega_{cldhgt}$  in magnitude by only 1-2 DU. Therefore, in terms of CTPs, using CCP and CCD cloud points improves the derived tropospheric ozone by ~2-3 DU over the Atlantic Ocean and Africa and ~1-

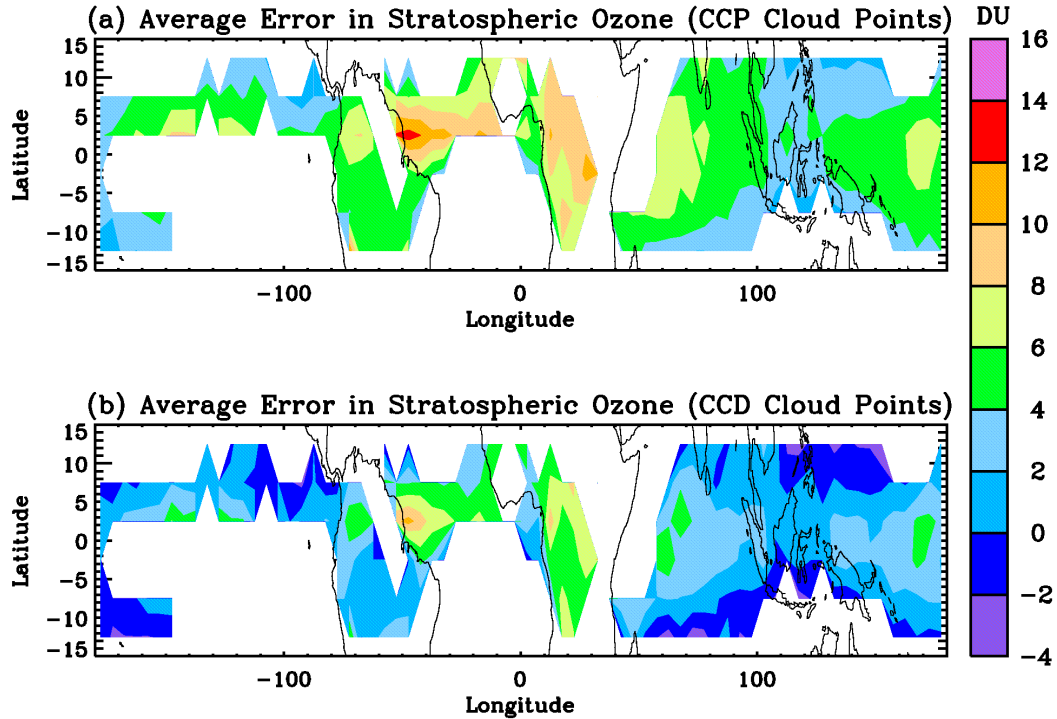


**Figure 6.11** (a) Same as Figure 6.6 (e) except using the CCP cloud points. (b) Same as Figure 6.6 (e) except using the CCD cloud points.

2 DU over the Pacific Ocean. It is the reduction in the ICOAEN effect that contributes more to improving the derived tropospheric ozone when using the CCP and CCD cloud points. First, clouds with minimum OZAC may be those clouds with less ozone distributed in the clouds, especially in the upper part of the clouds (i.e., the CCP and CCD methods only use cloud points with less ICOAEN effect). Second, clouds with minimum OZAC may be those clouds with extreme low values within a period; so selecting those clouds may partly cancel or even over-cancel the ICOAEN effect, leading to smaller  $\Delta\Omega_{strat}$  values. According to Table 6.1, the ICOAEN effect is negative over the Pacific Ocean for both using CCP and CCD cloud points, but of course this is incorrect. This result occurs because the values listed in Table 6.1, which are derived from the TOC differences between all the clear-sky points and a few cloud points with extremely low values, cannot represent the actual ICOAEN effect. But the processes from Section 6.1 to Section 6.4 still serve to correct errors and make the assumption of the same clear/cloudy SOC more

accurate. Although the derived stratospheric ozone and tropospheric ozone before corrections are very different using different cloud points, the corresponding values after corrections are almost the same, within 1 DU, as shown in Table 6.1 and Figure 6.12, Figure 6.13, and Figures 6.5-6.10 (e).

The final CCP tropospheric ozone corrects the  $\Delta\Omega_{strat}$  during the N7 TOMS period. In the CCD method, only cloud points with minimum OZAC over the Pacific Ocean are used, therefore containing very small  $\Delta\Omega_{strat}$  in the N7 TOMS period,  $\sim 0.6$  DU as shown in Table 6.1. Previous sections have shown the assumption of the same cloudy/clear SOC is more correct during the EP TOMS period; however, using the minimum OZAC will over-correct other positive errors in the derived stratospheric ozone and overestimates the derived tropospheric ozone. The CCP method takes the N7/EP offset ( $\sim 4.3$  DU) into account in the correction of OREs associated with clouds [Newchurch *et al.*, 2002]. The CCD method does not take this N7/EP bias into account in the archived data, but the authors suggest subtracting 5 DU from the tropospheric ozone derived in the EP TOMS period [Ziemke *et al.*, 2000].

The CCD method assumes zonally invariant stratospheric ozone and derives stratospheric ozone over the Pacific Ocean (120°E-120°W). Table 6.1 shows that the derived tropospheric ozone will be overestimated by about 0.6 DU over the Pacific Ocean. Applying this derived stratospheric ozone over the Pacific Ocean,  $\sim 233.6$  DU, to areas over the Atlantic Ocean and Africa will overestimate the derived tropospheric ozone by  $\sim 3.5$  DU ( $0.6 + 236.5 - 233.6$ ). The derived tropospheric ozone is expected to be larger by  $\sim 2$  DU with the use of CCD method than with the CCP method in the N7 TOMS period, according to the above analysis. Comparison of the archived CCD and CCP tropospheric ozone shows that the average CCD tropospheric ozone (29.0 DU) is larger by 3.0 DU than the corresponding CCP value (26.0 DU) in 1979-1992, and larger by 7.9 DU (about 3.0 DU after subtracting the N7/EP bias in the CCD values) than the corresponding CCP value (26.4 DU) in 1997-2000.

## 6.6 Summary

This chapter estimates the ozone absorption enhancement in the clouds (i.e., ICOAEN effect) from the cloudy/clear TOC difference, and evaluates OREs in the derived tropospheric ozone using the cloudy/clear difference method in the tropics (15°S-15°N). All the high-reflectivity ( $\geq 80\%$ ) and high-

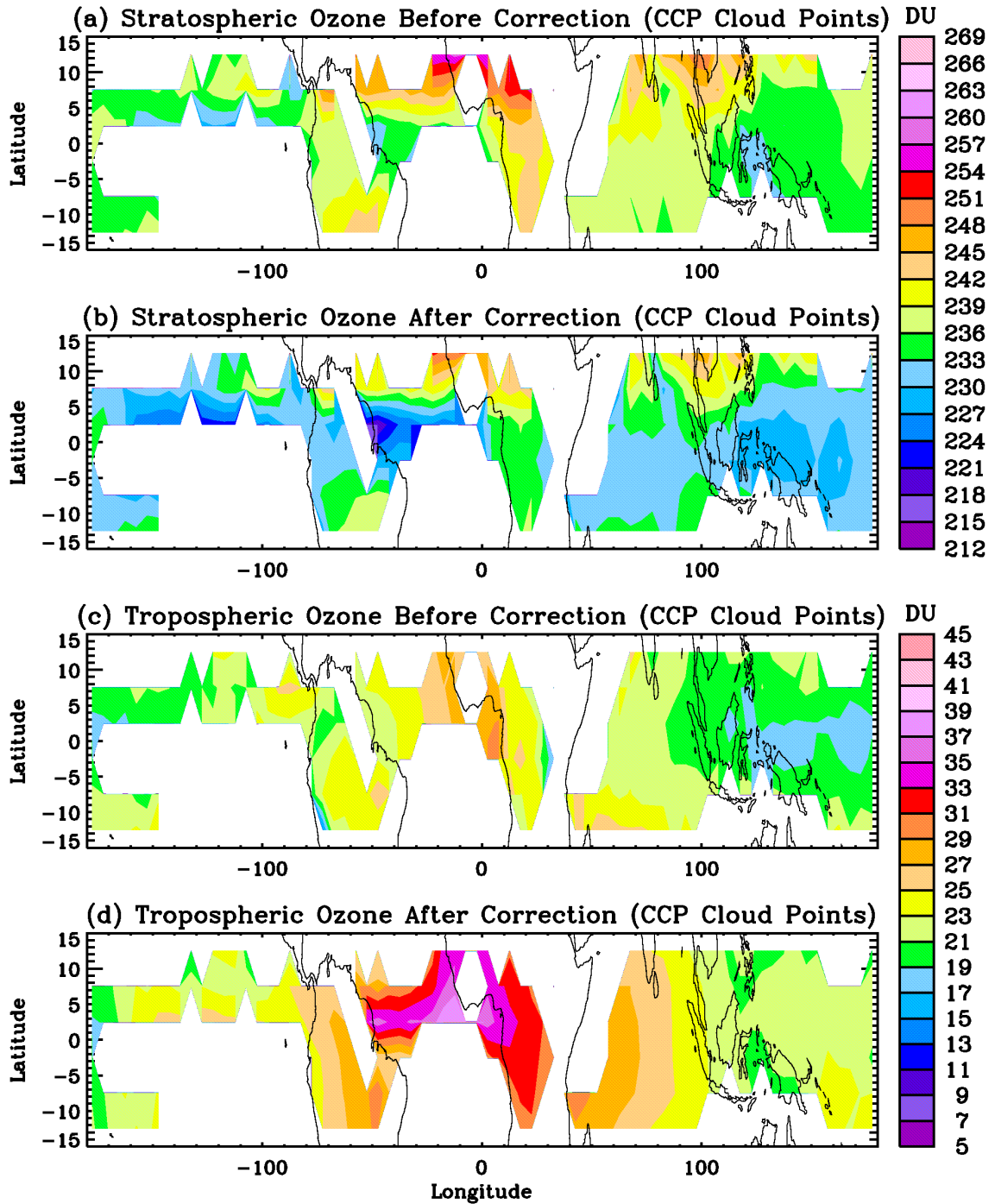


**Figure 6.12** (a) Annually averaged SOC derived using CCP cloud points during the 1979-1983 N7 TOMS data before correcting  $\Delta\Omega_{strat}$ . (b) Same as (a) except after correcting  $\Delta\Omega_{strat}$ . (c) Same as (a) except for the derived tropospheric ozone before correcting  $\Delta\Omega_{strat}$  and  $\Delta\Omega_{clr}$ . (d) Same as (a) except after correcting  $\Delta\Omega_{strat}$  and  $\Delta\Omega_{clr}$ .

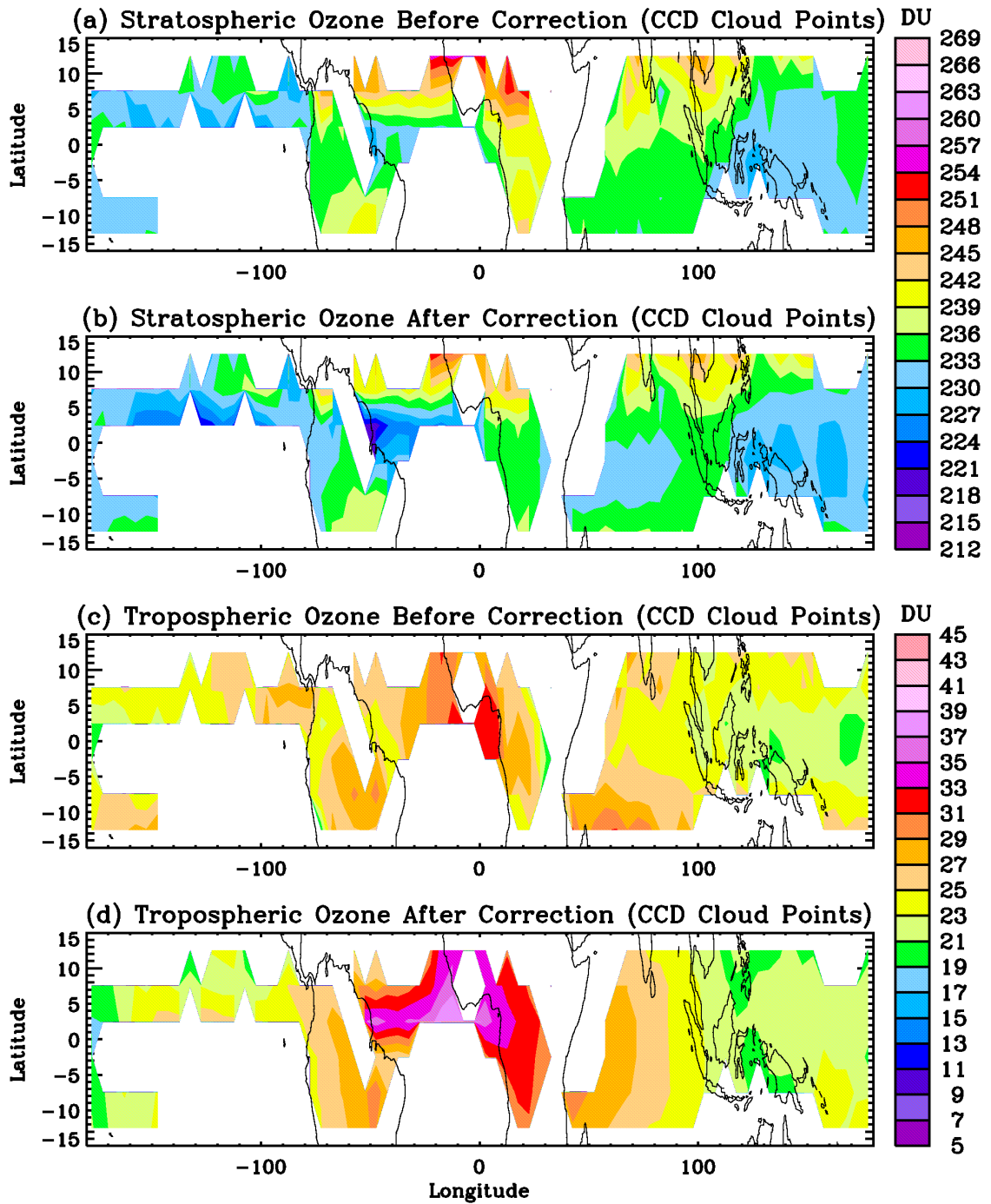


Figure 6.13 Same as Figure 6.12 except using the CCD cloud points.

altitude (THIR CTP  $\leq$  300 hPa) cloud pixels are used. Using collocated THIR CTPs, we correct cloud-height-induced errors and compute the monthly mean cloudy/clear TOC difference during 1979-1983. The cloud-height-induced error in OZAC is  $-3.4 \pm 1.0$  DU on average. The computed cloud/clear TOC difference still contains errors arising from the a priori climatological profiles in the TOMS V7 algorithm. The SHADOZ measurements are used to approximate the actual tropospheric ozone for correcting errors in clear TOC and OZBC. The corrected TOC cloudy/clear difference indicates consistent cloudy ozone excess, of 11-15 DU over the Atlantic Ocean and Africa and 7-11 DU over the Pacific Ocean. The dynamical and chemical contributions to cloudy ozone excess are estimated to be small. We ascribe cloudy ozone excess to the ICOAEN effect and to the nonlinear calibration error probably in the N7 TOMS data. The non-linear calibration error, derived from the difference in the cloudy/clear TOC difference between N7 TOMS data and EP TOMS data, is about  $4.4 \pm 1.1$  DU. The estimated ICOAEN effect is typically about 5-13 DU over the Atlantic Ocean and Africa and about 1-7 DU over the Pacific Ocean. The larger ICOAEN effect over the Atlantic Ocean and Africa occurs probably because of the higher surface ozone environment so that the convection redistributes more ozone in the clouds. In addition, the clouds usually do not reach the tropopause, and the OZAC includes some of the upper tropospheric ozone, overestimating the stratospheric ozone by about  $4.2 \pm 1.2$  DU. The error in the derived stratospheric ozone  $\Delta\Omega_{strat}$  from OZAC is then the sum of the cloud-height-induced error in OZAC, the ICOAEN effect, the nonlinear calibration error, and the inclusion of upper tropospheric ozone. Large errors occur in the derived stratospheric ozone, typically 11-21 DU over the Atlantic Ocean and Africa and 5-15 DU over the Pacific Ocean. Correcting this error in the derived stratospheric ozone works toward making the assumption of the same cloudy/clear stratospheric ozone more accurate. The derived stratospheric ozone before corrections exhibits a typical wave-1 pattern, highest over the Atlantic Ocean and Africa and lowest over the Pacific Ocean. However, the stratospheric ozone after corrections is relatively more zonally invariant, suggesting that the typical stratospheric wave-1 pattern may result from artifacts arising from OREs associated with clouds. The derived tropospheric ozone before the corrections is always smaller than 25 DU, indicating that the derived tropospheric ozone will be underestimated. The tropospheric ozone after the correction exhibits more realistic values comparable to observed SHADOZ data.

The operational CCP and CCD methods do not use all the cloud points for tropospheric ozone derivation, but use the six cloud points with minimum OZAC in a five-day period and the cloud points with monthly minimum OZAC, respectively. Repeating the same processes as using all cloud points finds that the error in the derived stratospheric ozone is largely reduced by 6-8 DU using the CCP cloud points and by 9-11 DU using the CCD cloud points. In the N7 TOMS period, the error using the CCD cloud points is negligible and the error using the CCP cloud points is about 3-7 DU. Although the average CTP using the CCP and CCD cloud points is smaller by 30-50 hPa than that using all high-reflectivity cloudy pixels, using such higher-altitude clouds improves the derived stratospheric ozone by 2-3 DU. It is the selection of minimum OZAC that greatly improves the derived tropospheric ozone. Clouds with minimum OZAC may be clouds with a small ICOAEN effect. In addition, those clouds may show extremely low values of OZAC within a period so that the use of such clouds cancels other positive errors in the derived stratospheric ozone. Although the assumption of the same cloudy/clear stratospheric ozone is more valid in the EP TOMS period, using clouds with minimum OZAC overestimates the derived tropospheric ozone instead. The archived CCP data are corrected with the above described OREs associated with clouds, and the authors of the CCD method suggest subtracting 5 DU from the derived tropospheric ozone in the EP TOMS period. The assumption of zonally invariant stratospheric ozone may overestimate the derived tropospheric ozone over the Atlantic Ocean and Africa by ~3 DU.

## CHAPTER 7

### ANALYSIS OF ANOMALY OCCURRENCE

Comparison with collocated THIR CTPs indicates large errors in the assumed CTPs, as was shown in Section 4.1. Such large errors in the assumed CTPs can lead to large errors in the derived TOC, especially due to the error in the added OZBC. Applying the  $\Delta P$  correction to tropical areas consistently increases the ozone over high-altitude cloudy areas, as shown in Chapter 6, actually leading to consistent POAs with strong correlation coefficients. Therefore, cloud-height errors play an important role in affecting the fraction of occurrence of OAs and the partition of POAs and NOAs. Correcting cloud-height-related errors in the TOC facilitates our understanding of OAs that result from other reasons.

We applied the  $\Delta P$  correction to TOMS V7 data during 1979-1983 when THIR data are available. Section 3.2 shows that there is not much annual variation in OA distribution except for the N7/EP TOMS offset. The cloud height errors should be similar from year to year except at some local regions affected by dynamic perturbations such as El Niño events. Correcting cloud-height-related errors is expected to have similar effects on TOMS data in other years for which THIR data are not available. Section 7.1 shows the distribution of OAs after the  $\Delta P$  correction in TOMS V7 data during 1979-1983. The seasonal variation of OAs after the  $\Delta P$  correction is shown in Section 7.2. Section 7.3 analyzes the formation of TOMS data OAs that result from reasons other than incorrect cloud heights.

#### **7.1 Ozone Anomaly Distribution After the $\Delta P$ Correction**

Figure 7.1 shows the daily frequency distribution of correlation coefficients between TOC and reflectivity in January and July 1980, similar to Figure 3.3 except that Figure 7.1 depicts conditions after

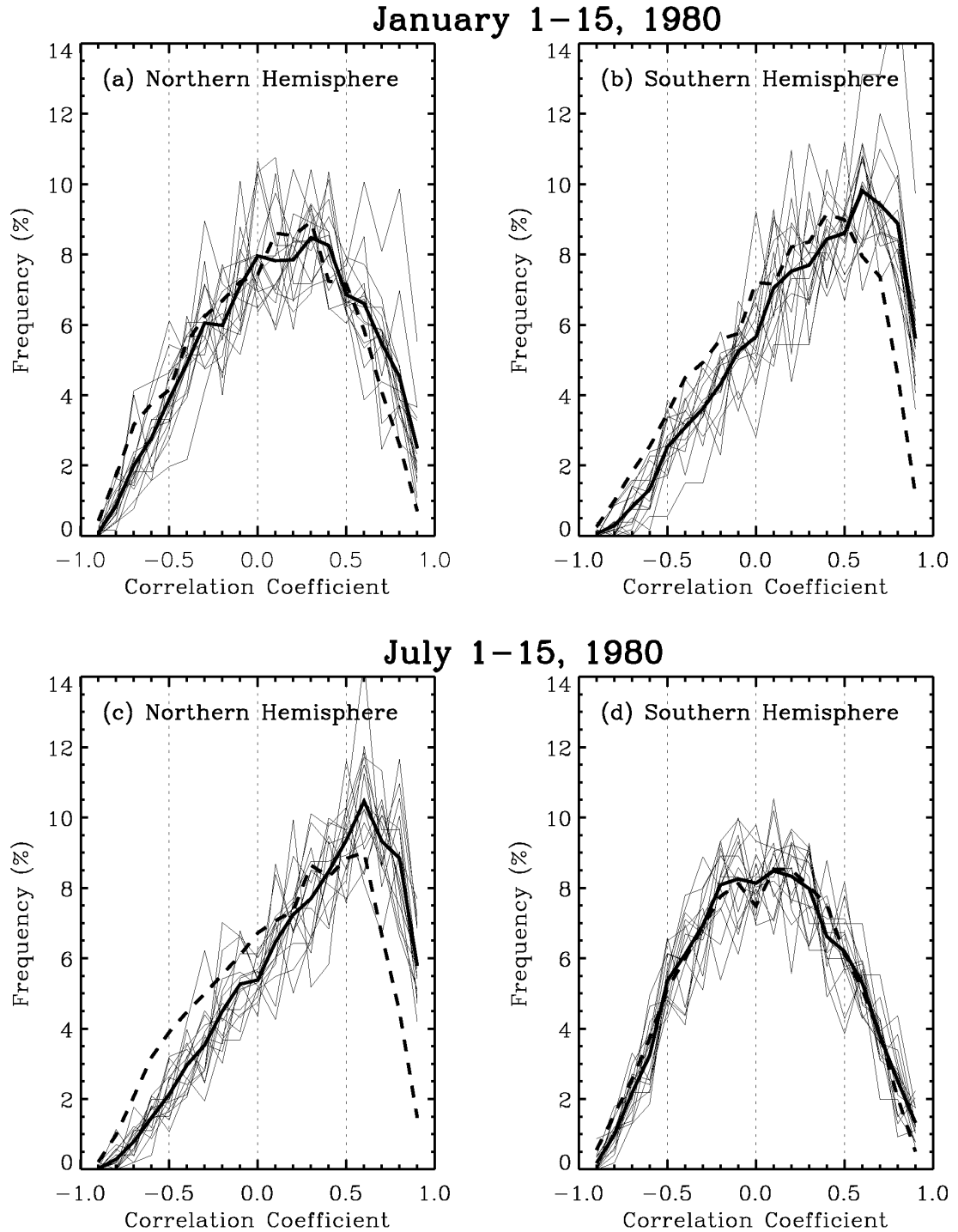


**Figure 7.1** Same as Figure 3.3 except after the  $\Delta P$  correction. The solid and dashed thick curves are the average distributions over the period after and before the  $\Delta P$  correction, respectively.

the  $\Delta P$  correction. Compared to the frequency distributions before the  $\Delta P$  correction, the corrected frequency distributions in the summer hemisphere shift right with more positive values, and the frequency distributions in the winter hemisphere do not shift much. On average, the fraction of NOAs decreases from 9.3% to 5.9% and the fraction of POAs increases from 20.8% to 29.0%. Because larger cloud height errors occur for high-altitude clouds, the changes are larger in the summer when there are more high-altitude clouds [Stowe *et al.*, 1989]. Because of the smaller ozone/reflectivity slopes for tropical OAs than mid-latitude OAs, cloud-height errors comprise a larger portion of the slopes of tropical OAs. The largest change occurs in the tropical summer hemisphere ( $0^{\circ}$ - $15^{\circ}$ N in July and  $15^{\circ}$ S- $0^{\circ}$  in January), where the fraction of POAs increases from 25.5% to 55.4% and the fraction of NOAs decreases from 5.2% to 1.1%.

Figures 7.2 (a) and (b) show the average spatial fraction distributions of POAs and NOAs after the  $\Delta P$  correction during 1979-1983, and Figures 7.2 (c) and (d) show changes compared to OAs before the  $\Delta P$  correction. Positive ozone anomalies with such high fractions as 50-70% occur extensively in the tropical and subtropical convective cloudy areas. These areas include the Pacific Ocean, the Indian Ocean, China, the tropical Atlantic Ocean, central Africa, and South America, some of which show dramatic increases by 20-50%. Most of the tropical NOAs seen before the  $\Delta P$  correction are caused by incorrect cloud-heights, and there are almost no tropical NOAs after the  $\Delta P$  correction. This large change in fraction of POAs and NOAs occurs because CTHs for tropical high-reflectivity clouds are mostly underestimated in the TOMS V7 algorithm. The  $\Delta P$  correction decreases the fraction of POAs by 5-10% over WCSAF and WCSAM because the assumed CTHs are sometimes overestimated for low marine stratocumulus clouds. The fractions of POAs and NOAs in mid-latitude cloudy regions change, usually within  $\pm 10\%$ , because of the  $\Delta P$  correction. Most of the regions show much fewer NOAs than POAs. The main region with more NOAs than POAs occurs in the Southern Hemisphere at  $60^{\circ}$ S- $50^{\circ}$ S. Another region with more NOAs lies in North Africa, but this region has very few broken cloud fields. On average, the fractions of POAs and NOAs are  $27.4 \pm 15.8\%$  and  $7.2 \pm 4.8\%$ , respectively. But the ratio of the fraction of POAs to that of NOAs is much larger in tropical areas than mid-latitudes. In tropical areas ( $15^{\circ}$ S- $15^{\circ}$ N), the average fractions of POAs and NOAs are  $42.1 \pm 16.2\%$  and  $3.1 \pm 3.2\%$ , respectively. In mid-latitudes ( $60^{\circ}$ S- $30^{\circ}$ S and  $30^{\circ}$ N- $60^{\circ}$ N), the average fractions of POAs and NOAs are  $20.8 \pm 6.2\%$  and  $9.1 \pm 3.7\%$ , respectively.

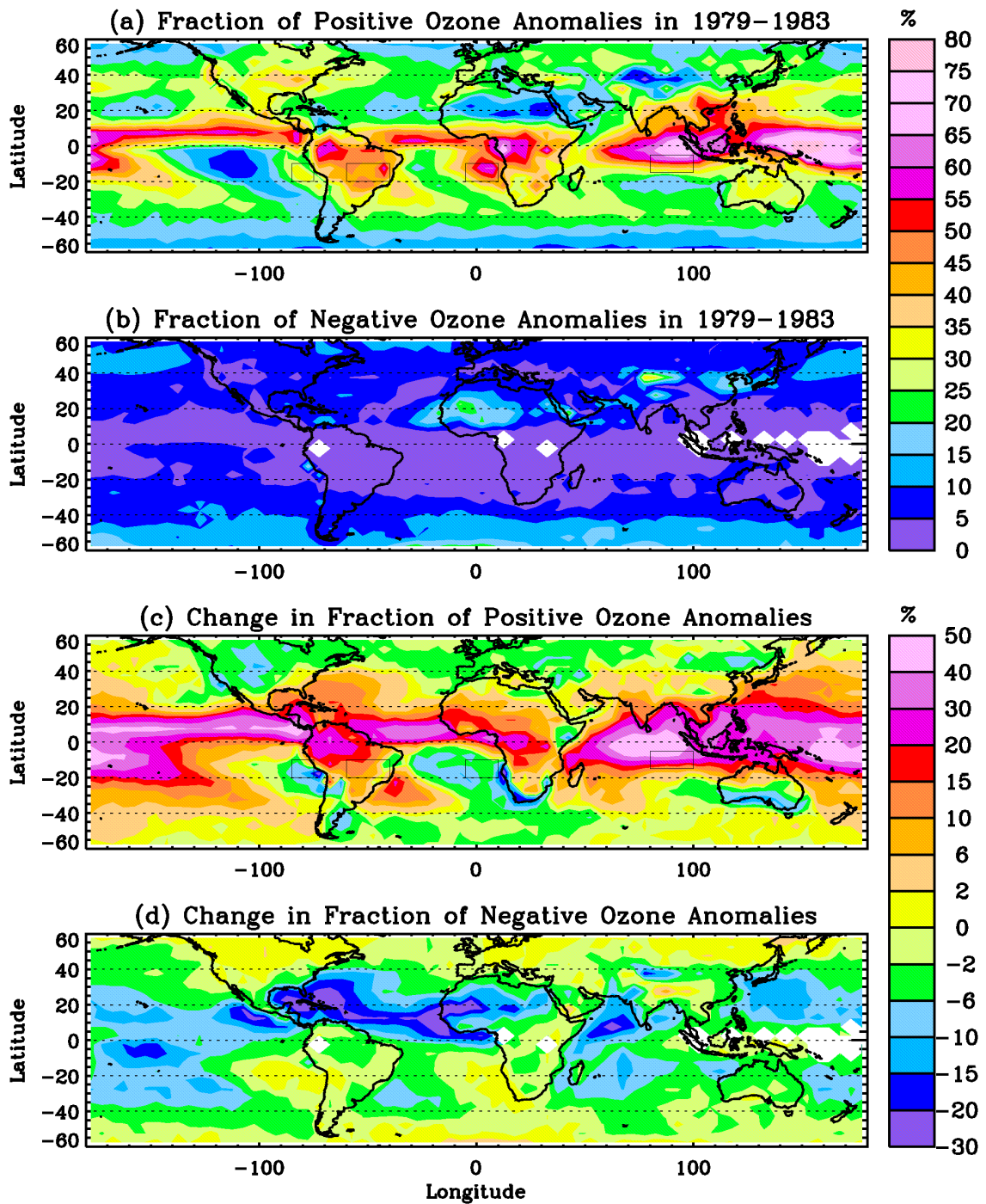


**Figure 7.2** OAs in 1978-1983 period after the  $\Delta P$  correction. (a) Average spatial fraction distribution of POAs. (b) Same as (a) except for NOAs. (c) and (d) are the changes in fractions of POAs and NOAs because of the  $\Delta P$  correction.

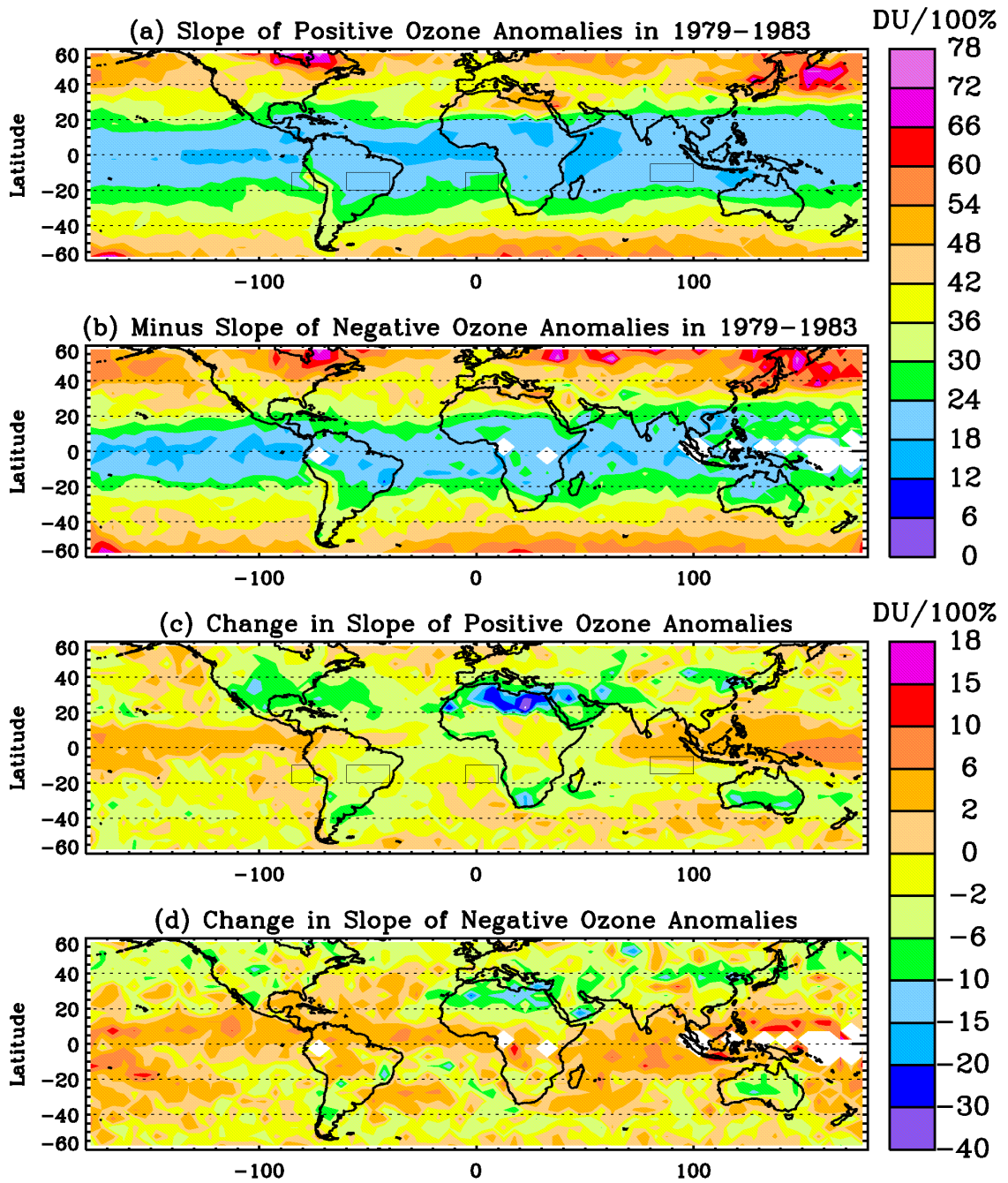
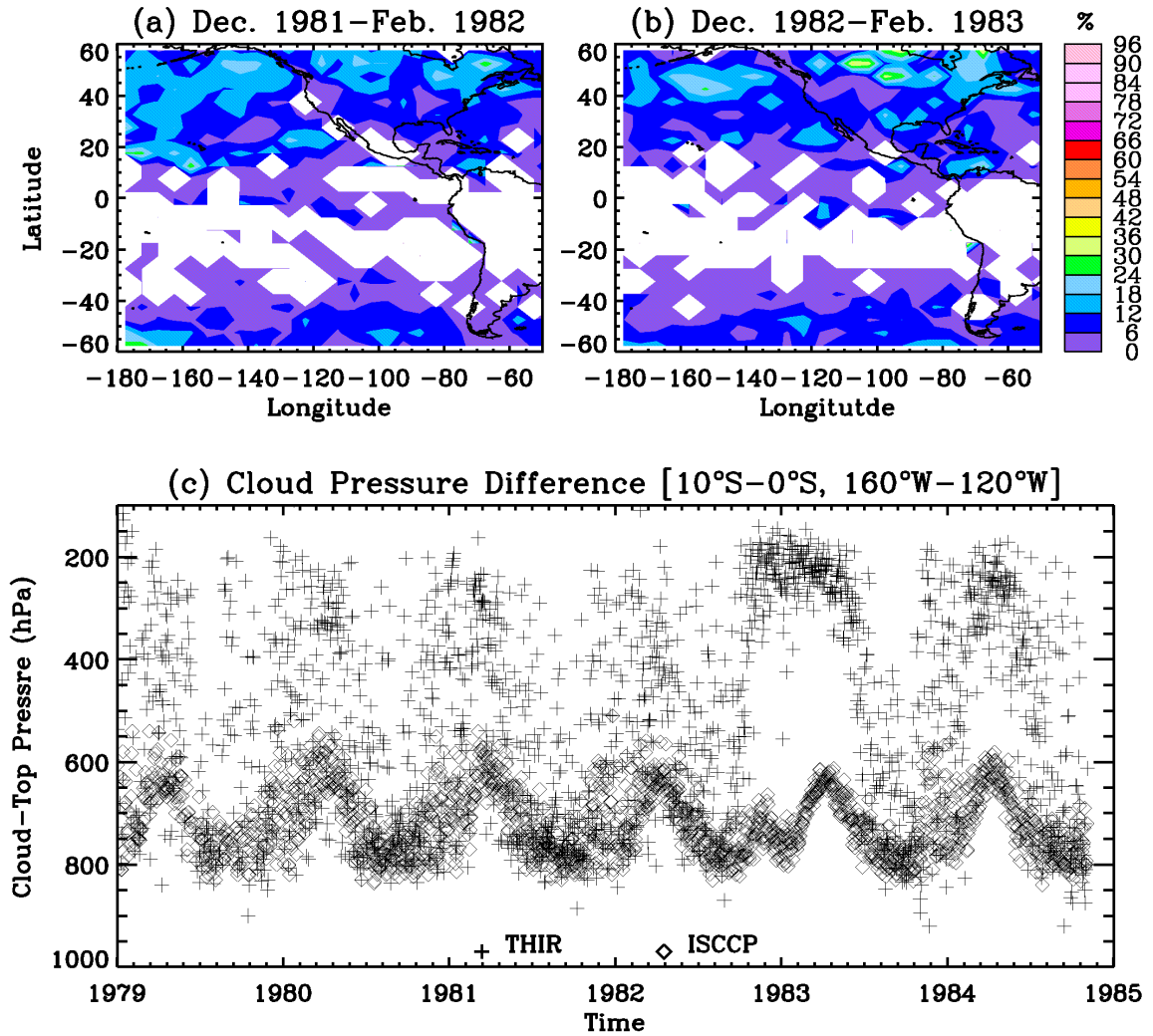


Figure 7.3 Same as Figure 7.2 except for the linear regression ozone/reflectivity slopes of OAs.

Figures 7.3 (a) and (b) show average ozone/reflectivity slopes for POAs and NOAs after the  $\Delta P$  correction during 1979-1983, and Figures 7.3 (c) and (d) show changes relative to slopes before the  $\Delta P$  correction. Compared to large changes shown in the average spatial fraction distribution, changes in slope are relatively small. The slope changes for both POAs and NOAs are usually within  $\pm 10$  DU/100% at all regions. In the tropical and subtropical convective cloudy areas, where there is a dramatic increase in the fraction of POAs, the slope increases by about 6 DU/100% over the tropical Pacific Ocean and nearly zero in the other regions. It may seem that these small slope changes are not consistent with the large cloud-height errors shown in Figure 4.1 and the large fraction changes. However, the smaller change in slope occurs because cloud-height errors could be negative or positive, so the slope changes for individual OAs could increase or decrease. Furthermore, although the  $\Delta P$  correction leads to significant changes in the slopes for regions with large cloud-height errors, it also transforms some non-OAs or even OAs of opposite signs to OAs with smaller slopes so that the average slope of OAs does not change much.

Although there is a large difference in the fraction of NOAs before the  $\Delta P$  correction between El Niño periods and non-El Niño periods over the eastern Pacific Ocean, there are almost no NOAs for both periods after the  $\Delta P$  correction as shown in Figures 7.4 (a) and (b). The shift in the convection pattern due to El Niño events increases not only cloud occurrence but also cloud height over the eastern Pacific Ocean [Wang *et al.*, 1996]. However, the ISCCP cloud climatology used in TOMS is from July 1983 to December 1990. When the ISCCP cloud climatology is not available during the other years, cloud climatology from mostly non-El Niño years is used. The assumed CTPs, mostly from 600 hPa to 900 hPa in the tropical eastern Pacific Ocean in all months, are much greater than the actual CTPs during the 1982-1983 and 1997-1998 El Niño events as shown in Figure 7.4 (c), leading to the large increase in fraction of NOAs. The much smaller increase in the 1986-1987 and 1991-1992 El Niño events relative to the non-El Niño periods is not only because of the weaker El Niño activities but also because the TOMS algorithm uses the ISCCP climatology from these two years.

Although we are not able to perform the  $\Delta P$  correction to EP TOMS data, similar corrections would lead to more POAs than NOAs in both tropical areas and mid-latitudes. However, because of the N7/EP TOMS offset, the fraction of NOAs is larger in EP TOMS data than in N7 TOMS data. This almost constant offset leads to a larger increase of NOAs in EP TOMS in the tropics than at mid-latitudes.



**Figure 7.4** (a) and (b) same as Figure 3.7 (a) and (b) except after the  $\Delta P$  correction, (c) comparison of daily ISCCP CTPs (diamond) used in the TOMS V7 ozone retrieval and collocated THIR CTPs (plus) during 1979–1984 averaged over the eastern Pacific Ocean (10°S–0°S, 160°W–120°W) for scenes with reflectivity greater than 40%.

Because the  $\Delta P$  correction is based on the TOMS standard ozone profiles, it would overestimate or underestimate the cloudy total ozone if the actual lower tropospheric ozone is different from the standard lower tropospheric ozone [Hudson *et al.*, 1995; Klenk *et al.*, 1982]. As shown in Chapter 6, the actual tropospheric ozone is usually smaller (larger) than the TOMS climatological tropospheric ozone over the Pacific Ocean (Atlantic Ocean); therefore, the  $\Delta P$  correction overestimates (underestimates) the fraction and slope of OAs over the western Pacific Ocean (Atlantic Ocean). Considering the incorrect tropospheric climatology used in TOMS data, the slope over the Atlantic Ocean and Africa will be higher than the slope over the Pacific Ocean. However, the extensive distribution of POAs across tropical regions indicates that considering the incorrect tropospheric ozone climatology would not have much effect on the overall OA distribution.

## 7.2 Seasonal and Latitudinal Distribution of Ozone Anomalies

Figure 7.5 shows the seasonal and latitudinal variation of the zonal-mean fraction of POAs and NOAs after the  $\Delta P$  correction during 1979-1983. The fraction of POAs at mid-latitudes peaks in the late spring and summer (25-30%) and is lowest in the winter (10-20%). The maximum fraction of POAs in the tropics follows the motion of ITCZ, while the minimum occurrence in subtropical areas is located immediately north (south) of the tropical peak in the Northern (Southern) Hemisphere. The above zonal feature and the seasonal variation of POAs are consistent with cloud occurrence in these regions [Stowe *et al.*, 1989; Wang *et al.*, 1996]. There is much less variation for NOAs except in the Southern Hemisphere 50°S-60°S. Negative ozone anomalies in this region peak in the late winter and early spring when the area is frequently covered with sea ice.

Figures 7.5 (c) and (d) show the seasonal and latitudinal variation of zonal mean ozone/reflectivity slope for POAs and NOAs. Positive OAs and NOAs show similar variations. In mid-latitudes, the slope is highest from winter to early spring in both hemispheres with a magnitude of 60-80 DU/100%, and is lowest in summer and fall with a magnitude of 30-40 DU/100%. The peak of the OA slope migrates toward the equator in the later spring. In tropical areas, the slope shows very little seasonal variation, with a magnitude of 18-24 DU/100%.

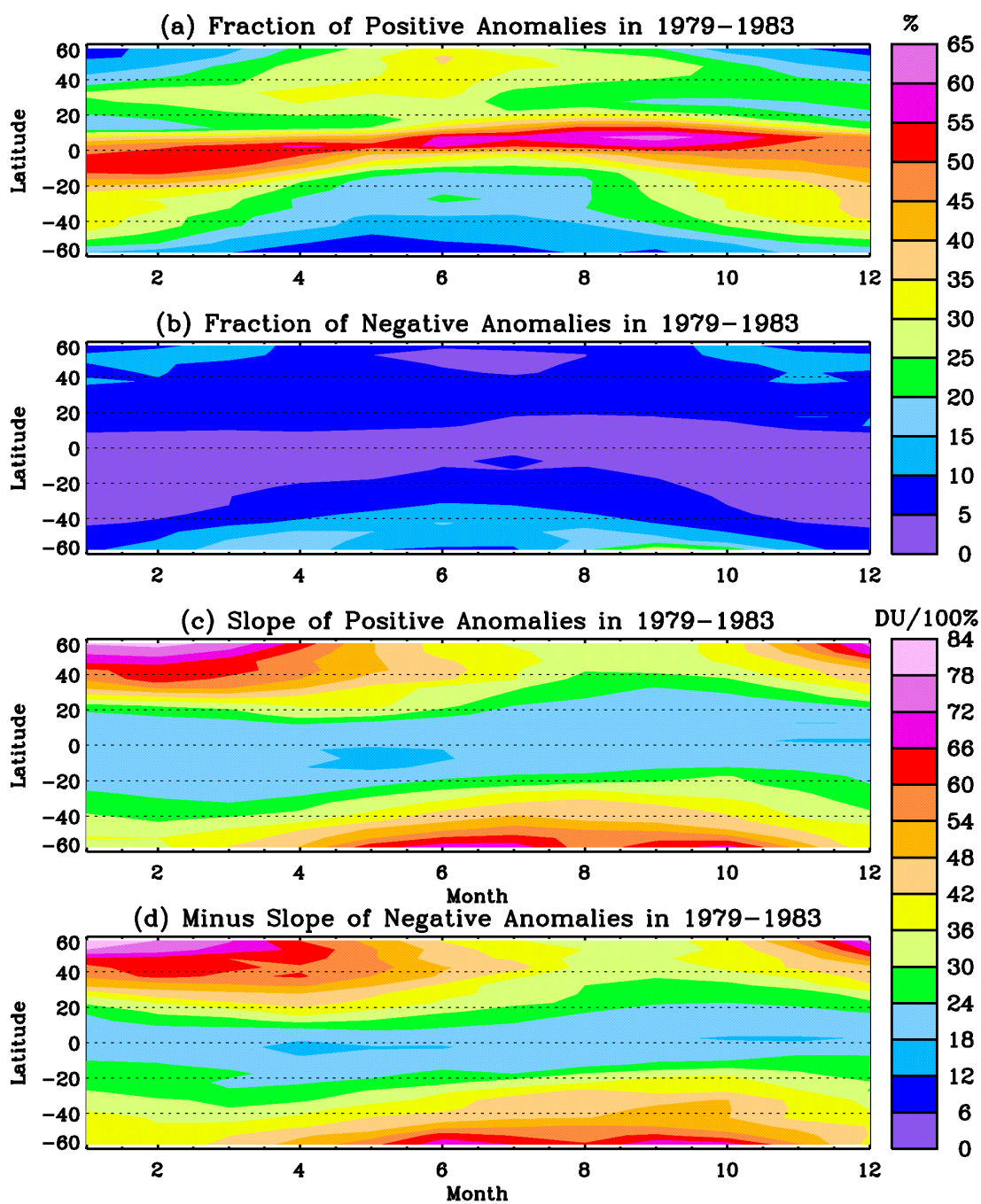


**Figure 7.5** Seasonal and latitudinal variation of OAs during 1979-1983 after the  $\Delta P$  correction. (a) and (b) are zonal average fractions of occurrence for POAs and NOAs, respectively, (c) and (d) are zonal average ozone/reflectivity slopes for POAs and NOAs, respectively.

### 7.3 Analysis of Ozone Anomaly Occurrence Over Cloudy Areas

This section determines the essential causes of OAs from their spatial distribution of fraction and ozone/reflectivity slope, and from their seasonal and latitudinal variations in fraction and slope. Particularly, we focus on the formation of OA major features in regions with a high frequency of broken cloud fields, such as tropical POAs, mid-latitude OAs, and POAs over WCSAF and WCSAM.

#### 7.3.1 Ozone Retrieval Errors Associated with Clouds

More than 90% of the OAs after the  $\Delta P$  correction in tropical convective cloudy areas are POAs. In Chapter 6, we analyzed the causes of persistent cloudy TOC excess relative to clear areas. The main sources of cloudy excess include ozone absorption enhancement in the clouds and possibly the non-linearity calibration error in N7 TOMS data. The ozone absorption enhancement in the clouds, as shown in Chapter 5, is largely dependent on the ozone distribution and the amount of ozone in the clouds. The large negative errors under high-altitude cloudy conditions induced by incorrect cloud heights, on the other hand, greatly reduce the fraction of POAs and increase the possibility of NOAs, as shown in the comparison of OA distribution before and after the  $\Delta P$  correction. The dynamics effect due to cumulonimbus penetration and the enhanced chemical production above high clouds are shown to be negligible in accounting for the cloudy ozone excess discussed in Chapter 6. The TOC fluctuation is much weaker in tropical areas than in mid-latitude areas. The root mean square day-to-day difference is about 2~3 DU and the primary source appears to be Kelvin waves [Allen and Reck, 1997]. This smaller variation in TOC could not lead to extensive POAs in tropical convective cloudy areas. Furthermore, Kelvin waves originate primarily from the lower-to-middle stratosphere region [Ziemke and Stanford, 1994], and are not correlated with the cloud fields.

#### 7.3.2 Planetary-Scale and Synoptic-Scale Activities

Although incorrect cloud heights could lead to large cloud-height errors, and ozone absorption enhancement in the clouds can overestimate ozone over cloudy areas, the large average ozone/reflectivity slope suggests that anomalies are mainly controlled by other factors. Allen and Reck [1997] analyzed the daily variations of TOC in 1979-1992 TOMS V7 data. The seasonal and latitudinal variation of root mean

square day-to-day differences (Figure 1 (d) in [Allen and Reck, 1997]) shows a pattern very similar to that in Figures 7.5 (c) and (d). Root mean square day-to-day differences maximize near 30 DU in the mid-latitudes of both hemispheres from late fall to early spring, and minimize near 16 DU in the summer. Stanford *et al.* [1996] analyzed the interannual variability of TOMS version-6 TOC and also found similar seasonal variation. The contributions of these fluctuations in the mid-latitudes result primarily from synoptic and planetary wave activities [Allen and Reck, 1997; Stanford *et al.*, 1996]. The consistency of seasonal variation between the ozone/reflectivity slope and the total ozone fluctuations suggests that both POAs and NOAs at mid-latitudes may be caused mainly by synoptic and planetary wave disturbances.

Synoptic scale systems have long been recognized as sources of total ozone variability [Dobson and Harrison, 1926; Dobson *et al.*, 1928]. Earlier surface ozone observations indicated that the total ozone at mid-latitudes is usually correlated with the surface pressure and upper-troposphere pressure. High ozone is usually associated with cyclones and low ozone with anticyclones. More recent studies have examined this ozone-meteorology relationship by analyzing satellite data [Hudson and Frolov, 2000; Salby and Callaghan, 1993; Vaughan and Price, 1991]. The dynamic disturbance associated with synoptic weather systems and planetary wave activities can change tropospheric ozone as well as lower stratospheric ozone with a magnitude up to 30% of the total ozone in the mid- and high- latitudes [WMO, 1998]. Of planetary-scale and synoptic scale disturbances, the latter contributes more to the daily total ozone fluctuation except during the Southern Hemispheric spring where vortex contortions and break-ups lead to large planetary-scale disturbance [Allen and Reck, 1997; Stanford *et al.*, 1996]. Strong dynamic disturbances associated with synoptic phenomena such as jet streams and fronts are also associated with strong clouds. More clouds in the mid-latitudes are formed in the east of a trough (above a surface low), where the vertical upward motion brings humid surface air upward. Since high ozone and cloud patterns are usually associated with surface lows in the mid-latitudes, they combine to form POAs. The much higher fraction of POAs than NOAs seen from TOMS data supports the fact that high ozone is usually associated with cyclones and low ozone is usually associated with anticyclones. However, there are exceptions to this ozone-meteorological relationship, as we can see from the smaller fraction of NOAs.

One particular region with more NOAs than POAs occurs near 60°S. Both fraction and ozone/reflectivity slope of NOAs in this region peak during September and early October, when the area is

frequently covered with sea ice. The polar vortex break-up leads to large planetary-scale disturbance and large total ozone fluctuations outside the polar vortex [Allen and Reck, 1997; Stanford et al., 1996], while catalytic ozone depletion largely decreases the ozone inside the polar vortex [Seinfeld and Pandis, 1997]. The reflectivity of the snow/ice surface inside the polar vortex is very high, and the reflectivity under clear conditions outside the polar vortex is lower because of higher temperatures. Therefore, higher reflectivity ice and lower ozone inside the polar vortex, and lower reflectivity and higher ozone outside the polar vortex probably cause the formation of these NOAs.

The zonal asymmetry in the mid-latitudes in Figures 7.3 (a) and (b) was also found in Allen and Reck [1997]. They ascribed the asymmetry to the larger meridional temperature gradient due to varying orography or baroclinic systems advected eastward from the instability source regions.

### 7.3.3 Marine Stratocumulus Clouds and Enhanced Tropospheric Ozone

The  $\Delta P$  correction reduces the fraction of POAs off the WCSAF and WCSAM by 5-10%; however, the remaining high fraction of 30-60% POAs indicates that these POAs are caused mainly by factors other than incorrect cloud-top heights. Figure 7.6 shows the seasonal variation of fraction (a) and ozone/reflectivity slope (b) of POAs for these two selected regions (boxes in Figures 7.2 and 7.3), along with the monthly variation of fraction and slope over the Indian Ocean and South America for comparison. The fraction of POAs over the Indian Ocean and South America peaks during January-February and minimize during May-July, slightly different from those in marine stratocumulus regions. The fraction of POAs in the marine stratocumulus regions maximizes from October to January, ~70% off the WCSAF and ~40% off the WCSAM, and minimizes from February to May off the WCSAM (~15%) and from April to July off the WCSAF (20%-30%). The slope variation in the two marine stratocumulus regions is obviously different from that in the two convective cloudy areas as shown in Figure 7.6 (b). The slope in these two convective cloudy areas shows very little variation, ~20 DU/100% throughout the year. The ozone/reflectivity slope in marine stratocumulus regions, however, maximizes from September to December (30-35 DU/100%), and minimizes from February to May off the WCSAM (~15 DU/100%) and from April to May off the WCSAF (~18 DU/100%). The different seasonal variation in slope suggests that POAs off the WCSAF and WCSAM are caused by different mechanisms from POAs in tropical convective

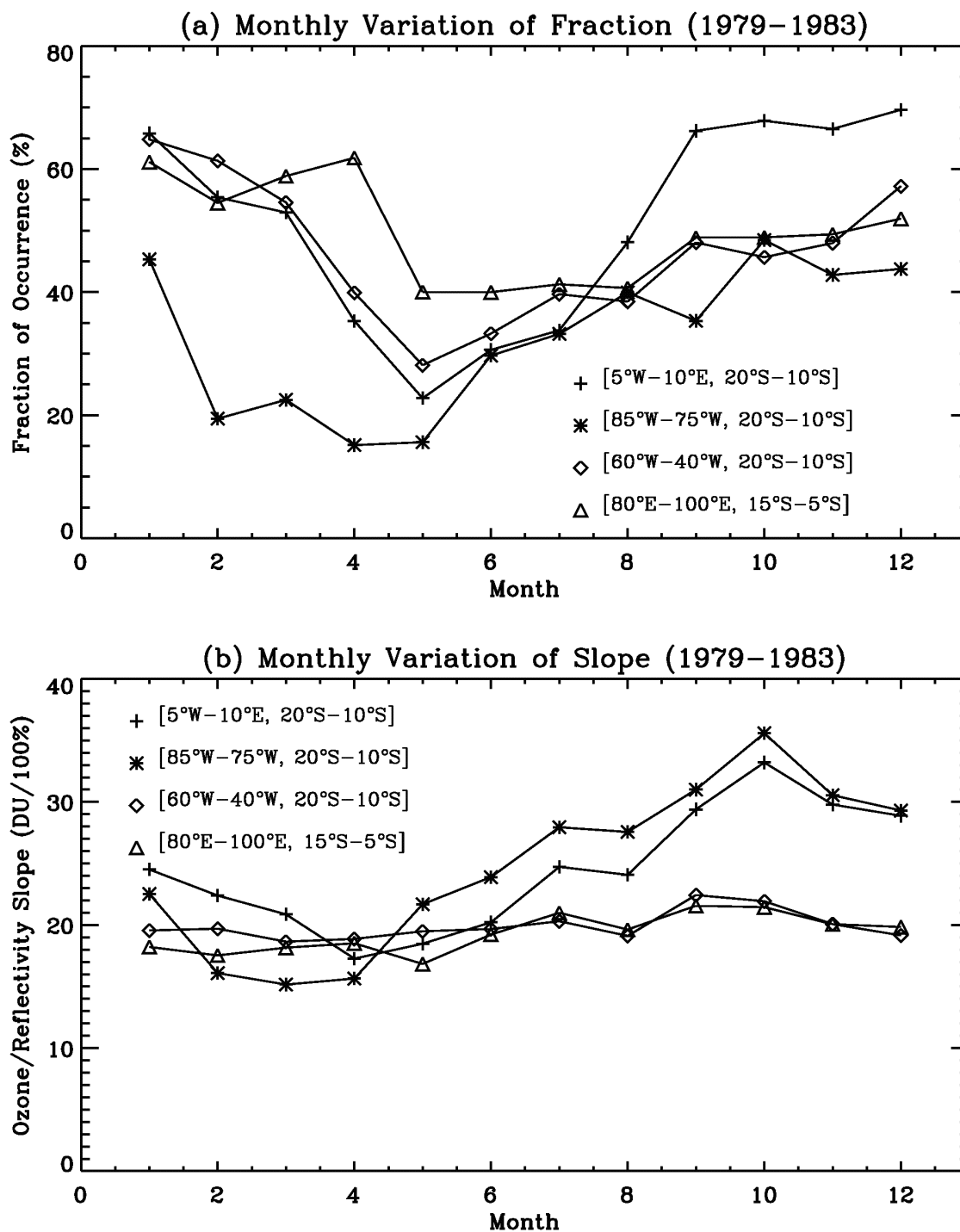


**Figure 7.6** (a) Seasonal variations of fraction of POA occurrence after the  $\Delta P$  correction during 1979–1983 over WCSAF (20°S–10°S, 5°W–10°E), WCSAM (20°S–10°S, 85°W–75°W), South America (20°S–10°S, 60°W–40°W), and the India Ocean (15°S–5°S, 80°E–100°E), (b) same as (a) except for ozone/reflectivity slope.

cloudy areas. The occurrence of marine stratocumulus clouds in these regions maximizes in October and minimizes in April [Stowe *et al.*, 1989; Thompson *et al.*, 1993]. The observed tropospheric ozone in these regions also shows similar seasonal patterns, highest from August to November (i.e., the biomass burning season) and lowest from February to April [Fishman *et al.*, 1991; Fishman *et al.*, 1990; Jiang and Yung, 1996; Kim and Newchurch, 1996; Kim and Newchurch, 1998; Kirchhoff *et al.*, 1996; Thompson *et al.*, 1996]. For example, the correlation coefficient between the slope variation at WCSAF and the 1998-2000 SHADOZ monthly mean tropospheric ozone at Ascension is 0.95. The similar seasonal pattern between the slope of POAs in marine stratocumulus regions and tropospheric ozone suggests that these POAs are related to both tropospheric ozone distribution and the existence of marine stratocumulus clouds. We conjectured this because POAs in South America, the source regions of biomass burning and convective cloudy areas, do not show this seasonal pattern in their slopes.

To understand the formation of POAs in marine stratocumulus regions, we simulate the ozone/reflectivity slope at WCSAF using 1998-2000 SHADOZ measurements [Thompson *et al.*, 2002] at Ascension. Figure 7.7 (a) shows the monthly mean tropospheric ozone profiles along with the TOMS standard profile L275 (33.8 DU tropospheric ozone). The tropospheric ozone at Ascension ranges from 29.0 DU in April to 48.7 DU in October. For months with more actual ozone than the standard profile, large differences occur in the middle troposphere (700 hPa-300 hPa). The standard profile puts much more ozone between 150 hPa and 100 hPa than do any of the monthly mean profiles. We use the Ascension tropospheric ozone profile (up to 100 hPa) along with the stratospheric ozone profile in L275 for both clear and cloudy conditions. We treat clouds as scattering clouds instead of Lambertian surfaces. For all the POAs at WCSAF, the average maximum reflectivity is about 55%, corresponding to a WC of COD  $\sim$ 15. Figure 7.7 (b) shows the ISCCP D1 CTP at WCSAF (5°W-10°E, 20°S-10°S) in October 1983 for clouds with a COD greater than 10 [Rossow *et al.*, 1996]. The average CTP is 749.5 hPa with 1 standard variation of 70 hPa. We simulate the cloud as a stratocumulus cloud of COD 15 with a geometrical depth of 1 km at 1.5-2.5 km (i.e., 852 hPa-756 hPa). For clear-sky condition, we assume a Lambertian surface of reflectivity 5% at 1013.15 hPa [Herman and Celarier 1997; Herman *et al.*, 2001]. We use PPGSRAD to simulate radiances for the assumed clouds as described in Chapter 5, and use the TOMS V7 algorithm to retrieve the TOC for both clear and cloudy conditions.

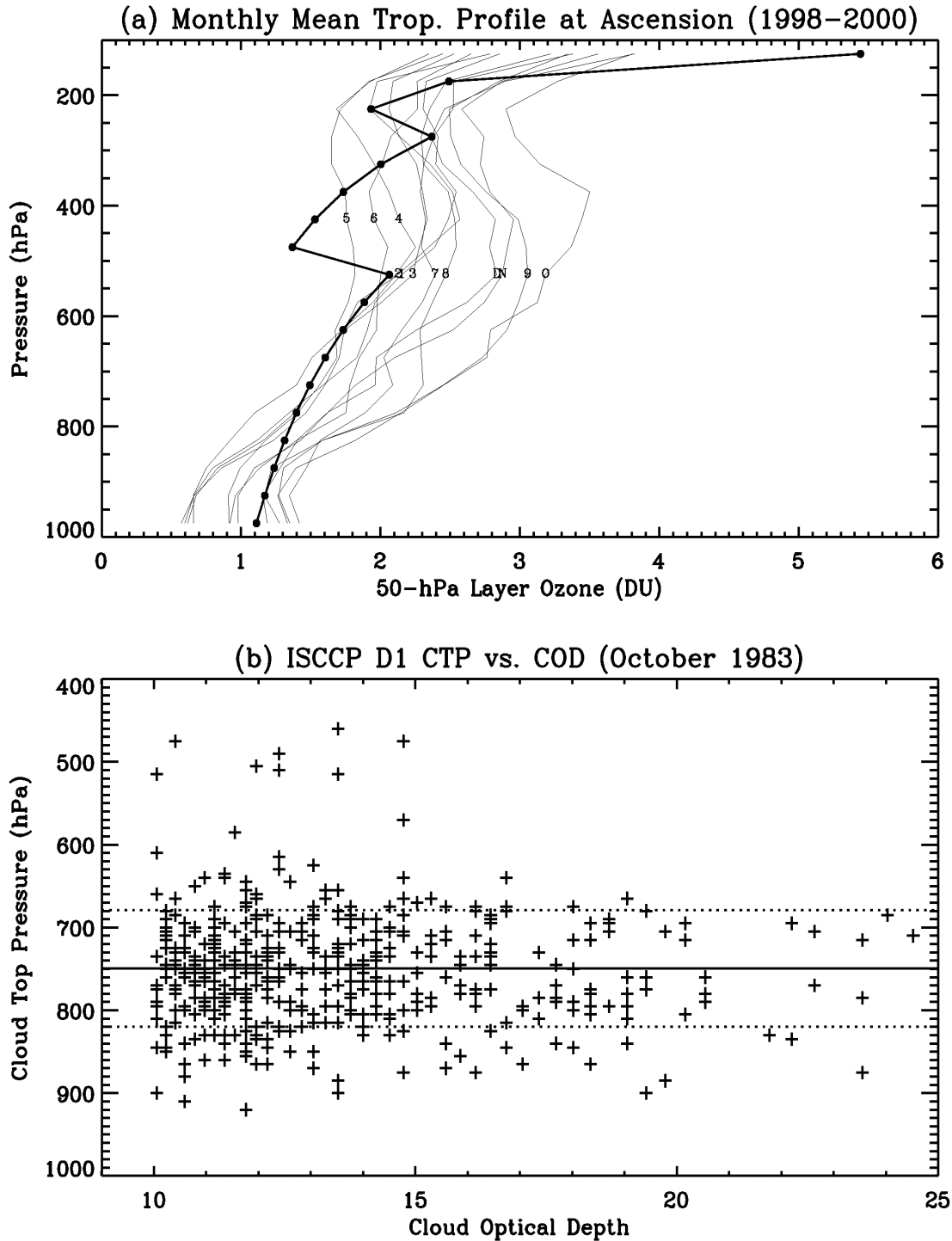


**Figure 7.7** (a) Monthly mean tropospheric ozone profiles (thin curves) measured at Ascension (1998–2000) along with the tropospheric portion of TOMS standard ozone profile L275 (solid curve). Each thin curve is identified by a number (1–9 means January–September) or a character (O, N, and D refers to October, November, and December, respectively). (b) ISCCP D1 CTP vs. COD in October 1983 over WCSAF (20°S–10°S, 5°W–10°E). Solid line is the average CTP and the two dashed lines are the deviations of 1 standard deviation from the average value.

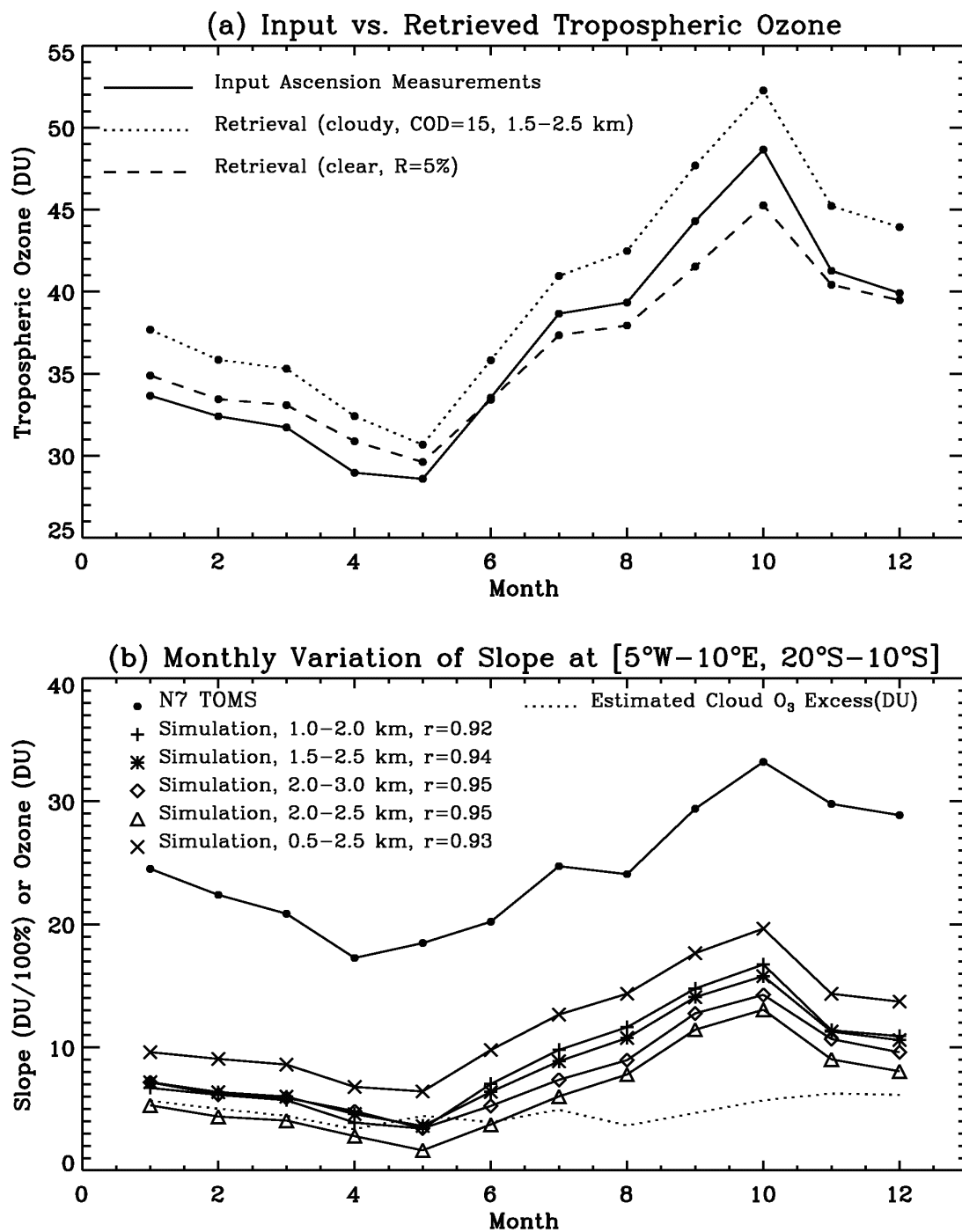


**Figure 7.8** (a) Monthly variation of tropospheric ozone measured at Ascension during 1998-2000 (solid), the retrieved ozone for a cloudy-sky with a WC of COD 15 at 1.5-2.5 km (dotted line), and the retrieved ozone for a clear-sky with ground reflectivity of 5%. (b) Monthly variation of the observed ozone/reflectivity slope (circle) over WCSAF (20°S-10°S, 5°W-10°E) and simulated ozone/reflectivity slopes under various cloudy conditions.

Figure 7.8 (a) shows the monthly variation of retrieved tropospheric ozone for both clear and cloudy conditions. In the simulation, we assume the average TOMS observation viewing geometry for this region,  $SZA \approx 20^\circ$  and  $VZA \approx 20^\circ$ . Under clear-sky conditions, the retrieved tropospheric ozone is higher than the input tropospheric ozone by 0.3-1.2 DU from January to May and smaller by 0.8-4.0 DU from June to December because the imperfect retrieval efficiency is smaller than 1 at TOMS wavelengths. Under cloudy-sky conditions, the retrieved tropospheric ozone is always overestimated because of a combination of various OREs, including radiation interpolation error ( $\sim 0.7$  DU), ozone absorption enhancement in the clouds (from 1.4 DU in April to 2.7 DU in October), error in added OZBC (from  $-1.0$  DU in October to 1.4 DU in April), and error due to imperfect retrieval efficiency that is slightly greater than 1 (from  $-0.8$  DU in May to 1.6 DU in October).

From the retrieved ozone difference between clear and cloudy conditions, we can derive the simulated ozone/reflectivity slopes. Figure 7.8 (b) shows the monthly variation of the simulated ozone/reflectivity slopes. There is a high correlation of 0.94 between the simulated slope and the observed slope of POAs, but the simulated slope is smaller than the observed slope by 12.7-18.4 DU/100% and the simulated slope difference between the maximum and minimum is 12.2 DU/100%, 0.76 of the corresponding observed value. Figure 7.8 (b) also shows the simulated slopes for the same cloud except at 1-2 km, 2-3 km, 2-2.5 km, and 1.5-2.5 km. The maximum and minimum slope difference varies within 1 DU for these four cloudy conditions. The decrease of CTH by 500 m changes the slopes by  $-0.5$  DU  $-0.9$  DU, and the increase of CTH by 500 m decreases the slopes by up to 1.8DU. The changes with CTH are caused by the variation of error in added OZBC, radiation interpolation error, and error due to retrieval efficiency with CTH. The decrease of CGD to 500 m reduces the slopes by 1.8-3.0 DU and the increase of CGD to 2000 m increases the slopes by 2.2-3.9 DU because the enhanced ozone changes with the amount of ozone in the clouds. The further increase of the CGD can match the observed value but the GCD for stratocumulus clouds is only about 500-1000 m. With all the known OREs considered, the simulated slopes are still far below the observed values. About 6 DU/100% in the difference between observed and simulated slopes can be ascribed to non-linearity calibration error if the N7/EP TOMS bias results from N7 TOMS data only. We suggest that the remaining simulated and observed difference results mainly from there being more ozone over cloudy areas than over clear areas due to chemical production. Approximately

3.3-6.2 DU cloudy ozone excess (dotted line in Figure 7.8 (b)) is required to explain the observed slopes for the cloud at 1.5-2.5 km. High reflectivity marine stratocumulus clouds increase the actinic flux and therefore increase the  $J$ -values to produce ozone above low-altitude clouds [Madronich, 1987; Pfister *et al.*, 2000]. Pfister *et al.* [2000] show that the  $J_{O_3}$  above clouds is about 50% higher than the corresponding clear-sky values. Because there is a high frequency of stratocumulus clouds [Stowe *et al.*, 1989; Thompson *et al.*, 1993] and rich ozone precursors during the biomass season at WCSAF [Lee *et al.*, 1998], it is possible to photochemically produce 3-6 DU more ozone relative to clear-sky conditions. Ozone-sonde measurements and photochemical models are needed to further examine this speculation.

#### 7.3.4 Solar Zenith Angle and Satellite Zenith Angle

The effects of satellite VZA on TOMS total ozone are apparent during the Mount Pinatubo eruption, with an order of 2% [Bhartia *et al.*, 1993; Torres and Bhartia, 1995]. A small scan-angle dependence, on the order of 1%, remains in the TOMS TOC even in the absence of aerosols [McPeters *et al.*, 1996]. In a 5°-longitude by 5°-latitude area, the SZA does not change much for different measurements and the VZA is usually within 20°. We examined both correlation coefficients and slopes between ozone and reflectivity to be a function of average SZA and VZA, but we did not find any relationship between OAs and viewing geometry. The smaller effects of viewing geometry on the formation of OAs are reasonable, because these angles are very similar in both clear and cloudy areas. Furthermore, the scan-angle dependence effects are too small to account for the larger observed ozone/reflectivity slope of OAs. In the presence of aerosols or sun glint, a larger scan-angle dependence, up to 2%, is apparent [McPeters *et al.*, 1996]. We tested the fraction of OA occurrence in 1980 and 1997 without performing aerosol and sun glint correction, and found little effects on the spatial distribution of OAs.

#### 7.4 Summary

Because of large cloud height errors in the TOMS V7 level-2 data, we corrected OREs induced by incorrect cloud height using collocated THIR data during 1979-1983 when THIR data are available. Correcting cloud-height-induced errors (called the  $\Delta P$  correction) dramatically increases the fraction of

POAs in the tropical convective cloudy areas by 20-50% and decreases the fraction of POAs off the WCSAF and WCSAM by 5-10%. The changes in ozone/reflectivity slope are relatively small, usually within  $\pm 10$  DU/100%. After the  $\Delta P$  correction, most of the tropical NOAs are eliminated, indicating that NOAs are caused mainly by underestimates of CTPs. The large increase of NOAs before the  $\Delta P$  correction over the tropical eastern Pacific Ocean during El Niño periods also originates from the increased CTP errors during these periods.

Some OAs are caused by geophysical phenomena, and some are caused by OREs. Peaks in the fraction of POAs in the tropical convective cloudy areas follow the motions of ITCZ regions. These anomalies are mainly caused by OREs associated with clouds, including ozone absorption enhancement in the clouds, incorrect tropospheric climatology, and some non-linearity calibration errors. The slope of POAs and NOAs at mid-latitudes peaks from late fall to early spring (60-80 DU/100%), and is lowest in the summer (30-40 DU/100%). The seasonal variation of slope is consistent with that of total ozone fluctuation, indicating that mid-latitude anomalies are mainly caused by planetary-scale wave and synoptic wave disturbances. The number of mid-latitude POAs is almost twice that of NOAs, supporting that high ozone is usually associated with high cyclones as well as with clouds. One particular mid-latitude region with more NOAs than POAs lies near 60°S. Both fraction and slope of NOAs in this region peak during September and early October, when the area is frequently covered with sea ice due to the Antarctic polar vortex. Catalytic ozone destruction and enhanced reflectivity inside the polar vortex region generate frequent NOAs. The slope of POAs in marine stratocumulus regions off the WCSAF and WCSAM shows a maximum from August to November (i.e., the biomass burning season) and a minimum from February to May, highly correlated with the tropospheric ozone variation originating from biomass burning activities. Simulating POA formation off the WCSAF using SHADOZ ozonesonde measurements at Ascension indicates about 2/3 of the slope of POAs can be explained by OREs under both clear and cloudy conditions. We speculate that there is more ozone over cloudy areas because of the enhanced  $j$ -values over the high frequency of low-altitude marine stratocumulus clouds and the rich ozone precursors above these clouds transported from biomass burning regions. About 3-6 DU cloudy ozone excess is required to explain the remaining unexplained slope. However, ozonesonde measurements and photochemical models are needed to examine the speculation.

## 7.5 Effects of Ozone Anomalies on TOMS Applications

Analysis of OAs indicates that some OAs are due to OREs and some are caused by actual geophysical phenomena such as planetary and synoptic wave activities. Including the cloudy total ozone that contains OREs will affect the corresponding results in particular applications such as calculations of monthly mean ozone climatology, analysis of the ozone seasonal variation, evaluation of ozone trends, and tropospheric ozone derivation.

However, analysis of the effects of clouds on these applications is very complicated, because the overall effect of different types of errors depends on factors such as cloud altitude, cloud-height errors, and cloud fraction, ozone amount and ozone distribution inside clouds; and these factors may have seasonal variations. In the current archived TOMS V7 level-2 data, the mainly negative cloud-height errors and other positive errors usually partly cancel, leading to an overall smaller error in tropical high-altitude cloudy areas. In applications related to global mean or zonal mean, the overall error is expected to be small. In some regions, such as oceanic regions off the WCSAF and WCSAM, errors in cloudy-sky measurements tend to cancel errors in clear-sky measurements, leading to small errors in the gridded level-3 data. For studies of a particular region during a special period, however, special care should be taken regarding the effects of clouds in those regions with high frequencies of POAs and NOAs. For example, over the eastern Pacific Ocean during El Niño periods, there would be persistent negative errors of about  $-10$  DU in cloudy areas due to using the incorrect cloud climatology mostly from non-El Niño periods.

In Chapter 6, we have analyzed the effects of positive OREs over tropical high-altitude clouds (i.e., POAs) on the derivation of tropospheric ozone using the CCD and CCP methods. Even without accounting for OREs above clouds, one can retrieve reasonable tropospheric ozone by using special sampling such as using the monthly minimum OZAC in the CCD method [Ziemke *et al.*, 1998] and the mean of the six lowest OZAC values within five days in the CCP method [Newchurch *et al.*, 2002]. However, in mid-latitudes, the large ozone/reflectivity slope due to planetary and synoptic wave disturbances makes it risky to apply the CCD or CCP methods unless we can develop a method to account for these wave effects.

Some N7/EP non-linearity calibration differences remain. However, the correct partitioning of this error between N7 TOMS and EP TOMS is not clear. Inclusion of both EP and N7 TOMS data for a trend analysis might lead to incorrect conclusions.

Knowledge of these different types of errors is important for studies using the TOMS measurements, because these errors might significantly affect particular applications. In addition, we have experienced some self-correcting effect in the TOMS data; i.e., errors of opposite sign partly cancel each other and lead to small errors in the archived TOMS data. Therefore, it is possible that correcting only one of these errors could lead to larger overall errors. Future instruments such as the OMI can avoid cloud-height-related errors by accurately determining the cloud height from visible and infrared channels. Then large errors in the retrieved ozone will come mainly from the ozone absorption enhancement in the clouds.

## CHAPTER 8

### CONCLUSIONS

Accurate remote sensing retrieval of atmospheric constituents over cloudy areas is very challenging because of insufficient knowledge of cloud parameters. Cloud treatments are highly idealized in most retrieval algorithms. For example, the TOMS V7 algorithm assumes that clouds are opaque Lambertian clouds. However, these idealizations may cause large OREs over cloudy areas. Applications such as the CCD and CCP methods, which take advantage of cloudy measurements, will suffer from these OREs. This study characterizes OREs associated with clouds in TOMS data resulting from the assumed CTPs from monthly mean ISCCP climatology, the assumed opaque Lambertian clouds, and the used PCM; investigates the effects of these errors on tropospheric ozone derivation; and analyzes anomalous ozone distributions over cloudy areas caused by either OREs or geophysical phenomena in TOMS data.

Using collocated THIR cloud data, we find that large errors occur in the TOMS-assumed CTPs. Three TOMS algorithm OREs from inaccurate CTPs are identified: radiation interpolation error, error in the added OZBC, and error in the retrieved OZAC; the most significant of these errors is the inappropriate OZBC to complete the TOC. Using PPGSRAD that treats in-cloud multiple scattering in the forward simulation, we study the effects on TOMS ozone retrieval of assuming opaque Lambertian clouds and employing the PCM. The assumption of angular-independent cloud reflection typically causes OREs within 1.5% of the TOC (i.e., within the accuracy of TOMS retrieval) for  $COD \geq 20$ , indicating this assumption is fairly good in terms of ozone retrieval. Because of the ICOAEN effect, the assumption of opaque clouds may introduce large OREs even for optically thick clouds. For a WC of COD 40 at 2-12 km and 20.8 DU ozone homogeneously distributed in the cloud, the ORE is 17.8 DU at nadir view. Assuming

clouds to be ice clouds only slightly decreases the ICOAEN effect. The ICOAEN effect varies greatly with viewing geometry and inter-cloud ozone amount and distribution. The TOMS PCM leads to negative errors because the retrieved ECF is being underestimated so that the added OZBC decreases correspondingly. However, this negative PCM effect due to the PCM partly cancels other positive errors, indicating the employed PCM is fairly good. Especially at  $COD \leq 5$ , the PCM effect almost offsets the positive effects so the TOMS V7 algorithm retrieves the approximately correct TOC. With increasing COD up to 20-40, the negative error from the PCM effect decreases more dramatically than does the positive error; therefore, the overall positive error increases and is dominated by the ICOAEN effect. The further increase of COD slightly decreases the overall positive error.

Because of poor knowledge of ozone distributions in the cloud, it is impossible to accurately estimate the ICOAEN effect directly. We indirectly estimate the ICOAEN effect in the tropics from cloudy/clear TOC differences after correcting the incorrect tropospheric climatology with SHADOZ measurements as a reference and correcting cloud-height-induced errors. The ICOAEN effect is typically 5-13 DU over the tropical Atlantic Ocean and Africa and 1-7 DU over the tropical Pacific Ocean. Because of the ICOAEN effect and other positive errors, deriving tropospheric ozone from cloudy/clear difference techniques using all high-altitude cloud measurements ( $R \geq 80\%$ ,  $THIR \leq 300$  hPa) largely underestimate the derived tropospheric ozone. The error in the derived SOC from such clouds shows a typical wave-1 pattern, highest over the tropical Atlantic Ocean and Africa and lowest over the Pacific Ocean, suggesting that the wave-1 pattern of the stratospheric ozone seen by *Newchurch et al.* [2001c] may result partly from the artifacts of OREs. The used minimum OZAC in the CCP and CCD methods greatly cancels other positive errors. A N7/EP TOMS offset exists in which the observed cloudy ozone excess relative to clear areas is larger by  $\sim 4.3$  DU on average in the N7 TOMS data than in the EP TOMS data. This bias is probably caused by nonlinearity calibration errors in either N7 or EP or both. The EP TOMS instrument is the most recent and probably the best calibrated. Furthermore, the assumption of the same SOC between cloudy and clear areas is more valid in EP TOMS data than in N7 TOMS data, suggesting that the non-linearity calibration error probably resides mainly in the N7 TOMS data. However, the use of minimum OZAC overestimates the derived tropospheric ozone during the EP period, as shown in the CCD method.

The cloudy ozone excess of 40 DU compared to nearby clear areas in the North Dakota case study [Poulida *et al.*, 1996] motivates us to study OREs associated with clouds and the frequency of such anomalous ozone distribution. A  $5^\circ$ -longitude  $\times$  by  $5^\circ$ -latitude region is defined to contain a POA or NOA if the correlation coefficient between ozone and reflectivity is  $\geq 0.5$  or  $\leq -0.5$ . The analysis of 20 years' TOMS data finds that average fractions of OA occurrence are  $31.8 \pm 7.7\%$  and  $35.8 \pm 7.7\%$  in N7 and EP TOMS data, respectively. Some OAs are caused by OREs, and others are caused by actual geophysical phenomena. Most tropical NOAs result from large cloud-height errors. The negative errors in the added OZBC offset other positive errors. Correcting cloud-height errors leads to 50-70% POAs in the tropics because of the ICOAEN and other effects. The large ozone/reflectivity slope for mid-latitude OAs, 30-40 DU/100% in the summer and 60-80 DU/100% in the winter, shows seasonal variation consistent with total ozone fluctuation. These anomalies are caused mainly by synoptic and planetary wave disturbances. POAs with a fraction of 30-60% occur in regions of marine stratocumulus off the WCSAF and WCSAM. Both fractions and ozone/reflectivity slopes of these POAs show seasonal variations consistent with that in the tropospheric ozone. About half the ozone/reflectivity slope is caused by OREs over clear and cloudy areas. The remaining slope may result from there being more ozone production because of rich ozone precursors and higher  $j$ -values than in clear areas over high-frequent, low-altitude clouds.

The knowledge of TOMS OREs applies as well to ozone retrieval from other satellites such OMI, GOME, and SCIAMACHY (Scanning Imaging Absorption SpectroMeter for Atmospheric Chartography). Some of the knowledge of OREs, especially the ICOAEN effect applies to satellite remote sensing of other atmospheric constituents unless new techniques can be developed to separate ozone/trace gas absorption inside the clouds from outside the clouds. Several problems need further study. In this study, we assumed single-layer homogeneous clouds. Although this cloud treatment is more realistic than the TOMS V7 treatment, it is still idealized. More detailed work is needed to study OREs for more realistic clouds such as multi-layer, inhomogeneous, and broken clouds. The current knowledge about how ozone and trace gases are distributed in the clouds is far from sufficient. Understanding how trace gases are distributed in convective clouds requires more measurements and further modeling effort using mesoscale transport and chemical models. Also, measurements and chemical models are needed to examine the speculation that there is more ozone over the marine stratocumulus off the WCSAF and WCSAM.

## **APPENDICES**

## APPENDIX A

### NEGLECT OF POLARIZATION ON RADIANCE AND OZONE RETRIEVAL

Most current radiative transfer models replace the rigorous vector radiative transfer equation with its approximate scalar counterpart when the incident light is unpolarized and only the intensity of multiply scattered light is to be computed [*Hansen, 1971; Lacis et al., 1998; Mishchenko et al., 1994*]. Although the scalar approximation has no physical background, the neglect of polarization not only enormously simplifies the theoretical work [*Hansen, 1971; Mishchenko et al., 1994*], but also largely reduces the amount of computation. Therefore, scalar approximation is very valuable when scalar treatment is adequate. *Hansen* [1971] examined the effect of scalar treatment on the reflected intensity for light scattered by spherical cloud droplets and concluded that the errors are less than 1% in most cases in the visible, making scalar approximation adequate for most cloud and aerosol radiance calculations. In climate studies, where radiative fluxes and albedos are of interest, the integration over scattering angle averages out radiance errors so that scalar treatment is adequate. However, it has been recognized that the neglect of polarization can produce errors as large as 10% in the computed intensity for pure Rayleigh scattering. These large errors arise in specific geometrical configurations with the maximum error occurring at an optical depth of near 1 [*Herman et al., 1995; Lacis et al., 1998; Mishchenko et al., 1994*]. *Mishchenko et al.* [1994] found that large errors in Rayleigh atmosphere are caused by the particular structure of the Rayleigh scattering matrix (perfect or almost perfect polarization at scattering angle  $90^\circ$  and nearly isotropic phase function), and these errors arise primarily from second scattering paths that involve right-angle scattering and right-angle rotations of the scattering plane.

In this appendix, we study the effects of the neglect of polarization on the calculated reflected and transmitted radiance for both clear and cloudy conditions at N7 TOMS wavelengths, where the Rayleigh scattering is significant, with Rayleigh scattering optical thickness ranging from  $\sim 1$  at 312 nm to 0.45 at 380 nm. Radiances are calculated using PPGSRAD with polarization and without polarization. L275 ozone and temperature profiles are used. The calculated reflected radiances are then inverted to retrieve TOC and reflectivity using the TOMSV7 algorithm. Corresponding errors in the retrieved TOC and reflectivity due to the scalar treatment are analyzed and discussed.

### A.1 Clear-Sky Conditions

Figure A.1 shows the relative intensity error resulting from scalar approximation for the calculated reflected radiance at TOA (left) and the transmitted radiance at the bottom of surface (right) at  $\theta_0 = 0^\circ, 30^\circ, 60^\circ,$  and  $75^\circ$  and at 312.3 nm for a ground surface reflectivity of 8%. The asterisk symbol on the abscissa identifies the SZA. The relative intensity error  $e$  is defined as

$$e = 100\% \times (I_s - I_v) / I_v, \quad (\text{A.1})$$

where  $I_s$  is the calculated radiance without polarization, and  $I_v$  is the calculated radiance with polarization. The percent error ranges from  $-8\%$  to  $10\%$  for the reflected radiance and from  $-14\%$  to  $11\%$  for the transmitted radiance. The errors are larger in transmitted radiance because transmitted photons, on average, experience less multiple scattering. The effect of neglecting polarization is highly angular-dependent for both reflection and transmission. For both reflection and transmission, the largest overestimation occurs at scattering angles near  $90^\circ$  and the largest underestimation occurs at forward scattering (for transmission) and backscattering (for reflection) angles. The errors are larger at azimuth angles  $\phi = 0^\circ$  and  $\phi = 180^\circ$ . There is an anti-symmetric similarity between the errors in reflection and transmission. The magnitude of the relative intensity error and its angular distribution are consistent with results obtained by *Mishchenko et al.* [1994] and *Lacis et al.* [1998]. In addition to the overall intensity, other terms in Equation (5.1) are examined. The relative error in  $T$  (transmitted radiance from the surface to TOA) is within 1%, and the error in  $S_b$  (fraction of reflected radiation from scattered back to surface by the atmosphere) is within

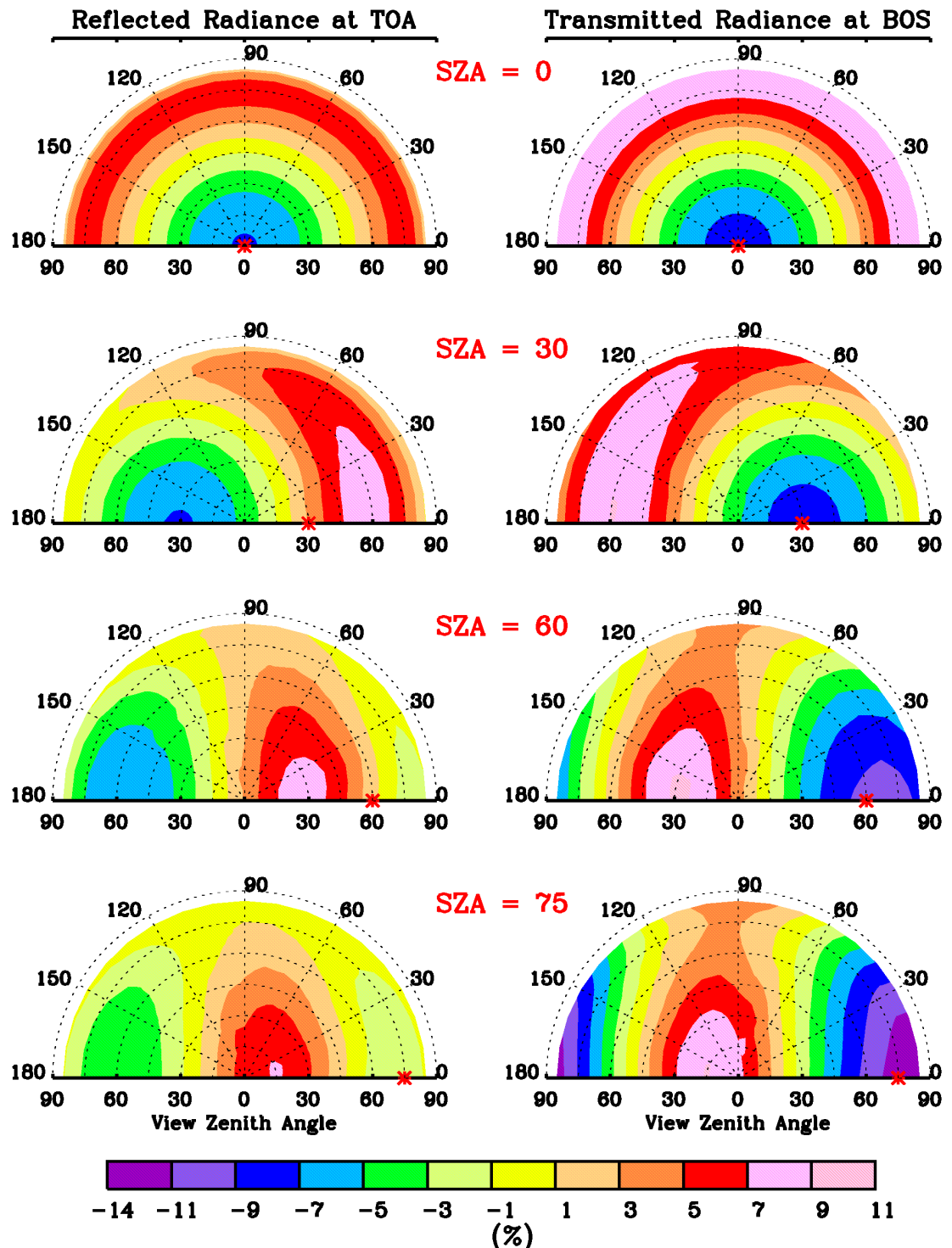


**Figure A.1** The difference in the calculated reflected radiance at TOA (left) and transmitted radiance at ground surface (right) with and without polarization at 312 nm for four different SZAs (0°, 30°, 60°, and 75°). The red asterisk symbol on the abscissa indicates the SZA.

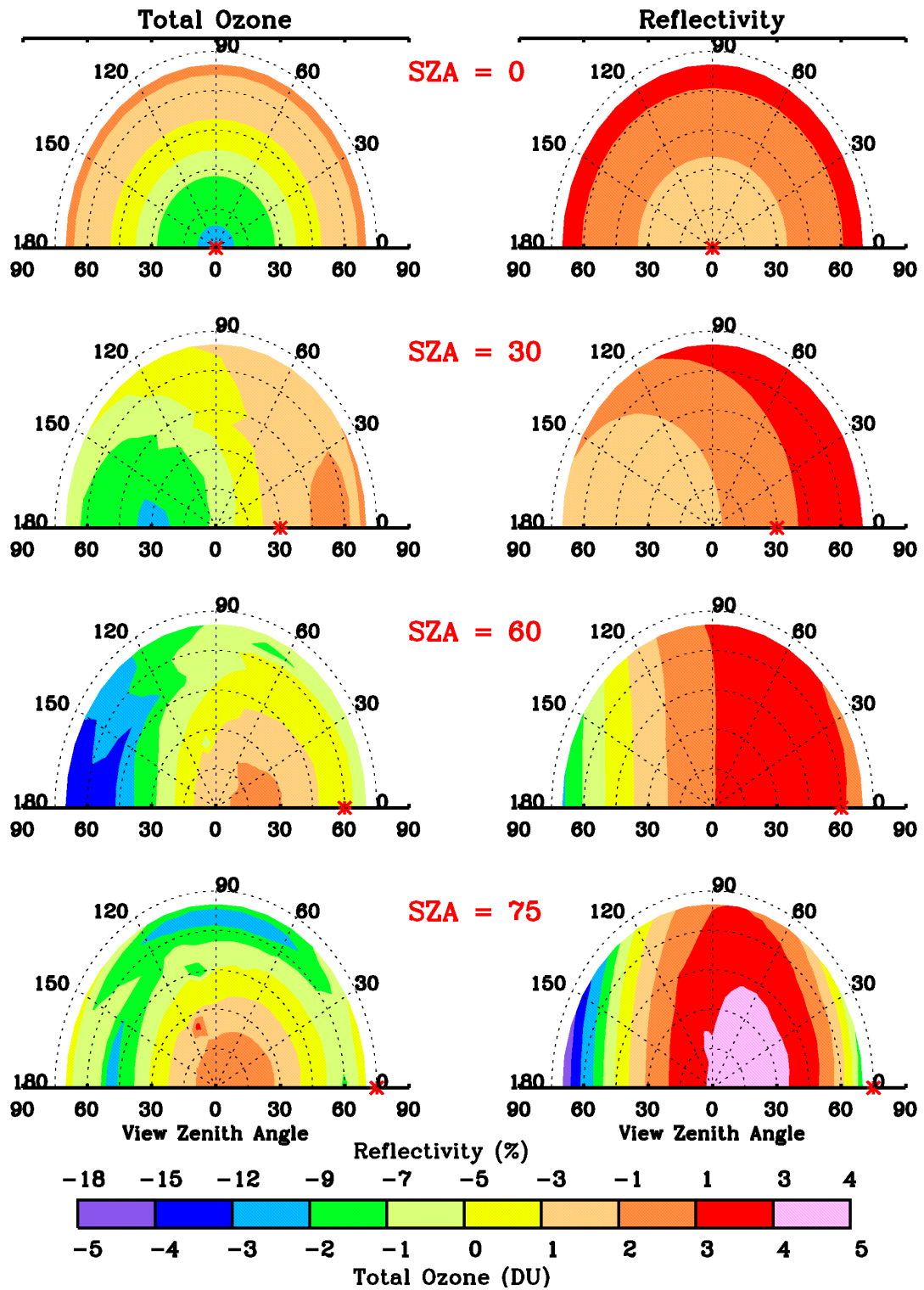
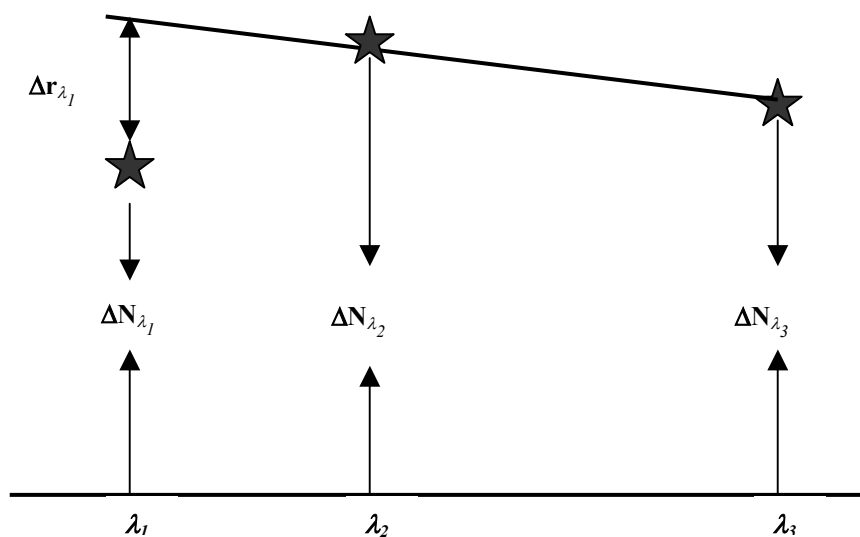


Figure A.2 The difference in the retrieved ozone and reflectivity from forward-calculated radiances with and without polarization. The TOMS V7 algorithm retrieves the ozone and reflectivity.

0.04%. The smaller errors in  $T$  and  $S_b$  explain why the overall intensity error decreases with increasing surface albedo. The error patterns are similar at other TOMS wavelengths, but the magnitudes vary slightly from wavelength to wavelength because of the change in Rayleigh scattering optical depth and ozone absorption (e.g., the overall single scattering albedo changes).

Figure A.2 shows the effect of scalar approximation on the retrieved ozone and reflectivity. The error in the retrieved total ozone ranges from  $-4.5$  DU to  $3.5$  DU; the error in the retrieved reflectivity (percentage points in the reflectivity, not the percent difference) ranges from  $-18\%$  to  $4\%$ . The error patterns in ozone and reflectivity are similar to the error pattern for reflected radiance but with less variation. We can see that neglecting polarization has significant effects on retrieved reflectivity. The error in ozone is still considerable even though the TOMS V7 algorithm uses a triplet method to reduce the relatively wavelength-independent effect resulting from neglecting polarization.



**Figure A.3** A schematic diagram that explains how the error in the calculated radiance from the neglect of polarization causes errors in the retrieved ozone and reflectivity using the TOMS V7 algorithm.

The error in the retrieved TOMS reflectivity results from the error in radiance at the reflectivity wavelength and the error in the retrieved total ozone results from the wavelength-dependence in the errors

in radiance at wavelengths for ozone retrieval. Figure A.3 shows a schematic diagram to explain how errors in ozone and reflectivity result from errors in the reflected radiance at TOA. In the TOMS V7 algorithm, a triplet method is used to retrieve the TOC. Let  $\lambda_1$ ,  $\lambda_2$ , and  $\lambda_3$  be the ozone sensitive, ozone insensitive, and reflectivity wavelength, respectively. The  $\Delta N_{\lambda_i}$  ( $i = 1, 2, 3$ ) is the N-value difference with and without polarization at each  $\lambda$ . The reflectivity is retrieved from the radiance at the reflectivity wavelength only. The error in the reflectivity  $\Delta R$  is directly related to the error in the radiance at the reflectivity wavelength,

$$\Delta R = \Delta N_{\lambda_3} / sr_{\lambda_3}. \quad (\text{A.2})$$

The ratio of  $\Delta N_{\lambda_3}$  to the sensitivity of radiance to reflectivity  $sr_{\lambda}$  approximates the error in the retrieved reflectivity. The error in ozone  $\Delta \Omega$  is related to the difference in N-value errors among the three wavelengths used to retrieve the ozone. Extrapolating the line between  $\Delta N_{\lambda_3}$  and  $\Delta N_{\lambda_2}$  to wavelength  $\lambda_1$ , we can get an extrapolated  $\Delta N_{\lambda_3}$  at  $\lambda_1$ , where the N-value difference is due only to the change in reflectivity. The difference between the actual  $\Delta N_{\lambda_1}$  and the extrapolated  $\Delta N_{\lambda_1}$  is the residue  $\Delta r_{\lambda_1}$  resulting from the slight wavelength dependence in the N-value difference,

$$\Delta r_{\lambda_1} = \Delta N_{\lambda_1} - \left\{ \Delta N_{\lambda_3} + [\Delta N_{\lambda_3} - \Delta N_{\lambda_2}] \times \frac{\lambda_3 - \lambda_1}{\lambda_3 - \lambda_2} \right\}. \quad (\text{A.3})$$

The error in ozone is approximated by the ratio of the residue to the sensitivity of radiance to ozone  $s_{\lambda_1}$ ,

$$\Delta \Omega = \Delta r_{\lambda_1} / s_{\lambda_1}. \quad (\text{A.4})$$

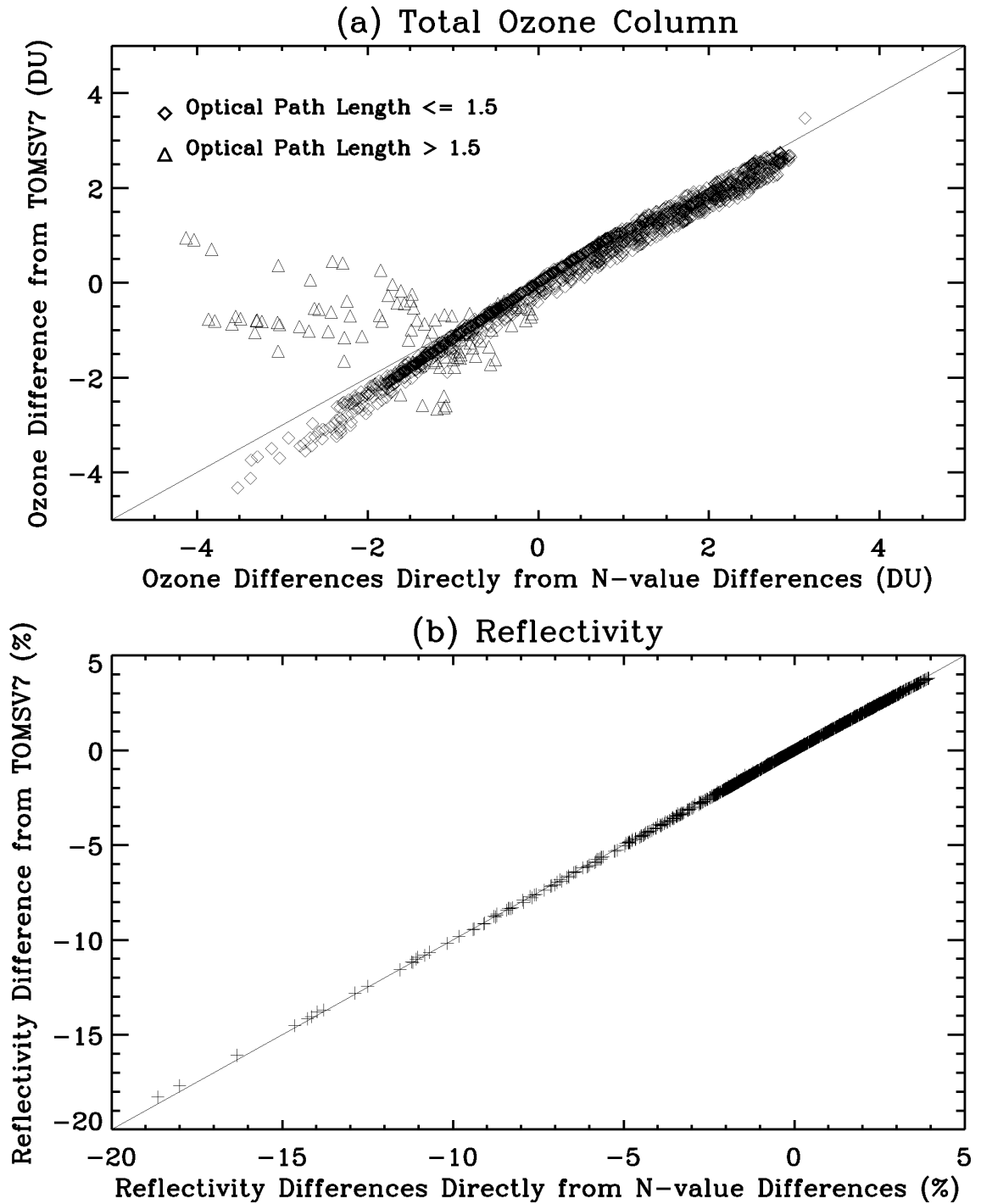


**Figure A.4** (a) Comparison of the ozone differences with and without polarization between using the TOMS V7 algorithm and directly calculating from the N-value differences. (b) Same as (a) Except for reflectivity.

Figure A.4 shows the relationships between the errors calculated using the TOMSV7 algorithm and the errors calculated using the above approximations for TOC (a) and reflectivity (b), respectively. There is a very good relationship for the retrieved reflectivity. For the error in total ozone, the relationship is good only for an optical path length  $\leq 1.5$ . This is because at the higher optical path  $> 1.5$ , the TOMS V7 algorithm uses a different approach for latitude interpolation that requires consistency between two triplets. The good relationship in Figure A.4 indicates that the schematic diagram in Figure A.3 provides an intuitive method to understand the TOMS V7 algorithm for optical path length  $\leq 1.5$ .

## A.2 Cloudy-Sky Conditions

A WC at 2-6 km is selected as a representative to study the effect of neglecting polarization on radiance, retrieved ozone, and reflectivity. Figure A.5 shows relative intensity error patterns resulting from scalar approximation similar to Figure A.1 except for a cloud of COD 1 (the upper 4 panels) and 40 (the lower 4 panels) at  $\theta_0 = 0^\circ$  and  $60^\circ$ . For the case with a COD of 1, the error patterns are similar to those under clear-sky conditions for both reflection and transmission except with smaller magnitudes. Errors range from  $-6.6\%$  to  $7.4\%$  for reflection and from  $-7.0\%$  to  $6.5\%$  for transmission. The multiple reflections between the cloud and the atmosphere and the multiple scattering in the cloud reduce the effect of neglecting polarization. At COD 40, the relative intensity error in the transmitted radiance is greatly reduced, ranging from  $-0.4\%$  to  $0.9\%$ ; although the error in reflected radiance still looms larger compared to the effect in visible wavelength [Hansen, 1971], ranging from  $-4.0\%$  to  $3.8\%$ . The large error up to  $4\%$  indicates that the polarization is not negligible for cloudy conditions in order to calculate accurate backscattered radiance at ultraviolet wavelengths.

For transmission, the transmitted photons at the ground surface penetrate through the clouds and most of them experience multiple scattering before they are transmitted to the ground. Therefore, the effect of neglecting polarization that occurs during clear-sky conditions has been largely washed out by in-cloud multiple scattering. For reflection, more reflected photons experience multiple scattering compared to during clear-sky conditions due to in-cloud multiple scattering and multiple reflections between the cloud and the atmosphere. However, a significant portion of backscattered photons experience only Rayleigh

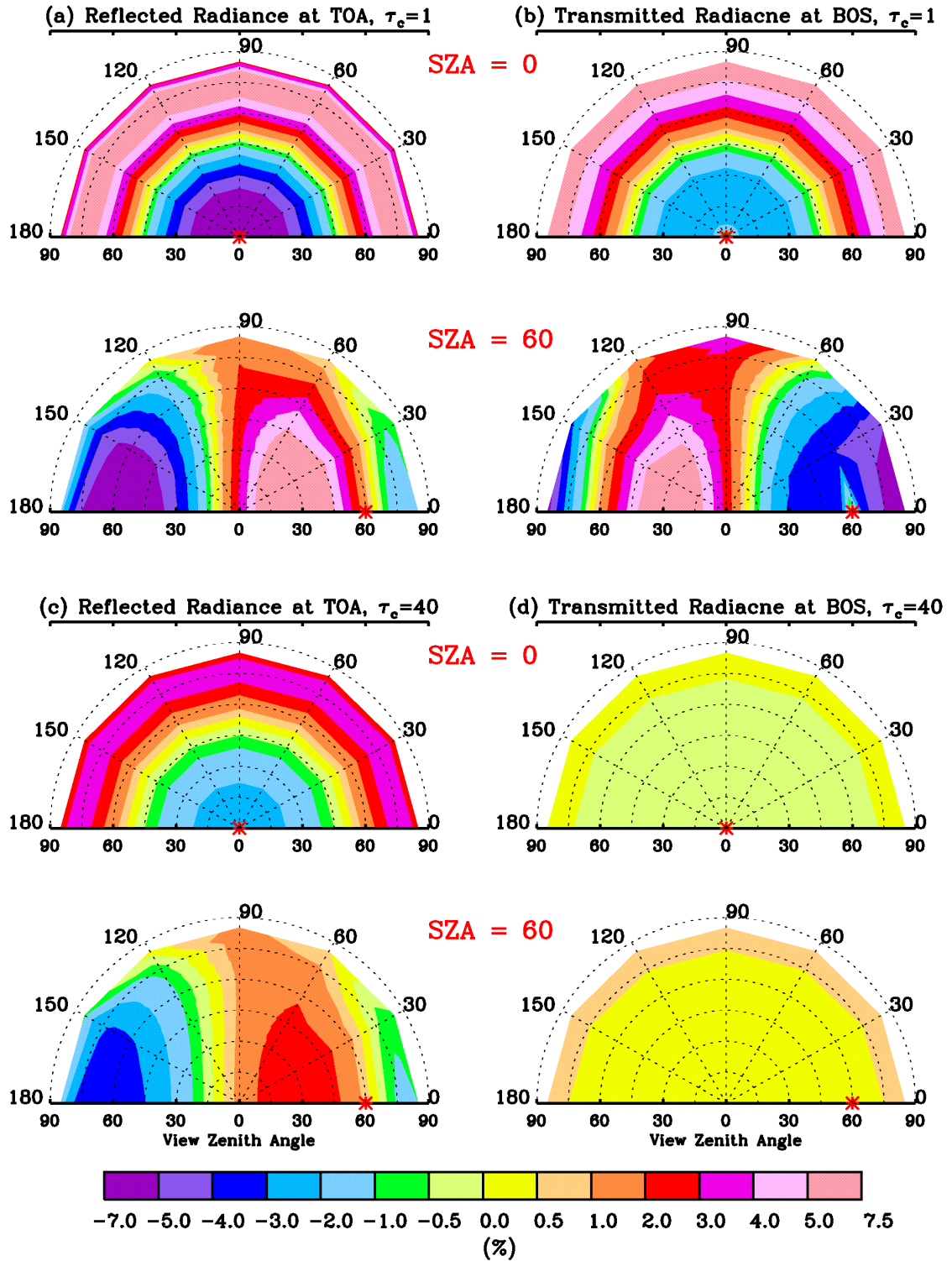


Figure A.5 (a) and (b) same as Figure A.1 (left) and (right) except for a cloudy-sky with a WC of COD 1 at 2-6 km and for SZAs 0° and 30°. (c) and (d) same as (a) and (b) except for COD 40.

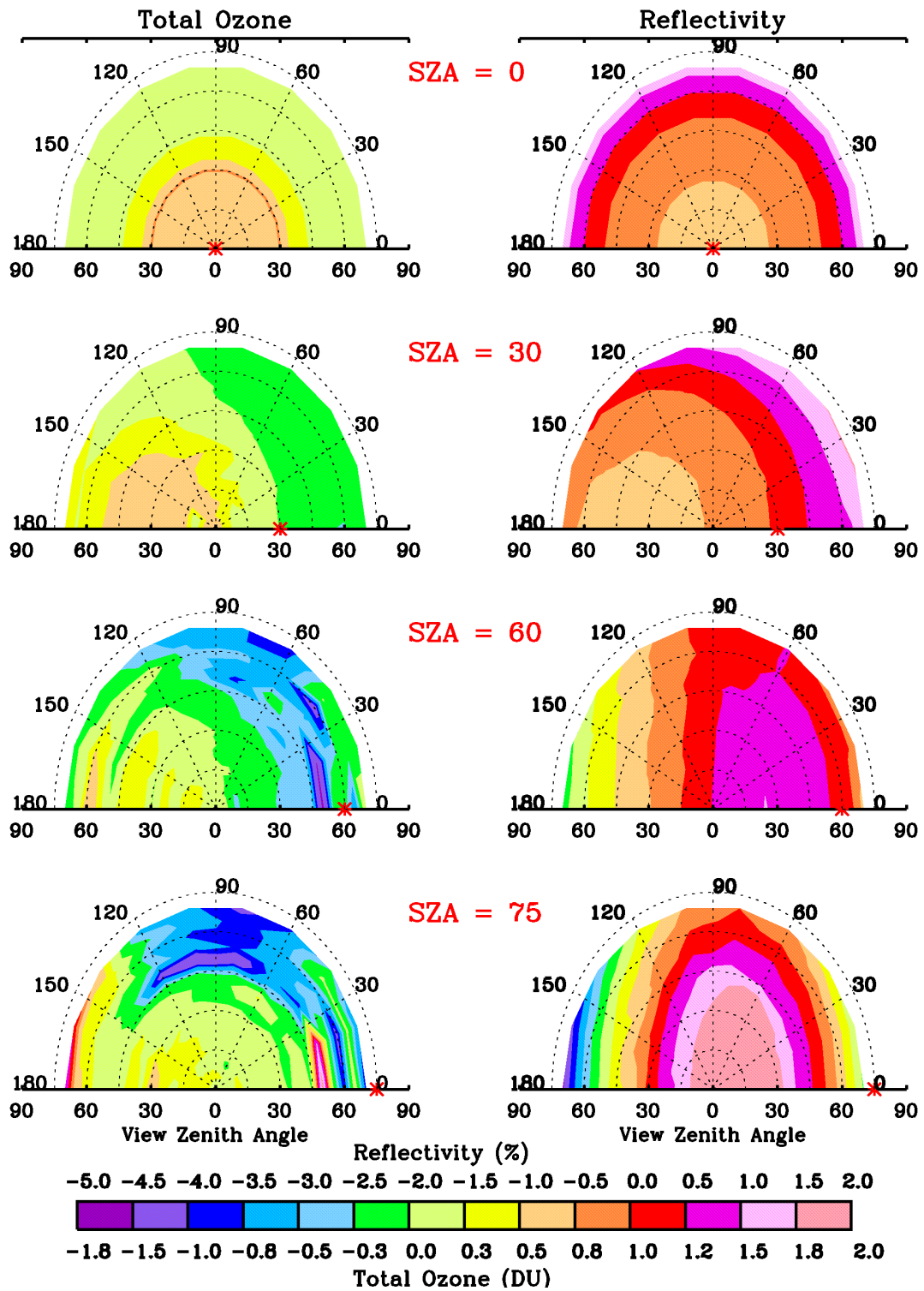


Figure A.6 Same as Figure A.2 except for a cloudy-sky with a WC of COD 40 at 2-6 km.

scattering (i.e., those photons are scattered back to TOA without reaching the cloud surface) and only a small portion of the photons penetrate through the clouds. Therefore, the error in the reflected radiance due to scalar approximation is still large. Similar calculations are done for cases similar to those in Figure A.2 except that there is no Rayleigh scattering, and the intensity errors in both reflection and transmission are reduced to within 0.2% even for a COD of 1. Therefore, it is still the particular structure of the Rayleigh scattering matrix that leads to larger errors resulting from scalar approximation for cloudy conditions.

Figure A.6 shows error patterns in the retrieved ozone and reflectivity due to scalar approximation for a WC of COD 40 at 2-6 km. As a result of the errors in the reflected radiance, the neglect of polarization causes errors to the retrieved reflectivity, ranging from  $-5\%$  to  $2\%$ . Due to the wavelength dependence in the effect of neglecting polarization on reflected radiance, the error in ozone is within 2 DU, smaller compared to the error under clear-sky conditions. The error in ozone and the angular dependence of the error pattern indicate that polarization is not negligible for accurate ozone retrieval.

### A.3 Summary

We study the effect of neglecting polarization on the calculated radiance at TOMS wavelengths, and the corresponding effects on the retrieved ozone and reflectivity. Because of the large Rayleigh scattering optical depth at TOMS wavelengths, ranging from 0.45 at 380 nm to about 1 at 312 nm, the scalar approximation causes significant errors in the calculated radiance under clear-sky conditions. The errors in radiance are highly angular-dependent, ranging from  $-8\%$  to  $10\%$  for the reflected radiance and from  $-14\%$  to  $11\%$  for the transmitted radiance. Correspondingly, the large errors in radiance at the TOMS reflectivity wavelength cause large errors in the retrieved reflectivity, from  $-18\%$  to  $4\%$ . Because of its wavelength dependence in the effect of neglecting polarization on the calculated radiance, the scalar treatment in the calculation of TOMS look-up table leads to angular-dependent OREs, ranging from  $-4.5$  DU to  $3.5$  DU.

Under cloudy conditions, the effect of neglecting polarization diminishes with increasing CODs because of the in-cloud multiple scattering and multiple reflections between clouds and the atmosphere. However, even for a cloud of COD 40, neglecting polarization still causes large errors in the reflected radiance at TOMS wavelengths, ranging from  $-4.0$  to  $3.8\%$ , because a significant portion of backscattered

photons experience Rayleigh scattering and are scattered back to the space before they interact with clouds. For transmitted radiance, the error is much smaller for a cloud of COD 40, from  $-0.4\%$  to  $0.9\%$ , because each photon transmitted to the surface must interact with the clouds. Because of the error in the calculated radiance, the neglect of polarization causes errors in the retrieved reflectivity from  $-5\%$  to  $2\%$  and in the retrieved ozone within 2 DU from TOMS measurements. Polarization cannot be ignored in the ultraviolet and near-ultraviolet wavelength regions (i.e., TOMS wavelengths) even under cloudy conditions for accurate radiance simulation and ozone retrieval because of the strong Rayleigh scattering in those wavelength regions.

## APPENDIX B

### TOMS OZONE RETIREVAL EFFICIENCY FACTORS

The reduced sensitivity of the TOMS instrument to lower tropospheric ozone has been well characterized [Hudson *et al.*, 1995; Kim *et al.*, 2001; Klenk *et al.*, 1982; Martin *et al.*, 2002; Wellemeyer *et al.*, 1997]. Because of the strong ozone absorption in the stratosphere, strong Rayleigh scattering, and low surface albedos, fewer photons penetrate the lower troposphere; therefore, the TOMS instrument captures limited lower tropospheric ozone information. The retrieved ozone from the troposphere depends on the TOMS standard climatological tropospheric ozone profiles used, and is underestimated (overestimated) if the actual tropospheric ozone is higher (lower) than the climatological tropospheric ozone. Hudson *et al.* [1995] introduced the tropospheric Retrieval Efficiency Factor (REF) relative to stratospheric ozone. The REF is calculated as the ratio of the calculated increase in N value as a result of adding 10 DU of ozone relative to the lower stratosphere. This calculation assumes the REF in the lower stratosphere is 1.

A slightly different method is presented to calculate the REF in both the troposphere and stratosphere using the TOMRAD and the TOMS V7 algorithm. The REFs are calculated for layers between two of nearby pressure levels: 1000, 950, 900, 850, 800, 750, 700, 650, 600, 550, 500, 450, 400, 350, 300, 250, 200, 150, 100, 62.5, 31.25, 15.6, 7.8, 3.9, 1.95, and 0.975 hPa. To obtain the REF for a particular layer, we add 10 DU ozone to that layer in the TOMS standard profile and then calculate the radiance using TOMRAD and retrieve the TOC using the TOMS V7 algorithm. The ratio of the difference between retrieved ozone and the TOC in the TOMS standard ozone profile to the ozone amount of

perturbation (i.e., 10 DU) is derived as the REF for that layer. Using the TOMS V7 algorithm instead of the N-values better represents the retrieval efficiency in the TOMS data.

Figure B.1 shows the derived profiles of REFs for different combinations of SZAs, VZAs, and surface reflectivities. The low-latitude TOMS standard ozone profile L275 is used. The tropospheric REFs between 1000 hPa and 100 hPa are similar to the results shown by *Hudson et al.* [1995]. The REF varies greatly with surface reflectivity in the troposphere, but the REF difference between different reflectivities decreases with increasing altitude and viewing geometry. At 975 hPa, the REFs are 20% for surface reflectivity 8% and 190% for surface reflectivity 100% at  $\theta_0 = 0^\circ$  and  $\theta = 0^\circ$ ; the corresponding REF values at  $\theta_0 = 60^\circ$  and  $\theta = 60^\circ$  are 8% and 88%. At 500 hPa, the REFs are 81% for surface reflectivity 8% and 150% for surface reflectivity 100% at  $\theta_0 = 0^\circ$  and  $\theta = 0^\circ$ ; the corresponding REF values at  $\theta_0 = 60^\circ$  and  $\theta = 60^\circ$  are 58% and 100%. At a given surface reflectivity and viewing geometry, the tropospheric REF has a peak in the troposphere. This peak altitude decreases with increasing surface reflectivity and increases with increasing viewing geometry. The REFs are 1 at  $\sim 100$  hPa under all conditions except for the case with surface reflectivity 80% at 200 hPa. *Hudson et al.* [1995] did not present the REF in the stratosphere but assumed the REF in the lower stratosphere is 1. However, we can see from Figure B.1 that the REFs in the stratosphere are not perfect, i.e., 1. In the stratosphere below  $\sim 100$  hPa, the REFs are mostly greater than 1 and increase with decreasing pressure. Unlike the REF in the troposphere, the stratospheric REF decreases with increasing surface reflectivity. If the TOMS standard stratospheric climatological profiles contain some errors, the retrieved ozone will have even larger errors. Because of the large amount of ozone in the stratosphere, the a priori stratospheric climatological profiles can have large effects on the derived tropospheric ozone as well as on the a priori tropospheric climatological profiles. The error in the a priori climatological profiles and the fact that the stratospheric REF is usually greater than 1 might contribute to the large TOMS overestimation (for SZA  $65^\circ$ - $75^\circ$ ) or underestimation (for SZA  $> 85^\circ$ ) relative to ground-based measurements [*Lambert et al.*, 1999; *Lloyd et al.*, 1999; *Nichol et al.*, 1996].

Figure B.1 also shows the REF profile for a surface reflectivity 8% at surface pressure 800 hPa and 500 hPa, respectively. The decreasing surface pressure may represent surface with increasing terrain height. We can see that the decreasing surface pressure decreases the REFs in the troposphere above the

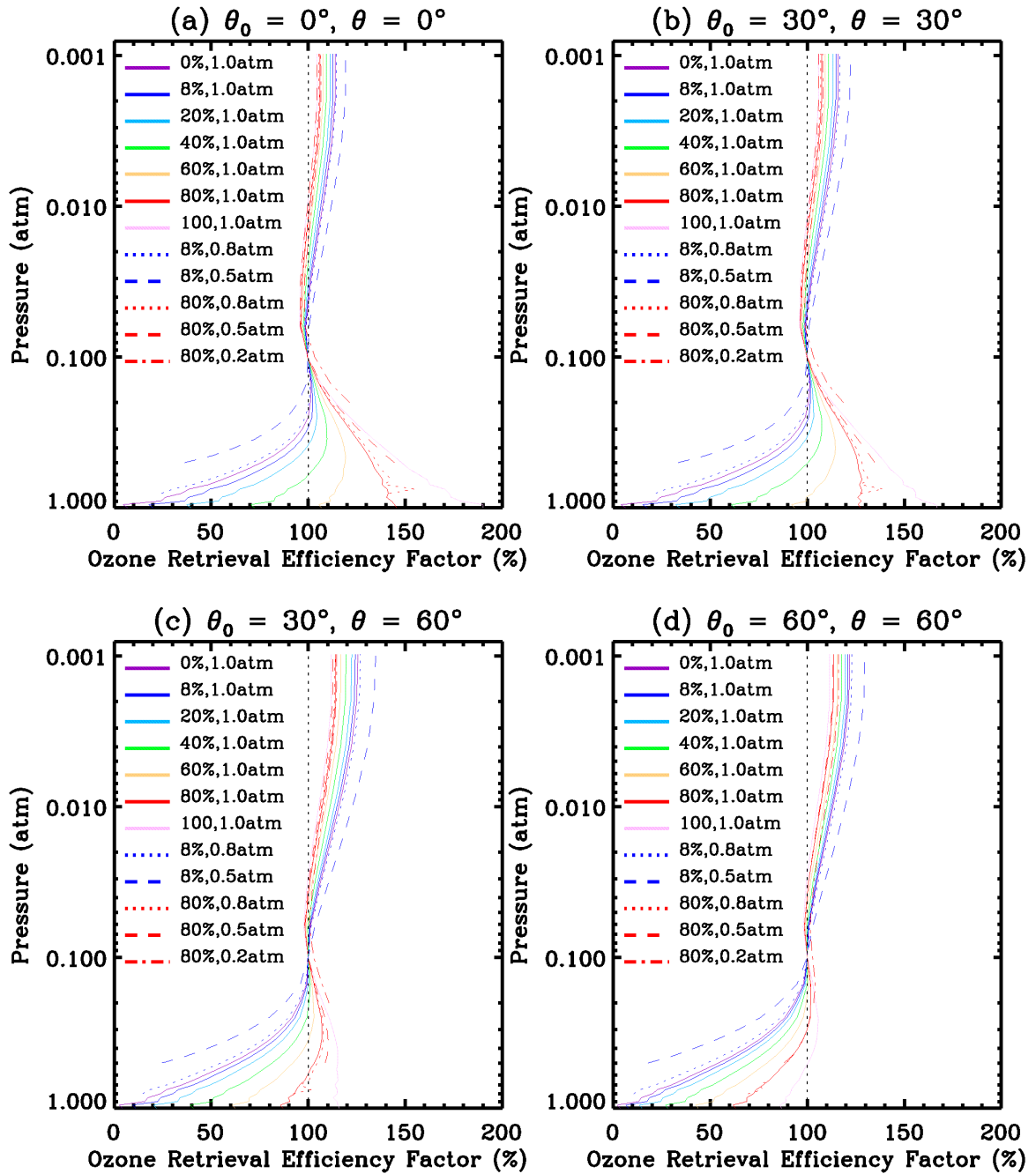


**Figure B.1** Ozone retrieval efficiency factors as function of pressure level for different viewing geometries, surface reflectivities, and surface pressures. The TOMS standard profile L275 is used.

surface but increases the REFs in the stratosphere. In addition to the small low-tropospheric RTE, the elevated terrain affects the REF above that terrain height. Therefore, the derived lower tropospheric ozone from topographic contrast method [*Jiang and Yung, 1996; Kim and Newchurch, 1996; Kim and Newchurch, 1998; Newchurch et al., 2001*] may not fully capture the actual lower tropospheric ozone. The REF profiles for surface reflectivity 80% at 800 hPa, 500 hPa, and 200 hPa characterize the retrieval efficiency for cloudy-sky conditions. Unlike the decrease of surface pressure for low-reflectivity conditions, the decreasing cloudy surface pressure increases the REFs in the troposphere but decreases the REFs in the stratosphere.

## REFERENCES

- Allen, D.R., and R.A. Reck, Daily variations in TOMS total ozone data, *J. Geophys. Res.*, *102*, 13,603-13,608, 1997.
- Arnott, W.P., Y.Y. Dong, J. Hallett, and M.R. Poellot, Role of small ice crystals in radiative properties of cirrus: A case study, FIRE II, November 22, 1991, *J. Geophys. Res.*, *99*, 1371-1381, 1994.
- Bass, A.M., and R.J. Paur, The ultraviolet cross-sections of ozone, I, The measurements, in Atmospheric Ozone, edited by C.S. Zerefos and A. Ghazi, D. Reidel, Massachusetts, 1984.
- Bates, D.R., Rayleigh scattering by air, *Planet. Space Sci.*, *32*, 785-799, 1984.
- Bell, G.D., M.S. Halpert, C.F. Ropelewski, V.E. Kousky, A.V. Douglas, R.C. Schnell, and M.E. Gelman, Climate assessment for 1998, *Bull. Amer. Meteorol. Soc.*, *80*, 1-48, 1999.
- Bey, I., D.J. Jacob, R.M. Yantosca, J.A. Logan, B. Field, A.M. Fiore, Q. Li, H. Liu, L.J. Mickley, and M. Schultz, Global modeling of tropospheric chemistry with assimilated meteorology: Model description and evaluation, *J. Geophys. Res.*, *106*, 23,073-23,096, 2001.
- Bhartia, P.K., OMI algorithm theoretical basis document, Volume II: OMI ozone products, 2001.
- Bhartia, P.K., J.R. Herman, and R.D. McPeters, Effect of Mount Pinatubo aerosols on total ozone measurements from Backscatter Ultraviolet (BUV) Experiments, *J. Geophys. Res.*, *98*, 18,547-18,554, 1993.
- Bohren, C.F., and D.R. Huffman, Absorption and scattering of light by small particles, John Wiley & Sons, New York, 1998.
- Brasseur, G.P., D.A. Hauglustaine, S. Walters, P.J. Rasch, J.-F. Muller, C. Granier, and X.X. Tie, MOZART, a global chemical transport model for ozone and related chemical tracers 1: Model description, *J. Geophys. Res.*, *103*, 28,265-28,289, 1998.
- Brewer, A.W., and J.B. Kerr, Total ozone measurements in cloudy weather, *Pure Appl. Geophys.*, *106-108*, 929-937, 1973.
- Chameides, W.L., P.S. Kasibhatla, J. Yienger, and H.L. II, Growth of continental-scale metro-agro-plexes, regional ozone pollution, and world food production, *Science*, *264*, 74-77, 1994.
- Chance, K., OMI algorithm theoretical basis document, Volume IV: OMI trace gas algorithms, 2001.
- Chandra, S., J.R. Ziemke, W. Min, and W.G. Read, Effects of 1997-1998 El Niño on tropospheric ozone and water vapor, *Geophys. Res. Lett.*, *25*, 3867-3870, 1998.
- Crutzen, P., and M. Lawrence, Ozone clouds over the Atlantic, *Nature*, *388*, 625-626, 1997.

- Cunnold, D.M., R.F. Weiss, R.G. Prinn, D. Hartley, P.G. Simmonds, P.J. Fraser, B. Miller, F.N. Alyea, and L. Porter, GAGE/AGAGE measurements indicating reductions in global emissions of CCl<sub>3</sub>F and CCl<sub>2</sub>F<sub>2</sub> in 1992-1994, *J. Geophys. Res.*, *102*, 1259-1269, 1997.
- Dave, J.V., Meaning of successive iteration of the auxiliary equation in the theory of radiative transfer, *Astrophys. J.*, *140*, 1292-1303, 1964.
- Dessler, A.E., The effect of deep, tropical convection on the tropical tropopause layer, *J. Geophys. Res.*, *107*, 2002.
- Dickerson, R.R., G.J. Huffman, W.T. Luke, L.J. Nunnermacker, K.E. Pikerling, A.C.D. Leslie, C.G. Lindsey, W.G.N. Slinn, T.J. Kelly, P.H. Daum, A.C. Delany, J.P. Greenberg, P.R. Zimmerman, J.F. Boatman, J.D. Ray, and D.H. Stedman, Thunderstorms: An important mechanism in the transport of air pollutants, *Science*, *235*, 460-465, 1987.
- Dobson, G.M.B., and D.N. Harrison, Measurements of the amount of ozone in the Earth's atmosphere and its relation to other geophysical conditions, *Proc. R. Soc. London A*, *110*, 660-693, 1926.
- Dobson, G.M.B., D.N. Harrison, and J. Lawrence, Measurements of the amount of ozone in the Earth's atmosphere and its relation to other geophysical conditions, *Proc. R. Soc. London A*, *122*, 456-486, 1928.
- Dobson, G.M.B., and C.W.B. Normand, Determination of constants used in the calculation of the amount of ozone from spectrophotometer measurements and an analysis of the accuracy of the results, *Ann. Int. Geophys. Yr.*, *XVI* (II), 161-191, 1962.
- Doutriaux-Boucher, M., Buriez, G. Brogniez, L. C.-Labonnote, and A.J. Baran, Sensitivity of retrieved POLDER directional cloud optical thickness to various ice particle models, *Geophys. Res. Lett.*, *27*, 109-112, 2000.
- Emmons, L.K., D.A. Hauglustaine, J.F. Muller, M.A. Carroll, G.P. Brasseur, D. Brunner, J. Staehelin, V. Thouret, and A. Marengo, Data composites of airborne observations of tropospheric ozone and its precursors, *J. Geophys. Res.*, *105*, 20,497-20,538, 2000.
- Erle, F., K. Pfeilsticker, and U. Platt, On the influence of tropospheric clouds on zenith-scattered-light measurements on stratospheric species, *Geophys. Res. Lett.*, *22*, 2725-2728, 1995.
- Feigelson, M.E., Radiation in a cloudy atmosphere, D. Reidel, Massachusetts, 1984.
- Fioletov, V.E., J.B. Kerr, and D.I. Wardle, The relationship between total ozone and spectral UV irradiance from Brewer observations and its use for derivation of total ozone from UV measurements, *Geophys. Res. Lett.*, *24*, 2997-3000, 1997.
- Fischer, J., and H. Grassl, Detection of cloud-top height from backscattered radiances within the oxygen A band-part I: Theoretical study, *J. Appl. Meteorol.*, *30*, 1245-1259, 1991.
- Fishman, J., and V.G. Brackett, The climatological distribution of tropospheric ozone derived from satellite measurements using version-7 Total Ozone Mapping Spectrometer and Stratospheric Aerosol and Gas Experiment data sets, *J. Geophys. Res.*, *102*, 19,275-19,278, 1997.
- Fishman, J., K. Fakhruzzaman, B. Cros, and D. Nganga, Identification of widespread pollution in the Southern Hemisphere deduced from satellite analyses, *Science*, *252*, 1693-1696, 1991.

- Fishman, J., V. Ramanathan, P.J. Crutzen, and S.C. Liu, Tropospheric ozone and climate, *Nature*, 282, 818-820, 1979.
- Fishman, J., C.E. Watson, J.C. Larsen, and J.A. Logan, Distribution of tropospheric ozone determined from satellite data, *J. Geophys. Res.*, 95, 3599-3617, 1990.
- Folkens, I., M. Loewenstein, J. Podolske, S.J. Oltmans, and M. Proffitt, A barrier to vertical mixing at 14 km in the tropics: Evidence from ozonesondes and aircraft measurements, *J. Geophys. Res.*, 104, 22,095-22,102, 1999.
- Foot, J.S., Some observations of the optical properties of clouds, II: Cirrus, *Q. J. R. Meteorol. Soc.*, 114, 145-164, 1988.
- Francis, P.N., Some aircraft observations of the scattering properties of ice crystals, *J. Atmos. Sci.*, 52, 1142-1154, 1995.
- Fu, Q., and K.N. Liou, Parameterization of the radiative properties of cirrus clouds, *J. Atmos. Sci.*, 50, 2008-2025, 1993.
- Fujita, T.T., The mystery of sever storms, *WRL Res. Pap.*, 239, pp298, 1992.
- Gottelman, A., M.L. Salby, and F. Sassi, Distribution and influence of convection in the tropical tropopause region, *J. Geophys. Res.*, 107, 2002.
- Hale, G.M., and M.R. Querry, Optical constants of water in the 200-nm to 200-m wavelength region, *Appl. Opt.*, 12, 555-563, 1973.
- Han, Q., W.B. Rossow, and A.A. Lacis, Near-global survey of effective droplet radii in liquid water clouds using ISCCP data, *J. Clim.*, 7, 465-497, 1994.
- Hansen, J.E., Multiple scattering of polarized light in planetary atmospheres. Part II: Sunlight reflected by terrestrial water clouds, *J. Atmos. Sci.*, 28, 1400-, 1971.
- Hansen, J.E., and L.D. Travis, Light scattering in planetary atmospheres, *Space Sci., Rev.*, 16, 527-610, 1974.
- Herman, B.M., W. Asous, and S.R. Browning, A semi-analytic technique to integrate the radiative transfer equation over optical depth, *J. Atmos. Sci.*, 37, 1828-1838, 1980.
- Herman, B.M., A. Ben-David, and K.J. Thome, Numerical technique for solving the radiative transfer equation for a spherical shell atmosphere, *Appl. Opt.*, 33, 1760-1770, 1994.
- Herman, B.M., and S.R. Browning, A numerical solution to the equation of radiative transfer, *J. Atmos. Sci.*, 22, 559-566, 1965.
- Herman, B.M., and S.R. Browning, The effect of aerosol on the Earth-atmosphere albedo, *J. Atmos. Sci.*, 32, 1430-1445, 1975.
- Herman, B.M., T.R. Caudill, D.E. Flittner, K.J. Thome, and A. Ben-David, Comparison of the Gauss-Seidel spherical polarized radiative transfer code with other radiative transfer codes, *Appl. Opt.*, 34, 4563-4572, 1995.

- Herman, J.R., P.K. Bhartia, A.J. Krueger, R.D. McPeters, C.G. Wellemeyer, C.J. Seftor, G. Jaross, B.M. Schlesinger, O. Torres, G. Labow, W. Byerly, S.L. Taylor, T. Swissler, R.P. Cebula, and X. Gu, Meteor-3 Total Ozone Mapping Spectrometer (TOMS) data products user's guide, *NASA Reference Publication*, 1996.
- Herman, J.R., E.A. Celarier, and D. Larko, UV 380 nm reflectivity of the Earth's surface, clouds, and aerosols, *J. Geophys. Res.*, *106*, 5335-5351, 2001.
- Herman, J.R. and E.A. Celarier, Earth surface reflectivity climatology at 340-380 nm from TOMS data, *J. Geophys. Res.*, *102*, 28,003-28,011, 1997.
- Heymsfield, A.J., and C.M.R. Platt, A parameterization of the particle size spectrum of ice clouds in terms of the ambient temperature and the ice water content, *J. Atmos. Sci.*, *41*, 846-855, 1984.
- Hsu, N.C., R.D. McPeters, C.J. Seftor, and A.M. Thompson, Effect of an improved cloud climatology on the total ozone mapping spectrometer total ozone retrieval, *J. Geophys. Res.*, *102*, 4247-4255, 1997.
- Hudson, R.D., and A.D. Frolov, Separation of total ozone by meteorological regimes, in *The Scientific Program of Quadrennial Ozone Symposium*, Sapporo, Japan, 2000.
- Hudson, R.D., J.H. Kim, and A.M. Thompson, On the derivation of tropospheric column from radiances measured by the Total Ozone Mapping Spectrometer, *J. Geophys. Res.*, *100*, 11,137-11,145, 1995.
- Hudson, R.D., and A.M. Thompson, Tropical tropospheric ozone from Total Ozone Mapping Spectrometer by a modified residual method, *J. Geophys. Res.*, *103*, 22,129-22,145, 1998.
- Jacob, D.J., Heterogeneous chemistry and tropospheric ozone, *Atmos. Environ.*, *34*, 2131-2159, 2000.
- Jiang, Y., and Y.L. Yung, Concentrations of tropospheric ozone from 1979 to 1992 over tropical Pacific South America from TOMS data, *Science*, *272*, 714-716, 1996.
- Kim, J.H., R.D. Hudson, and A.M. Thompson, A new method of deriving time-averaged tropospheric column ozone over the tropics using Total Ozone Mapping Spectrometer (TOMS) radiances: Intercomparison and analysis using TRACE-A data, *J. Geophys. Res.*, *101*, 24,317-24,330, 1996.
- Kim, J.H., and M.J. Newchurch, Climatology and trends of tropospheric ozone over the eastern Pacific Ocean: The influences of biomass burning and tropospheric dynamics, *Geophys. Res. Lett.*, *23*, 3723-3726, 1996.
- Kim, J.H., and M.J. Newchurch, Biomass-burning influence on tropospheric ozone over New Guinea and South America, *J. Geophys. Res.*, *103*, 1455-1461, 1998.
- Kim, J.H., M.J. Newchurch, and K. Han, Distribution of tropical tropospheric ozone determined by the scan-angle method applied to TOMS measurements, *J. Atmos. Sci.*, *58*, 2699-2708, 2001.
- Kinne, S., O.B. Toon, G.C. Toon, C.B. Farmer, E.V. Browell, and M.P. McCormick, Measurements of size and composition of aerosols in polar stratospheric clouds from infrared solar absorption spectra, *J. Geophys. Res.*, *94*, 16,481-16,491, 1989.
- Kirchhoff, V.W.J.H., J.R. Alves, F.R. da Silva, and J. Fishman, Observations of ozone concentrations in the Brazilian cerrado during the TRACE-A field expedition, *J. Geophys. Res.*, *101*, 24,029-24,042, 1996.

- Klenk, K.F., P.K. Bhartia, A.J. Fleig, V.G. Kaveeshwar, R.D. McPeters, and P.M. Smith, Total ozone determination from the Backscattered Ultraviolet (BUV) experiment, *J. Appl. Meteorol.*, *21*, 1672-1684, 1982.
- Kley, D., P.J. Crutzen, H.G.J. Smit, H. Vomel, S.J. Oltmans, H. Grassl, and V. Ramanathan, Observations of near-zero ozone concentrations over the convective Pacific: Effects on air chemistry, *Science*, *274*, 230-233, 1996.
- Knibbe, W.J.J., J.F. de Haan, J.W. Hovenier, D.M. Stam, R.B.A. Koelemeijer, and P. Stammes, Deriving terrestrial cloud-top pressure from photopolarimetry of reflected light, *J. Quant. Spectrosc. Radiat. Transfer*, *64*, 173-199, 2000.
- Koelemeijer, R.B.A., and P. Stammes, Effects of clouds on ozone column retrieval from GOME UV measurements, *J. Geophys. Res.*, *104*, 8281-8294, 1999.
- Krueger, A.J., P.K. Bhartia, R.D. McPeters, J.R. Herman, C.G. Wellemeijer, G. Jaross, C.J. Seftor, O. Torres, G. Labow, W. Byerly, S.L. Taylor, T. Swissler, and R.P. Cebula, ADEOS Total Ozone Mapping Spectrometer (TOMS) data products user's guide, *NASA Reference Publication*, 1998.
- Kurosu, T., V.V. Rozanov, and J.P. Burrows, Parameterization schemes for terrestrial water clouds in the radiative transfer model GOMETRAN, *J. Geophys. Res.*, *102*, 21,809-21,823, 1997.
- Kylling, A., A. Albold, and G. Seckmeyer, Transmittance of a cloud is wavelength-dependent in the UV-range: Physical interpretation, *Geophys. Res. Lett.*, *24*, 397-400, 1997.
- Lacis, A.A., J. Chowdhary, M.I. Mishchenko, and B. Cairns, Modeling errors in diffuse-sky radiation: Vector vs. scalar treatment, *Geophys. Res. Lett.*, *25*, 135-138, 1998.
- Lambert, J.-C., M. Van Roozendael, M. De Maziere, P.C. Simon, J.-P. Pommereau, F. Goutail, A. Sarkissian, and J.F. Gleason, Investigation of pole-to-pole performances of spaceborne atmospheric chemistry sensors with the NDSC, *J. Atmos. Sci.*, *56*, 176-193, 1999.
- Lee, M., B.G. Heikes, and D.J. Jacob, Enhancements of hydroperoxides and formaldehyde in biomass burning impacted air and their effect on atmospheric oxidant cycles, *J. Geophys. Res.*, *103*, 13,201-13,212, 1998.
- Lelieveld, J., and P.J. Crutzen, Influences of cloud photochemical processes on tropospheric ozone, *Nature*, *343*, 227-233, 1990.
- Lloyd, S., W.H. Swatz, T. Kusterer, D. Anderson, C.T. McElroy, C. Midwinter, R. Hall, K. Nassim, D. Jaffe, W. Simpson, J. Kelley, D. Nicks, D. Griffin, B. Johnson, R. Evans, D. Quincy, S. Oltmans, P. Newman, R. McPeters, G. Labow, L. Moy, C. Seftor, G. Toon, B. Sen, and J.F. Blavier, Intercomparison of total ozone observations at Fairbanks, Alaska, during POLARIS, *J. Geophys. Res.*, *104*, 26,767-26,778, 1999.
- Logan, J.A., Tropospheric ozone: Seasonal behavior, trends, and anthropogenic influence, *J. Geophys. Res.*, *90*, 10,463-10,482, 1985.
- Logan, J.A., An analysis of ozonesonde data for the lower stratosphere: Recommendations for testing models, *J. Geophys. Res.*, *104*, 16,151-16,170, 1999.

- Logan, J.A., I.A. Megretskaya, A.J. Miller, G.C. Tiao, D. Choi, L. Zhang, R.S. Stolarski, G.J. Labow, S.M. Hollandsworth, G.E. Bodeker, H. Claude, D.D. Muer, J.B. Kerr, D.W. Tarasick, S.J. Oltmans, B. Johnson, F. Schmidlin, J. Staehelin, P. Viatte, and O. Uchino, Trends in the vertical distribution of ozone: A comparison of two analyses of ozonesonde data, *J. Geophys. Res.*, *104*, 26,373-26,399, 1999.
- Logan, J.A., M.J. Prather, S.C. Wofsy, and M.B. McElroy, Tropospheric chemistry: A global perspective, *J. Geophys. Res.*, *86*, 7210-7254, 1981.
- Macke, A., Scattering of light by polyhedral ice crystals, *Appl. Opt.*, *32*, 2780-2788, 1993.
- Macke, A., M.I. Mishchenko, and B. Cairns, The influence of inclusions on light scattering by large ice particles, *J. Geophys. Res.*, *101*, 23,311-23,316, 1996a.
- Macke, A., J. Muller, and E. Raschke, Single scattering properties of atmospheric ice crystals, *J. Atmos. Sci.*, *53*, 2813-2825, 1996b.
- Madronich, S., Photodissociation in the atmosphere 1: Actinic flux and the effects of ground reflections and clouds, *J. Geophys. Res.*, *92*, 9740-9752, 1987.
- Marshak, A., A. Davis, W. Wiscombe, and R. Cahalan, Radiative smoothing in fractal clouds, *J. Geophys. Res.*, *100*, 26,247-26,261, 1995.
- Martin, R.V., D.J. Jacob, J.A. Logan, I. Bey, R.M. Yantosca, A.C. Staudt, Q. Li, A.M. Fiore, B.N. Duncan, H. Liu, P. Ginoux, and V. Thouret, Interpretation of TOMS observations of tropical tropospheric ozone with a global model and in-situ observations, *J. Geophys. Res.*, in press, 2002.
- Mattingly, S.R., The contribution of extratropical severe storms to the stratospheric water vapor budget, *Meteorol. Mag.*, *106*, 256-262, 1977.
- Mayer, B., A. Kylling, S. Madronich, and G. Seckmeyer, Enhanced absorption of UV radiation due to multiple scattering in clouds: Experimental evidence and theoretical explanation, *J. Geophys. Res.*, *103*, 31,241-31,254, 1998.
- McFarquhar, G.M., and A.L. Heymsfield, The definition and significance of an effective radius for ice clouds, *J. Atmos. Sci.*, *55*, 2039-2052, 1997.
- McPeters, R.D., P.K. Bhartia, A.J. Krueger, J.R. Herman, B.M. Schlessinger, C.G. Wellemeyer, C.J. Seftor, G. Jaross, S.L. Taylor, T. Swissler, O. Torres, G. Labow, W. Byerly, and R.P. Cebula, Nimbus-7 Total Ozone Mapping Spectrometer (TOMS) data products user's guide, *NASA Reference Publication*, 1996.
- McPeters, R.D., P.K. Bhartia, A.J. Krueger, J.R. Herman, C.G. Wellemeyer, C.J. Seftor, G. Jaross, O. Torres, L. Moy, G. Labow, W. Byerly, S.L. Taylor, T. Swissler, and R.P. Cebula, Earth Probe Total Ozone Mapping Spectrometer (TOMS) data product user's guide, *NASA Reference Publication*, 1998.
- McPeters, R.D., and G.J. Labow, An assessment of the accuracy of 14.5 years of Nimbus-7 TOMS version-7 ozone data by comparison with the Dobson network, *Geophys. Res. Lett.*, *23*, 3695-3698, 1996.
- Mishchenko, M.I., J.M. Dlugach, E.G. Yanovitskij, and N.T. Zakharova, Bidirectional reflectance of flat, optically thick particulate layers: An efficient radiative transfer solution and applications to snow and soil surfaces, *J. Quant. Spectrosc. Radiat. Transfer*, *63*, 409-432, 1999.

- Mishchenko, M.I., A.A. Lacis, and L.D. Travis, Errors induced by the neglect of polarization in radiance calculations for rayleigh scattering atmospheres, *J. Quant. Spectrosc. Radiat. Transfer*, *51*, 491-510, 1994.
- Mishchenko, M.I., W.B. Rossow, A. Macke, and A.A. Lacis, Sensitivity of cirrus cloud albedo, bidirectional reflectance, and optical thickness retrieval accuracy to ice particle shape, *J. Geophys. Res.*, *101*, 16,973-16,985, 1996.
- Newchurch, M., D. Sun, X. Liu, L. Emmons, L. Horowitz, J.H. Kim, D. Kinnison, G. Brasseur, D. Jacob, J. Logan, R.V. Martin, K. Han, and S. Na, Critical Assessment of TOMS-derived tropospheric ozone: Comparisons with other measurements and model evaluation of controlling processes, *Eos. Trans. AGU*, *82*, Spring Meet. Suppl. Abstract A52A-09, 2001a.
- Newchurch, M.J., X. Liu, and J.H. Kim, Lower Tropospheric Ozone (LTO) derived from TOMS near mountainous regions, *J. Geophys. Res.*, *106*, 20,403-20,412, 2001b.
- Newchurch, M.J., D. Sun, and J.H. Kim, Zonal wave-1 structure in TOMS tropical stratospheric ozone, *Geophys. Res. Lett.*, *28* (16), 3151-3154, 2001c.
- Newchurch, M.J., D. Sun, J.H. Kim, and X. Liu, Tropical tropospheric ozone derived using Clear-Cloudy Pairs (CCP) of TOMS measurements, *submitted to Atmospheric Chemistry and Physics*, 2002.
- Nichol, S.E., J.G. Keys, S.W. Wood, P.V. Johnston, and G.E. Bodeker, Intercomparison of total ozone data from a Dobson spectrophotometer, TOMS, visible wavelength spectrometer, and ozonesondes, *Geophys. Res. Lett.*, *23*, 1087-1090, 1996.
- Paur, R.J., and A.M. Bass, The ultraviolet cross-sections of ozone, II: Results and temperature dependence, in *Atmospheric Ozone*, edited by C.S. Zerefos and A. Ghazi, D. Reidel, Massachusetts, 1984.
- Pfister, G., D. Baumgartner, R. Maderbacher, and E. Putz, Aircraft measurements of photolysis rate coefficients for ozone and nitrogen dioxide under cloudy conditions, *Atmos. Environ.*, *34*, 4019-4029, 2000.
- Pickering, K.E., A.M. Thompson, R.R. Dickerson, W.T. Luke, D.P. McNamara, J.P. Greenberg, and P.R. Zimmerman, Model calculations of tropospheric ozone production potential following observed convective events, *J. Geophys. Res.*, *95*, 14,049-14,062, 1990.
- Pickering, K.E., A.M. Thompson, J.R. Scala, W.-K. Tao, J. Simpson, and M. Garstang, Photochemical ozone production in tropical squall line convection during NASA Global Tropospheric Experiment/Amazon Boundary Layer Experiment 2A, *J. Geophys. Res.*, *96*, 3099-3114, 1991.
- Pickering, K.E., A.M. Thompson, W.K. Tao, and T.L. Kucsera, Upper tropospheric ozone production following mesoscale convection during STEP/EMEX, *J. Geophys. Res.*, *98*, 8737-8749, 1993.
- Posse, P., and W.V. Hoyningen-Huene, Information about scattering properties and particle characteristics of stratiform cloud at Helgoland by remote optical measurements, *Beitr. Phys. Atmos.*, *68*, 359-366, 1995.
- Poulida, O., R.R. Dickerson, and A. Heymsfield, Stratosphere-troposphere exchange in a mid-latitude mesoscale convective complex 1: Observations, *J. Geophys. Res.*, *101*, 6823-6836, 1996.
- Ramanathan, V., R.D. Cess, E.F. Harrison, P. Minnis, B.R. Barkstrom, E. Ahmad, and D. Hartmann, Cloud-radiative forcing and climate: Results from the Earth radiation budget experiment, *Science*, *243*, 57-63, 1989.

- Ramanathan, V., and R.E. Dickinson, The role of stratospheric ozone in the zonal and seasonal radiation energy balance of the earth tropospheric system, *J. Atmos. Sci.*, 36, 1084-1104, 1979.
- Randel, W.J., F. Wu, and D.J. Gaffen, Interannual variability of the tropical tropopause derived from radiosonde data NCEP reanalysis, *J. Geophys. Res.*, 105, 15,509-15,523, 2000.
- Ridley, B.A., J.G. Walega, J.E. Dye, and F.E. Grahek, Distributions of NO, NO<sub>x</sub>, NO<sub>y</sub>, and O<sub>3</sub> to 12 km altitude during the summer monsoon season over New Mexico, *J. Geophys. Res.*, 99, 25,519-25,534, 1994.
- Rossow, W.B., and R.A. Schiffer, ISCCP cloud data products, *Bull. Am. Meteorol. Soc.*, 72, 2-20, 1991.
- Rossow, W.B., A.W. Walker, D.E. Beuschel, and M.D. Roiter, International Satellite Cloud Climatology Project (ISCCP) documentation of new cloud dataset, WMO/TD, Geneva, Switzerland, 1996.
- Saiedy, F., H. Jacobowitz, and D.Q. Wark, On cloud-top determination from Gemini-5, *J. Atmos. Sci.*, 24, 63-69, 1965.
- Salby, M.L., and P.F. Callaghan, Fluctuations of total ozone and their relationship to stratospheric air motions, *J. Geophys. Res.*, 98, 2715-2727, 1993.
- Sassen, K., N.C. Knight, Y. Takano, and A.J. Heymsfield, Effects of ice-crystal structure on halo formation: Cirrus cloud experimental and ray tracing modeling studies, *Appl. Opt.*, 33, 4590-4601, 1994.
- Seinfeld, J.H., and S.N. Pandis, Atmospheric chemistry and physics, John Wiley & Sons, New York, 1997.
- Stanford, J.L., J.R. Ziemke, R.D. McPeters, A.J. Krueger, and P.K. Bhartia, Spectral analyses, climatology, and interannual variability of Nimbus-7 TOMS version-6 total column ozone, *Bull. Am. Meteorol. Soc.*, 77, 353-357, 1996.
- Stolarski, R.S., R.D. McPeters, G.J. Labow, S.H. Frith, and L. Flynn, On the long-term calibration of the TOMS total ozone record, in *The Scientific Program of Quadrennial Ozone Symposium*, Sapporo, Japan, 2000.
- Stowe, L.L., C.G. Wellemeyer, T.F. Eck, H.Y.M. Yeh, P.H. Hwang, H.L. Kyle, P.P. Pellegrino, H.Y.M. Yeh, and T.F. Eck, Nimbus-7 global cloud climatology. Part I: Algorithms and validation, *J. Clim.*, 1, 445-470, 1988.
- Stowe, L.L., H.Y.M. Yeh, T.F. Eck, C.G. Wellemeyer, and T.N.-C.D.P. Team, Nimbus-7 global cloud climatology. Part II: First year results., *J. Clim.*, 671-709, 1989.
- Strom, J., H. Fischer, J. Lelieveld, and F. Schroder, In-situ measurements of microphysical properties and trace gases in two cumulonimbus anvils over western Europe, *J. Geophys. Res.*, 104, 12,221-12,226, 1999.
- Suhre, K., J.-P. Cammas, P. Nedelec, R. Rosset, A. Marengo, and H.G.J. Smit, Ozone-rich transients in the upper equatorial Atlantic troposphere, *Nature*, 388, 661-663, 1997.
- Sun, Z., and K.P. Shine, Parameterization of ice cloud radiative properties and its application to the potential climatic importance of mixed-phase clouds, *J. Clim.*, 8, 1874-1888, 1995.
- Takano, Y., and K.-N. Liou, Solar radiative transfer in cirrus clouds. Part II: Theory and computation of multiple scattering in an anisotropic medium, *J. Atmos. Sci.*, 46, 20-46, 1989.

- Thompson, A.M., D.P. McNamara, K.E. Pickering, and R.D. McPeters, Effect of marine stratocumulus on TOMS ozone, *J. Geophys. Res.*, *98*, 23,051-23,057, 1993.
- Thompson, A.M., S.J. Oltmans, F.J. Schmidlin, J.A. Logan, M. Fujiwara, V.W.J.H. Kirchhoff, F. Posny, G.J.R. Coetzee, B. Hoegger, S. Kawakami, T. Ogawa, B.J. Johnson, H. Vömel, and G. Labow, The 1998-2000 SHADOZ (Southern Hemisphere Additional Ozonesondes) tropical ozone climatology. 1: Comparison with TOMS and ground-based measurements, *J. Geophys. Res.*, in press, 2002.
- Thompson, A.M., K.E. Pickering, D.P. McNamara, M.R. Schoeberl, R.D. Hudson, J.H. Kim, E.V. Browell, V.W.J.H. Kirchhoff, and D. Nganga, Where did tropospheric ozone over southern Africa and the tropical Atlantic come from in October 1992? Insights from TOMS, GTE, TRACE-A, and SAFARI 1992, *J. Geophys. Res.*, *101*, 24,251-24,278, 1996.
- Thompson, A.M., and J.C. Witte, SHADOZ (Southern Hemisphere ADDitional OZonesondes): A new data set for the Earth science community, *Earth Obs.*, *11*, 27-30, 1999.
- Torres, O., and P.K. Bhartia, Effect of stratospheric aerosol on ozone profile from BUV measurements, *Geophys. Res. Lett.*, *22*, 235-238, 1995.
- Torres, O., and P.K. Bhartia, Impact of tropospheric aerosol absorption on ozone retrieval from backscattered ultraviolet measurements, *J. Geophys. Res.*, *104*, 21,569-21,577, 1999.
- Torres, O., P.K. Bhartia, J.R. Herman, Z. Ahmad, and J. Gleason, Derivation of aerosol properties from satellite measurements of backscattered ultraviolet radiation: Theoretical basis, *J. Geophys. Res.*, *103*, 17,099-17,110, 1998.
- Twomey, S., H. Jacobowitz, and H.B. Howell, Light scattering by cloud layers, *J. Atmos. Sci.*, *24*, 70-79, 1967.
- Vaughan, G., and J.D. Price, On the relationship between total ozone and meteorology, *Q. J. R. Meteorol. Soc.*, *117*, 1281-1298, 1991.
- Wang, P.-H., P. Minnis, M.P. McCormick, G.S. Kent, and K.M. Skeens, A 6-year climatology of cloud occurrence frequency from Stratospheric Aerosol and Gas Experiment II observations (1985-1990), *J. Geophys. Res.*, *101*, 29,407-29,429, 1996.
- Warren, S.G., Optical constants of ice from ultraviolet to the microwave, *Appl. Opt.*, *23*, 1205-1225, 1984.
- Wellemeyer, C.G., S.L. Taylor, C.J. Seftor, R.D. McPeters, and P.K. Bhartia, A correction for total ozone mapping spectrometer profile shape errors at high latitude, *J. Geophys. Res.*, *102*, 9029-9038, 1997.
- Winterrath, T., T.P. Kurosu, A. Richter, and J.P. Burrows, Enhanced O<sub>3</sub> and NO<sub>2</sub> in thunderstorm clouds: Convection or production? *Geophys. Res. Lett.*, *26*, 1291-1294, 1999.
- WMO, Global Ozone Research and Monitoring Project--Rep. 16, Atmospheric Ozone 1985, Vol. I, pp. 478, NASA, FAA, NOAA, UNEP, WMO, CEC, BFFT, Geneva, Switzerland, 1985.
- WMO, SPARC/IO3C/GAW Assessment of trends in the vertical distribution of ozone, pp. 293, WMO Global Ozone Res. Monit. Proj., Geneva, Switzerland, 1998.
- Wu, M.C., Remote sensing of cloud-top pressure using reflected solar radiation in the oxygen A-band, *J. Clim. & Appl. Meteorol.*, *24*, 539-546, 1985.

- Ziemke, J.R., S. Chandra, and P.K. Bhartia, Two new methods for deriving tropospheric column ozone from TOMS measurements: Assimilated UARS MLS/HALOE and convective-cloud differential techniques, *J. Geophys. Res.*, *103*, 22,115-22,127, 1998.
- Ziemke, J.R., S. Chandra, and P.K. Bhartia, A new NASA data product: Tropospheric and stratospheric column ozone in the tropics derived from TOMS measurements, *Bull. Am. Meteorol. Soc.*, *81*, 580-583, 2000.
- Ziemke, J.R., S. Chandra, and P.K. Bhartia, "Cloud slicing": A new technique to derive upper tropospheric ozone from satellite measurements, *J. Geophys. Res.*, *106*, 9853-9867, 2001.
- Ziemke, J.R., and J.L. Stanford, Kelvin waves in total column ozone, *Geophys. Res. Lett.*, *21*, 105-108, 1994.